Phase-field fracture modeling, numerical solution, and simulations for compressible and incompressible solids

von der Fakultät für Mathematik und Physik
der Gottfried Wilhelm Leibniz Universität Hannover

zur Erlangung des akademischen Grades
Doktorin der Naturwissenschaften
Dr. rer. nat.

genehmigte Dissertation von

M. Sc. Katrin Mang

2022

Referent: Prof. Dr. Thomas Wick, Gottfried Wilhelm Leibniz Universität Hannover
Korreferent: Prof. Dr. Winnifried Wollner, Technische Universität Darmstadt
Korreferent: Prof. Dr. Sven Beuchler, Gottfried Wilhelm Leibniz Universität Hannover
Tag der Promotion: 21.02.2022

Abstract

In this thesis, we develop phase-field fracture models for simulating fractures in compressible and incompressible solids. Classical (primal) phase-field fracture models fail due to locking effects. Hence, we formulate the elasticity part of the phase-field fracture problem in mixed form, avoiding locking. For the elasticity part in mixed form, we prove inf-sup stability, which allows a stable discretization with Taylor-Hood elements. We solve the resulting (3×3) phase-field fracture problem – a coupled variational inequality system – with a primal-dual active set method. In addition, we develop a physics-based Schur-type preconditioner for the linear solver to reduce the computational workload. We confirm the robustness of the new solver for five benchmark tests. Finally, we compare numerical simulations to experimental data analyzing fractures in punctured strips of ethylene propylene diene monomer rubber (EPDM) stretched until total failure to check the applicability on a real-world problem in nearly incompressible solids. Similar behavior of measurement data and the numerically computed quantities of interest validate the newly developed quasi-static phase-field fracture model in mixed form.

Keywords: incompressibility, mixed finite elements, phase-field fracture modeling, rubber-like materials, Schur preconditioning

Contents

Chapter 1

Introduction

Many industrial applications crucially depend on the predictability of material behavior. Nearly incompressible solids, as rubber-like materials, are used in many industry sectors and are of interest in various sciences, i.e., engineering [95, 164] or medicine [96, 152]. Differences in temperature, external forces and internal failures are factors that can ultimately force the material to crack – a process whose understanding and simulation is an ongoing and highly relevant topic in engineering sciences and numerical mathematics.

Within fracture mechanics, the classical (primal) phase-field fracture model [72, 35] is a well-established approach for simulating crack propagation. Still, a reliable numerical simulation often is challenging. Numerical simulations of cracks in nearly incompressible and incompressible solids on the basis of the phase-field fracture model pose an additional challenge. The formulation leads to a coupled variational inequality system (CVIS) – a nonlinear system of partial differential equations whose inequality constraint must be solved carefully. Additionally, the particular property of incompressible solids does not allow standard models. Employing a non-standard mixed problem formulation results in solving an expensive (3×3) system, thereby increasing the computational workload concerning memory and run-time, thus the computational cost. Therefore, the need for developing a problem-specific parallel solver, preconditioned for efficiency, presents another challenge.

In this thesis, we develop phase-field fracture models for simulating fractures in compressible and incompressible solids. We formulate the well-known primal quasi-static phase-field fracture model with elasticity equations in mixed form, avoiding volume-locking. The elasticity problem in mixed form is inf-sup stable on a continuous level, allowing a stable finite element discretization with Taylor-Hood elements. The newly developed phase-field fracture model can be used for simulating fractures for the range from compressible to incompressible solids. In order to solve the resulting CVIS, we transfer a primal-dual active set method from Heister et al. [87] to the mixed phase-field fracture formulation. We derive a physics-based Schur-type preconditioner for the linear solver, chosen to allow for robust and efficient solving. As an iterative linear solver, we use the generalized minimal residual method (GMRES). Further on, we test our solver against five benchmark examples in two spatial dimensions up to the incompressible limit. We compare numerical results to experimental data observing fractures in punctured strips of nearly incompressible ethylene propylene diene monomer rubber (EPDM) to check the applicability of the mixed model to a real-world problem. For the experiments and measurement data, we collaborated with Deutsches Institut für Kautschuktechnologie e.V. (DIK), whose

research focuses on rubber-like materials. The experimental data allows us to evaluate the performance of the newly developed mixed model and, at the same time to point out both possible challenges and opportunities.

In the following, we embed the topic of the thesis into the current state-of-the-art of modeling, numerical solving, and validation with the help of experimental measurement data. We start with the beginning of phase-field fracture modeling and end looking at the available experimental data to progressively assemble the key research questions.

At the beginning of the 20th century, Griffith [81] developed an energetic approach for brittle fracture. His work is regarded as the basis of the modern linear elastic fracture mechanics theory. According to Griffith, a crack propagates when the reduction in potential energy due to crack growth is greater or equal to the increase in surface energy [194]. We can apply his concept to elastic materials that fracture in a brittle fashion. Francfort and Marigo [72], in 1998, formulated Griffith's concept as a handier energy functional depending on a sharp crack C. The resulting functional describes the energy of a crack in an elastic medium.
From a numerical point of view, we still have an intractable problem since we do not know the location of the sharp crack. Thanks to Bourdin et al. [35], and the idea of a diffusive approach for fractures, we can work with a regularized energy functional. Instead of a sharp crack C, we get a smoothed indicator function $\varphi : \Omega \to [0, 1]$, a length scale ϵ of the crack width, and a regularization parameter. A rough idea of the indicator function generally known as the phase-field function φ is depicted in Figure 1.1.

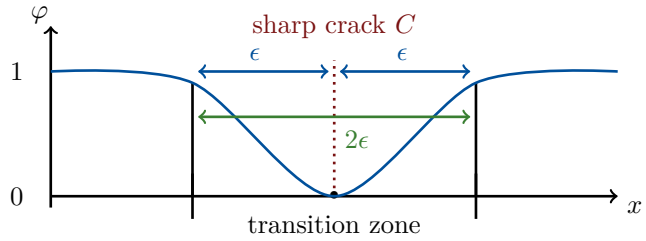

Figure 1.1: A smooth indicator function called phase-field φ, here depicted over a one-dimensional cracked domain. The sharp crack C is approximated with a diffusive crack of bandwidth ϵ.

Kuhn and Müller [112] introduced the name 'phase-field modeling' for a variational approach of the regularized energy functional. The method is applied in numerous studies in the calculus of variations, numerical analysis, and computational engineering. Detailed overviews on phase-field fracture modeling from mechanical and mathematical perspectives are given by Ambati et al. [4], Wu et al. [192], Bourdin and Francfort [34], and Wick [184]. They agree that quasi-static brittle phase-field fracture is a well-established approach to simulate complex crack phenomena, unknown cracks, crack nucleation, branching, and merging. A further positive aspect of phase-field modeling is the relatively simple realization in three dimensions. However, fractures are discontinuities in the displacement field. The smeared crack surface is one of the disadvantages of phase-field fracture modeling, especially in the crack tip: we need a reasonable resolution of the crack area for accurate results and a proper stress intensity representation. At this point, mesh refinement strategies (pure refinement strategies or error estimators) become relevant for reducing numerical simulations' computational cost. Further, adaptive

mesh refinement can significantly improve the quality of the numerical solution. We use an efficient refinement strategy from Heister et al. [87, 88] and manufactured geometric refinement for specific stationary tests. In this context, having an error estimator and localized crack tip mesh refinement would be even more beneficial. We developed a residual-based error estimator for the primal quasi-static phase-field variational inequality in [124], also used by Basava et al. [22].

Concerning the discretization of phase-field fracture problems, we establish the Galerkin finite element method [35]. We use a mesh of quadrilaterals and bilinear or biquadratic H^1-conforming finite elements. Alternatively, Borden et al. [30] first used an isogeometric analysis discretization, and recently, Goswami et al. [80] employed a physics-informed neural network.

Back to the underlying regularized energy functional, mainly in the context of phase-field fracture problems, the Ambrosio-Tortorelli functionals [5, 6] with a linear or quadratic energy degradation function (named AT_1 or AT_2, respectively) are considered. Wu [189, 190] and Wu and Nguyen [191] suggested a unified phase-field theory for damage and quasi-brittle failure with different softening laws. In contrast to the Ambrosio-Tortorelli functionals AT_1 and AT_2, in Wu's model, the phase-field regularization arises in a linear and a quadratic term. We propose the three mentioned energy functionals and discuss differences substantiated with numerical studies. With the notion of Γ-convergence, we can show for the AT_2 functional under certain conditions on the regularization parameters that the regularized phase-field functional converges towards the non-regularized functional from Francfort and Marigo [72]. We retrace the proof of Γ-convergence in 1d according to Braides [40, 41] and present numerical studies on the impact of the regularization parameters for a well-known benchmark test. For the proof of Γ-convergence in higher dimensions and pressurized fractures, we refer to Sommer [157].

Another more mechanical tool is the chosen splitting approach of the Cauchy stress tensor arising in all energy functionals to distinguish between fracture behavior in tension and compression [4]. A commonly used approach is based on a spectral decomposition given by Miehe et al. [130]. Amor et al. [7] derive a volumetric-deviatoric decomposition of the elastic energy density. This thesis investigates the two well-known approaches according to Miehe et al. [130] and Amor et al. [7]. Based on the proposed modeling, we pass on to the numerical solving.

From a computational perspective, based on the considered energy functional, we have to solve a minimization problem. We propose a first-order optimality system that yields the Euler-Lagrange equations by minimizing the energy functional, which we have to solve numerically. As a solution, we achieve stationary points of the energy functional.

According to Griffith's law [81], we assume that cracks are irreversible, which means they cannot heal. The crack irreversibility condition is an additional time-dependent constraint on the phase-field variable yielding a CVIS. Several nonlinear solvers for the inequality constraint exist in the field of phase-field fracture. A relatively simple approach concerning implementation is penalization, which may suffer from ill-conditioning and slow convergence, e.g., Artina et al. [12]. Augmented Lagrangian methods, e.g., presented by Wheeler et al. [176] and Wick [181] are closely related to penalization. Miehe et al. [132, 130] proposed a history field [98] to realize the irreversibility constraint. Another method derived from contact problems is proposed by Mang et al. [128, 124]. The idea is to use a complementarity system and fix the constraint nodes embedded in the discrete system. We use a primal-dual active set method from Heister et al. [87] to handle the inequality constraint. An active set method is attractive since no adjustment of additional parameters is necessary, and it can be interpreted as a semi-smooth Newton method yielding fast convergence of the solver [87].

In this thesis, we concentrate on the fracture behavior of rubber-like materials and the modeling of

their incompressibility property. Incompressible solids do not change their volume under pressure. Mathematically, this property leads to an ill-conditioned system because of a large material parameter. If the considered solid is nearly incompressible, i.e., ethylene propylene diene monomer rubber (EPDM), solving the primal Euler-Lagrange equations fails due to volume locking effects. Locking in finite element simulations results in underestimated solid displacements yielding unreliable solutions. References on phase-field fracture and rubber-like materials are given for rate-dependent phase-field damage models, e.g., Loew et al. [119, 120], and Faye et al. [68] for mass sink models from Volohk [172]. Three options to overcome the problem of locking effects in (nearly) incompressible solids could be a Discontinuous Galerkin method, proposed by Cockburn et al. [57], Wihler [187], and Hansbo and Larson [84], higher-order methods, or mixed methods. We avoid locking effects with the help of the elasticity equation in mixed form, similarly to Braess [39] for saddle point problems with a penalty term: we split the pure elasticity problem into a mixed system by introducing a Lagrange parameter, namely pressure [128]. Using a mixed form embedded in the phase-field fracture problem is new and yields a partial differential equations (PDE) system with three instead of two unknown solution variables. It allows simulating fractures in compressible, nearly incompressible, and incompressible solids. Fulfilling a continuous inf-sup condition allows a discrete inf-sup condition for problem stability. We choose the discrete space for the displacement one order higher than for the introduced pressure variable. Via Taylor-Hood elements, we achieve a stable discretization of the displacement-pressure system, achieving a unique numerical solution. The mixed phase-field fracture problem formulation is a (3×3) system, which increases the computational workload significantly. Efficient iterative solving and preconditioning become indispensable.

Since the 1990s, multilevel, geometric, and especially algebraic multigrid methods (AMG) have gained importance [160] in efficient linear solving. Farrell and Maurini [67] proposed a nonlinear Gauss-Seidel scheme with a Schur-complement preconditioner for elasticity problems. Heister and Wick [88] derived a block-diagonal algebraic multigrid for solving the linear system. Recent works on geometric multigrid, which enable solving the problem in parallel and matrix-free, are given by Jodlbauer et al. [99, 98]. Further, Liu et al. [118] proposed a preconditioned conjugate gradient-based multigrid method for heterogeneous materials in 3d. In the mentioned works, efficient preconditioning for compressible solids is considered.

To the best of the author's knowledge, no robust parallel linear solver for phase-field fracture in mixed form is available in the literature. This thesis develops a robust and efficient Schur-type preconditioner for the three-component phase-field fracture model. Apart from modeling and numerical solving, we aim to simulate fractures in compressible up to incompressible solids, extending phase-field fracture modeling.

In the recent past, many authors contributed improving the understanding of the fatigue behavior of elastomeric (nearly incompressible) materials with phase-field fracture: Kumar et al. [114] discussed a phase-transition theory to model cavitation and healing phenomena for Gent-Park experiments with polydimethylsiloxane containing glass beads. Talamini et al. [162] applied their fracture model to crack propagation experiments of styrene butadiene rubber of the model presented by Hocine et al. [94]. Li and Bouklas [117] proposed a variational phase-field model based on a mechanical network model for polydisperse elastomers combined with phase-field fracture modeling for large deformations. Classical approaches to simulate the crack growth are based on energetic failure criteria using the virtual crack extension method by Charrier et al. [51] or the crack tip closure method by Timbrell et al. [166]. Similar approaches consider cohesive elements, e.g., Kaliske et al. [100] for an application

using inelastic cohesive models.
We collaborated with the DIK within the department 'Simulation and Continuum Mechanics' to validate our newly developed phase-field fracture model with a real-world fracture phenomenon. They conducted experiments and systematic parameter identification on punctured EPDM strips with the help of digital image correlation [127, 123]. EPDM is a nearly incompressible solid matching our new mixed model related to this property. As quantities of interest, we evaluate the crack paths, load-displacement curves, the maximal loading force, and the traverse displacements, which are available from the qualitative experimental measurements.
In summary, the three significant novelties of this thesis are the following:

- Chapter 5: We develop a stable quasi-static phase-field fracture model in mixed form for compressible and incompressible solids;
- Chapter 6: We derive a robust and efficient physics-based Schur-type preconditioner for the phase-field fracture model from Chapter 5;
- Chapter 7: We validate the phase-field fracture model from Chapter 5 with the help of simulating fractures in punctured EPDM strips and comparing the results with experimental data.

The implementation is derived from Example 8 of the instationary PDE Examples in DOpElib [62, 79], and from the parallel-adaptive open-source framework *pfm-cracks* [89], which is based on the deal.II finite element library [9, 18]. DOpElib and deal.II are sustainable open-source software libraries.

The thesis' outline is given in the following:
Chapter 2: Preliminaries
We introduce the basic notation and define finite element spaces. Required key results from functional analysis are given in Section 2.3. We list used symbols and abbreviations in Section 2.4.

Chapter 3: Discretization
In Chapter 3, the numerical discretization of the mixed phase-field fracture problem is described intentionally before the modeling Chapters 4 and 5. We start with a linear-in-time extrapolation in the phase-field variable φ to 'convexify' the equations. Then, we explain the overall solution algorithm: a primal-dual active set method realizes the irreversibility constraint with a two-staged Newton method. A stable discretization in space with Taylor-Hood elements is given in Section 3.2.3. In the last section, we present the used adaptive mesh refinement strategies and available alternatives.

Chapter 4: Phase-field fracture modeling & simulations
Starting from Griffith's concept of fracture mechanics [81], we give a brief introduction to the phase-field approach and the first energy formulation from Francfort and Marigo [72]. Section 4.2 derives the Euler-Lagrange equations from the energy minimization problem, where we embed the irreversibility constraint in the function space of the phase-field function φ. The proof of Γ-convergence of the variational phase-field fracture model (in 1d) links to Francfort and Marigo and Griffith's concept for a crack width $\epsilon \to 0$. In Section 4.6, we give the definitions of three energy functionals. Further, in Section 4.7, we propose two well-known stress splitting approaches. The subsequent sections present numerical studies based on the primal model where we investigate the impact of different energy func-

tionals and stress splitting approaches for well-known academic examples.

Chapter 5: Modeling & simulations for incompressible solids
Considering incompressible solids and using the primal phase-field fracture model leads to the problem of locking effects explained in Section 5.1. We derive a phase-field fracture model with the elasticity part of the problem in mixed form to overcome locking. We prove well-posedness and an inf-sup condition on the continuous level yielding a stable mixed formulation of the displacement-pressure system. For the stable problem, we formulate a stable discrete problem with Taylor-Hood elements from Chapter 3. The subsequent sections present numerical studies concerning locking effects and the first numerical tests for simulating crack propagation based on the newly developed model. The last section discusses and justifies a model modification we implemented to achieve a realistic pressure solution.

Chapter 6: Efficient & robust linear solver
For efficient and parallel solving of the new phase-field fracture model for incompressible solids, we develop in Chapter 6 a physics-based Schur-type block preconditioner and investigate numerical studies based on five numerical examples. We confirm the robustness of the solver for specific tests. Further, we point out and discuss the sensitivity of the solver concerning the parameters' limit in Section 6.3.

Chapter 7: Simulating fractures in punctured EPDM strips
In Chapter 7 we compare experimental and numerical results considering crack propagation in punctured EPDM strips that are elongated until total failure. In the first two sections, we investigate the material compounding at the DIK, the mechanical properties, and the parameter identification. A detailed comparison of numerical results and available experimental data for five test setups follows. We address the most critical challenges to simulate cracks in punctured rubber-like strips. Inclusions play a particular role, and we discuss the crack paths' dependency on the underlying energy functional and the chosen stress splitting in Section 7.5.

Chapter 8: Conclusions & outlook
We conclude the thesis with a recapitulation of the presented results and give ideas for future tasks established from findings and challenges within the thesis.

Some results of the thesis at hand have been published in peer-reviewed journals, conference proceedings, or are recently submitted: [123, 128, 124, 69, 125, 153, 127, 22, 126]. References to own publications are marked with an extra footnote at the beginning of the respective section.

Chapter 2

Preliminaries

This chapter contains the basic notation and preliminaries used throughout the thesis. In Section 2.1, function spaces are defined, including a short outline of Hilbert and Sobolev spaces, norms, and bilinear forms. Definitions of finite element spaces are given in Section 2.2. The most important symbols and abbreviations are listed in Section 2.4.

2.1 Basic notation

We emanate from an open and bounded two-dimensional domain $\Omega \subset \mathbb{R}^2$ with a boundary $\partial\Omega$, which can be decomposed of Dirichlet and Neumann boundaries, $\partial\Omega_D$ and $\partial\Omega_N$, respectively. The outer normal of $\partial\Omega$ is denoted by n [178]. On Ω, we denote the space of continuous functions by $C(\Omega)$, and continuously differentiable functions by $C^1(\Omega)$.

The Frobenius scalar product of two matrices $A, B \in \mathbb{R}^{n\times n}$ of the same dimension is defined as

$$(A : B) \coloneqq \sum_{i=1}^{n}\sum_{j=1}^{n} a_{ij}b_{ij}.$$

The maximum or minimum of two values is denoted by $\max\{.,.\}$ or $\min\{.,.\}$, respectively. We define the trace operator of a symmetric matrix $A \in \mathbb{R}^{n\times n}$ to be

$$\operatorname{tr} A \coloneqq \sum_{j=1}^{n} A_{jj} = (A : \mathbb{1}) = \sum_{j=1}^{n} \lambda_j,$$

where $\mathbb{1}$ denotes the n-dimensional identity matrix, and λ_j are the eigenvalues of the matrix A. The transpose of a quadratic matrix A is A^T, the inverse is denoted as A^{-1}. For sufficiently smooth functions, we use the gradient operator (∇), the divergence operator ($\nabla \cdot u$) and the Laplace operator

(Δ) defined by

$$\nabla p \coloneqq \sum_{j=1}^{d} \frac{\partial p}{\partial x_j} e_j = (\partial_1 u, \ldots, \partial_d u)^T, \quad \nabla u \coloneqq \sum_{i,j=1}^{d} \frac{\partial u}{\partial x_i} e_i \otimes e_j,$$

$$\nabla \cdot u \coloneqq \sum_{j=1}^{d} \frac{\partial u_j}{\partial x_j} = \operatorname{tr} \nabla u, \quad \Delta u = \nabla \cdot (\nabla u) \coloneqq \sum_{j=1}^{d} \frac{\partial^2 u}{\partial x_j^2},$$

for a scalar-valued function $p : \Omega \to \mathbb{R}$, and a vector-valued function $u : \Omega \to \mathbb{R}^d$, where $d = 2$ in the frame of this thesis. The symbol $\otimes$ denotes the tensor product of two unit vectors e_i and $e_j \in \mathbb{R}^d$.

The standard Lebesgue space of measurable functions $u : \Omega \to \mathbb{R}$ is defined as $L^p(\Omega), 1 \leq p \leq \infty$, which is Lebesgue-integrable to the p-th power. The space $L^p(\Omega)$ forms a Banach space with the norm $\|u\|_{L^p(\Omega)}$. A Banach space is a complete and normed space. Complete means that we have a normed space, and all Cauchy sequences converge with their limits in the same space. Sobolev spaces are commonly denoted as $W^{m,p}(\Omega), m \in \mathbb{N}, 1 \leq p \leq \infty$, containing functions with distributional derivatives of order up to m belonging to $L^p(\Omega)$ [177]. For $p = 2$, Hilbert spaces are defined as $H^2(\Omega) \coloneqq W^{m,2}(\Omega)$ with the norm $\|\cdot\|_{H^2(\Omega)}$ [188]. All functions in $W^{m,p}(\Omega)$ with zero traces on the boundary $\partial\Omega$ are denoted as $W_0^{m,p}(\Omega)$.

As one of the most important spaces we define the space $L^2(\Omega)$ as

$$L^2(\Omega) \coloneqq \{u : \Omega \to \mathbb{R}^2 \text{ is Lebesgue measurable } | \int_\Omega u^2 \, dx < \infty\}. \tag{2.1}$$

The space $L^2(\Omega)$ contains all square-integrable functions, and as a complete space it is a Banach space. For functions $u, v \in L^2(\Omega)$, by

$$(u, v) \coloneqq \int_\Omega u \; v \; dx,$$

the standard Euclidean $L^2(\Omega)$ scalar-product is denoted. For tensor-valued functions $U, V \in (L^2(\Omega))^{2\times 2}$, it holds

$$(U, V) \coloneqq \int_\Omega (U : V) \, dx.$$

Further, $L^2(\Omega)$ is a Hilbert space with the associated norm

$$\|\cdot\|_V = \sqrt{(u, u)} = \left(\int_\Omega |u(x)|^2 \, dx \right)^{\frac{1}{2}}.$$

Further, we define the space

$$L^\infty(\Omega) \coloneqq \{a : \Omega \to \mathbb{R}^d : \|a\|_\infty < \infty\},$$

with the norm

$$\|a\|_\infty \coloneqq \operatorname{ess}\ \sup_{x\in\Omega} |a(x)|.$$

We define the Sobolev space $H_0^1(\Omega)$ consisting of (weakly) differentiable functions which vanish on the Dirichlet boundary:

$$H_0^1(\Omega) \coloneqq \{u \in H^1(\Omega) \mid u = 0 \text{ on } \Gamma_D \subset \partial\Omega\}, \tag{2.2}$$

with

$$H^1(\Omega) \coloneqq \{u \in L^2(\Omega) \mid \nabla u \in [L^2(\Omega)]^2\}, \tag{2.3}$$

and the scalar product

$$(u,v)_{H^1(\Omega)} = \int_\Omega uv\,dx + \int_\Omega \nabla u \nabla v\,dx.$$

The corresponding norm is defined as

$$\|u\|_{H^1(\Omega)} \coloneqq \left((u,u)_\Omega + (\nabla u, \nabla u)_\Omega\right)^{\frac{1}{2}}.$$

Together it leads to the definition of the Hilbert space $\left(H^1(\Omega), \|\cdot\|_{H^1(\Omega)}\right)$. The corresponding vector-valued function spaces for $d = 2$ are denoted by $H^1(\Omega;\mathbb{R}^2) = H^1(\Omega) \times H^1(\Omega)$. The $H^1(\Omega)$ dual parings are denoted as $(u,v)_{-1,1}$. For further details on Lebesgue and Sobolev spaces, we refer, e.g., to [188, 1].
Preparatory for the Galerkin finite element method, we define a bilinear form [28].

Definition 1 (Bilinear form)**.** *Let V be a linear space over $\mathbb{R}$. A map $a : V \times V \to \mathbb{R}$ is said to be a bilinear form on V, if for every $\beta, \gamma \in \mathbb{R}$ and every $u, v, w \in V$, it holds*

$$a(u, \beta v + \gamma w) = \beta a(u,v) + \gamma a(u,w),$$
$$a(\beta u + \gamma v, w) = \beta a(u,w) + \gamma a(v,w).$$

A bilinear form $a(u,v)$ is said to be symmetric if $a(u,v) = a(v,u)$. The associated norm $\|\cdot\|_a$ of the scalar product is defined by

$$\|u\|_a \coloneqq \left((u,u)_V\right)^{\frac{1}{2}} \quad \forall v \in V.$$

2.2 Finite element spaces

In this thesis, we employ a Galerkin finite element discretization method in space. Basic literature on finite elements can be found, e.g., in [39, 43, 53]. First, we define a finite element.

Definition 2 (Finite element (K, Q, Ψ) according to Ciarlet [53])**.** *We decompose Ω into a discrete mesh $\mathcal{T}_h = \{K_1, K_2, \ldots, K_N\}$ with mesh size h. For a cell $K \in \mathcal{T}_h$ we define the finite element triple (K, Q, Ψ) consisting of*

1. *subdomains* $K \in \mathcal{T}_h$,
2. *a finite-dimensional space* Q *of functions on* $\mathcal{T}_h$*, which are the shape functions,*
3. *and a set of linearly independent functionals* Ψ *on* Q*, which are the degrees of freedom (dof).*

In this thesis, we partition the domain into regular quadrilaterals $K_i, i = 1, \ldots, N$. The cells $K \in \mathcal{T}_h$ are disjoint and cover the whole domain Ω. We assume having a regular mesh. For adaptive meshes we allow one hanging node at each edge of cells. Instead of exact integrating, numerical quadrature approximates the integrals over all dofs on each cell K. We use the Gauss-Legendre quadrature using roots of the normalized Legendre polynomials [98]. The integrals are evaluated only on a master element $K_0 = (0,1)^2$ and mapped to a particular element K with a bilinear transformation $T : K_0 \to K$. We define two continuous H^1-conforming finite element spaces [43, 53] as

$$Q_1^c \coloneqq \{u_h \in C(\bar{\Omega}) \cap L_0^2(\Omega); u_h|_K \in Q_1(K) \quad \forall K \in \mathcal{T}_h\} \subseteq H^1(\Omega), \tag{2.4}$$
$$Q_2^c \coloneqq \{u_h \in C(\bar{\Omega}) \cap H_0^1(\Omega); u_h|_K \in Q_2(K) \quad \forall K \in \mathcal{T}_h\} \subseteq H^1(\Omega), \tag{2.5}$$

where Q_p, $p = 1, 2$ denotes the space of polynomial-like functions of degree p on each cell $K \in \mathcal{T}_h$. On the reference cell K_0, the space $Q_p(K_0)$ is defined as

$$Q_p(K_0) \coloneqq \left\{ \text{span} \prod_{j=1}^{d} x_j^{\alpha_j}, \quad 0 \le \alpha_j \le p \right\}.$$

With the help of a transformation mapping $T : K_0 \to K$, we can define Q_2^c and Q_1^c elements on a cell K as

$$Q_1^c(K) \coloneqq \left\{ q \circ T^{-1} : q \in \text{span}\,\{1, x, y, xy\} \right\},$$
$$Q_2^c(K) \coloneqq \left\{ q \circ T^{-1} : q \in \text{span}\,\{1, x, y, xy, x^2, y^2, x^2y, y^2x, x^2y^2\} \right\}.$$

The dimension of the space Q_p is $(p+1)^d$, yielding dimension four for Q_1^c elements and dimension nine for Q_2^c elements. For visualization, see Figure 2.1.

Figure 2.1: Left: conforming quadrilateral elements of the type Q_1^c defined in Equation (2.4) with four dof per cell. Right: conforming quadrilateral elements of the type Q_2^c defined in Equation (2.5) with nine dof per cell.

In the frame of this thesis, bilinear and biquadratic H^1-conforming elements are used to discretize a vector-valued function u (displacements), a scalar-valued pressure p, and a scalar-valued phase-field φ. For the coupled pair (u, p) we use well-known finite elements, namely Taylor-Hood elements $Q_2^c Q_1^c$, which fulfill an inf-sup condition (stability estimate) on the discrete level; see Section 5.3 for

the well-posedness of the proposed problem and a proof of inf-sup stability on the continuous level. Taylor-Hood elements are commonly used for the finite element discretization of the Navier-Stokes equations, where the space of the velocities has a higher degree than the pressure polynomial. Bi-quadratic shape functions (Q_2^c) are employed for the two-dimensional displacement field u and bilinear shape functions (Q_1^c) for a pressure variable p. For the phase-field, bilinear shape functions (Q_1^c) are used.

2.3 Tools from functional analysis

Let V be a Hilbert space with norm $\|\cdot\|_V$. We consider a variational problem formulation of the following form:
Find $u \in V$ such that

$$a(u, \psi) = l(\psi) \quad \forall \psi \in V. \tag{2.6}$$

For the Lax-Milgram lemma, and Céa's lemma, the following three properties are required for a variational form of Equation (2.6):

- The right hand side $l(\cdot)$ is a bounded linear form:

$$\exists\, c > 0 : \quad |l(u)| \leq c\|u\|_V \quad \forall u \in V. \tag{2.7}$$

- The bilinear form $a(\cdot, \cdot)$ is continuous on $V \times V$:

$$\exists\, \gamma > 0 : |a(u, v)| \leq \gamma\|u\|_V\|v\|_V \quad \forall u, v \in V. \tag{2.8}$$

- $a(\cdot, \cdot)$ is coercive (or V-elliptic):

$$\exists\, \delta > 0 : a(u, u) \geq \delta\|u\|_V^2 \quad \forall u \in V. \tag{2.9}$$

Lemma 1 (Lax-Milgram according to Ern and Guermond [65])**.** *Let $a(\cdot, \cdot) : V \times V \to \mathbb{R}$ be a continuous and V-elliptic bilinear form. Then for each $l \in V^*$ (dual space of V) the variational problem*

$$a(u, \psi) = l(\psi) \quad \forall \psi \in V,$$

has a unique solution $u \in V$. Moreover, we have the stability estimate

$$\|u\|_V \leq \frac{1}{\alpha}\|l\|_{V^*} = \frac{1}{\alpha} \sup_{\psi \neq 0} \frac{|l(\psi)|}{\|\psi\|_V},$$

where $\alpha > 0$.

Remark 1 (Lax-Milgram for linear PDEs)**.** *The Lax-Milgram lemma yields existence and uniqueness of solutions to linear partial differential equations (PDE) plus a first stability estimate. The fully-coupled phase-field fracture problem with stress splitting is a non-linear problem. If we decouple the elasticity and phase-field problem, Lax-Milgram can be applied as presented in Section 5.1.*

Lemma 2 (Céa's lemma according to Brenner and Scott [43]). *Let V be a Hilbert space with norm $\|\cdot\|_V$, and $V_h \subset V$ be a finite dimensional subspace. Let the three assumptions from Equations (2.7), (2.8), and (2.9) hold true. Let $u \in V$ and $u_h \in V_h$ be the solution of the variational problem*

$$a(u, \psi) = l(\psi) \quad \forall \psi \in V.$$

Then it holds

$$\|u - u_h\|_V = \frac{\gamma}{\alpha} \inf_{\psi_h \in V_h} \|u - \psi_h\|_V,$$

with $\alpha, \gamma > 0$.

Céa's lemma shows that the discrete solution u_h is quasi-optimal in the sense that the error $\|u - u_h\|_V$ is proportional to the best it can be using the subspace V_h.

Lemma 3 (Cauchy-Schwarz inequality). *A special form of Hölder's inequality for $f, g \in L^2(\Omega)$ states that*

$$\|fg\|_{L^1(\Omega)} \leq \|f\|_{L^2(\Omega)} \|g\|_{L^2(\Omega)}.$$

Lemma 4 (Inequality used in Chapter 5). *We will use the following relation:*

$$r \leq \frac{s^2}{r} + t \quad \Rightarrow \quad r \leq s + t \quad \text{for } r, s, t \in \mathbb{R}^+.$$

Proof We show that if $r > s + t$ it follows $r > \frac{s^2}{r} + t$. Let $r > s + t$

$$\Rightarrow r - t > s \quad \Rightarrow 1 > \quad \frac{s}{r - t} \quad \Rightarrow r > s \cdot \frac{s}{r - t} + t = \frac{s^2}{r - t} + t > \frac{s^2}{r} + t \quad \text{for } r, s, t \in \mathbb{R}^+.$$

□

For standard literature on functional analysis we refer, e.g., to [2, 109, 175, 195].

2.4 Symbols and abbreviations

The used symbols and abbreviations are listed in the following Tables 2.1 and 2.2.

Symbol	description
Ω	two-dimensional domain
$\partial\Omega$	surface of the domain Ω
$\bar{\Omega}$	closure of domain Ω
Γ	boundary of Ω
$\mathbb{1}$	two-dimensional identity matrix
$\mathcal{V}$	function space $H_0^1(\Omega;\mathbb{R}^2)$
$\mathcal{W}$	function space $H^1(\Omega)$
$\mathcal{K}$	convex subset of $\mathcal{W}$, $\mathcal{K} \coloneqq \{\varphi^n \in \mathcal{W} \,\vert\, \varphi^n - \varphi^{n-1} \leq 0 \text{ a.e. in } \Omega\}$
$\mathcal{U}$	function space $L^2(\Omega)$
(U, V)	Frobenius scalar product of two matrices U and V
(u, v)	L^2 scalar product of two functions u, v
$a(\cdot,\cdot)$	bilinear form
tr()	trace operator
$\|.\|_n$	Sobolev-norm of order n
d	spatial dimension
$\max\{\cdot,\cdot\}$	maximum function
sup, inf	supremum/infimum function
t	loading time in incremental problems, unit s
C	one-dimensional fracture/crack, unit m
l	crack length
l_0	initial crack length
I	time/loading interval, unit s
T	end time of loading interval I, unit s
n	index of incremental step
δt	incremental step size
$\mathcal{T}_h$	discrete mesh of domain Ω
h	spatial discretization parameter/cell diameter, unit m
u	vector-valued displacement field with components u_x and u_y
u_D	continuation of the Dirichlet data of u
∇u	gradient of displacements $u : \Omega \to \mathbb{R}^2$
Δu	Laplacian of displacements $u : \Omega \to \mathbb{R}^2$
$\sigma(u)$	Cauchy stress tensor
$E_{\text{lin}}(u)$	linearized strain tensor
ρ	pressure quantity for pressurized fractures, unit Pa
φ	continuous phase-field function between 0 and 1
φ_0	initial value for phase-field function φ
$\partial_t\varphi$	time derivative of phase-field φ
τ	Lagrange multiplier
U	total solution vector for $(u, \varphi)^T$ or $(u, p, \varphi)^T$
κ	regularization parameter of the bulk term
ϵ	regularization of the crack, unit m
$g(\varphi)$	degradation function of bulk term
G_C	critical energy release rate, material dependent, unit N/mm
E	Young's modulus, unit MPa
K	bulk modulus, unit MPa
λ, μ	Lamé coefficients, material dependent, unit N/mm^2
ν	Poisson's ratio
$\mathcal{H}^1$	1-dimensional Hausdorff measure
$E_S(C)$	crack surface energy
$E_T(u, C)$	total energy

Table 2.1: List of the most important used symbols.

Abbreviation	description
1d, 2d, 3d	one, two or three dimensional in space
AS	primal-dual active set method
AT_1, AT_2	Ambrosio-Tortorelli functionals
AMG	algebraic multigrid method
COD	crack opening displacement
CG	conjugate gradients method
CPU	central processing unit
CVIS	coupled variational inequality system
deal.II	C++ finite element library (Differential Equations Analysis Library)
DIC	digital image correlation
DIK	Deutsches Institut für Kautschuktechnologie e. V., Hannover
dof	degrees of freedom
DOpElib	C++ package - Differential Equations and Optimization Environment library
EPDM	ethylene propylene diene monomer rubber
FE	finite element
FEM	finite element method
GMRES	generalized minimal residual method
LBB	Ladyzhenskaya–Babuška–Brezzi condition
ML	Multi Level preconditioning package of Trilinos
PDE	partial differential equations
SI	International System of Units
TCV	total crack volume

Table 2.2: List of abbreviations.

Conclusions of the chapter

Further theorems and lemmas are given in the thesis, where they are discussed or proven. Based on the given notation, the next chapter describes the discretization of the CVIS derived in later Chapters 4 and 5.

Chapter 3

Discretization

In this chapter, we explain the discretization of the Euler-Lagrange equations derived in Chapter 4. Further, in Chapter 5, the elasticity part of the phase-field fracture problem is formulated in mixed form, which leads to a coupled variational inequality system (CVIS) with three unknowns. Since the following two chapters on modeling contain first numerical results, the discretization of the primal (Chapter 4) and the mixed phase-field fracture problem (Chapter 5) is the subject of this chapter. We consider the following (later derived) primal problem formulation for pressurized fractures from Chapter 4:

Formulation 1 (Primal phase-field fracture problem, pressure driven)**.**
Let a pressure $\rho \in L^\infty(\Omega)$ be given. Find a vector-valued displacement function $u \in \mathcal{V} + \{u_D\}$, where u_D is a continuation of the Dirichlet data, and a phase-field function $\varphi \in \mathcal{K} := \{\varphi^n \in \mathcal{W} \,|\, \varphi^n - \varphi^{n-1} \leq 0 \text{ a.e. in } \Omega\}$, such that

$$\begin{aligned} \Big(g(\varphi)\sigma(u)\,, E_{lin}(w)\Big) + (\varphi^2\rho, \nabla \cdot w) = 0 \quad \forall w \in \mathcal{V}, \\ (1-\kappa)(\varphi\sigma(u) : E_{lin}(u), \psi - \varphi) + 2(\varphi\rho\nabla \cdot u, \psi - \varphi) \\ + G_C\Big(-\frac{1}{\epsilon}(1-\varphi, \psi-\varphi) + \epsilon(\nabla\varphi, \nabla(\psi-\varphi))\Big) \geq 0 \quad \forall \psi \in \mathcal{K}, \end{aligned}$$

with the Cauchy stress tensor $\sigma(u) := 2\mu E_{lin}(u) + \lambda \operatorname{tr}(E_{lin})\mathbb{1}$, where $E_{lin}(u) = \frac{1}{2}(\nabla u + \nabla u^T)$, and $\lambda, \mu > 0$. Further, $g(\varphi) = (1-\kappa)\varphi^2 + \kappa$, with $\kappa > 0$ sufficiently small, and $G_C > 0$ is the critical energy release rate or material toughness. The proposed formulation coincides with Proposition 3 from Section 4.2. The time-dependency is embedded in the convex subset $\mathcal{K}$ containing the crack irreversibility condition.

The mixed problem formulation from Chapter 5 will be derived as:

Formulation 2 (Mixed phase-field fracture problem, pressure driven)**.**
Let a pressure $\rho \in L^\infty(\Omega)$ be given. Find a vector-valued displacement function $u \in \mathcal{V} + \{u_D\}$, a pressure function $p \in \mathcal{U} := L^2(\Omega)$ (defined in Equation (2.1)) and a phase-field function $\varphi \in \mathcal{K}$, such

that

$$\begin{aligned}
\Big(g(\varphi)\sigma(u,p)\,,E_{lin}(w)\Big) + (\varphi^2\rho, \nabla\cdot w) = 0 \quad \forall w \in \mathcal{V},\\
g(\varphi)(\nabla\cdot u, q) - (\frac{1}{\lambda}p, q) = 0 \quad \forall q \in \mathcal{U},\\
(1-\kappa)(\varphi\sigma(u,p) : E_{lin}(u), \psi-\varphi) + 2(\varphi\rho\nabla\cdot u, \psi-\varphi)\\
+G_C\Big(-\frac{1}{\epsilon}(1-\varphi, \psi-\varphi) + \epsilon(\nabla\varphi, \nabla(\psi-\varphi))\Big) \geq 0 \quad \forall \psi \in \mathcal{K},
\end{aligned}$$

with the Cauchy stress tensor defined pressure-dependent as $\sigma(u,p) \coloneqq 2\mu E_{lin}(u) + p\mathbb{1}$*, and* $\kappa > 0$ *sufficiently small. This formulation coincides with Formulation 11 from Section 5.2 aside from time-lagging.*

Remark 2 (Solving of the primal problem)**.** *For completeness, both the primal and the mixed problem formulation are given above. In the following, we concentrate on the discretization of the mixed problem Formulation 2. Numerical results in later chapters based on Formulation 1 are solved exactly as by Heister et al. [87].*

We want to solve the proposed CVIS numerically. The inequality arises from a constraint on the crack behavior, which is explained in Section 4.2.
In both systems, products of φ and u intuitively lead to staggered/partitioned solving schemes, e.g., [47]. The problem becomes strictly convex by fixing one variable and solving the other equation. Proofs on alternating minimization are presented by Bourdin [32] and Burke et al. [49], stabilized staggered iterations are employed by Brun et al. [47]. However, the convergence of the iteration between the two minimization problems can be slow, and the coupling conditions are not fulfilled exactly as in a monolithic solving scheme. Regarding robustness and efficiency, we prefer treating the phase-field fracture problem in a monolithic fashion, e.g., [181, 182]. For example, for the single-edge notched pure shear test, Gerasimov and de Lorenzis [76] stated that a pure monolithic scheme is more efficient than alternating minimization. Another approach of Gerasimov et al. [77] is stochastic phase-field modeling.
The coupling term $g(\varphi)(E_{\text{lin}}(u), E_{\text{lin}}(w)) \approx \varphi^2(\nabla u)^2$ makes the PDE non-convex. If the existence of a solution can be proved, it need not be unique [35]. To deal with the non-convex elasticity equation in a monolithic approach, we use linearization by linear extrapolation in φ in the u-equation, according to Heister et al. [87].
We explain the overall solution strategy and the spatial discretization in the adjacent section. We use a primal-dual active set method from Heister et al. [87] applied to the proposed mixed elasticity problem, which can be interpreted as a semi-smooth Newton method. In Section 3.3, we address adaptive mesh refinement, where we employ a predictor-corrector refinement scheme from Heister et al. [87].

3.1 Extrapolation and quasi-time discretization

Due to a quasi-static problem formulation, we have incremental steps instead of true time steps, indexed by $n = 1, \ldots, N$ [184], which corresponds to a backward Euler discretization. The size of the incremental steps in quasi-time is denoted as $\delta t > 0$, the quasi-time in incremental step n is denoted

as t_n. Formulation 2 in incremental form convexifies the displacement equation via extrapolation in quasi-time.

3.1.1 Phase-field extrapolation

Extrapolation allows approximating a value via an estimation based on an iteration starting with unknown values. A visualization of the linear-in-time extrapolation is given in Figure 3.1.

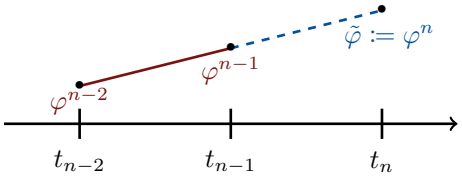

Figure 3.1: Linear-in-time extrapolation in time of $\tilde{\varphi}$; φ^{n-2} and φ^{n-1} from the previous time/incremental steps are given.

Linear interpolation in time is stated as follows for the phase-field function φ [184]:

Proposition 1 (Linear-in-time extrapolation according to Heister et al. [87])**.**
Let φ^n be the phase-field solution in time step t_n at incremental step n, $n = 1, \dots, N$. Linearize the first term from Formulation 2 by a time-lagged extrapolation with

$$\tilde{\varphi} \coloneqq \tilde{\varphi}(\varphi^{n-1}, \varphi^{n-2}) = \varphi^{n-2} \frac{t_n - t_{n-1}}{t_{n-2} - t_{n-1}} + \varphi^{n-1} \frac{t_n - t_{n-2}}{t_{n-1} - t_{n-2}}. \tag{3.1}$$

We follow a common abuse of language by referring to t as *time*. Rigorously, as we place ourselves in the context of quasi-static evolution, t is an increasing loading parameter [33]. Further, we emphasize that the required regularity in time for extrapolation cannot be ensured by quasi-static problems, which means that jumps in time can arise; see [184, 133, 181]. Recent work on a fully monolithic scheme with a modified Newton method is given by Lampron et al. [115] who use an extrapolation correction loop controlled by a damage-based criterion and promise a significant reduction in computation time.

Remark 3 (Enhanced extrapolation)**.** *There exist a simple but effective method to improve the approximation quality from the extrapolation in Equation (3.1); see Wick [184, Section 7.7.3] for further details.*

The incremental form of Formulation 2 is as follows:

Formulation 3 (Incremental form of mixed phase-field fracture problem, pressure driven)**.** *Let a pressure $\rho \in L^\infty(\Omega)$ be given. We define $\tilde{\varphi} \coloneqq \tilde{\varphi}(\varphi^{n-1}, \varphi^{n-2})$. Given the initial data $\varphi^{n-1}, \varphi^{n-2} \in \mathcal{K}$. Find $u^n \in \mathcal{V}$, $p^n \in \mathcal{U}$ and $\varphi^n \in \mathcal{K}$ for incremental steps $n = 1, 2, \dots, N$ such that*

$$\begin{aligned}
\big(g(\tilde{\varphi}(\varphi^{n-1}, \varphi^{n-2}))\sigma(u^n, p^n), E_{lin}(w)\big) + ((\tilde{\varphi}(\varphi^{n-1}, \varphi^{n-2}))^2 \rho, \nabla \cdot w) = 0 \quad \forall w \in \mathcal{V},\\
g(\tilde{\varphi}(\varphi^{n-1}, \varphi^{n-2}))(\nabla \cdot u^n, q) - \frac{1}{\lambda}(\nabla p^n, \nabla q) = 0 \quad \forall q \in \mathcal{U},\\
(1-\kappa)(\varphi^n \sigma(u^n, p^n) : E_{lin}(u^n), \psi - \varphi^n) + 2(\varphi^n \rho \nabla \cdot u^n, \psi - \varphi^n)\\
+ G_C\Big(-\frac{1}{\epsilon}(1 - \varphi^n, \psi - \varphi^n) + \epsilon(\nabla \varphi^n, \nabla(\psi - \varphi^n))\Big) \geq 0 \quad \forall \psi \in \mathcal{K},
\end{aligned}$$

with $\sigma(u^n, p^n) = 2\mu E_{lin}(u^n) + p^n \mathbb{1}$, *and* $\kappa > 0$ *sufficiently small.*

In the following, we use as short notation $\tilde{\varphi}$ instead of $\tilde{\varphi}(\varphi^{n-1}, \varphi^{n-2})$, and omit the incremental index in the solution variables for readability. We define

$$F = \begin{pmatrix} F^u \\ F^p \\ F^\varphi \end{pmatrix}, \tag{3.2}$$

where

$$\begin{aligned} F^u &:= (g(\tilde{\varphi})\sigma(u^n, p^n), E_{\text{lin}}(w)) + (\tilde{\varphi}^2 \rho, \nabla \cdot w), \\ F^p &:= g(\tilde{\varphi})(\nabla \cdot u^n, q) - \frac{1}{\lambda}(\nabla p^n, \nabla q), \\ F^\varphi &:= (1-\kappa)(\varphi^n \sigma(u^n, p^n) : E_{\text{lin}}(u^n), \psi - \varphi^n) + 2(\varphi^n \rho \nabla \cdot u^n, \psi - \varphi^n) \\ &\quad + G_C\Big(-\frac{1}{\epsilon}(1-\varphi^n, \psi - \varphi^n) + \epsilon(\nabla \varphi^n, \nabla(\psi - \varphi^n))\Big). \end{aligned} \tag{3.3}$$

3.1.2 Numerical studies on monolithic versus quasi-monolithic solving

The following numerical study analyzes the impact of extrapolation in φ on the solution for a well-known test example. Numerical results are presented for the single-edge notched shear test à la Miehe et al. [132, 130], visualized in Figure 3.2.

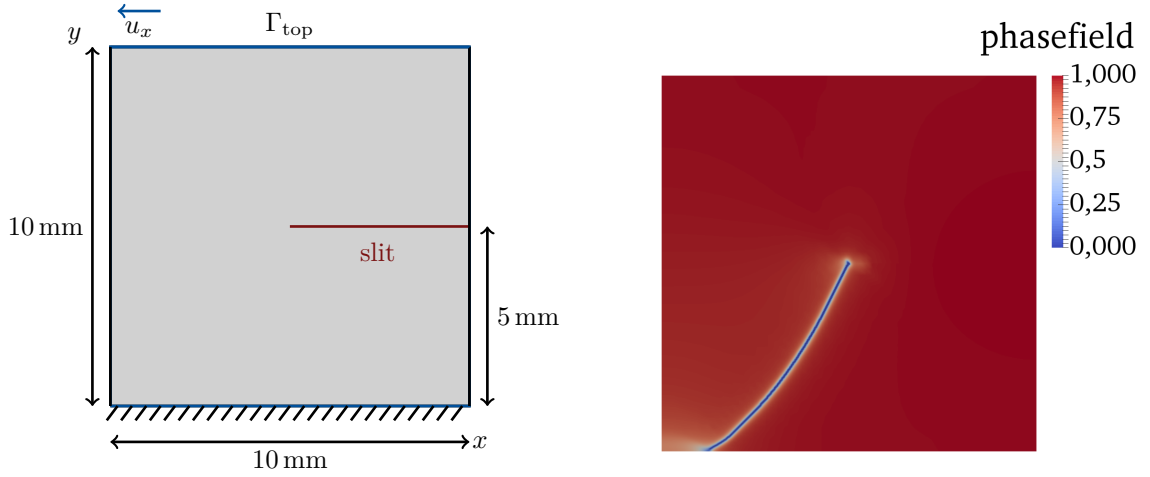

Figure 3.2: Left: geometry and boundary conditions of the single-edge notched shear test. On the left and right side and the lower part of the slit, the boundary condition in the y-direction is $u_y = 0\,\text{mm}$ and traction-free in the x-direction. On the bottom boundary, it holds $u_x = u_y = 0\,\text{mm}$. On the top boundary, it holds $u_y = 0\,\text{mm}$ and in the x-direction we determine a time-dependent non-homogeneous Dirichlet condition: $u_x = t \cdot 1\,\text{mm/s}$ with an incremental step size $\delta t > 0$. Right: Snapshot of the phase-field solution for the single-edge notched shear test after total failure.

The domain Ω is a two-dimensional square of 10 mm length with a given crack (called geometrical slit) on the right side at 5 mm tending to the midpoint of the square. On the bottom boundary, the

square is fixed, and on the top boundary, a given displacement in the x-direction pulls to the left. We follow the boundary conditions defined by Wick [182]: On the left and right sides, the boundaries are defined to be traction-free (homogeneous Neumann conditions). The bottom boundary is fixed via $u_x = u_y = 0\,\text{mm}$. On the top boundary, it holds $u_y = 0\,\text{mm}$ and in the x-direction we determine a time-dependent non-homogeneous Dirichlet condition: $u_x = t \cdot 1\,\text{mm/s}$ for an interval $I := [0, T]$, $T > 0$ with an incremental step size, $\delta t = t_n - t_{n-1}$ with $\delta t > 0$. The end time T is the incremental loading once the specimen is broken. We emphasize that δt only arises in the inequality constraint due to

$$\partial_t \varphi \approx \frac{\varphi_n - \varphi_{n-1}}{\delta t} \leq 0.$$

Multiplying with δt yields

$$\varphi_n - \varphi_{n-1} \leq 0.$$

In practice, the equations on the boundary conditions are scaled with δt. For further details, we refer to an open-source implementation in DOpElib [62, 79], |kmExample 8 and 9 of the instationary PDE Examples. There, two files are available for assembling the PDE system:
`localpde_fully_implicit.h` and `localpde_quasi_monolithic.h`.
The implicit version is a fully monolithic scheme, while the quasi-monolithic assembly is extrapolated in time. In the following, we compare the two assemblies.

The material and model parameters are given as follows: the Lamé coefficients are stated as $\lambda = 121.15\,\text{kN/mm}^2$ and $\mu = 80.77\,\text{kN/mm}^2$. The critical energy release rate of the considered material is $G_C = 2.7\,\text{N/mm}$. The incremental step size is chosen as $\delta t = 10^{-4}\,\text{s}$. We chose the bulk regularization parameter $\kappa = 10^{-8}$.
As a quantity of interest, we evaluate the load functions on the top boundary Γ_{top} computed via

$$(F_x, F_y) := \frac{1}{|\Gamma_{\text{top}}|} \int_{\Gamma_{\text{top}}} g(\tilde{\varphi}) \sigma(u_h) \cdot n \, \mathrm{d}s, \tag{3.4}$$

with the stress tensor $\sigma(u_h)$ depending on the discrete solution variable u_h and the outer normal vector n. Within the single-edge notched shear test, we are interested in the evaluation of F_x. The computations are executed on a uniform refined mesh with 3 315 dof (Q_1^c elements for u and φ, primal Formulation 1) per loading/incremental step and end time for all tests is 0.014 s. In Table 3.1, the maximal loading values F_x defined in Equation (3.4) are given for a fully monolithic scheme with 140 incremental steps from 0 to 0.014 s (which corresponds to an incremental step size of 10^{-4} s) compared to results based on the quasi-monolithic approach using extrapolation.

With 1 400 incremental steps, which corresponds to an incremental step size of 10^{-5} s, the crack starts propagating at a similar quasi-time point compared to the results based on the fully monolithic approach even if the loading values differ, the maximal value is at a similar time point. Based on this simple study, we can hope to decrease the incremental step size by around 1/10 (or more) if we use an extrapolated phase-field in the displacement equation.

Miehe et al. [130] stated an incremental step size of 10^{-5} s for the first 500 incremental steps and reduced to 10^{-6} s when crack propagation starts. With this, the crack starts propagating at a displacement of around 0.009 mm, depending on the mesh size (around 20 000 cells).

Model	#incremental steps	time crack start $[s]$	maximal loading F_x $[N]$
quasi-monolithic	140	0.01010	551.784
quasi-monolithic	160	0.00998	550.277
quasi-monolithic	180	0.00995	549.200
quasi-monolithic	200	0.00994	548.138
quasi-monolithic	280	0.00980	546.365
quasi-monolithic	700	0.00974	544.732
quasi-monolithic	1 400	0.00968	553.503
fully monolithic	140	0.00960	538.596

Table 3.1: Comparison of time of crack initiation for the single-edge notched shear test along to Miehe et al. [130] for a fully monolithic approach (last line in blue) and the proposed quasi-monolithic one. In the last column, the computed maximal loading force is given. These results were also contributed to [184, Section 8.9.3].

Remark 4 (Qualitative study)**.** *We emphasize, that the study on the monolithic and quasi-monolithic scheme allows only to evaluate the behavior of extrapolation for one well-known academic test example based on a relatively coarse uniform mesh. The result decreasing the step size around* $1/10$*th can just be seen as a magnitude to classify the error produced via extrapolation in time.*

3.2 A primal-dual active set method

Several possibilities can be found in the literature to impose the irreversibility constraint. We just name a few: simple penalization with a penalization parameter that penalizes the PDE when the constraint is violated, Augmented Lagrangian, primal-dual active set method, or interior-point methods. For further details, we refer to Wick [184, Section 5.2]. In this thesis, a primal-dual active set method is used. One can show for model problems that the primal-dual active set method is equivalent to a semi-smooth Newton method [93]. We employ Newton's method instead of solving the system from Formulation 3 directly for a solution vector $U := (u, p, \varphi) \in \mathcal{V} \times \mathcal{U} \times \mathcal{K}$ subject to the irreversibility condition. As we see in Chapter 4, the inequality constraint arises from the inequality constraint on φ such that $\partial_t \varphi \leq 0$, and a convex subset of $\mathcal{W} := H^1(\Omega)$ (defined in Equation (2.3)) which contains the irreversibility condition: $\mathcal{K} := \{\varphi^n \in \mathcal{W} \,|\, \varphi^n - \varphi^{n-1} \leq 0 \text{ a.e. in } \Omega\}$. In the following, the constraint is separated from the equations for introducing the primal-dual active set scheme.
The next two subsections follow basically [87] and [106] applied to the mixed problem Formulation 2 from Chapter 3 (derived in Chapter 5).

3.2.1 Newton's method

We propose Newton's method for solving Formulation 2 from Chapter 3.

Algorithm 1 (Newton's method for the mixed phase-field fracture problem, pressure driven)**.**
The solution vector in incremental step n *is defined as* $U^n := (u^n, p^n, \varphi^n) \in \mathcal{V} \times \mathcal{U} \times \mathcal{K}$ *for* $n = 1, 2, \ldots, N$*. Let* $U^0, U^1, U^2, \ldots, U^K$ *be a sequence of solutions and* U^0 *is a given initial guess. Find* δU^k *for* $k = 1, 2, \ldots, K$ *with*

$$\nabla F(U^k)\delta U^k = -F(U^k), \quad \text{with } (\delta U^k)^\varphi \leq 0 \quad \text{on } \Theta := \{0\} \times \{0\} \times \mathcal{W}, \tag{3.5}$$

and the update is computed via

$$U^{k+1} = U^k + \delta U^k,$$

until a stopping criterion (relative tolerance of 10^{-7}*) is fulfilled. From Equation (3.5),* $(\delta U^k)^\varphi \leq 0$ *on* Θ *implies that*

$$U^{k+1} = U^k + \delta U^k \leq U^k \leq U^{k-1} \leq \ldots \leq U^0 \quad \text{on } \Theta,$$

where U^0 *is the initial condition on* Θ*.*

Equation (3.5) can be written as a system of the form

$$\mathcal{M}^k \delta U^k = -F(U^k), \quad \text{for } k = 1, 2, \ldots, K, \tag{3.6}$$

with the Jacobian $\mathcal{M}^k := \nabla F(U^k)$, where F is the right hand side consisting of the residuals defined in Equation (3.3). The Jacobian and the solution vector are defined as

$$\mathcal{M} = \begin{pmatrix} M^{uu} & M^{up} & M^{u\varphi} \\ M^{pu} & M^{pp} & M^{p\varphi} \\ M^{\varphi u} & M^{\varphi p} & M^{\varphi\varphi} \end{pmatrix}, \quad \delta U^k = \begin{pmatrix} \delta U^u \\ \delta U^p \\ \delta U^\varphi \end{pmatrix},$$

where we omit the incremental index k from the quasi-time discretization in the following for readability. The components for the right hand side and the component-wise block entries of the Jacobian $\mathcal{M}$ are defined as:

$$\begin{aligned}
F_i^u &:= (g(\tilde{\varphi}) 2\mu E_{\text{lin}}(u), E_{\text{lin}}(\chi_i^u)) + (g(\tilde{\varphi}) p, \nabla \cdot \chi_i^u) + (\tilde{\varphi}^2 \rho, \nabla \cdot \chi_i^u), \\
F_i^p &:= g(\tilde{\varphi})(\nabla \cdot u, \chi_i^p) - \frac{1}{\lambda}(p, \chi_i^p), \\
F_i^\varphi &:= (1-\kappa)(\varphi 2\mu E_{\text{lin}}(u) : E_{\text{lin}}(u), \chi_i^\varphi) + (1-\kappa)(\varphi(p\mathbb{1} : E_{\text{lin}}(u), \chi_i^\varphi) \\
&\quad + 2\rho(\varphi \nabla \cdot u, \chi_i^\varphi) + G_C(-\frac{1}{\epsilon}(1-\varphi, \chi_i^\varphi) + \epsilon(\nabla\varphi, \nabla\chi_i^\varphi)), \\
M_{i,j}^{uu} &= (g(\tilde{\varphi}) 2\mu E_{\text{lin}}(\chi_j^u), E_{\text{lin}}(\chi_i^u)), \\
M_{i,j}^{pu} &= g(\tilde{\varphi})(\nabla \cdot \chi_j^u, \chi_i^p), \\
M_{i,j}^{\varphi u} &= (1-\kappa)(\varphi 2\mu(E_{\text{lin}}(\chi_j^u) : E_{\text{lin}}(u) + E_{\text{lin}}(u) : E_{\text{lin}}(\chi_j^u)), \chi_i^\varphi) + 2\rho(\varphi \nabla \cdot \chi_j^u, \chi_i^\varphi), \\
M_{i,j}^{up} &= (g(\tilde{\varphi}) \chi_j^p, \nabla \cdot \chi_i^u), \\
M_{i,j}^{pp} &= -\frac{1}{\lambda}(\chi_j^p, \chi_i^p), \\
M_{i,j}^{\varphi p} &= (1-\kappa)(\varphi \chi_j^p \mathbb{1} : E_{\text{lin}}(u), \chi_i^\varphi), \\
M_{i,j}^{u\varphi} &= 0, \\
M_{i,j}^{p\varphi} &= 0, \\
M_{i,j}^{\varphi\varphi} &= (1-\kappa)(\chi_j^\varphi 2\mu E_{\text{lin}}(u) : E_{\text{lin}}(u), \chi_i^\varphi) + (1-\kappa)(\chi_j^\varphi (p\mathbb{1} : E_{\text{lin}}(u)), \chi_i^\varphi), \\
&\quad + 2\rho(\chi_j^\varphi \nabla \cdot u, \chi_i^\varphi) + G_C(\frac{1}{\epsilon}(\chi_j^\varphi, \chi_i^\varphi) + \epsilon(\nabla\chi_j^\varphi, \nabla\chi_i^\varphi)),
\end{aligned} \tag{3.7}$$

with ansatz functions $(\chi_j^u, \chi_j^p, \chi_j^\varphi) \in \mathcal{V}_h \times \mathcal{U}_h \times \mathcal{K}_h$ and test functions $(\chi_i^u, \chi_i^p, \chi_i^\varphi) \in \mathcal{V}_h \times \mathcal{U}_h \times \mathcal{K}_h$ for $i, j = 1, \ldots, N$ with N total nodes.

3.2.2 Active set method

In a discrete form, the constraint can be rewritten as: $\varphi^n \leq \varphi^{n-1}$. The rough idea of the primal-dual active set method is to split the domain Ω into two subdomains: one with a Lagrange multiplier $\tau \in \{0\} \times \{0\} \times \mathcal{W}^*$ ($\mathcal{W}^*$ is the dual space of $\mathcal{W}$), where the inequality constraint is an equality constraint: $\varphi^n = \varphi^{n-1}$. The second domain is located where the inequality constraint holds strictly: $\varphi^n < \varphi^{n-1}$. The problem is solved on the latter while the former subdomain is ignored. It results in a two-staged Newton algorithm: a Newton iteration for the PDE on Ω and a linear Newton iteration after eliminating all rows to be ignored. We can rewrite the variational inequality system with the help of a Lagrange multiplier $\tau \in \{0\} \times \{0\} \times \mathcal{W}^*$ as:

$$\begin{aligned} (\mathcal{M}\delta U, Z) + (\tau, Z) &= (-F, Z) \quad \forall Z \in \mathcal{V} \times \mathcal{U} \times \mathcal{W}, \\ C(\delta U, \tau) &= 0, \end{aligned} \tag{3.8}$$

where

$$C(\delta U, \tau) = \tau - \max\{0, \tau + c\delta U\},$$

for a given $c > 0$. The max-operation works component-wise. We gain good computational experience with the heuristic choice $c = \frac{E}{\epsilon}$, where E is Young's modulus, and ϵ the crack's bandwidth.
In the next step, Equation (3.8) is eliminated via splitting the domain into an active set $\mathcal{A}$ and an inactive set $\mathcal{N}$. On the active set, the constraint holds, and the solution U does not change, so no PDE is solved. The unconstrained PDE system is solved on the inactive set and the constraint is ignored; see Figure 3.3 for a simple visualization for an obstacle problem.

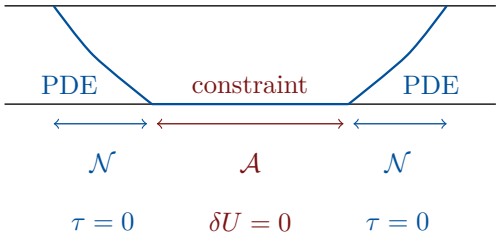

Figure 3.3: Exemplary in one dimension for an obstacle problem: a clothesline touching the ground. Visualized is the definition of the active set ($\mathcal{A}$), the inactive set ($\mathcal{N}$), the Lagrange multiplier (τ) and the Newton update (δU).

The active set algorithm on a continuous level is given as follows:

Algorithm 2 (Active set on a continuous level according to Heister et al. [87])**.** *Repeat for* $k = 0, \ldots$ *until* $\mathcal{A}^k$ *does no longer change:*

1. *Compute the active and the inactive set via:*

$$\begin{aligned} \mathcal{A}^{k+1} &= \left\{x |\ \tau^k(x) + c\ U^k(x) > 0\right\}, \\ \mathcal{N}^{k+1} &= \left\{x |\ \tau^k(x) + c\ U^k(x) \leq 0\right\}. \end{aligned}$$

2. *Find* $\delta U^{k+1} \in \mathcal{V} \times \mathcal{U} \times \mathcal{W}$ *and* $\tau^{k+1} \in \{0\} \times \{0\} \times \mathcal{W}^*$ *with*

$$\begin{aligned}(\mathcal{M}\delta U^{k+1}, Z) + (\tau^{k+1}, Z) &= (-F, Z) \quad \forall Z \in \mathcal{V} \times \mathcal{U} \times \mathcal{W},\\ (\delta U^{k+1}, \xi) &= 0 \text{ on } \mathcal{A}^k \quad \forall \xi \in \{0\} \times \{0\} \times \mathcal{W}^*,\\ \tau^{k+1} &= 0 \text{ on } \mathcal{N}^k.\end{aligned}$$

As seen in Algorithm 2, the Newton algorithm proceeds in two steps: For a given δU^k and τ^k we compute the active set $\mathcal{A}^k$ and the inactive set $\mathcal{N}^k$ and solve the system to find δU^{k+1} and τ^{k+1}. The iteration is repeated until $\mathcal{A}^k$ and $\mathcal{A}^{k+1}$ coincide.

3.2.3 Discrete active set

We employ a finite element discretization by subdividing the domain $\Omega \subset \mathbb{R}^2$ into a regular mesh $\mathcal{T}_h$ of quadrilaterals [87]. A brief introduction to the finite element method was given in Section 2.2. The mesh $\mathcal{T}_h$ consists of N open cells $\{K_1, K_2, \dots, K_N\}$ with mesh size h.

For the mixed problem, the vector-valued displacements $u = (u_x, u_y)^T$ are discretized using H^1-conforming bi-quadratic elements, i.e., as the ansatz and test space, we employ Q_2^c finite elements defined in Equation (2.5). The pressure p and the phase-field φ are discretized with H^1-conforming bilinear elements, i.e., as ansatz and test space, we use Q_1^c finite elements defined in Equation (2.4); see Figure 3.4 on the right. It leads to conforming discrete spaces $\mathcal{V}_h \times \mathcal{U}_h \times \mathcal{W}_h \subset \mathcal{V} \times \mathcal{U} \times \mathcal{W}$, defined

Figure 3.4: Left: conforming quadrilateral elements of the type $Q_1^c Q_1^c$ for Chapter 4: Q_1^c for the displacement variable u and for the scalar-valued pressure variable p (red bullets). Right: conforming quadrilateral Stokes-elements of the type $Q_2^c Q_1^c Q_1^c$ for Chapter 5: Q_2^c for the displacement components u_x and u_y (blue and red bullets) and Q_1^c for the scalar-valued pressure variable p and the phase-field function φ (red bullets).

as

$$\begin{aligned}\mathcal{V}_h &:= \{u_h \in H_0^1(\Omega; \mathbb{R}^2),\ u_h|_K \in (Q_2^c(K))^2 \quad \forall K \in \mathcal{T}_h\},\\ \mathcal{U}_h &:= \{p_h \in L^2(\Omega),\ p_h|_K \in Q_1^c(K) \quad \forall K \in \mathcal{T}_h\},\\ \mathcal{W}_h &:= \{\varphi_h \in H^1(\Omega),\ \varphi_h|_K \in Q_1^c(K) \quad \forall K \in \mathcal{T}_h\}.\end{aligned}$$

Remark 5 (Number of degrees of freedom)**.** *Recall, that with Q_2^c elements for the discretization in both displacement components u_x and u_y, the total number of dofs increases significantly compared to bilinear elements for u.*

Based on the discretization of U, we can formulate a discrete active set scheme. We state Step 2 from

Algorithm 2 as a linear system with block structure:

$$\begin{pmatrix} \mathcal{M} & B \\ B^T & 0 \end{pmatrix} \begin{pmatrix} \delta U_h^{k+1} \\ \tau_h^{k+1} \end{pmatrix} = \begin{pmatrix} -F \\ 0 \end{pmatrix}. \tag{3.9}$$

By using quadrature only in the support points of τ_h^k, the block entry B^T becomes a diagonal matrix defined as

$$B_{ii} = \begin{cases} 0 & \text{if } \tau_h^{k,i} \neq 0, \\ 1 & \text{if } \tau_h^{k,i} = 0, \end{cases}$$

with $\tau_h^{k,i}$ the i-th entry of τ from the last Newton iteration. Equation (3.9) is the system that is solved in each iteration. The second row is used to eliminate entries in $\mathcal{M}$ where the phase-field is constrained on the active set $\mathcal{A}^k$. The eliminated entries are exactly those where the ith entry of τ_h^{k+1} is non-zero. With $\hat{\mathcal{M}}$ and $\hat{F}$, instead of $\mathcal{M}$ and F, where the constrained rows are removed, we end up with a simplified linear system:

$$\hat{\mathcal{M}}\ \delta\hat{U}_h^{k+1} = -\hat{F}.$$

The new entry τ_h^{k+1} can be computed from U_h^{k+1} via

$$(B)_{ii}(\tau_h^{k+1})_i = -(F)_i - (\mathcal{M}\delta U_h^{k+1})_i,$$

where $(\cdot)_i$ indicates the ith degree of freedom. For $i \in \mathcal{A}^k$, it leads to

$$(\tau_h^{k+1})_i = (B^{-1})_{ii}(-(F)_i - (\mathcal{M}\delta U_h^{k+1})_i).$$

The new active set $\mathcal{A}^{k+1}$ and the new inactive set $\mathcal{N}^{k+1}$ are computed via

$$\mathcal{A}^{k+1} = \{(B^{-1})_{ii}(-(F)_i - (\mathcal{M}\delta U_h^{k+1})_i) + c(\delta U_h^{k+1})_i > 0\},$$
$$\mathcal{N}^{k+1} = \{(B^{-1})_{ii}(-(F)_i - (\mathcal{M}\delta U_h^{k+1})_i) + c(\delta U_h^{k+1})_i \leq 0\}.$$

The final primal-dual active set algorithm combines two Newton iterations. One outer iteration computes the nonlinear problem and determines the active set. One inner iteration solves in each outer step the linear system via computing the updates δU_h^{k+1} and τ_h^{k+1}. Since the inner iteration can cause that $\delta U_h^k \leq 0$ is violated, we replace the condition with

$$U_h^k + \delta U_h^k \leq U_h^{\text{old}},$$

where U_h^{old} is the solution of the last incremental step. Further, we replace the residual used to compute the active set by a nonlinear residual

$$R(U_h^{k+1}) = -F(U_h^{k+1}).$$

Algorithm 3 (Primal-dual active set method according to Heister et al. [87])**.** *Repeat for k starting from $k = 0$ until $\mathcal{A}^k$ no longer changes ($\mathcal{A}^{k+1} = \mathcal{A}^k$) and the inactive set residual $\hat{R}(U_h^k) < TOL$*

(given tolerance):

1. *Assemble the full residual* $R(U_h^k) = -F(U_h^k)$.
2. *Compute the active set* $\mathcal{A}^k = \{i|\ (B^{-1})_{ii} R(U_h^k)(\tau_h^k)_i = -(F)_i - (\mathcal{M}\delta U_h^k)_i\}$.
3. *Assemble the matrix* $\mathcal{M} = \nabla F(U_h^k)$ *and the right hand side* $F(U_h^k)$.
4. *Eliminate rows and columns in* $\mathcal{A}^k$ *from* $\mathcal{M}$ *and* F *to obtain* $\hat{\mathcal{M}}$ *and* $\hat{F}$.
5. *Find* $\delta\hat{U}_h^k \in \mathcal{V}_h \times \mathcal{U}_h \times \mathcal{W}_h$ *such that*

$$\hat{\mathcal{M}}(\delta\hat{U}_h^k, \Psi) = -\hat{\mathcal{F}}(U_h^k)(\Psi) \quad \forall \Psi \in \mathcal{V}_h \times \mathcal{U}_h \times \mathcal{W}_h. \tag{3.10}$$

6. *Find a step size* $0 < \omega \leq 1$ *using line search to get*

$$U_h^{k+1} = U_h^k + \omega\delta\hat{U}_h^k,$$

with the residual $\hat{R}(U_h^{k+1}) < \hat{R}(U_h^k)$ *on the inactive set* $\mathcal{N}^k$.

For details on the used backtracking line search method in the last step of the algorithm, we refer to [136].

3.2.4 Setup of the weak system

In each iteration of the active set algorithm, the discrete system from Equation (3.10) has to be solved:

$$\mathcal{M}(\delta U_h^k, \Psi) = -F(U_h^k)(\Psi),$$

where $\Psi = (\psi_i)_{i=1,\dots,N}$ is the basis function with N total dof; the right hand side is defined in Equation (3.3) on a continuous level.
With a primitive order of the basis function (only non-zero in one component), we can separate the vector valued basis into displacements, pressure, and phase-field functions and sort them in the named order:

$$\psi_i = \begin{pmatrix} \chi_i^u \\ 0 \\ 0 \end{pmatrix}, \quad \text{for } i = 1, \dots, N_u,$$

$$\psi_i = \begin{pmatrix} 0 \\ \chi_i^p \\ 0 \end{pmatrix}, \quad \text{for } i = N_{u+1}, \dots, N_p,$$

$$\psi_i = \begin{pmatrix} 0 \\ 0 \\ \chi_i^\varphi \end{pmatrix}, \quad \text{for } i = N_{p+1}, \dots, N_\varphi,$$

with $N = N_u + N_p + N_\varphi$.
For non-pressurized fractures, in the block entries of the Jacobian $\mathcal{M}$ we set $\rho = 0$.

In the matrix $\mathcal{M}$, the columns and rows are eliminated on dof that belong either to Dirichlet conditions or to the active set (see Step 4 in Algorithm 3).
As a linear solver for the discretized mixed problem from Equation (3.10) with three components, in Chapters 4, 5, and 7, a sparse direct solver is used, provided by UMFPACK [60, 59]. In Chapter 6, a newly developed parallel solver based on a physics-based Schur-type block preconditioner is employed. The base of the implementation is documented in the framework *pfm-cracks* by Heister and Wick [89]. This parallel-adaptive open-source framework is embedded in deal.II [9, 11, 18], which offers scalable parallel algorithms for finite element computations. The deal.II library in turn, uses functionalities from other libraries such as Trilinos [90].

3.2.5 Alternative realizing crack irreversibility

An alternative to realize the inequality constraint is based on a complementarity formulation[1] of Formulation 2 (Chapter 5), which was developed in [128, 124]. The crack irreversibility constraint can be enforced with the help of a Lagrange multiplier $\zeta \in \mathcal{W}^*$, where $\mathcal{W}^*$ is the dual space of $\mathcal{W}$, similar to, e.g., [102, 97, 144, 171].
We present the fundamental idea from [128, 124] based on the mixed phase-field fracture problem in incremental and weak form (similar to Formulation 2 from Chapter 3 derived in Chapter 5), which is stated as:
We assume φ^{n-1} be given from the previous incremental step. Find $u^n \in \mathcal{V}$, $p^n \in \mathcal{U}$, and $\varphi^n \in \mathcal{K}$ for incremental steps $n = 1, 2, \dots, N$ such that

$$\begin{aligned} \big(g(\varphi^{n-1})\sigma(u^n, p^n), E_{\text{lin}}(w)\big) &= 0 \quad \forall w \in \mathcal{V}, \\ g(\varphi^{n-1})(\nabla \cdot u^n, q) - (\frac{1}{\lambda} p^n, q) &= 0 \quad \forall q \in \mathcal{U}, \\ (1-\kappa)(\varphi^n \sigma(u^n, p^n) : E_{\text{lin}}(u^n), \psi - \varphi^n) - \frac{G_C}{\epsilon}(1 - \varphi^n, \psi - \varphi^n) & \\ + \epsilon G_C(\nabla \varphi^n, \nabla(\psi - \varphi^n)) \geq 0 \quad \forall \psi \in \mathcal{K}. & \end{aligned} \tag{3.11}$$

To discretize the problem in space, we define a discrete subset

$$\mathcal{K}_h^n := \{\psi_h \in \mathcal{W}_h^n \mid \psi_h(\iota) \leq (I_h^n \varphi_h^{n-1})(\iota) \quad \forall \iota \in \mathbb{P}\},$$

where $\mathbb{P}$ is the set of dof on the current mesh, and I_h^n the nodal interpolation operator.
For $n = 1, \dots, N$ and φ^{n-1} given, find $(u_h^n, p_h^n, \varphi_h^n)$ such that

$$\begin{aligned} \big(g(I_h^n \varphi_h^{n-1})\sigma(u_h^n, p_h^n), E_{\text{lin}}(w_h)\big) &= 0 \quad \forall w_h \in \mathcal{V}_h^n, \\ g(I_h^n \varphi_h^{n-1})(\nabla \cdot u_h^n, q_h^n) - (\frac{1}{\lambda} p_h^n, q_h^n) &= 0 \quad \forall q_h \in \mathcal{U}_h^n, \\ (1-\kappa)(\varphi_h^n \sigma(u_h^n, p_h^n) : E_{\text{lin}}(u_h^n), \psi_h - \varphi_h^n) - \frac{G_C}{\epsilon}(1 - \varphi_h^n, \psi_h - \varphi_h^n) & \\ + \epsilon G_C\,(\nabla \varphi_h^n, \nabla(\psi_h - \varphi_h^n)) \geq 0 \quad \forall \psi_h \in \mathcal{K}_h^n. & \end{aligned} \tag{3.12}$$

With the help of a Lagrange multiplier $\zeta \in \mathcal{W}^*$, the problem formulation from Equation (3.11) can be written equivalently as the following complementarity system:

[1] Parts of this section are published in [124].

For $n = 1, \dots, N$ and φ^{n-1} given, find $(u^n, p^n, \varphi^n, \zeta^n)$ such that

$$\begin{aligned}
(g(\varphi^{n-1})\sigma(u^n, p^n), E_{\text{lin}}(w)) &= 0 \quad \forall w \in \mathcal{V}, \\
g(\varphi^{n-1})(\nabla \cdot u^n, q) - (\frac{1}{\lambda} p^n, q) &= 0 \quad \forall q \in \mathcal{U}, \\
(1-\kappa)(\varphi^n \sigma(u^n, p_h^n) : E_{\text{lin}}(u^n), \psi) - \frac{G_C}{\epsilon}(1 - \varphi^n, \psi) & \\
+ \epsilon G_C(\nabla \varphi^n, \nabla \psi) + (\zeta^n, \psi)_{-1,1} &= 0 \quad \forall \psi \in \mathcal{W}, \\
(\zeta^n, \psi)_{-1,1} &\geq 0 \quad \forall \psi \in \mathcal{W}, \psi \geq 0, \\
\varphi^n &\leq \varphi^{n-1}, \\
(\zeta^n, \varphi^{n-1} - \varphi^n)_{-1,1} &= 0.
\end{aligned} \tag{3.13}$$

In Equation (3.13), the duality paring of $\mathcal{W}$ is denoted as $(\cdot, \cdot)_{-1,1}$. For the complementarity system on a discrete level we define a dual basis $\mathcal{W}_h^{n,*}$ of $\mathcal{W}_h^n$ as

$$\mathcal{W}_h^{n,*} \coloneqq \text{span } \{\chi_\iota^* |\ \iota \in \mathbb{P}\}, \quad \text{where } (\chi_\iota^*, \chi_\xi) = \delta_{\iota\xi},$$

for the nodal basis χ_ξ of $\mathcal{W}_h^n$. We define $\zeta_h^n = \sum_{\iota \in \mathbb{P}} (\zeta_h^n)_\iota \chi_\iota^*$, with

$$(\zeta_h^n, \chi_\iota) = -(1-\kappa)(\varphi_h^n \sigma(u_h^n) : E_{\text{lin}}(u_h^n), \psi_h) + \frac{G_C}{\epsilon}(1 - \varphi_h^n, \psi_h) - \epsilon G_C(\nabla \varphi_h^n, \nabla \psi_h) \quad \forall \iota \in \mathbb{P},$$

the analogous discrete complementarity system reads as follows:

$$\begin{aligned}
(g(I_h^n \varphi_h^{n-1})\sigma(u_h^n), E_{\text{lin}}(w_h)) &= 0 \quad \forall w_h \in \mathcal{V}_h^n, \\
g(I_h^n \varphi_h^{n-1})(\nabla \cdot u_h^n, q_h^n) - (\frac{1}{\lambda} p_h^n, q_h^n) &= 0 \quad \forall q_h \in \mathcal{U}_h^n, \\
(1-\kappa)(\varphi_h^n \sigma(u_h^n) : E_{\text{lin}}(u_h^n), \psi_h) - \frac{G_C}{\epsilon}(1 - \varphi_h^n, \psi_h) & \\
+ \epsilon G_C(\nabla \varphi_h^n, \nabla \psi_h) + (\zeta_h^n, \chi_\iota) &= 0 \quad \forall \psi_h \in \mathcal{W}_h^n, \\
(\zeta_h^n, \chi_\iota) &\geq 0 \quad \forall \iota \in \mathbb{P}, \\
\varphi^n(\iota) &\leq \varphi^{n-1}(\iota) \quad \forall \iota \in \mathbb{P}, \\
(\zeta_h^n, I_h^n, \varphi^{n-1} - \varphi^n) &= 0.
\end{aligned} \tag{3.14}$$

With the help of a complementarity function $(x, y) \mapsto x - \max\{0, x + cy\},\ c > 0$ (we use $c = 1$), we can formulate Equation (3.14) as an equality system:

$$\begin{aligned}
(g(I_h^n \varphi_h^{n-1})\sigma(u_h^n), E_{\text{lin}}(w_h)) &= 0 \quad \forall w_h \in \mathcal{V}_h^n, \\
g(I_h^n \varphi_h^{n-1})(\nabla \cdot u_h^n, q_h^n) - (\frac{1}{\lambda} p_h^n, q_h^n) &= 0 \quad \forall q_h \in \mathcal{U}_h^n, \\
(1-\kappa)(\varphi_h^n \sigma(u_h^n) : E_{\text{lin}}(u_h^n), \psi_h) - \frac{G_C}{\epsilon}(1 - \varphi_h^n, \psi_h) & \\
+ \epsilon G_C(\nabla \varphi_h^n, \nabla \psi_h) + (\zeta_h^n, \chi_\iota)_{-1,1} &= 0 \quad \forall \psi_h \in \mathcal{W}_h^n, \\
(\zeta_h^n)_\iota - \max\{0, (\zeta_h^n)_\iota + c((I_h^n \varphi^{n-1} - \varphi^n)(\iota))\} &= 0, \quad \forall \iota \in \mathbb{P}.
\end{aligned} \tag{3.15}$$

A code snippet of the implementation of the last equality of Equation (3.15) from Example 11 of the

instationary PDE Examples in the open-source library DOpElib [62, 79] is given in the following:

```
if(fabs(state_fe_values[multiplier].value(i,q_point) - 1.) < std::numeric_limits<double>::epsilon())
{
        //Equation for multiplier
       local_vector(i) += scale * weight* (uvalues_[q_point][4]
                                  - std::max(0.,uvalues_[q_point][4]+s_*(pf-old_timestep_pf)));
       //Add Multiplier to the state equation
       //find corresponding basis of state
       for(unsigned int j = 0; j < n_dofs_per_element; j++)
       {
              if(fabs(state_fe_values[phasefield].value(j,q_point) - 1.)
              < std::numeric_limits<double>::epsilon())
              {
                  local_vector(j) += scale * weight* uvalues_[q_point][4];
           }
       }
}
```

We can see in the code snippet showing the assembly of the right hand side for the Lagrange multiplier, that the Lagrange multiplier is the fourth component of the system (u, p, φ, ζ) and evaluated on all quadrature points of φ.
Equation (3.15) is solved in [128, 124] with a residual-based Newton's method. For further details using a complementarity formulation, we refer to [124, Section 4.1].

Remark 6 (System of four components)**.** *The Lagrange multiplier ζ acts as a fourth variable in the implementation. In contrast to other well-known methods as simple penalization or Augmented Lagrangian [184], the proposed method using a Lagrange multiplier, is embedded in the whole system, which allows a more accurate discretization without the necessity of additional iterations. On the other hand, the PDE system has one further unknown variable, which leads to higher computational costs.*

Remark 7 (Implementation in DOpElib [62, 79])**.** *The proposed complementarity system with a Lagrange multiplier as an additive solution variable is implemented in Examples 8, 10, 11, and 12 of the instationary PDE Examples from DOpElib [62, 79]. In Example 8, 10, and 11, the primal phase-field fracture model is considered, which yields three unknowns. Example 12, as presented in the code snippet above, has four solution variables and allows computing fracture simulation in incompressible solids.*

3.3 Adaptive mesh-refinement

Considering fractures, mesh adaptivity could allow a good resolution of the crack width measured by ϵ related to the spatial discretization parameter h such that $h \ll \epsilon$ (at least for low order finite elements). Further, in many applications, the crack tip is of specific interest. We notice that mesh refinement for phase-field fracture problems may be problematic since the (unknown) fracture path may depend on the locally refined mesh. Then, numerical solutions would purely depend on the mesh refinement algorithm, see e.g., Artina et al. [12], and discussions and references provided therein.
One of the first studies on local mesh adaptivity for phase-field fracture was undertaken by Burke et al. [49]. Artina et al. [12] presented anisotropic mesh adaptivity. Goal-oriented error estimation using dual-weighted residuals was addressed by Wick [180, 184]. Another method that purely focuses

on fine meshes without error estimation in the crack region was developed by Heister et al. [87] for simulations in two spatial dimensions, and the extension for three-dimensional computations was considered by Lee et al. [116]. With these last developments, a computational convergence analysis using high-performance parallel computing and local mesh adaptivity was carried out [88].
All listed studies show that local mesh refinement is a key ingredient for phase-field fractures, particularly in working with sufficiently small phase-field regularization parameters ϵ and κ.

3.3.1 Predictor-corrector adaptivity

For adaptively refined meshes, we employ a predictor-corrector scheme from Heister et al. [87, Chapter 4], which allows refining the mesh locally depending on a propagating fracture with a chosen threshold for the phase-field variable. Consequently, the mesh grows during the computation. If some cells within the damage bands are not sufficiently refined (its refinement level is smaller than the present maximum refinement level) at the end of a time step, the step is computed again with a refined mesh. It was shown [87] that this intuitive refinement strategy is efficient and robust. A visualization of the scheme is presented in Figure 3.5, where the mesh in the crack zone is refined adaptively from left to right. With a certain threshold for the phase-field refinement (mostly between 0.5 and 0.8) we decide how extensively the crack zone is resolved.

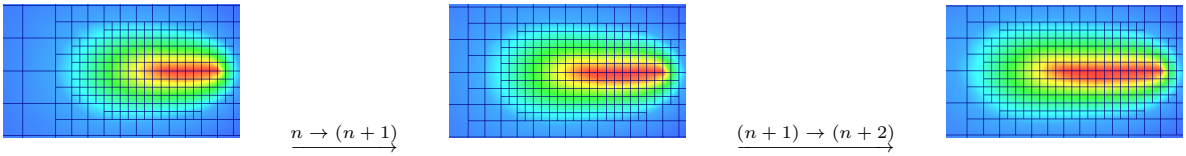

Figure 3.5: Adaptive mesh refinement via predictor-corrector scheme from [87]. Three incremental steps (from left to right), which were re-computed to catch the current crack zone with the finest mesh size.

Algorithm 4 (Predictor-corrector mesh adaptivity according to Heister et al. [87])**.** *We assume to be in incremental step n:*

1. *Given the solution (u_n, p_n, φ_n) at incremental step n,*
2. *Predictor step: solve for $(\tilde{u}_{n+1}, \tilde{p}_{n+1}, \tilde{\varphi}_{n+1})$ at step n to predict the fracture path,*
3. *Refine the mesh in accordance with the preliminary solution $(\tilde{u}_{n+1}, \tilde{p}_{n+1}, \tilde{\varphi}_{n+1})$ by the given threshold for the phase-field variable and go back to the solution and mesh (u_n, p_n, φ_n),*
4. *Corrector step: Solve on the new mesh the new solution $(u_{n+1}, p_{n+1}, \varphi_{n+1})$ in step $n+1$.*

Go one incremental step further via $n \mapsto n+1$ and go back to Step 1.

We briefly point out the most important advantages (☺) and drawbacks (☹) of the predictor-corrector scheme [87]:

- ☹ Even if the mesh is refined during the computation, which decreases the size of h, the crack's bandwidth ϵ is fixed, which does not allow to reduce the discretization error depending on ϵ;
- ☹ The incremental step size has to be small enough, especially for fast fractures, to capture the crack properly. It leads to the fact that with more incremental steps, the overall workload increases due to the re-computed steps;

☺ The crack location can be totally unknown, which is a great advantage, especially, if real-world problems are considered; see Chapter 7;

☺ The algorithm is relatively simple to implement, especially in contrast to error estimators.

3.3.2 Geometric refinement

In stationary test cases, where the crack location is known, it is efficient to use geometrically pre-refined meshes. See Figure 3.6 for an idea of the geometric refinement for a known crack location. Further, for tests with inclusions or circular holes, such as the EPDM test from Chapter 7, having

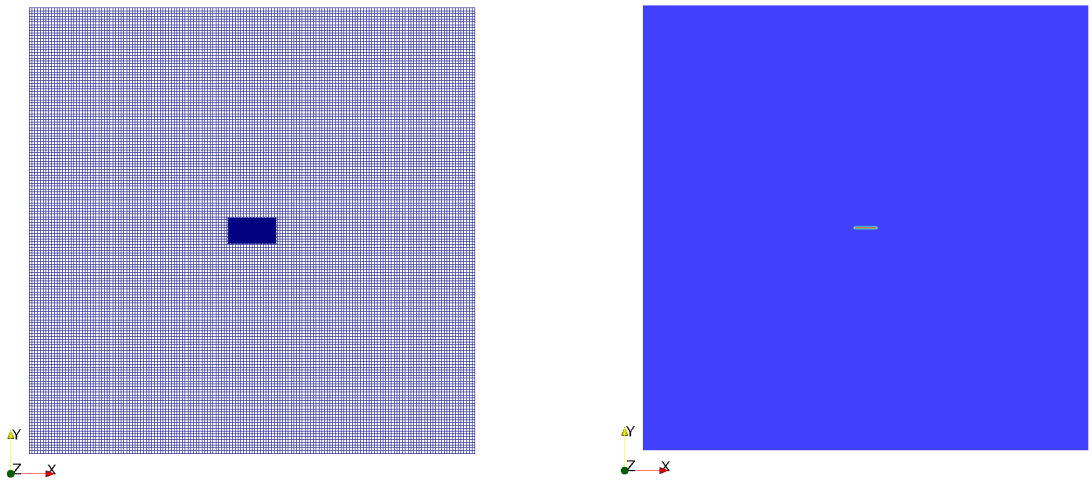

Figure 3.6: Example for geometric mesh refinement for Sneddon's benchmark. Domain of size $(-20, 20)^2$, zone of geometric refinement $(-2, 2) \times (-1, 1)$. Left: mesh after five steps of geometric refinement. Right: corresponding snapshot of phase-field solution (blue unbroken, green to red in the broken zone) of Sneddon's pressure-driven benchmark with a stationary crack in the center of a 2d-square.

a sufficiently fine mesh around the inclusion can be relevant to avoid locking in the mesh. Strictly speaking, geometric refinement is not a refinement scheme, but it is a simple approach to decreasing the computational workload and still having a refined finite element mesh where a crack propagates or a sufficiently fine mesh is required for other reasons. We denote it as geometric refinement in the following since the mesh is refined according to the information on the geometry of the test setup.

3.3.3 Error-controlled adaptivity

Having an error estimator along with localized crack tip mesh refinement would be even more beneficial. Considering a posteriori error estimation for adaptive refinement, the main difficulty lies in the proof of efficiency since we focus on nonlinear and non-smooth problems. Regardless, some groups present a convergence analysis for an adaptive finite element scheme, i.e., Burke et al. [49]. Recent work on goal-oriented adjoint-based a posteriori error estimates for a nonlinear phase-field discontinuity problem is given by Wick [186]. Further, we developed a residual-based error estimator for the primal quasi-static phase-field variational inequality in [124]. We briefly introduce our approach in the following[2], even if the error estimator is not used in subsequent chapters of this thesis.

[2]Numerical results of this section are published in [124].

In [124], we developed a residual-type a posteriori error estimator for the phase-field variational inequality, which is efficient, reliable, and robust concerning the phase-field regularization parameter ϵ. The theoretical results are given for meshes of simplices and quadrilaterals and based on the previous work of Walloth [108, 173]. We implemented the estimator in DOpElib [62, 79] and tested it for the primal quasi-static phase-field fracture model derived in Chapter 4. Numerical results have been published in [124, 125]. Further, we tested the estimator for the quasi-static fracture phase-field model for nearly incompressible solids [128] (based on the model derived in Chapter 5). The main advantages of the residual-based a posteriori error estimator of the variational inequality are:

☺ We improve the quality of the solution for given computational resources;

☺ We resolve the transition zone between $\varphi = 0$ and $\varphi = 1$, and the fracture tip;

☺ We avoid over-refinement in the full-contact zone.

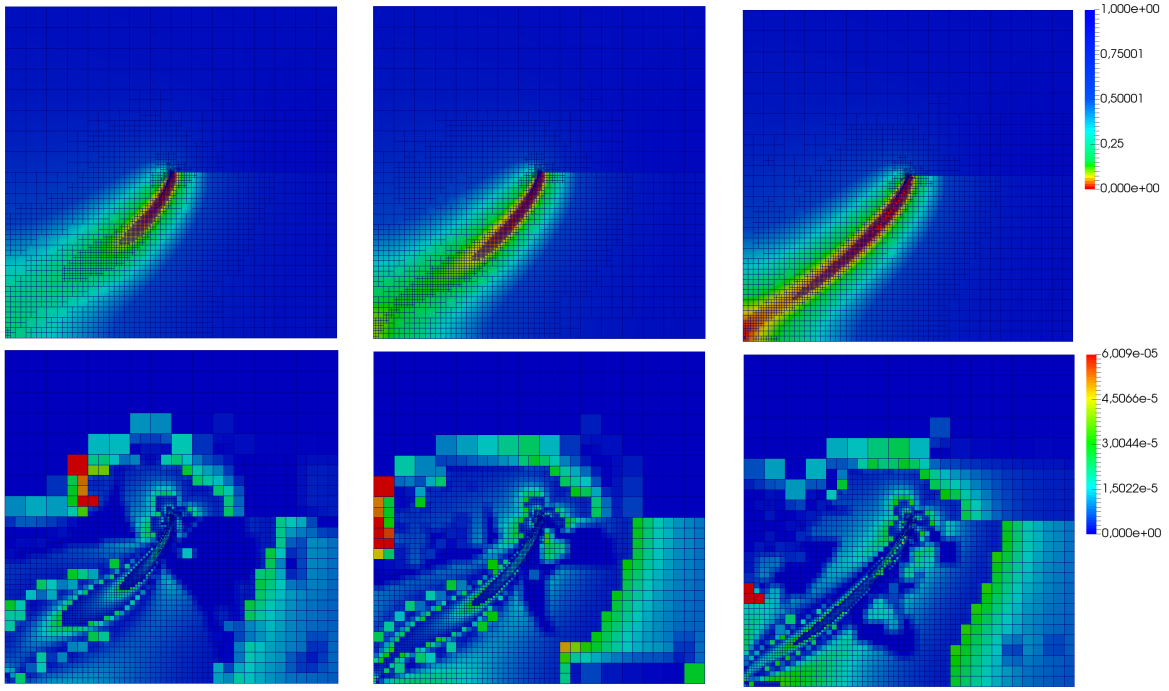

Figure 3.7: Results from Mang et al. [124]. The phase-field function and the error indicators, respectively, after six refinement steps depicted in specific time points (after 0.0116, 0.0118 and 0.0125 s) for the single-edge notched shear test given on the current adaptive mesh to visualize the refinement strategy.

To get an idea how the developed error estimator works for adaptive refinement, we propose numerical results in Figure 3.7, taken from [124]. Snapshots of the phase-field function and the error indicators on the current mesh are presented for the single-edge notched pure shear test, described in Section 3.1. Figure 3.7 shows, that the error estimation and the corresponding refinement strategy allows resolving the zone around the crack. Further, in the last snapshot of the phase-field solution (upper row on the right), we observe the advantage from the third bullet: in the broken zone we do not have over-refinement.

Remark 8 (Error estimator in DOpElib [62, 79])**.** *The developed residual-based error estimator requires varying spatial meshes in time, i.e., we use Rothe discretization*[3]*, where different spatial meshes at different time-points are allowed in DOpElib [62, 79].*

The implementation of the error estimator can be found in the open-source library DOpElib [62, 79]. DOpElib in turn, is based on the deal.II finite element library [10]. The error estimator is available in Examples 8, 10, and 11 of the instationary PDE Examples in DOpElib [62, 79]. Further developments on the error estimator for the adaptive solution of quasi-static phase-field fracture models are recently presented by Walloth and Wollner [174].

Conclusions of the chapter

Time extrapolation in the phase-field function allows us to overcome the nonlinear behavior of the displacement equation. We use a primal-dual active set method to solve the coupled variational inequality system of phase-field fracture. For discretization in space, we employ H^1-conforming elements Q_2^c and Q_1^c. We use a predictor-corrector scheme for adaptively refined meshes and geometric mesh refinement for stationary tests with a known crack location. With Chapter 3, we prepared the following chapters: The next chapter derives the primal phase-field fracture model stated in Formulation 1 at the beginning of the current chapter. Numerical results from Chapter 4 base upon the solving and discretization from Heister et al. [87]. The numerical results in Chapters 5, 6, and 7 are based on the discretization and solving scheme from Chapter 3. Instead of a direct solver from UMFPACK [60, 59], Chapter 6 poses a preconditioned iterative linear solver.

[3]Thanks to Prof. Dr. Winnifried Wollner and Dr. Mirjam Walloth for working together in Darmstadt on the implementation of Rothe's method in 2018/19, providing the basis for joint publications [124, 22].

Chapter 4

Phase-field fracture modeling & simulations

In this chapter, we derive the classical (primal) variational phase-field fracture model, starting from Francfort and Marigo [72], who formulated Griffith's theory as an energy functional in 1998. In order to get a numerically solvable problem, we adopt in Section 4.1 the approach by Bourdin et al. [35] from 2000, who derived a regularized energy functional depending on two variables: displacements u and a phase-field φ – to which we refer hereafter as the primal phase-field energy problem. In Section 4.2, we derive the first variation of the energy functional yielding the corresponding Euler-Lagrange equations and our numerical problem. For completeness, we formulate in Section 4.3 the phase-field fracture problem in strong form. We conclude the theoretical part of this chapter with Section 4.4 by formulating the notion of Γ-convergence. Hence, we achieve a kind of convergence of the phase-field fracture formulation to the non-regularized functional, describing the fracture behavior according to Griffith's criterion for crack propagation. Following up Γ-convergence in numerical computations, Section 4.5 conducts a detailed error analysis for a well-known benchmark test with analytical reference values. The final two Sections 4.6 and 4.7 introduce modifications in the regularization function and Cauchy stress tensor implemented to cure observed inaccuracies of the regularized energy function compared to well-known benchmark tests.

4.1 Primal phase-field energy minimization problem

Francfort and Marigo [72], in 1998, picked up Griffith's link from the existence of cracks and surface energy, and proposed a variational model of quasi-static crack evolution.

Definition 3 (Surface energy according to Francfort and Marigo [72])**.** *The surface energy $E_S(C)$ of a crack $C \subset \bar{\Omega}$ is defined as*

$$E_S(C) = \int_C G_C(s)\, d\mathcal{H}^1(s),$$

where $\mathcal{H}^1$ is the one-dimensional Hausdorff measure (in 2d) [85]. The surface energy $E_S(C)$ is strictly increasing in C. The critical energy release rate is denoted by $G_C > 0$.

Remark 9 (Critical energy release rate G_C)**.** *G_C is the toughness of the material or energy per area required for crack propagation. It describes the resistance of a material to break [30]. The critical energy release rate depends on the considered material but is assumed to be constant over domain and time. We use the unit* N/mm*, which is not a SI unit.*

Definition 4 (Bulk energy according to Francfort and Marigo [72])**.** *For a displacement field $u : \Omega \to \mathbb{R}^2$ and a lower-dimensional crack $C \subset \mathbb{R}$, the bulk energy $E_B(u, C)$ is defined as*

$$E_B(u, C) = \inf \int_{\Omega \setminus C} \sigma(u) : E_{lin}(u)\, dx,$$

where $(\sigma(u) : E_{lin}(u))$ is the elastic energy density with the Cauchy stress tensor $\sigma(u)$ of linearized elasticity defined as

$$\sigma(u) \coloneqq 2\mu E_{lin}(u) + \lambda \operatorname{tr}(E_{lin}(u))\mathbb{1}, \tag{4.1}$$

with material-dependent Lamé parameters $\mu, \lambda > 0$. By $\mathbb{1}$, the (two-dimensional) identity matrix is denoted. The symmetric linearized strain tensor $E_{lin}(u)$ is defined as

$$E_{lin}(u) \coloneqq \frac{1}{2}(\nabla u + \nabla u^T). \tag{4.2}$$

The bulk energy $E_B(u, C)$ is monotonically non increasing in C for any fixed u.

With the help of the two definitions, the total energy of a body with a given crack C is given by

$$E_T(u, C) = E_B(u, C) + E_S(C).$$

Remark 10 (Dimension $d = 2$)**.** *In the frame of this thesis, we restrict ourselves to two-dimensional domains. Of course, the presented definitions can be stated for higher d-dimensional displacement fields with $d > 2$. Then, the Hausdorff measure would be $(d-1)$-dimensional.*

According to Francfort and Marigo [72], the total energy functional describes the energy of a crack of an elastic solid concerning the displacement u, yielding an energy minimization problem of the following form:

Formulation 4. *Find $u : \Omega \to \mathbb{R}^2$ and a crack $C \subset \mathbb{R}$ such that*

$$\min_{u,C} E_T(u, C) = \frac{1}{2}(\sigma(u), E_{lin}(u)) - \int_C \tau \cdot u \, \mathrm{d}s + G_C \mathcal{H}^1(C),$$
$$\text{with } \partial_t l(C) \geq 0.$$

Traction forces are denoted by τ. The quantity $l(C)$ in the additional time-dependent constraint is the current crack length of C which increases or stays equal in time. The energy functional $E_T(u, C)$ consists of three terms: the bulk energy term, the traction energy term, and the crack energy contribution.

Since the dependency of the functional on the actual crack C is intractable for numerical solution approaches, we regularize Formulation 4. In the following, we give an explanation of the phase-field method and its application to the energy functional $E_T(u, C)$.
The starting point of phase-field is the behavior of the displacement u when a crack occurs. The

vector-valued function u describes the deformation in material points on a continuous level. If the material tears, u becomes discontinuous in the fracture since there occurs a gap between two material points. Thus, the idea is an indicator function, which displays discontinuities of u on Ω instead of a lower-dimensional crack C. To be more precise, the function is equal to one, where u is continuous and equal to zero, where u may have discontinuities (in the crack). This function would be called the exact phase-field function.

Such an exact phase-field function is still a discontinuous function with discontinuities between zero and one. So, we introduce an approximative phase-field function φ. The crack C is framed and approximated with Ω_F (fracture domain), which has a thickness of 2ϵ, where $\epsilon > 0$. The phase-field function φ is still supposed to be 1 within the unbroken domain and 0 within C, as depicted in Figure 4.1. In the transition zone between the broken and unbroken domain, it holds $0 < \varphi < 1$.

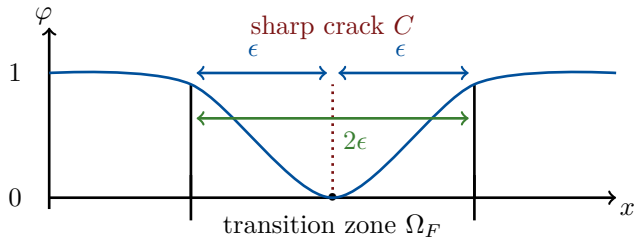

Figure 4.1: Approximative phase-field function φ, here depicted over a one-dimensional cracked domain. The sharp crack C is approximated with a diffusive crack of width ϵ.

For the regularized energy minimization problem, we introduce a loading (time) interval $I := [0, T]$, where $T > 0$ is the end time value. A displacement function $u : (\Omega \times I) \to \mathbb{R}^2$ is defined on a domain $\Omega \subset \mathbb{R}^2$. Using the elliptic functional proposed by Ambrosio-Tortorelli [6, 5], we approximate a lower-dimensional crack $C \subset \mathbb{R} \in \Omega$ by a phase-field variable $\varphi : (\Omega \times I) \to [0, 1]$ with $\varphi = 0$ in the crack (broken material) and $\varphi = 1$ in the unbroken material. The parameter $\epsilon > 0$ determines the width of the transition zone between the unbroken and the broken material; see Figure 4.1. On the boundary $\partial\Omega$, we assume homogeneous Dirichlet boundary conditions for simplicity. For a complete formulation of the phase-field model, further definitions are needed. A degradation function $g(\varphi)$ is defined as

$$g(\varphi) := (1 - \kappa)\varphi^2 + \kappa, \tag{4.3}$$

with a small regularization parameter $\kappa > 0$. The Cauchy stress tensor $\sigma(u)$ (under the assumption of isotropy, homogeneity, and symmetry [52]) was defined in Equation (4.1). The stress tensor depends on the Lamé coefficients $\lambda > \frac{2}{3}\mu$ and $\mu > 0$. The relation of the first Lamé coefficient λ, the second Lamé coefficient μ (also called shear modulus), and the Poisson ratio $\nu \in [0, 0.5]$, is given by

$$\lambda = \frac{2\nu\mu}{1 - 2\nu}.$$

This relation plays an essential role in this thesis because nearly incompressible solids are considered, where $\nu \to 0.5$, which is equivalent to $\lambda \to \infty$.

Remark 11 (Lamé constants)**.** *We emphasize that the experimental determination of the Lamé constants is derived from an expansion of the constitutive equation concerning the (nonlinear) Green-Saint-*

Venant strain tensor $E(u) = \frac{1}{2}(\nabla u + \nabla u^T + \nabla u^T \nabla u)$*, and is not related to the defined linearized strain tensor* $E_{lin}(u)$ *[52, Chapter 3].*

Remark 12 (Poisson ratio)**.** *The Poisson ratio is a unit-less quantity in* $[-1, 0.5]$*, where* 0.5 *is the incompressible limit. It describes the compressed material's ratio into the two directions orthogonal to the compression direction [184].*

With the help of the definitions above, a fracture in a solid under deformation can be described via minimizing the following energy functional $E_\epsilon(u, \varphi)$:

Formulation 5 (Energy minimization)**.** *Let* $\mathcal{V} \coloneqq H_0^1(\Omega; \mathbb{R}^2)$ *and* $\mathcal{W} \coloneqq H^1(\Omega)$*. Find a pair* $(u, \varphi) \in \mathcal{V} \times \mathcal{W}$*, where* $u : (\Omega \times I) \to \mathbb{R}^2$ *and* $\varphi : (\Omega \times I) \to [0, 1]$ *such that*

$$\min_{(u,\varphi)\in\mathcal{V}\times\mathcal{W}} E_\epsilon(u, \varphi) = \frac{1}{2}\int_\Omega g(\varphi)\sigma(u) : E_{lin}(u)\, dx + G_C \int_\Omega \frac{1}{2\epsilon}(1-\varphi)^2 + \frac{\epsilon}{2}|\nabla\varphi|^2\, dx, \quad \text{and } \partial_t\varphi \leq 0. \tag{4.4}$$

In Equation (4.4), the crack irreversibility condition is given as an additional constraint. The phase-field function has to decrease in time. The constraint contains Griffith's idea similar to Formulation 4 that a crack cannot heal. Only the irreversibility condition is time-dependent in a stationary minimization problem formulation.
If pressure acts as an internal force on the crack boundary, pressure terms are added with a given pressure ρ, yielding the following minimization problem:

Formulation 6 (Energy minimization pressure driven)**.** *Let a pressure* $\rho \in L^\infty(\Omega)$ *be given. Find a pair* $(u, \varphi) \in \mathcal{V} \times \mathcal{W}$*, such that*

$$\begin{aligned}\min_{(u,\varphi)\in\mathcal{V}\times\mathcal{W}} E_\epsilon(u, \varphi) = \frac{1}{2}\int_\Omega g(\varphi)\sigma(u) : E_{lin}(u)\, dx + \int_\Omega \varphi^2\rho\nabla\cdot u\, dx \\ + \int_\Omega \varphi^2\nabla\rho\, u\, dx + G_C\int_\Omega \frac{1}{2\epsilon}(1-\varphi)^2 + \frac{\epsilon}{2}|\nabla\varphi|^2\, dx, \\ \text{and } \partial_t\varphi \leq 0,\end{aligned} \tag{4.5}$$

with regularization parameters $\kappa, \epsilon > 0$*. The degradation function* $g(\varphi)$ *is defined in Equation (4.3). A proper choice of the regularization parameters* ϵ *and* κ *is discussed in Section 4.5.*

Because we assume the pressure to be constant, with $\nabla\rho = 0$, the third term in Equation (4.5) vanishes [184]. The last integral is called Ambrosio-Tortorelli approximation [5, 6] for the weighted Hausdorff measure $G_C\mathcal{H}^1(C)$ [85] of the lower-dimensional crack C.

4.2 Primal phase-field fracture problem in weak form

For a variational problem formulation, we reformulate the problem statement as a CVIS. Therefore, proper ansatz and test spaces have to be chosen. For the variational form, directional derivatives of the energy functional are needed for minimizing the functional.

Definition 5 (Directional derivatives in Banach spaces)**.** *Let $\mathcal{A}, \mathcal{B}$ be normed vector spaces and let $\mathcal{D}$ be non-empty. Let $f : \mathcal{D} \to \mathcal{B}$ be a given mapping. If the limit*

$$f'(v)(h) = \lim_{s \to 0} \frac{f(v + sh) - f(v)}{s} = \frac{d}{ds} f(v + sh)|_{s=0}, \quad v \in \mathcal{D}, h \in \mathcal{A},$$

exists, then $f'(v)(h)$ is called the directional derivative of the mapping f at v into the direction h.

We derive the Euler-Lagrange equations, which arise if we solve the first variation instead of a minimization problem (first-order optimality conditions). In the calculus of variation and classical mechanics, Leonhard Euler and Joseph-Louis Lagrange developed a system of second-order PDEs whose solutions are stationary points of the given minimized functional [71].
Further, we have to handle the time-dependent crack irreversibility condition for a variational form of the energy minimization problem from Formulation 5 or 6 (Section 4.1). We need two definitions for using a common approach for obstacle problems. We formulate optimality conditions for a minimizer φ from a convex subset of $\mathcal{W}$, which fulfills the irreversibility [20]. In the context of quasi-static modeling, we use incremental steps instead of time steps. The index of increments is denoted as n in the following. Two definitions are required to reformulate the time-dependent irreversibility constraint as a constraint on the current phase-field $\varphi^n := \varphi(t_n)$ related to the phase-field from the previous incremental step $\varphi^{n-1} := \varphi(t_{n-1})$.

Definition 6 (Convex set)**.** *A set K is called a convex set if it holds for any $u, v \in K$*

$$su + (1 - s)v \in K, \quad \text{for all } s \in [0, 1].$$

Definition 7 (Convex functional)**.** *Assume K to be a convex set. A functional $E : K \to \mathbb{R}$ is convex if and only if*

$$E(su + (1 - s)v) \leq sE(u) + (1 - s)E(v) \quad \forall u, v \in K \text{ and } s \in [0, 1].$$

Proposition 2. *The subset $\mathcal{K} := \{\varphi^n \in \mathcal{W} \,|\, \varphi^n - \varphi^{n-1} \leq 0 \quad \text{a.e. in } \Omega\}$, with $\mathcal{W} = H^1(\Omega)$, is a convex set.*

Proof Let $\varphi, \psi \in \mathcal{K}$ be given. Then it holds

$$s\varphi + (1 - s)\psi \in H^1(\Omega) \quad \text{for } s \in [0, 1].$$

Further,

$$0 \leq s\varphi + (1 - s)\psi \leq s\varphi^{n-1} + (1 - s)\varphi^{n-1} = \varphi^{n-1} \leq 1.$$

Thus also $s\varphi + (1 - s)\psi \in \mathcal{K}$. □
Based on the definition of the convex subset

$$\mathcal{K} := \{\varphi^n \in \mathcal{W} \,|\, \varphi^n - \varphi^{n-1} \leq 0 \,\text{a.e. in } \Omega\},$$

the Euler-Lagrange equations with variational inequality are stated first and proven afterwards.

Proposition 3 (Primal phase-field fracture problem/Euler-Lagrange equations)**.**
Find a pair $(u, \varphi) \in \mathcal{V} \times \mathcal{K}$ *such that*

$$\begin{aligned} (g(\varphi)\sigma(u), E_{lin}(w)) = 0 \quad \forall w \in \mathcal{V}, \\ (1-\kappa)\Big(\varphi\sigma(u) : E_{lin}(u), \psi - \varphi\Big) + G_C(-\frac{1}{\epsilon}(1-\varphi), \psi - \varphi) \\ + G_C\epsilon(\nabla\varphi, \nabla(\psi - \varphi)) \geq 0 \quad \forall \psi \in \mathcal{K}. \end{aligned} \tag{4.6}$$

Derived from the energy minimization problem from Formulation 6, the Euler-Lagrange equations for pressurized phase-field fractures are given in the following.

Proposition 4 (Primal phase-field fracture problem/Euler-Lagrange equations, pressure driven)**.**
Let a pressure $\rho \in L^\infty(\Omega)$ *be given. Find a pair* $(u, \varphi) \in \mathcal{V} \times \mathcal{K}$ *such that*

$$\begin{aligned} \Big(g(\varphi)\sigma(u)\,, E_{lin}(w)\Big) + (\varphi^2\rho, \nabla \cdot w) = 0 \quad \forall w \in \mathcal{V}, \\ (1-\kappa)(\varphi\sigma(u) : E_{lin}(u), \psi - \varphi) + 2(\varphi\rho\nabla \cdot u, \psi - \varphi) \\ + G_C\Big(-\frac{1}{\epsilon}(1-\varphi, \psi - \varphi) + \epsilon(\nabla\varphi, \nabla(\psi - \varphi))\Big) \geq 0 \quad \forall \psi \in \mathcal{K}. \end{aligned}$$

The Propositions 3 and 4 build the basis for all later chapters. We state the proof of Proposition 4, derived from Formulation 6. For the proof of Proposition 3, the proof coincides to the given one with $\rho = 0$.

Proof For simplicity, the index n is omitted in the proof. We obtain the coupled system via computing the directional derivatives of $E_\epsilon(u, \varphi)$ into the directions w and $(\psi - \varphi)$ denoted as

$$\begin{aligned} &E'_\epsilon(u, \varphi)(w), \\ &E'_\epsilon(u, \varphi)(\psi - \varphi), \end{aligned}$$

and use the convexity of the energy functional in the second argument while keeping the displacements u fixed for $u, w \in \mathcal{V}$ and $\psi \in \mathcal{K}$. The derivation of the Euler-Lagrange equations is split into two parts for the two directional derivatives:

a) We start with $E'_\epsilon(u, \varphi)(w)$.
For the first term of the u-equation from Formulation 6, we use [184, Proposition 18], which states that

$$(\sigma(u) : E_{\text{lin}}(u))'(w) = 2\sigma(u) : E_{\text{lin}}(w),$$

since the Cauchy stress tensor $\sigma(u)$ is symmetric. It leads to

$$\begin{aligned} \left(\frac{1}{2}\int_\Omega (g(\varphi)\sigma(u) : E_{\text{lin}}(u)\,dx\right)'(w) &= \frac{1}{2}\int_\Omega g(\varphi)(\sigma(u) : E_{\text{lin}}(u))'(w)\,dx \\ &= \int_\Omega g(\varphi)\sigma(u) : E_{\text{lin}}(w)\,dx \\ &= (g(\varphi)\sigma(u), E_{\text{lin}}(w)). \end{aligned}$$

For the pressure term, the linearity of the divergence operator gives

$$\left(\int_\Omega \varphi^2 \rho \nabla \cdot u \, dx\right)'(w) = \int_\Omega \varphi^2 \rho \nabla \cdot w \, dx = (\varphi^2 \rho, \nabla \cdot w).$$

The last two terms from Proposition 4 (Ambrosio-Tortorelli approximation of a crack C) are independent of u. Next, building the sum of all directional derivatives for $E'_\epsilon(u,\varphi)(w)$ reads

$$E'_\epsilon(u,\varphi)(w) = (g(\varphi)\sigma(u), E_{\text{lin}}(w)) + (\varphi^2 \rho, \nabla \cdot w).$$

b) We obtain the second directional derivative $E'_\epsilon(u,\varphi)(\psi-\varphi)$ via computing the directional derivatives into the direction $(\psi-\varphi) \in \mathcal{K}$ for $\psi, \varphi \in \mathcal{K}$ and using the convex property of $\mathcal{K}$, see Proposition 2. We assume u to be fixed and let φ be the minimum of $E_\epsilon(u,\varphi)$. Since $\mathcal{K}$ is convex, it holds

$$\varphi + s(\psi - \varphi) = s\psi + (1-s)\varphi \in \mathcal{K}, \quad \text{for } s \in [0,1], \tag{4.7}$$

and further

$$E_\epsilon(u, \varphi + s(\psi - \varphi)) \geq E_\epsilon(u,\varphi), \tag{4.8}$$

because φ is assumed to be a minimizer. So, $E_\epsilon(u, \varphi + s(\psi-\varphi))$ is non decreasing on $[0,1]$, thus its right-sided derivative at 0 is non-negative [20]. With the help of Equations (4.7) and (4.8) it follows

$$\begin{aligned} E'_\epsilon(u,\varphi)(\psi-\varphi) &= \frac{d}{ds} E_\epsilon(u, \varphi + s(\psi-\varphi))|_{s=0} \\ &= \frac{d}{ds} E_\epsilon(u, s\psi + (1-s)\varphi)|_{s=0} \geq 0. \end{aligned}$$

We build gradually the directional derivative of the stress term, the pressure term and the crack

regularization terms:

$$
\begin{aligned}
E'_\epsilon(u,\varphi)(\psi-\varphi) &= \frac{d}{ds}E_\epsilon(u,\varphi+s(\psi-\varphi))|_{s=0} \\
&= \frac{d}{ds}\frac{1}{2}\int_\Omega [(1-\kappa)(\varphi+s(\psi-\varphi))^2+\kappa]\sigma(u):E_{\text{lin}}(u)\,dx|_{s=0} \\
&+ \frac{d}{ds}\int_\Omega (\varphi+s(\psi-\varphi))^2\rho\nabla\cdot u\,dx|_{s=0} \\
&+ \frac{d}{ds}G_C\int_\Omega \frac{1}{2\epsilon}(1-\varphi-s(\psi-\varphi))^2\,dx|_{s=0} \\
&+ \frac{d}{ds}G_C\int_\Omega \frac{\epsilon}{2}(\nabla(\varphi+s(\psi-\varphi)))^2\,dx|_{s=0} \\
&= \frac{1}{2}\int_\Omega [(1-\kappa)(2\varphi(\psi-\varphi)+2s(\psi-\varphi)(\psi-\varphi))]\sigma(u):E_{\text{lin}}(u)\,dx|_{s=0} \\
&+ \int_\Omega 2(\psi-\varphi)(\varphi+s(\psi-\varphi))\rho\nabla\cdot u\,dx|_{s=0} \\
&+ G_C\int_\Omega \frac{1}{2\epsilon}2(1-\varphi-s(\psi-\varphi))(-(\psi-\varphi))\,dx|_{s=0} \\
&+ G_C\int_\Omega \frac{\epsilon}{2}2(\nabla(\varphi+s(\psi-\varphi))\nabla(\psi-\varphi))\,dx|_{s=0} \\
&= \int_\Omega [(1-\kappa)\varphi(\psi-\varphi)]\sigma(u):E_{\text{lin}}(u)\,dx \\
&+ \int_\Omega 2(\psi-\varphi)\varphi\rho\nabla\cdot u\,dx + G_C\int_\Omega \frac{1}{\epsilon}(1-\varphi)(\psi-\varphi)\,dx \\
&+ G_C\int_\Omega \epsilon(\nabla(\psi-\varphi)\varphi)\,dx \\
&= ((1-\kappa)\varphi\sigma(u):E_{\text{lin}}(u),\psi-\varphi)+(2\varphi\rho\nabla\cdot u,\psi-\varphi) \\
&+ G_C\left(-\frac{1}{\epsilon}(1-\varphi,\psi-\varphi)+\epsilon(\nabla\varphi,\nabla(\psi-\varphi))\right)\geq 0
\end{aligned}
$$

The computed directional derivatives lead to Proposition 4: a CVIS with the irreversibility condition embedded in a convex subset $\mathcal{K}\subset\mathcal{W}$. Details on constraints of obstacle and contact problems can be found, e.g., in [102, 103]. □

4.3 Primal phase-field fracture problem in strong form

We started with an energy minimization phase-field fracture problem with irreversibility condition (Section 4.1) and derived the Euler-Lagrange equations with inequality constraint (Section 4.2). In this section, we formulate the problem in strong form. The equivalence of the minimization problem, the weak form, and a strong problem could be shown, which has to be conducted carefully and goes beyond the scope of this thesis. For completeness, the continuous problem formulation of phase-field fracture referred to Miehe et al. [130] is given in the following.

Formulation 7 (Primal phase-field fracture model in strong form)**.** *Find* $u:(\Omega\times I)\to\mathbb{R}^2$ *and*

$\varphi : (\Omega \times I) \to \mathbb{R}$ *such that*

$$\begin{aligned} -\nabla \cdot (g(\varphi)\sigma(u)) &= 0 \quad \text{in } (\Omega \times I), \\ (1-\kappa)\varphi\sigma(u) : E_{lin}(u) - \frac{G_C}{\epsilon}(1-\varphi) - \epsilon G_C \Delta\varphi &\leq 0 \quad \text{in } (\Omega \times I). \end{aligned} \tag{4.9}$$

The crack irreversibility condition is determined by

$$\partial_t \varphi \leq 0 \quad \text{in } (\Omega \times I). \tag{4.10}$$

For simplicity, we assume Dirichlet boundary conditions for the displacement function u stated as

$$u = u_D \quad \text{on } (\partial\Omega \times I),$$

and boundary conditions for the phase-field function via

$$\epsilon \partial_n \varphi = 0 \quad \text{on } (\partial\Omega \times I),$$

To link the phase-field equation from Equation (4.9) and the crack irreversibility constraint from Equation (4.10), a complementarity condition is required:

$$\left((1-\kappa)\varphi\sigma(u) : E_{lin}(u) - \frac{G_C}{\epsilon}(1-\varphi) - \epsilon G_C \Delta\varphi\right) \cdot (\partial_t \varphi) = 0 \quad \text{in } (\Omega \times I).$$

An initial condition

$$\varphi(x, 0) = \varphi_0 \quad \text{in } (\Omega \times \{0\}),$$

completes the problem formulation.

If a pressurized fracture phenomenon is considered, pressure terms (with given pressure ρ) are added in the strong problem formulation:

Formulation 8 (Pressure-driven primal phase-field fracture model in strong form)**.** *Let $\rho : (\Omega \times I) \to \mathbb{R}$ be a given (constant) pressure. Find $u : (\Omega \times I) \to \mathbb{R}^2$ and $\varphi : (\Omega \times I) \to [0, 1]$ such that*

$$\begin{aligned} -\nabla \cdot \left(g(\varphi)\sigma(u) - \varphi^2\rho\right) &= 0 \quad \text{in } (\Omega \times I), \\ (1-\kappa)\varphi\sigma(u) : E_{lin}(u) - \frac{G_C}{\epsilon}(1-\varphi) - \epsilon G_C \Delta\varphi + 2\varphi\rho\nabla \cdot u &\leq 0 \quad \text{in } (\Omega \times I). \end{aligned}$$

As denoted in Formulation 7, the complementarity condition of the two stated equations, boundary and initial conditions are required. The crack irreversibility is an added constraint.

Proving the equivalence of a similar strong and weak problem formulation would require a careful use of the fundamental lemma of the calculus of variations, see [54]. Further, embedding theorems for Sobolev spaces have to be used to transition from a weak to a strong form. For further details, we refer to Adams and Fournier [1], and Ciarlet [53].

4.4 Notion of Γ-convergence for phase-field fracture

We use the notion of Γ-convergence to establish sharp interface limits when working with phase-field fracture formulations. For $\epsilon \to 0$ ($h \to 0$) we can prove that minima of the regularized energy functional converges in the sense of Γ-limits to minima of the non-regularized functional which describes the fracture behavior according to Griffith. In this section, the Γ-convergence theorem is given for an energy functional similar to Formulation 5 from Section 4.1 $\Omega \subset \mathbb{R}$. The section is based on [41, 64].

Formulation 9 (General energy functional for phase-field fracture modeling)**.**

$$E_\epsilon(u,\varphi) = \frac{1}{2}\int_\Omega \Big(\left((1-\kappa)\varphi^2 + \kappa\right)(2\mu+\lambda)|\nabla u|^2 + \rho\ \varphi\nabla u \Big)\, dx \\ + \frac{1}{2} G_C \int_\Omega \left(\frac{1}{\epsilon}(1-\varphi)^2 + \epsilon|\nabla\varphi|^2 \right) dx. \tag{4.11}$$

Remark 13 (Simplified notation in elasticity term)**.** *In the proof of Γ-convergence, an energy functional as in Formulation 9 is assumed. In Formulation 6 from Section 4.1, we have the bulk energy term* $(\sigma(u) : E_{lin}(u))$ *instead of* $(2\mu+\lambda)|\nabla u|^2$*. In one dimension one can easily see that*

$$\sigma(u) : E_{lin}(u) = (2\mu+\lambda)|\nabla u|^2.$$

The proof of Γ-convergence in higher dimensions for the pressurized phase-field fracture problem is given by Sommer [157].

We see that under certain conditions, the phase-field fracture problem from Formulation 9 is a valid choice as an approximation of the Ambrosio-Tortorelli [5, 6] functional

$$E_T(u,C) = \frac{1}{2}\int_\Omega \Big((2\mu+\lambda)|\nabla u|^2 + \rho\nabla u \Big)\, dx + G_C \#(S(u)), \tag{4.12}$$

where $S(u)$ is the set of discontinuities of u and $\#(S(u))$ is the cardinality of $S(u)$. To formulate the Γ-convergence theorem, the following definitions are required.

Definition 8. *(Space of piecewise constant functions) For* $\Omega \in \mathbb{R}^n$ *the space of piecewise constant functions is defined by*

$$PC(\Omega) = \left\{ f : \Omega \to \mathbb{R} \quad \middle| \quad \exists \text{ non-overlapping } I_i \subset \Omega \text{ s.t. } \bigcup_i \bar{I}_i = \Omega,\ c_i \in \mathbb{R} : f|_{I_i} = c_i \quad \forall\, i \right\}.$$

Definition 9. *(Space of piecewise* H^1*-functions) For* $\Omega \in \mathbb{R}^n$ *the space of functions, which are piecewise of* H^1*, is defined by*

$$PH^1(\Omega) = \left\{ f : \Omega \to \mathbb{R} \quad \middle| \quad \exists \text{ non-overlapping } I_i \subset \Omega \text{ s.t. } \bigcup_i \bar{I}_i = \Omega : f \in H^1(I_i) \quad \forall\, i \right\}.$$

The general definition of Γ-convergence reads:

Definition 10. *(Γ-convergence) Let* X *be Banach space. For a given sequence of functions* $(f_j) : X \to \mathbb{R}$ *and a function* $f_\infty : X \to \mathbb{R}$*, the sequence* (f_j) *Γ-converges in* X *to* f_∞ *if for all* $x \in X$ *it*

holds

(i) for every sequence (x_j) *converging to* x

$$f_\infty(x) \leq \liminf_{j\to\infty} f_j(x_j) \qquad \textit{(lim inf inequality)},$$

(ii) there exists a sequence (x_j) *converging to* x *such that*

$$f_\infty(x) \geq \limsup_{j\to\infty} f_j(x_j) \qquad \textit{(lim sup inequality)}.$$

The function f_∞ *is called the* Γ*-limit of* (f_j) *and we write* $f_\infty = \Gamma\text{-}\lim_j f_j$.

The following theorem verifies the use of the developed approximation functional and guarantees that a minimizer of the functional in Equation (4.11) converges to a minimizer of the functional in Equation (4.12) as $\epsilon \to 0$. Note that Theorem 1 is formulated for one incremental step, and since it holds for each step, the indices are dropped for better readability.

Theorem 1. *The regularized functional* $G_j : L^1(\Omega) \times L^1(\Omega) \to \mathbb{R}$*, defined by*

$$G_j(u_j, \varphi_j) = \begin{cases} E_{\epsilon_j}(u_j, \varphi_j) & \textit{if } (u_j, \varphi_j) \in H^1(\Omega) \times \mathcal{K}, \\ +\infty & \textit{otherwise}, \end{cases}$$

Γ*-converges, as*

$$\epsilon_j \to 0^+ \textit{ for } j \to \infty \textit{ and } \kappa = o(\epsilon_j),$$

to the functional $G : L^1(\Omega) \times L^1(\Omega) \to \mathbb{R}$*, given by*

$$G(u, \varphi) = \begin{cases} E_T(u, C) & \textit{if } \varphi = 1 \textit{ a.e. and } u \in PH^1(\Omega), \\ +\infty & \textit{otherwise}. \end{cases}$$

Further, if (u_j, φ_j) *is a minimizer of* G_j*, then* (u_j, φ_j) *(possibly a subsequence) converges to a minimizer of* G.

Proof The proof in 1d is separated into three parts: the lower semicontinuity inequality (*Part 1*), the upper semicontinuity inequality (*Part 2*), and the property of convergence of minimizers of G_j to a minimizer of G (*Part 3*). We stress that the execution of this proof[1] is a detailed version of the proof given by Braides [40, 41], which we present in Appendix A. □

Theorem 1 allows stating that $E_\epsilon(u, \varphi)$ is a valid choice as an approximation of $E_T(u, C)$ if the conditions for Γ-convergence are fulfilled: $\kappa_j = o(\epsilon_j)$, and the displacement function u_j and the phase-field function φ_j converge as $\epsilon \to 0$. It implies that the choices of κ_j and ϵ_j are crucial for the validity of the results, which leads to the next section.

[1] The proof was prepared by Kolditz [106]. His Bachelor's thesis was co-supervised by the author of the thesis on hand.

4.5 Error analysis on the relation of h, κ, and ϵ

In this section[2], the impact of the regularization parameters $\epsilon > 0$ and $\kappa > 0$, and the discretization parameter h, is discussed. A regularization parameter κ regularizes the bulk energy and should be as small as possible to avoid over-estimating the bulk energy (resulting in an under-estimation of the surface crack energy). In practice, it means: the greater the value of κ, the slower the crack grows. Bellettini and Coscia [24] proved Γ-convergence of the regularized energy functional for $\kappa \to 0$, $\epsilon \to 0$ and $h \to 0$ with $\kappa \ll \epsilon$ and $h \ll \epsilon$. In 1999, Bourdin et al. [31] presented the Γ-convergence of the discretized Mumford and Shah functional [135] $E_{\epsilon,h}(u, \varphi)$ for image segmentation with the assumption $h \ll \kappa \ll \epsilon$, which allows that $E_{\epsilon,h}(u, \varphi)$ converges to $\min(F)$, as $\epsilon \to 0$. In the first numerical results on images, the parameters are chosen such that $h \ll \kappa \ll \epsilon$. Bourdin et al. [35] presented a phase-field fracture model based on the Ambrosio-Tortorelli functional [5, 6] with the restrictions $h \ll \epsilon$ and $h \ll \kappa$. Borden in 2012 [29] determined $\kappa = 0$ for a dynamic phase-field fracture model and argues that a positive small κ is not necessary to obtain Γ-convergence, proved by Braides 1998 [40]. In a dynamic phase-field fracture model, the second time derivative in u is not degraded, avoiding zero entries in the discrete system [184], and confirming the statement from a numerical perspective. The idea of the following tests is to understand the conducted error analysis for a reliable setting for κ, ϵ and h, for one benchmark test with exact reference values. Throughout the series of numerical tests, we use the Landau notation for evaluating the limit behavior of the considered parameters:

$$k = \mathcal{O}(f) \quad \Longleftrightarrow \quad \frac{k}{f} \to 0.$$

4.5.1 Configuration of Sneddon's benchmark

We consider a stationary benchmark test [153], where constant pressure is applied in the inner of a pre-existing crack in the middle of a domain, and only the crack width varies. This test setup is motivated by Sneddon [155], and Sneddon and Lowegrub [156], and used in several other publications, e.g., [33, 176, 134, 88, 153, 22, 181, 180, 116]. We restrict ourselves to a 1d fracture C on a two-dimensional domain $\Omega = (-10, 10)^2$ as depicted in Figure 4.2 on the left. The fracture is centered horizontally within Ω and has a constant half crack length $l_0 = 0.25$ and varying width. Precisely, the crack width corresponds to $2\,h$, where h is the minimal cell diameter of the mesh. The mesh is pre-refined geometrically in the crack zone, as depicted exemplarily for one adaptive refinement step in Figure 4.2 on the right, where the crack zone is resolved with the smallest mesh size. The driving force is given by a constant pressure $\rho = 10^{-3}\,\mathrm{Pa}$ in the inner crack. The parameter setting is given in Table 4.1.

Two specific quantities of interest are discussed: the crack opening displacement (COD) and the total crack volume (TCV). The COD is defined on an infinite domain via

$$\mathrm{COD}(x) \coloneqq [u \cdot n](x) \approx \int_{-\infty}^{\infty} u(x, y) \cdot \nabla\varphi(x, y)\, dy.$$

[2]Results from Section 4.5 are under review, see [107].

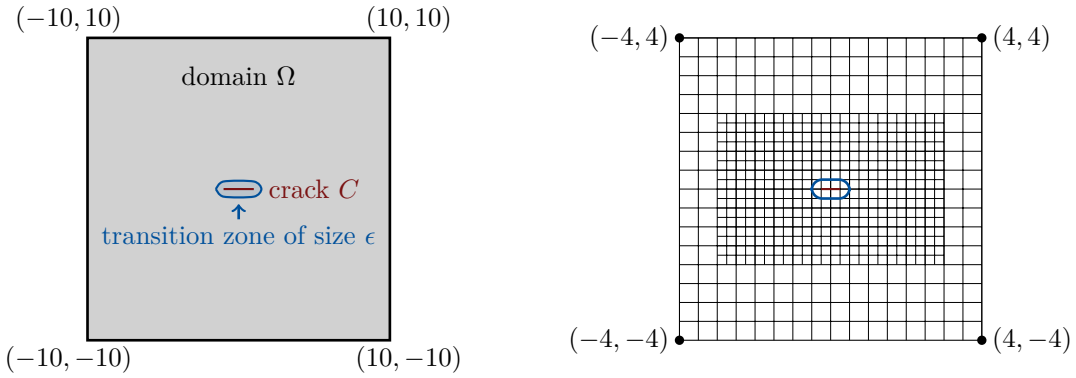

Figure 4.2: Left: geometry of the two-dimensional Sneddon's test. Right: zoom-in to the pre-refined crack zone in $[-4, 4] \times [-4, 4]$ with two global refinement steps and one local refinement step (geometrically pre-refined).

The maximum of COD is reached in $x = 0$ and thus given by

$$\mathrm{COD}_{\max} := [u \cdot n](0) \approx \int_{-\infty}^{\infty} u(0, y) \cdot \nabla\varphi(0, y)\, dy.$$

The analytical solution for an infinite domain is given by Sneddon and Lowengrub [156], via

$$\mathrm{COD}_{\mathrm{ref}} = 2\frac{\rho l_0}{E'}\left(1 - \frac{x^2}{l_0^2}\right)^{\frac{1}{2}},$$

where $E' := \frac{E}{1-\nu^2}$ with the Young's modulus E, and the Poisson ratio ν. The TCV can be computed numerically via

$$\mathrm{TCV} = \int_{\Omega} u(x, y) \cdot \nabla\varphi(x, y)\, d(x, y).$$

The analytical solution [156] is given by

$$\mathrm{TCV}_{\mathrm{ref}} = \frac{2\pi\rho l_0^2}{E'}.$$

4.5.2 Numerical studies on the relation of h, κ, and ϵ

As stated in Theorem 1 on a continuous level, for Γ-convergence, a specific choice of the regularization parameters κ and ϵ is required. Further, we need to choose $\epsilon > h$ to ensure that the mesh does not omit the crack (at least for linear finite elements). Transferred from the notion of Γ-convergence from Section 4.4, we state:

$$\kappa = \mathcal{O}(\epsilon) \quad \text{and} \quad h = \mathcal{O}(\epsilon), \tag{4.13}$$

Parameter	definition	value
Ω	domain	$(-10, 10)^2$
h	diagonal cell diameter	test-dependent
l_0	half crack length	0.25
G_C	material toughness	$1.0\,\mathrm{N/mm}$
E	Young's modulus	$1.0\,\mathrm{MPa}$
μ	Lamé parameter	$0.42\mathrm{N/mm}^2$
λ	Lamé parameter	$0.28\mathrm{N/mm}^2$
ν	Poisson's ratio	0.2
ρ	applied pressure	$10^{-3}\,\mathrm{Pa}$
ϵ	bandwidth of the initial crack	test-dependent
κ	regularization parameter	test-dependent

Table 4.1: Setting of the material and numerical parameters used for the numerical tests with Sneddon's benchmark.

as $\epsilon \to 0$, which is numerically desirable but challenging. A possible choice, similar to Wheeler at al. [176, Case 4], is

$$\text{Case 1:} \quad \kappa = 0.25\, h^{0.5} \quad \text{and} \quad \epsilon = 0.25\, h^{0.25}. \tag{4.14}$$

This setting satisfies the Γ-convergence conditions introduced in Equation (4.13) for all $h < 0.5$. Further, $h < \epsilon$ is satisfied for all $h < 0.5$.

Remark 14 (Comparison to literature)**.** *In contrast to Engwer and Schumacher [64], ϵ, κ and h are not decreased proportionally, but according to the above condition, such that $\kappa \ll \epsilon$ and $h \ll \epsilon$.*

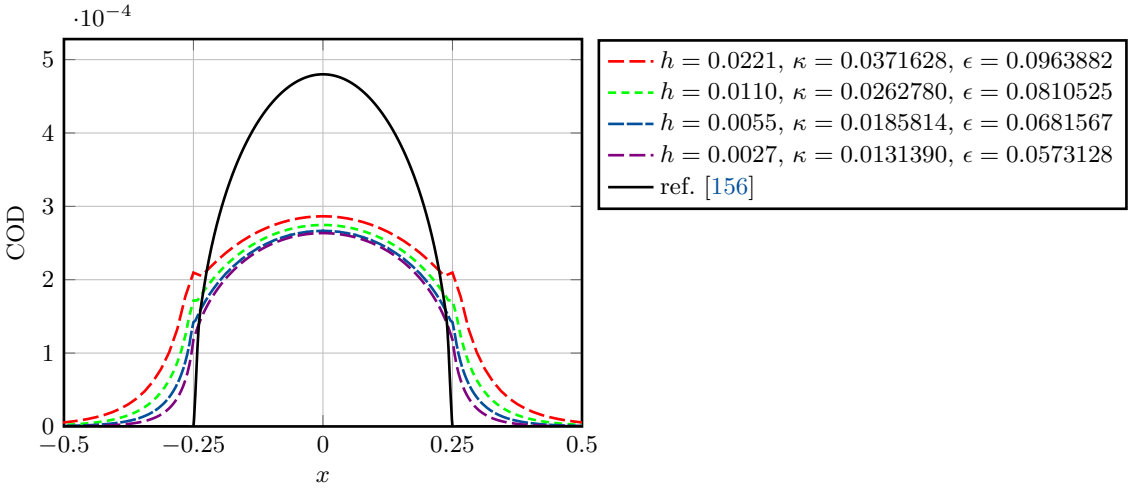

Figure 4.3: Visualization of the CODs for different h with κ and ϵ set as in Case 1 from Equation (4.14). The corresponding TCV and $\mathrm{COD}_{\max}$ values are given in Table 4.2.

Satisfying the relations of κ and ϵ as denoted in Case 1, the numerically achieved COD values and TCV values are given in Figure 4.3 and Table 4.2 for different minimal mesh sizes h. By decreasing h, the COD values do not converge to the analytical solution proposed by Sneddon and Lowengrub [156].

Misleadingly, the TCV value for $h = 0.022$ is relatively close to the exact reference. Since TCV is the integral of the COD curve, and even if the exact COD is underestimated, the approximative bell curve is wider than the exact one, which results in a larger (or in this case better) TCV value. Resolving the crack area, h can be assumed to be sufficiently small for satisfactory COD and TCV values compared to the literature, e.g., [88]. One reason for imprecise COD values may be the regularization parameter κ. To give quantitative arguments for this observation, in Table 4.3, an error analysis on κ for the TCV value is given.

h	$\mathrm{COD}_{\max}$	TCV	# dof
0.0221	0.000286517	0.000313325	43 605
0.0110	0.000274623	0.000276284	100 089
0.0055	0.000267051	0.000253393	176 709
0.0027	0.000263680	0.000239692	628 533
ref. [156]	0.000480000	0.000376991	-

Table 4.2: Results of maximal crack opening displacement ($\mathrm{COD}_{\max}$), total crack volume (TCV) and degrees of freedom (# dof) for different mesh sizes h and the relations of Case 1 from Equation (4.14) compared to the reference values of Sneddon and Lowengrub [156].

We identify possible reasons for the non-satisfactory results for two relevant quantities of interest (COD and TCV). The idea is to analyze the TCV-error for different parameter settings, especially for different values of κ. Thus, Table 4.3 provides detailed test results.

κ	TCV	TCV error
$h = 5.52427 \cdot 10^{-3}$	0.000239171	36.5 %
$0.5\,h = 2.762135 \cdot 10^{-3}$	0.000290719	22.8 %
$0.25\,h = 1.381068 \cdot 10^{-3}$	0.000330106	12.4 %
$10^{-1}\,h = 5.52427 \cdot 10^{-4}$	0.000361447	4.1 %
$10^{-2}\,h = 5.52427 \cdot 10^{-5}$	0.000384297	1.9 %
$10^{-3}\,h = 5.52427 \cdot 10^{-6}$	0.000386788	2.60 %
$10^{-12}\,h = 5.52427 \cdot 10^{-15}$	0.000387067	2.67 %
ref. [156]	0.000376991	-

Table 4.3: Error in the total crack volume (TCV error) in percentage (compared to the exact $\mathrm{TCV}_{\mathrm{ref}} = 0.000376991$ on an infinite domain) for different choices of κ depending on the diagonal cell diameter $h = 0.00552427$ and fixed $\epsilon = 2\,h$.

With a tolerance of less than 4 % TCV error, κ should be smaller than 10^{-5}, see Table 4.3. Thus we determine

$$\kappa = 0.25\,h^{0.5} < 10^{-5},$$

which leads to a discretization parameter $h \approx 10^{-9}$. This would yield an unrealistic number of dof. Even if only the known crack zone $[-0.26, 0.26] \times [-0.4, 0.4]$ is refined, the problem would have a size of approximately 10^{17} dof. Thus we need to find a setting for κ, which does not violate the Γ-convergence

conditions, but tends to zero faster with h. Another possible choice is given by:

$$\text{Case 2:} \quad \kappa = 10^{-3}\, h^{0.75} \quad \text{and} \quad \epsilon = 0.25\, h^{0.25}. \tag{4.15}$$

In Case 2, $h = \mathcal{O}(\kappa)$ and $\kappa = \mathcal{O}(\epsilon)$ is satisfied, and κ is small enough for promising results of the two chosen quantities of interest with $h \approx 10^{-5}$, without exceeding the computational capacity. The behavior of κ, ϵ and h for Case 2 is visualized in Figure 4.4. We can see that κ is small, even for large h. This is a major computational advantage compared to Case 1 since we do not need as many dof as in Case 1. Figure 4.5 provides results for Case 2.

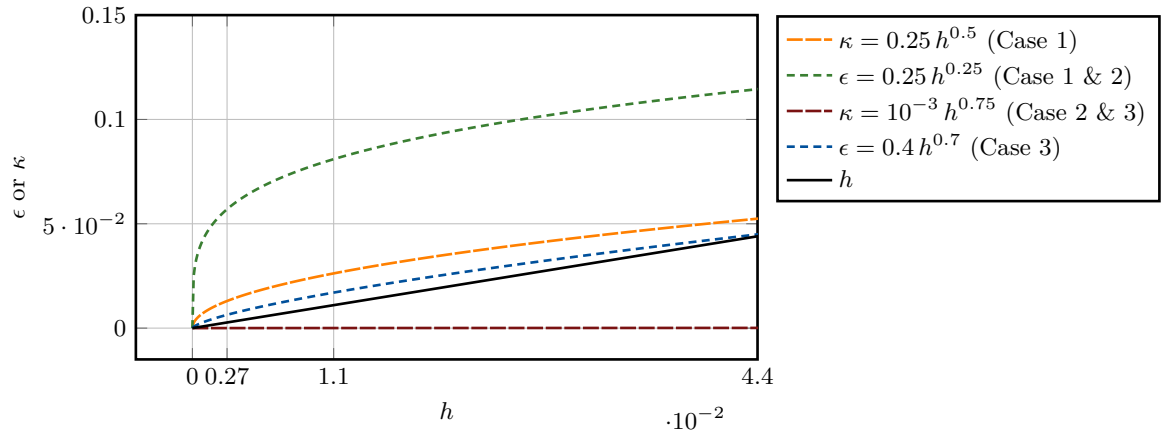

Figure 4.4: Visualization of ϵ and κ set as in Case 1 from Equation (4.14), and Case 2 from Equation (4.15). We can see that κ is small in Case 3 from Equation (4.16) even for large h, and ϵ satisfies $\epsilon > h$ and $h = \mathcal{O}(\epsilon)$ for reasonable h while being close to h.

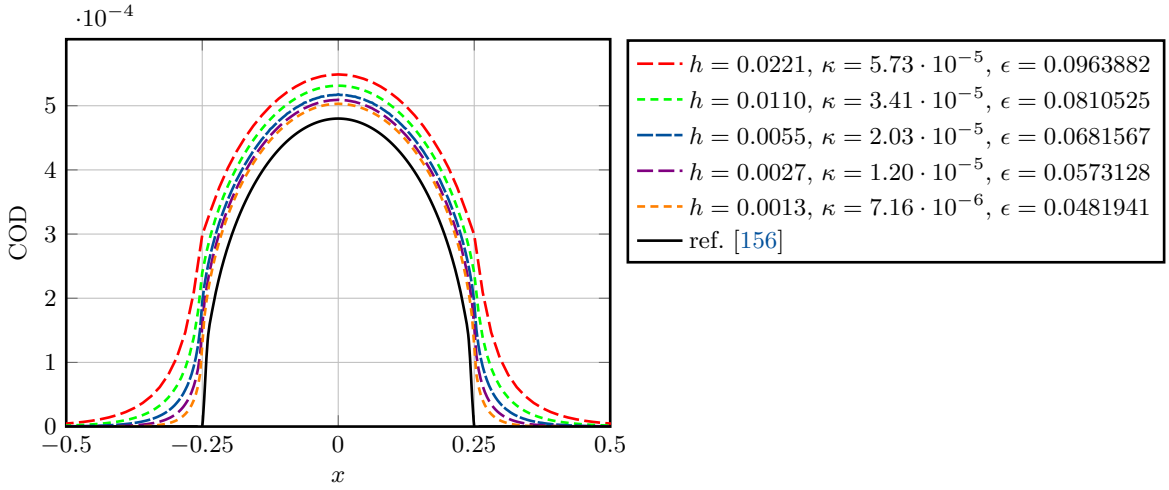

Figure 4.5: Visualization of the COD values for different h with h-dependent κ, and ϵ set as in Case 2 from Equation (4.15). The corresponding TCV and COD_{max} values are given in Table 4.4.

As we can see in Figure 4.5 and Table 4.4, the results are closer to the reference values for Case 2 than for Case 1 but there is still a recognizable error.

h	$\mathrm{COD}_{\max}$	TCV	# dof
0.0221	0.000548804	0.000536082	43 605
0.0110	0.000531268	0.000487890	100 089
0.0055	0.000517768	0.000456257	176 709
0.0027	0.000509288	0.000435760	628 533
0.0013	0.000503050	0.000421441	2 416 869
ref. [156]	0.000480000	0.000376991	-

Table 4.4: Results of computations based on the relations of Case 2 from Equation (4.15).

ϵ	TCV	TCV error
$64\,h = 0.35355328$	0.000909849	141.35 %
$32\,h = 0.17677664$	0.000608694	61.46 %
$16\,h = 0.08838832$	0.000478809	27.00 %
$8\,h = 0.04419416$	0.000425164	12.78 %
$4\,h = 0.02209708$	0.000402041	6.64 %
$2\,h = 0.01104854$	0.000390668	3.63 %
$h = 0.00552427$	0.000384213	1.92 %
ref. [156]	0.000376991	-

Table 4.5: Error in TCV in percentage (compared to the exact TCV = 0.000376991 on an infinite domain) for different choices of ϵ depending on the diagonal cell diameter $h = 0.0055$ and fixed $\kappa = 10^{-6}\,h$.

Since κ is small enough, in the next step, we investigate the error in the bandwidth ϵ. The error analysis in Table 4.5 indicates that the impact of ϵ is sufficiently small for $\epsilon \approx 3.8 \times 10^{-4}$. We expect the error to reduce further for smaller h yielding smaller ϵ. For the error analysis, we chose $\epsilon = h$ as the smallest reasonable choice since ϵ indicates the thickness of the crack, and if $\epsilon < h$, the numerical grid could omit the crack with linear finite elements. We propose a third setting, where ϵ is smaller compared to Case 1 and Case 2 and closer to h while not violating $\epsilon > h$:

$$\text{Case 3:} \quad \kappa = 10^{-3}\,h^{0.75} \text{ and } \epsilon = 0.4\,h^{0.7}. \tag{4.16}$$

The numerical results of the same tests based on the setting in Case 3 are given in Figure 4.6 and Table 4.6. Compared to the reference solution given by Sneddon and Lowengrub [156], we achieve good results for small discretization parameters h.

h	$\mathrm{COD}_{\max}$	TCV	# dof
0.0221	0.000513461	0.000432474	43 605
0.0110	0.000499444	0.000406175	100 089
0.0055	0.000489812	0.000391876	176 709
0.0027	0.000484421	0.000384389	628 533
0.0013	0.000481000	0.000380047	2 416 869
ref. [156]	0.000480000	0.000376991	-

Table 4.6: Numerical results of two quantities of interest ($\mathrm{COD}_{\max}$ and TCV), and dof (# dof) for different h with h-dependent κ and ϵ set as in Case 3 defined in Equation (4.16).

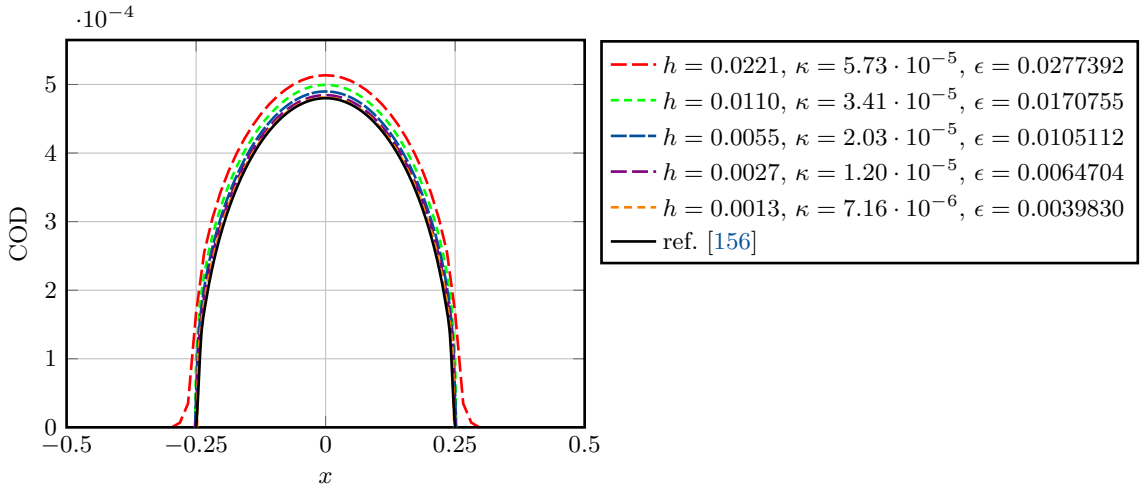

Figure 4.6: Visualization of the COD values for different h with h-dependent κ and ϵ, set as in Case 3 defined in Equation (4.16). For the smallest h, the numerical and the reference values coincide nearly perfectly. The corresponding TCV and COD_{max} values are given in Table 4.6.

The results of this section show that the best setting for the three relevant parameters is

$$\kappa = 10^{-3}\, h^{0.75},$$
$$\epsilon = 0.4\, h^{0.7},$$

if $h \to 0$. In this case, we obtain for the largest h a TCV error of 14.72 % and a COD error of 6.97 %. The errors reduce to 0.81 % (TCV) and 0.2 % (COD) on a mesh with around 2.5 million dof. This is a major improvement compared to the settings of Case 1 and Case 2 and handles the requirements on ϵ and κ satisfactorily while not being restricted to a too fine mesh resolution.

Remark 15 (The relation of ϵ and h in practice)**.** *The often-used setting $\epsilon = 2\ h$ and κ set sufficiently small, can give satisfactory results for a certain application even if conditions for Γ-convergence are violated.*

4.6 Three definitions of the energy functional

The regularized phase-field fracture approach of Bourdin et al. [35] was inspired by the Ambrosio-Tortorelli functionals [5, 6]. In the following, three energy functionals are presented: AT_2, the Ambrosio-Tortorelli functional with a quadratic energy degradation function; AT_1, the Ambrosio-Tortorelli functional with a linear energy degradation function; and Wu's functional [189] with a linear and a quadratic part in the energy degradation function. In the previous chapters, the problem formulations were based on the classically used functional AT_2. In phase-field fracture, also AT_1 is an often used energy functional. Via the linear term depending on φ, it guarantees an ideally linear stress-strain response up to the elastic limit stress for linearly elastic solids [193]. The focus of this section is the pure definition of the energy functionals. The previously introduced pressure terms are omitted in the following.

4.6.1 AT_2 functional

The AT_2 functional (named according to Tanné et al. [163]) is defined as

$$\begin{aligned} \mathrm{AT}_2: \quad E_\epsilon(u,\varphi) &= \frac{1}{2}\int_\Omega g(\varphi)\sigma(u) : E_{\mathrm{lin}}(u)\,dx \\ &\quad + G_C \int_\Omega \frac{1}{2\epsilon}(1-\varphi)^2\,dx + G_C \int_\Omega \frac{\epsilon}{2}|\nabla\varphi|^2\,dx. \end{aligned} \tag{4.17}$$

It is the energy functional we used in all previous sections, especially in Section 4.4, where we dicussed the notion of Γ-convergence (in 1d).

4.6.2 AT_1 functional

Bourdin et al. [37] introduced a similar functional with a stress-softening behavior. The damage model remains purely elastic without damage until the stress reaches the critical value [123]. The functional is defined as

$$\begin{aligned} \mathrm{AT}_1: \quad E_\epsilon(u,\varphi) &= \frac{1}{2}\int_\Omega g(\varphi)\sigma(u) : E_{\mathrm{lin}}(u)\,dx \\ &\quad + G_C \int_\Omega \frac{3}{8\epsilon}(1-\varphi)\,dx + G_C \int_\Omega \frac{3}{8}\epsilon|\nabla\varphi|^2\,dx. \end{aligned} \tag{4.18}$$

The proof of Γ-convergence can also be conducted for the AT_1 functional, see [70].

4.6.3 Wu's functional

To decrease the impact of a possibly material-dependent length scale parameter ϵ, Wu [189, 190] and Wu and Nguyen [191] proposed a unified phase-field theory for damage and quasi-brittle failure with different softening laws. For simulating fractures in EPDM rubber in Chapter 7, we follow Wu's energy functional defined as

$$\begin{aligned} \text{Wu:} \quad E_\epsilon(u,\varphi) &= \frac{1}{2}\int_\Omega g(\varphi)\sigma(u) : E_{\mathrm{lin}}(u)\,dx \\ &\quad + G_C \int_\Omega \frac{1}{\pi\epsilon}\left(2(1-\varphi) - (1-\varphi)^2\right)\,dx + G_C \int_\Omega \frac{1}{\pi}\epsilon|\nabla\varphi|^2\,dx. \end{aligned} \tag{4.19}$$

Aside from different coefficients, Wu's energy functional in Equation (4.19) compared to the functionals in Equations (4.17) and (4.18) uses a combination of a linear and a quadratic part in the crack energy term, which yields the useful property of finite support for a localized phase-field [189]. The numerical consequences for a real-world application of this choice are described in Section 7.5. The Euler-Lagrange equations of Wu's energy functional in Equation (4.19) can be stated as follows:

Proposition 5 (CVIS of Wu's energy functional)**.** *Given the initial data* $\varphi^{n-1}, \varphi^{n-2} \in \mathcal{K}$. *Find* $\varphi \in \mathcal{K}$

and $u \in \mathcal{V} + \{u_D\}$*, such that*

$$\begin{aligned}(g(\tilde{\varphi})2\mu E_{lin}(u), E_{lin}(w)) + (g(\tilde{\varphi})\lambda tr E_{lin}(u)\mathbb{1}, E_{lin}(w)) = 0 \quad \forall w \in \mathcal{V},\\ (1-\kappa)(\varphi 2\mu E_{lin}(u) : E_{lin}(u), \psi - \varphi) + (1-\kappa)(\varphi\lambda\nabla \cdot u\ \mathbb{1} : E_{lin}(u), \psi - \varphi)\\ + \frac{2G_C}{\pi}(-\frac{1}{\epsilon}\varphi, \psi - \varphi) + \frac{2G_C}{\pi}\epsilon(\nabla\varphi, \nabla(\psi - \varphi)) \geq 0 \quad \forall \psi \in \mathcal{K}.\end{aligned} \tag{4.20}$$

Proof The proof works analogously to the proof of Proposition 3. □

Wu's energy functional builds the basis for the problem formulation used in Chapter 7, where we simulate fractures in punctured rubber strips.

4.6.4 Numerical studies on the choice of the energy functional

We conduct numerical tests for the three proposed energy functionals from the previous section to understand the differences considering crack propagation. As a test case, we use the well-known single-edge notched tension test adopted from [130]. The geometry and boundary conditions are displayed in Figure 4.7 on the left. The domain Ω is a two-dimensional square of 10 mm length with a given crack (geometrical slit) on the right side at 5 mm, tending to the midpoint of the square. On the bottom boundary, the square is fixed, and on the top boundary, a time-dependent force in the x-direction pulls to the left. We follow the boundary conditions described by Wick [182]: On the left and right sides, the boundaries are defined to be traction-free (homogeneous Neumann conditions). The bottom boundary is fixed via $u_y = 0\,\text{mm}$. On the top boundary, it holds $u_x = 0\,\text{mm}$, and in the y-direction, we determine a time-dependent non-homogeneous Dirichlet condition:

$$u_y = t \cdot 1\,\text{mm/s},$$

where $t \in I = (0, T)$, $T > 0$ with an incremental step size $\delta t > 0$. The end time T corresponds to the loading once the specimen is broken.
The material and model parameters are given as follows: the Lamé coefficients are $\lambda = 121.15\,\text{kN/mm}^2$ and $\mu = 80.77\,\text{kN/mm}^2$. The critical energy release rate of the considered material is $G_C = 2.7\,\text{N/mm}$. The loading increment is chosen as $\delta t = 10^{-4}\,\text{s}$ and decreased to $10^{-6}\,\text{s}$ if the crack starts propagating. We determine the bulk regularization parameter $\kappa = 10^{-8}$. To compare the numerical results for the three energy functionals, we evaluate the load functions on the top boundary Γ_{top} computed via

$$(F_x, F_y) \coloneqq \frac{1}{|\Gamma_{\text{top}}|}\int_{\Gamma_{\text{top}}} g(\tilde{\varphi})\sigma(u_h) \cdot n\,\mathrm{d}s, \tag{4.21}$$

with the stress tensor $\sigma(u_h)$ depending on the discrete solution variable u_h and the outer normal vector n. Within the single-edge notched tension test, we are interested in the evaluation of F_y. Our goal is to observe and discuss the behavior of the single-edge notched tension test for the three energy functional approaches, as defined in Equations (4.17), (4.18), and (4.19). We conduct three computations ($\epsilon = h, 2\,h, 4\,h$) with $h = 0.011$ for each functional on the same uniform mesh. In Table 4.7, the maximal loading values and the real time at the maximal loading point are given, respectively.

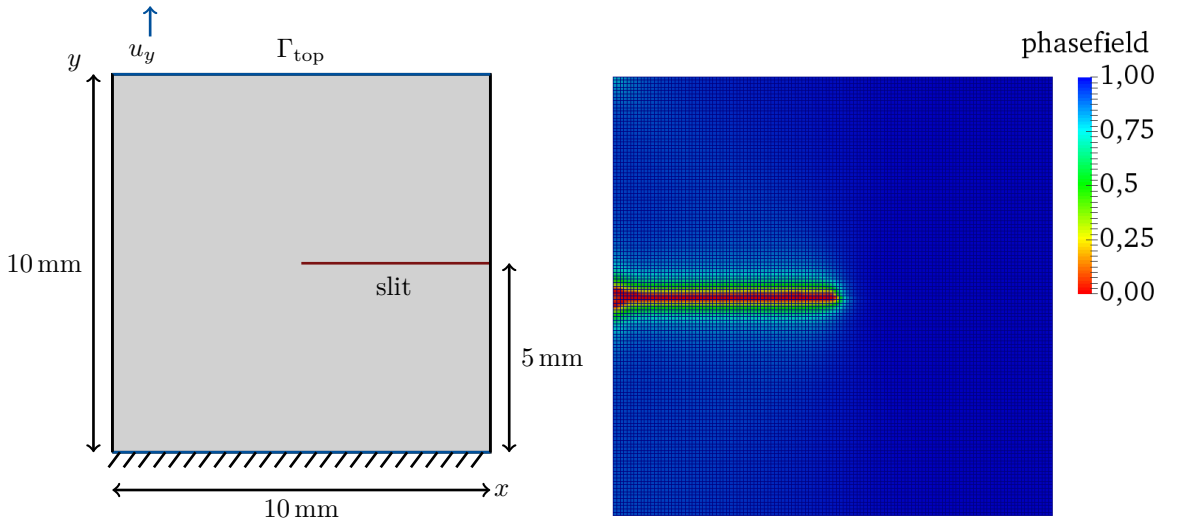

Figure 4.7: Single edge notched tension test. Left: geometry and boundary conditions. Right: phase-field result at the end of the simulation for all three test runs based on the three energy functionals.

Functional	ϵ	maximal loading [N]	time at maximal loading [s]
AT_2	h	852.903	0.0063
AT_1	h	915.169	0.0066
Wu	h	1 021.820	0.0076
AT_2	$2\,h$	802.978	0.0061
AT_1	$2\,h$	874.401	0.0065
Wu	$2\,h$	942.652	0.0069
AT_2	$4\,h$	761.452	0.0060
AT_1	$4\,h$	825.228	0.0061
Wu	$4\,h$	889.830	0.0066

Table 4.7: Study on the three energy functionals for the single-edge notched tension test: maximal loading values and time values for AT_2, AT_1 and Wu, for three settings of the crack width $\epsilon = h, 2\,h, 4\,h$. Same tests as in Figures 4.8 and 4.9.

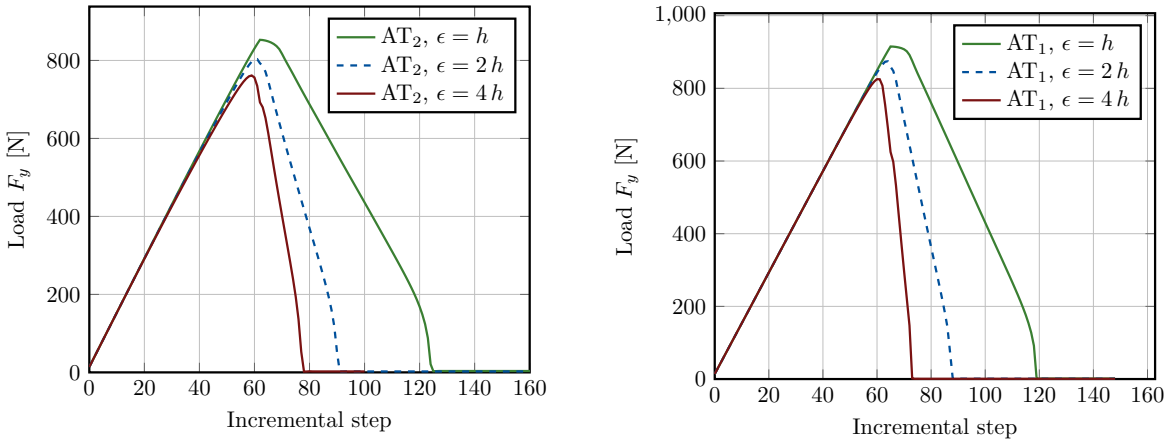

Figure 4.8: Left: load-time step curves for the single-edge notched tension test with the AT_2 functional, uniform refined meshes and three relations for ϵ and h. The incremental step size is 10^{-4} s for the first 62 steps and reduced to 10^{-6} s. Right: load-time step curves for the single-edge notched tension test with the AT_1 functional, uniform refined meshes and three relations for ϵ and h. The incremental step size is 10^{-4} s for the first 65 steps and reduced to 10^{-6} s.

The load-time step curves in Figure 4.8 on the left and on the right are similar. For AT_1 in Figure 4.8 (the plot on the right), the maximal value is approximately 75 N above the results for AT_2. Further, for both Ambrosio-Tortorelli functionals [5, 6], the maximal value is smaller, and the descent of the curve is steeper for larger ϵ when the cracks starts propagating.

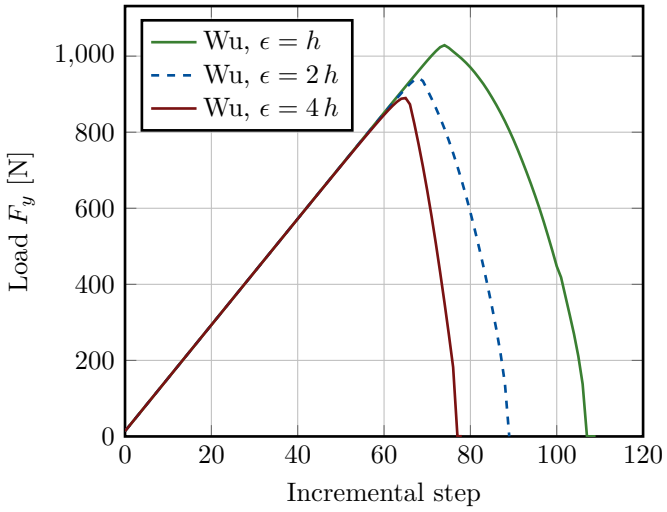

Figure 4.9: Load-time step curves for the single-edge notched tension test with Wu's functional, uniform refined meshes and three relations for ϵ and h. The incremental step size is 10^{-4} s for the first 100 steps and reduced to 10^{-6} s.

In Figure 4.9, the maximal value is larger than the maximal value based on AT_1. Further, the loading decreases slower than with AT_1 or AT_2. On the other hand, the curves look smoother, and we can observe the same behavior as for the Ambrosio-Tortorelli functionals [5, 6], that with a larger ϵ-h relation, the energy releases faster.

4.7 Splitting of the Cauchy stress tensor

In the classical Euler-Lagrange equations from Proposition 3 (Section 4.2), only damage or fracture due to tensile forces is considered. In the following, we consider the two most popular approaches to consider shear stresses in a material, given by Miehe et al. [130] and Amor et al. [7]. There exist several further stress splitting definitions; see e.g., [196, 159, 158, 48, 73, 27, 66]. Comparison studies on different approaches are given, e.g., in [3, 66, 184]. The Euler-Lagrange equation with degraded stress tensor

$$g(\tilde{\varphi})\sigma(u) = g(\tilde{\varphi})\sigma^{+}(u) + \sigma^{-}(u),$$

have the following form:

Proposition 6 (Euler-Lagrange equations with stress splitting)**.** *Given the initial data $\varphi^{n-1}, \varphi^{n-2} \in \mathcal{K}$. Find a pair $(u, \varphi) \in \mathcal{V} \times \mathcal{K}$ such that*

$$(g(\tilde{\varphi})\sigma^{+}(u), E_{lin}(w)) + (\sigma^{-}(u), E_{lin}(w)) = 0 \quad \forall w \in \mathcal{V},$$

$$(1-\kappa)\Big(\varphi\sigma^{+}(u) : E_{lin}(u), \psi - \varphi\Big) + G_C(-\frac{1}{\epsilon}(1-\varphi), \psi - \varphi) + G_C\epsilon(\nabla\varphi, \nabla(\psi - \varphi)) \geq 0 \quad \forall \psi \in \mathcal{K}.$$

Remark 16 (Wording for stress splitting)**.** *In the literature, there are several names for the same meaning of splitting σ properly: stress splitting, Cauchy stress splitting, strain energy splitting, or energy splitting.*

The two most common approaches by Miehe et al. [130] and Amor et al. [7] are given in the following subsections, where we define $\sigma^{+}(u)$ and $\sigma^{-}(u)$ from Proposition 6.

4.7.1 Stress split à la Miehe

Based on thermo-dynamical arguments from Miehe, Hofacker, and Welschinger [132], we distinguish between compressive and tensile loading [30]. By only applying the phase-field parameter to the tensile part of the elastic energy density, crack propagation under compression would be prohibited [30]. The definition of Miehe et al. [130] is based on a spectral decomposition. The tensile stresses are named $\sigma^{+}(u)$, the compressive stresses are summarized in $\sigma^{-}(u)$. They are defined as:

$$\sigma^{+}_{\text{Miehe}}(u) = 2\mu E^{+}_{\text{lin}}(u) + \lambda \max\{0, \operatorname{tr}(E_{\text{lin}}(u))\}\,\mathbb{1},$$

$$\sigma^{-}_{\text{Miehe}}(u) = 2\mu\left(E_{\text{lin}}(u) - E^{+}_{\text{lin}}(u)\right) + \lambda\left(\operatorname{tr}(E_{\text{lin}}(u)) - \max\{0, \operatorname{tr}(E_{\text{lin}}(u))\}\right)\mathbb{1},$$

with the strains [184]

$$E_{\text{lin}}(u) \coloneqq P\Lambda P^{T}, \quad E^{+}_{\text{lin}}(u) \coloneqq P\Lambda^{+}P^{T}.$$

We introduce the cut-off function

$$[x]^+ := \begin{cases} x, & \text{if } x > 0, \\ 0, & \text{if } x \leq 0. \end{cases}$$

The matrices P and Λ form the spectral decomposition with the help of the eigenvalues $\lambda_1(u)$ and $\lambda_2(u)$ of the strain tensor $E_{\text{lin}}(u)$ [184]:

$$\Lambda = \begin{pmatrix} \lambda_1 & 0 \\ 0 & \lambda_2 \end{pmatrix}, \quad \Lambda^+ = \begin{pmatrix} [\lambda_1]^+ & 0 \\ 0 & [\lambda_2]^+ \end{pmatrix}.$$

The corresponding eigenvectors are denoted by $v_1(u)$ and $v_2(u)$. The matrix P in $E^+_{\text{lin}}(u)$ is defined as

$$P := (v_1(u), v_2(u)).$$

The thermodynamic consistency of $\sigma^+(u)$ and $\sigma^-(u)$ has been discussed by Miehe et al. [132] and Pham et al. [138]. A detailed description of the spectral decomposition and its implementation are given in [87, Appendix A].

4.7.2 Stress split à la Amor

Alternatively, Amor et al. [7] propose a volumetric-deviatoric decomposition of the elastic energy density [4], splitting the stress tensor into a volumetric and a deviatoric part.

$$\sigma^+_{\text{Amor}}(u) = (\lambda + \mu) \max\{0, \operatorname{tr}(E_{\text{lin}}(u))\}\, \mathbb{1} + 2\mu \left(E_{\text{lin}}(u) - \frac{1}{3} \operatorname{tr}(E_{\text{lin}}(u))\, \mathbb{1} \right),$$

$$\sigma^-_{\text{Amor}}(u) = (\lambda + \mu) \left(\operatorname{tr}(E_{\text{lin}}(u)) - \max\{0, \operatorname{tr}(E_{\text{lin}}(u))\} \right) \mathbb{1}.$$

The Cauchy stress splitting à la Amor et al. [7] allows preventing interpenetration of the crack faces under compression [4]. A relevant technical advantage is that it is easier to implement than Miehe's splitting.

Remark 17 (Drawback Amor's splitting)**.** *We emphasize that for the single-edge notched pure shear test according to Miehe et al. [130], different crack paths are observed if Amor's splitting is used with less than* 20 000 *quadrilateral elements (uniform refinement and bilinear Q_1^c elements) [3]. The drawback is that a sufficiently fine mesh is required for realistic crack paths.*

4.7.3 Numerical studies on the choice of strain energy split

With the help of the well-known single-edge notched shear test described in Section 3.1, we point out differences in the numerical results if Miehe's or Amor's splitting approach is considered, or if no splitting of $\sigma(u)$ is used (as in Section 4.7). For all tests in this study, the underlying energy functional is the functional AT_2 from Equation (4.17) (Section 4.6.1). We use the predictor-corrector scheme from Section 3.3.1 for adaptive mesh refinement.

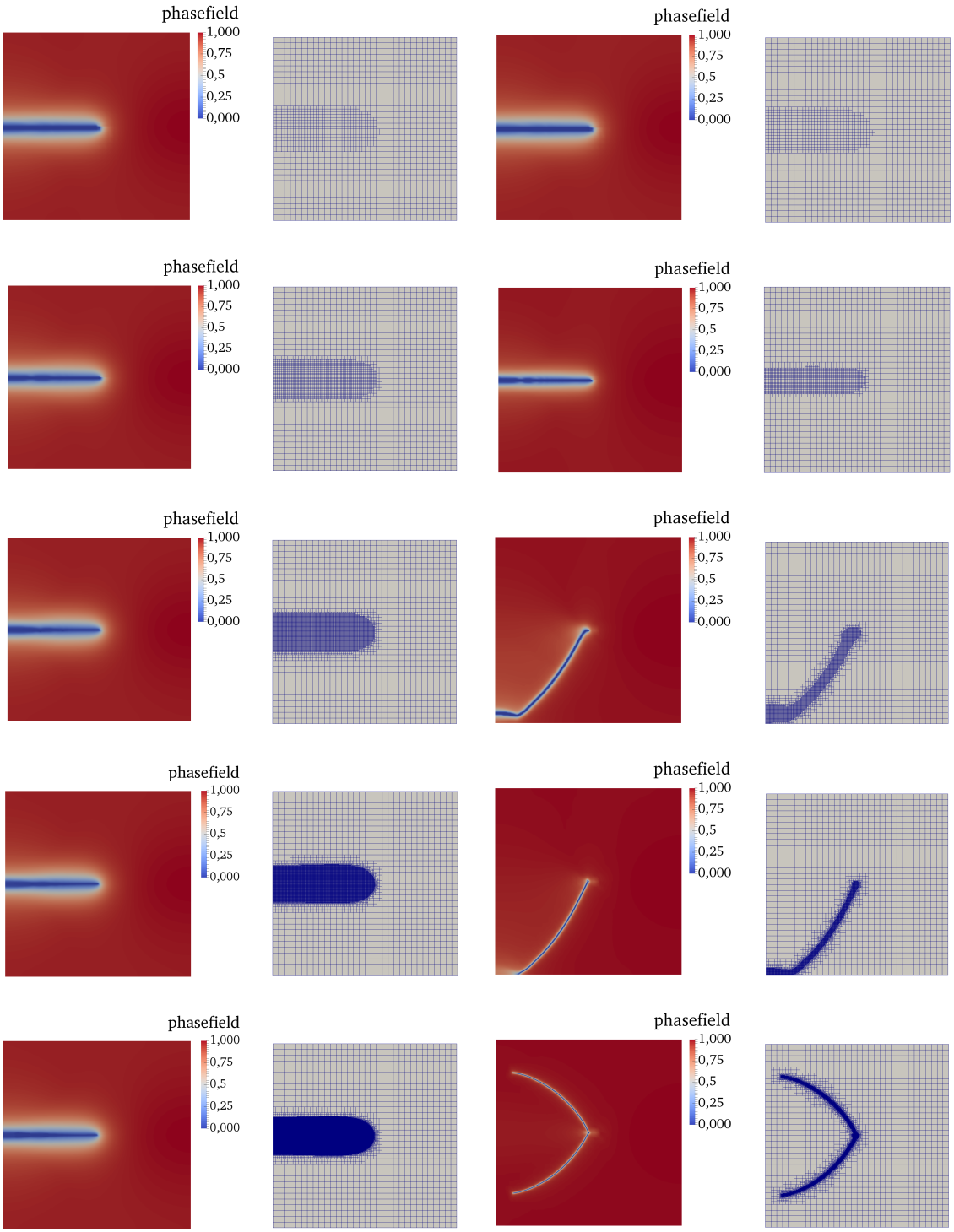

Figure 4.10: Snapshots of the phase-field function φ at the end-time $T = 0.02\,\mathrm{s}$ of the single-edge notched shear test without Cauchy stress splitting for five refinement levels; 1 to 5 refinement steps from top to bottom with the predictor-corrector scheme according to [87], threshold 0.8. Left two columns: $\epsilon = 0.044$ fixed for all computations. Right two columns: $\epsilon = 2\,h$ depending on the current minimal mesh size.

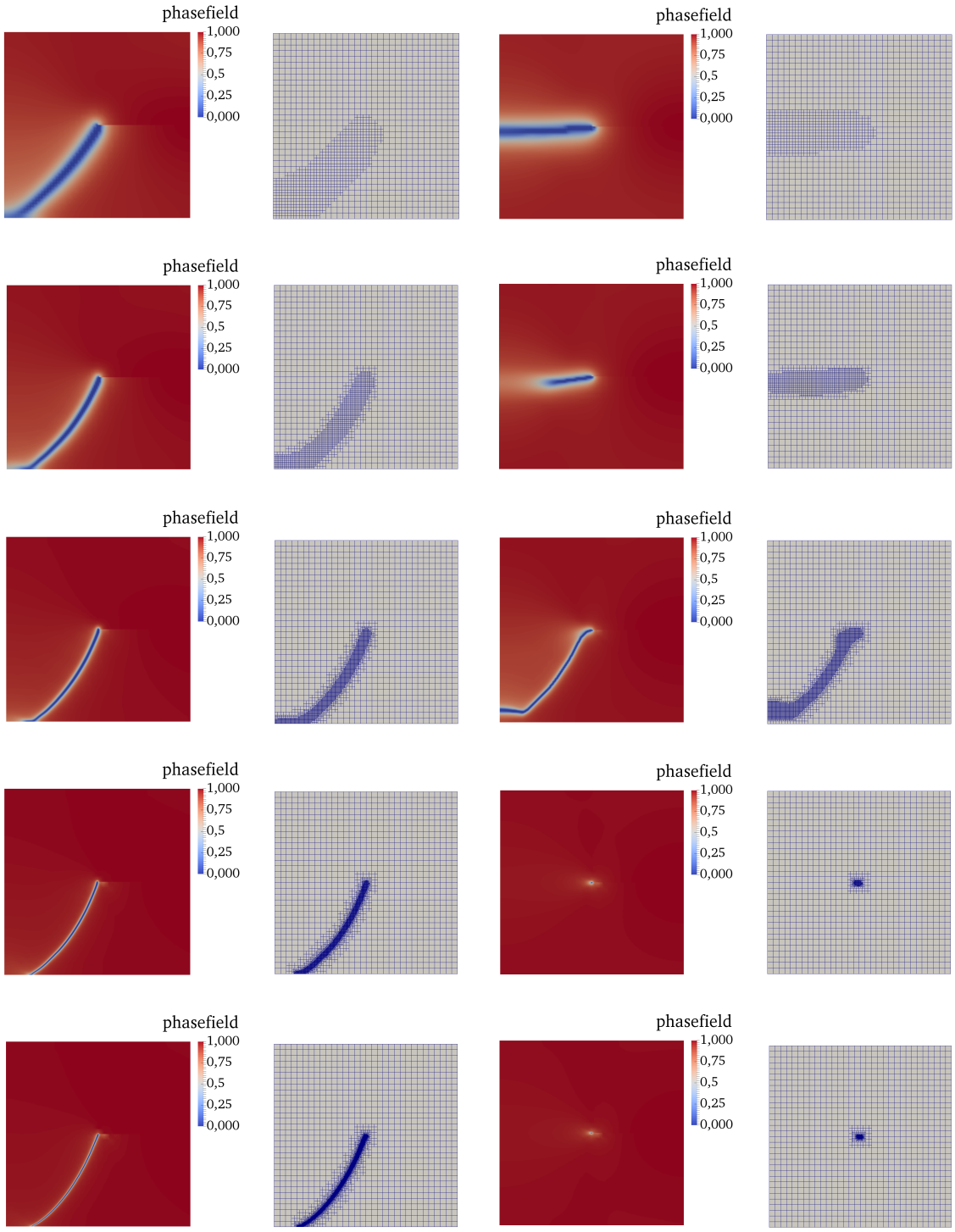

Figure 4.11: Snapshots of the phase-field function φ at the end-time $T = 0.02\,\mathrm{s}$ of the single-edge notched shear test according to Miehe et al. [130] (left) and Amor et al. [7] (right) for five adaptive refinement levels; 1 to 5 refinement steps from top to bottom with the predictor-corrector scheme according to [87], threshold 0.8. For all computations $\epsilon = 2\,h$ depending on the current minimal mesh size.

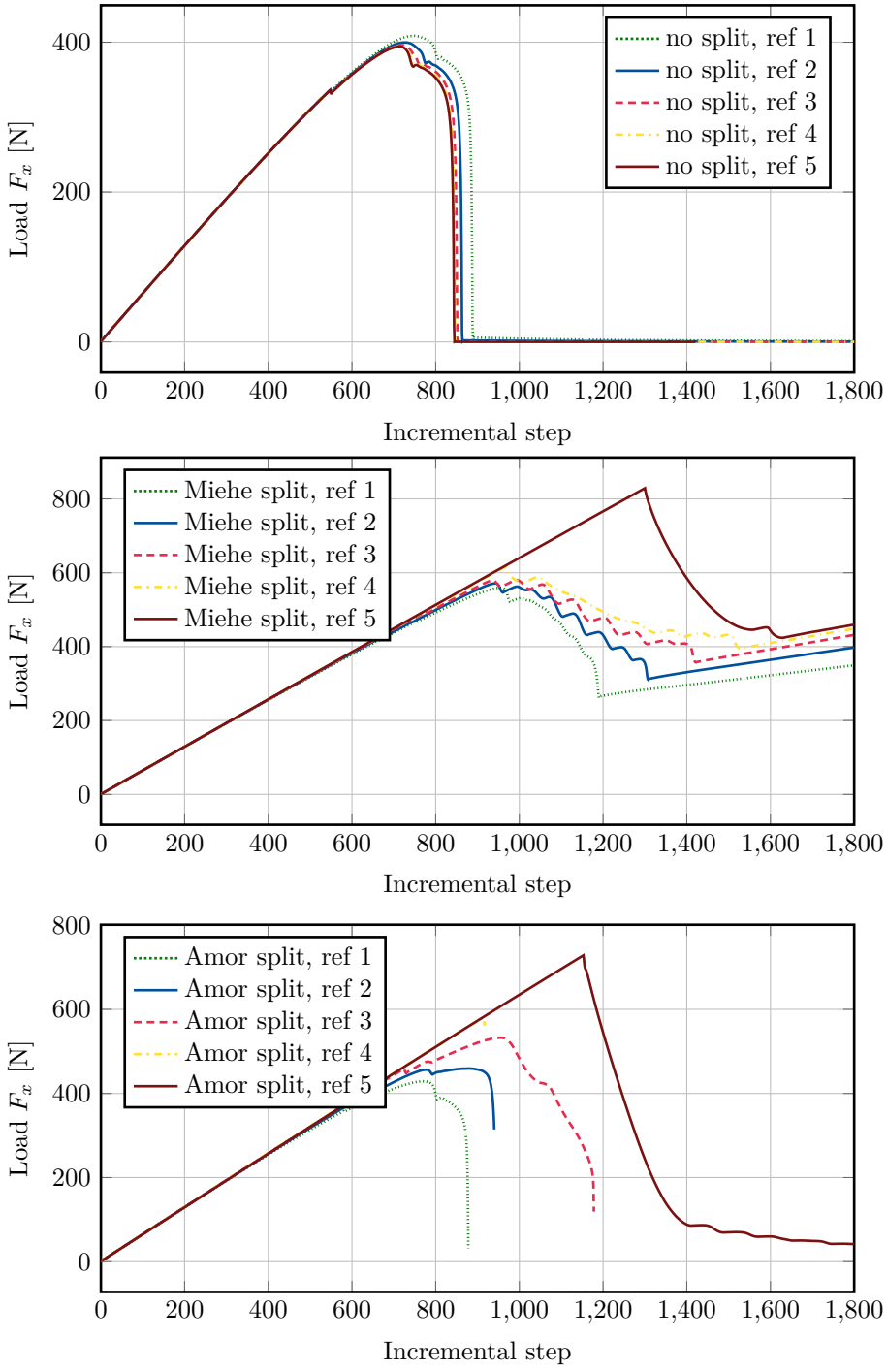

Figure 4.12: Load-displacement curves related to the results from Figures 4.10, and 4.11 from top to bottom: in the first plot, the load-displacement curves for five refinement levels (1 to 5 refinement steps from top to bottom with the predictor-corrector scheme according to [87], threshold 0.8) , are given without stress splitting, in the second plot with Miehe splitting, and the bottom plot with Amor splitting. The computed loading on the top boundary is plotted versus the number of incremental steps. The incremental step size is 10^{-5} s.

The results without any splitting approach in Figure 4.10 show three crack path behaviors depending on the chosen mesh refinement level for $\epsilon = 2\,h$ (right two columns). The crack grows straight to the left boundary for one and two levels of adaptive refinement (first two rows), which differs from the expected crack path for this test. For three and four refinement steps (third and fourth row), the crack pattern is more realistic and similar to Miehe's splitting results. In the last row, the crack splits in the initial crack tip, and two cracks propagate in a curved pattern (crack branching) to the left boundary, similar to the (isotropic) results presented by Ambati et al. [3].
In Figure 4.11, the phase-field results for five computations with different refinement levels are given for both splitting schemes (on the left Miehe, on the right Amor). Further, the meshes are given to observe the adaptively refined mesh with the predictor-corrector scheme described in Section 3.3.1 with a threshold of 0.8. For all computations with $\epsilon = 2\,h$, the crack is getting sharper with a higher resolution of the crack zone. For the results based on Amor's split, we observe what we mentioned in Remark 17: for refinement levels one and two, the crack propagates nearly straight to the left boundary, which does not give the expected crack behavior within the single-edge notched shear test. With three refinement levels, in Figure 4.11, in the middle row on the right, with a sharper crack zone, the phase-field solution becomes more realistic. For refinement level four and five, the Newton/Active set solver does not converge within 100 steps. The results with Miehe's split in Figure 4.11 on the left are robust with refinement, so the crack behavior is independent of h.
In Figure 4.12, the load-displacement curves are given for the three cases: no splitting, splitting according to Miehe and splitting according to Amor. In the first given load-displacement curves, we observe the natural behavior of the loading force on the top boundary of the considered two-dimensional square: the loading force increases until a certain maximum of around 400 N. At the point where the crack starts propagating, the loading force is immediately decreasing until the material is broken. In the second and third load-displacement plot, first, the maximal loading is much higher (≈ 800 N) and at total failure of the material (fracture until the left boundary), there is still a loading force. Especially with Miehe's splitting, the loading does not release as physically expected if the material is broken. Scattering effects in the curves can be ignored due to adaptively refined meshes, especially with coarse starting grids.

Conclusions of the chapter

Starting from the energy minimization problem of Francfort and Marigo [72], we derived the Euler-Lagrange equations for the primal phase-field fracture model based on different energy functionals and stress splitting approaches. Especially the studies in Section 4.6.4 and 4.7.3 will be taken up in Section 7.5 for the application of interest, observing the crack behavior for a more complex real-world problem. The Euler-Lagrange equations from Formulations 3 and 4 (Section 4.2) form the basis for the next chapter. Chapter 5 comprises phase-field fracture modeling for crack propagation in compressible and incompressible solids. The key idea is formulating the elasticity part of the Euler-Lagrange equations in mixed form to avoid locking effects in incompressible solids.

Chapter 5

Modeling & simulations for incompressible solids

In this chapter[1], we focus on phase-field fracture modeling for incompressible solids. Nearly incompressible solids as rubber-like materials arise in various sciences, i.e., engineering [95, 164] or medicine [96, 152]. Relevant for industry is the design of reliable rubber products [111]. Rubbers are frequently used in engineering, e.g., for tires, shock absorbers, seals, and laminated bearing packages [169]. Hyperelastic rubbers are attractive because they withstand high strain levels without permanent rupture deformation [137]. Considering numerical simulations, the particular property of incompressible solids makes it challenging to successfully explain or reproduce crack propagation in rubbers [161]. Section 5.1 clarifies the problematic effects in incompressible solids within the primal phase-field fracture Formulations 3 and 4 from Section 4.2. In the subsequent Section 5.2, we derive a new model that simulates fractures in compressible and incompressible solids. We show an inf-sup condition in Section 5.3 and further the well-posedness of the elasticity part of the problem. With the help of the new form and the discretization from Chapter 3, we present the first numerical results in Sections 5.4 and 5.5. We complete this chapter with Section 5.6 by substantiating the benefit of a modification in the problem formulation with numerical results.

5.1 Locking effects

Compressibility is a material property describing the volume change under forces. Purely incompressible solids do not exist, but in theory, rubber-like materials are often assumed to be incompressible. This property requires a lot of energy to produce a small change of density [39].
Six relevant material parameters can determine the compressibility behavior of a material: bulk modulus (K), Young's modulus (E), Lamé's first parameter (λ), shear modulus or Lamé's second parameter (μ), Poisson's ratio (ν), and the P-wave modulus (M). The relation of the Lamé coefficient $\lambda > 0$ to the Poisson ratio $\nu \in [0, 0.5]$ and the Lamé coefficient $\mu > 0$ is given by

$$\lambda(\mu, \nu) = \frac{2\nu\mu}{1 - 2\nu}. \tag{5.1}$$

[1] Parts of this chapter are already published in [128].

If ν tends to 0.5 (incompressible limit), the parameter λ increases such that $\lambda \gg \mu$. With the help of the other quantities, λ could be defined as

$$\lambda(K,E) = \frac{3K(3K-E)}{9K-E}, \qquad \lambda(K,\mu) = K - \frac{2\mu}{3},$$
$$\lambda(K,\nu) = \frac{3K\nu}{1+\nu}, \qquad \lambda(E,\nu) = \frac{E\nu}{(1+\nu)(1-2\nu)}.$$

The elastic properties of homogeneous linear elastic materials are uniquely determined by any two moduli among these. In this thesis, we consider linear elasticity, constant temperature and focus on the relation of the Lamé coefficient and the Poisson ratio as defined in Equation (5.1). From a modeling perspective, incompressibility is challenging. To understand why, we consider the phase-field fracture model from Formulation 3 (Section 4.2) as a baseline and reduce the PDE system to the linear elasticity problem. For the following discussion on locking effects, we show the problem statement's boundedness, continuity, and coercivity for well-posedness. Further, and more relevant for a discussion on locking effects, specific properties of the bilinear form $a(\cdot,\cdot)$ allow proposing Céa's Lemma 2 for our problem of interest.

Proposition 7 (Well-posedness of the linear elasticity problem)**.** *Let $\mathcal{V} \coloneqq H_0^1(\Omega;\mathbb{R}^2)$, defined in Equation (2.2), and we assume Dirichlet and Neumann boundary conditions. Let $f \in L^2(\Omega)$. The problem of finding $u \in \mathcal{V}$ such that*

$$(2\mu E_{lin}(u) + \lambda \operatorname{tr}(E_{lin}(u))\mathbb{1}, E_{lin}(w)) = (f,w), \quad \forall w \in \mathcal{V},$$

is well-posed.

Proof For the proof of existence and uniqueness of a solution, we use Lax-Milgram from Lemma 1. We define the bilinear form

$$a(u,w) \coloneqq (2\mu E_{\text{lin}}(u) + \lambda \operatorname{tr}(E_{\text{lin}}(u))\mathbb{1}, E_{\text{lin}}(w)),$$

and the right hand side

$$l(w) \coloneqq (f,w).$$

a) The linearity of the right hand side is obtained with standard arguments [184], yielding

$$|l(w)| \leq \|f\|_{L^2(\Omega)} \|w\|_{\mathcal{V}}.$$

b) For the continuity of the bilinear form $a(\cdot,\cdot)$ we use two estimates:

$$E_{\text{lin}}(u) : E_{\text{lin}}(u) \leq \nabla u : \nabla u,$$
$$(\nabla \cdot u)^2 \leq d \nabla u : \nabla u,$$

where d denotes the dimension of the vector field. In this thesis, we determine $d = 2$. Proofs of

the estimates in two dimensions are given by Cinatl [55]. Further, it holds

$$\begin{aligned}(\sigma(u), E_{\text{lin}}(w)) &= 2\mu(E_{\text{lin}}(u), E_{\text{lin}}(w)) + \lambda(\operatorname{tr}(E_{\text{lin}}(u))\mathbb{1}, E_{\text{lin}}(w)) \\ &= 2\mu(E_{\text{lin}}(u), E_{\text{lin}}(w)) + \lambda(\nabla \cdot u, \nabla \cdot w),\end{aligned}$$

which leads to the following estimate

$$\begin{aligned}a(u,w) = &\ (2\mu E_{\text{lin}}(u) + \lambda \operatorname{tr}(E_{\text{lin}}(u))\mathbb{1}, E_{\text{lin}}(w)) \\ &= 2\mu(E_{\text{lin}}(u), E_{\text{lin}}(w) + \lambda(\nabla \cdot u, \nabla \cdot w) \\ &= \int_\Omega 2\mu E_{\text{lin}}(u) : E_{\text{lin}}(w)\, dx + \int_\Omega \lambda(\nabla \cdot u\ \nabla \cdot w)\, dx \\ &\leq 2\mu \int_\Omega \nabla u : \nabla w\, dx + 2\lambda \int_\Omega \nabla u : \nabla w\, dx \\ &\leq 2(\mu+\lambda) \int_\Omega uw + \nabla u : \nabla w\, dx \\ &= 2(\mu+\lambda)\|u\|_{\mathcal{V}}\|w\|_{\mathcal{V}}.\end{aligned}$$

c) Coercivity:
For proving the coercivity of $a(\cdot,\cdot)$, Korn's inequality is used according to Ciarlet [52, Chapter 6], which yields

$$\begin{aligned}a(u,u) = &\int_\Omega 2\mu E_{\text{lin}}(u) : E_{\text{lin}}(u)\, dx + \int_\Omega \lambda(\nabla \cdot u)^2\, dx \\ &\geq 2\mu c \int_\Omega E_{\text{lin}}(u) : E_{\text{lin}}(u)\, dx = 2\mu c\ \|E_{\text{lin}}(u)\|^2_{L^2(\Omega)} \\ &\geq 2\mu c\ \|u\|^2_{\mathcal{V}},\end{aligned}$$

where $c > 0$ is constant. Thus, $a(u,v)$ is coercive and we conclude via Lax-Milgram (Lemma 1), that the problem is well-posed.

□

Remark 18 (Excursus: Coercivity of $a(\cdot,\cdot)$ depending on κ)**.** *In Proposition 7, we consider the pure elasticity equation. In the context of phase-field fracture, the bilinear form $a(\cdot,\cdot)$ has a time-lagged coefficient $g(\tilde{\varphi})$. We define $\tilde{\varphi} := \tilde{\varphi}(\varphi^{n-1}, \varphi^{n-2})$, see Proposition 1, and use in the following the time-lagged $\tilde{\varphi}$ with given φ^{n-1} and φ^{n-2}. The degradation function is defined as*

$$g(\tilde{\varphi}) = (1-\kappa)\tilde{\varphi}^2 + \kappa,$$

with $\kappa > 0$ sufficiently small. For $\tilde{\varphi} = 0$ (in the fracture zone), we have

$$g(\tilde{\varphi}) = \kappa.$$

In the unbroken material, i.e., $\tilde{\varphi} = 1$, it holds

$$g(\tilde{\varphi}) = 1.$$

In particular, we define (analogously to Proposition 7):

$$\alpha := \inf_{x\in\Omega} \alpha_\mu g\left(\varphi(x)\right), \quad c := \sup_{x\in\Omega} c_\mu g\left(\varphi(x)\right).$$

for given $\alpha_0 > 0$ and $c_0 > 0$. The constants α_μ and c_μ arise in considering the coercivity and continuity of the bilinear form from Equation (5.5).

We recall, that via

$$\begin{aligned} |a_{\tilde{\varphi}}(u,w)| &\leq c\|u\|_{\mathcal{V}}\|w\|_{\mathcal{V}} \quad \text{for } c > 0 \quad \forall u, w \in \mathcal{V}, \quad \text{(continuity)} \\ a_{\tilde{\varphi}}(w,w) &\geq \alpha\|w\|_{\mathcal{V}}^2 \qquad \text{for } \alpha > 0 \quad \forall w \in \mathcal{V}, \quad \text{(coercivity)} \end{aligned}$$

the bilinear form $a(\cdot,\cdot)$ is continuous and $\mathcal{V}$-elliptic. For small κ, the coercivity estimate may become critical.

The properties of the bilinear form $a(\cdot,\cdot)$ from Proposition 7 allow giving a first best approximation error bound for the discrete solution u_h of the problem via Céa's lemma; see Lemma 2.

Proposition 8 (Céa lemma for linear elasticity according to Wick [183])**.** *Let $\mathcal{V}_h \subset \mathcal{V}$ be a finite dimensional subspace of $\mathcal{V}$. Let $a(\cdot,\cdot) : \mathcal{V}\times\mathcal{V}$ be a symmetric, continuous, and $\mathcal{V}$-elliptic bilinear form. Let $u \in \mathcal{V}$ be the solution and $u_h \in \mathcal{V}_h$ be the discrete solution of the variational problem. Then it holds*

$$\|u - u_h\|_{\mathcal{V}} \leq \frac{\gamma(\mu,\lambda)}{\alpha} \inf_{v_h\in\mathcal{V}_h} \|u - v_h\|_{\mathcal{V}},$$

where $\gamma(\mu,\lambda) > 0$ is the continuity constant depending on the Lamé coefficients λ and μ. Further, $\alpha > 0$ is the coercivity constant of $a(\cdot,\cdot)$ on $\mathcal{V}$ [43]. As shown above, we can specify the best approximation estimate for the linear elasticity problem such that

$$\|u - u_h\|_{\mathcal{V}} \leq \frac{2(\mu+\lambda)}{2\mu c} \inf_{v_h\in\mathcal{V}_h} \|u - v_h\|_{\mathcal{V}}.$$

Proof For the linear PDE, Galerkin orthogonality holds:

$$a(u - u_h, w_h) = 0 \quad \forall w_h \in \mathcal{V}_h.$$

For $w_h = (u_h - v_h) \in \mathcal{V}_h$ it holds

$$\begin{aligned} 2\mu c\, \|u - u_h\|_{\mathcal{V}}^2 \leq a(u - u_h, u - u_h) &= a(u - u_h, u - v_h) + a(u - u_h, w_h) \\ &= a(u - u_h, u - v_h) \leq 2(\mu+\lambda)\|u - u_h\|_{\mathcal{V}}\|u - v_h\|_{\mathcal{V}}, \end{aligned}$$

which yields

$$\|u - u_h\|_{\mathcal{V}} \leq \frac{2(\mu + \lambda)}{2\mu c} \|u - v_h\|_{\mathcal{V}},$$

and gives us the best approximation estimate

$$\|u - u_h\|_{\mathcal{V}} = \inf_{v_h \in \mathcal{V}_h} \frac{2(\mu + \lambda)}{2\mu c} \|u - v_h\|_{\mathcal{V}}.$$

□

Considering $\lambda \to \infty$, the constant $\frac{2(\mu+\lambda)}{2\mu c}$ becomes large and leads to significantly larger errors than the approximation error [39]. This situation is well-known in solid mechanical simulations as Poisson or volume-locking [15]. Secondly, considering the discretized elasticity problem, the choice of finite elements plus a large λ have an impact on the norm of the discretized displacement [55] since

$$\|u_h\|_{\mathcal{V}} \leq \frac{1}{2(\mu + \lambda) \cdot c_h} \|f\|_{\mathcal{V}},$$

with a mesh-dependent constant c_h. For $\lambda \to \infty$, $\|u_h\|_{\mathcal{V}}$ is forced to be small for fixed h [39]. For $h \to 0$, c_h is decreasing which allows for balancing a large λ. Thus, for finer meshes or a more accurate discretization of u we can expect $\|u_h\|_{\mathcal{V}}$ to be not underestimated for large λ [55]. In the next section, we reformulate the elasticity problem avoiding Poisson locking.

5.2 A quasi-static phase-field fracture model in mixed form

One possibility to avoid locking effects is a Discontinuous Galerkin (DG) method, e.g., [57]. Wihler [187] used the DG method for linear elasticity problems, Hansbo et al. [84] studied in particular (nearly) incompressible elasticity problems. We choose to split the displacement equation into a mixed system, see for instance, Braess [39] for saddle point problems with a penalty term.
For this, we define $p : \Omega \to \mathbb{R}$

$$p := \lambda \nabla \cdot u \quad \text{with } p \in \mathcal{U} := L^2(\Omega),$$

and formulate the primal linear elasticity problem as a mixed system:

Formulation 10 (Linear elasticity in weak and mixed form)**.** *For given $\varphi \in \mathcal{K}$, find $u \in \mathcal{V} + \{u_D\}$ and $p \in \mathcal{U}$ such that*

$$\begin{aligned} 2\mu \left(g(\varphi) E_{lin}(u), E_{lin}(w)\right) + \left(g(\varphi) p, \nabla \cdot w\right) &= 0 \quad \forall w \in \mathcal{V}, \\ \left(g(\varphi) \nabla \cdot u, q\right) - \frac{1}{\lambda} \left(g(\varphi) p, q\right) &= 0 \quad \forall q \in \mathcal{U}. \end{aligned} \tag{5.2}$$

Remark 19 (Comment on λ)**.** *In Equation (5.2), the coefficient λ arises in the denominator. For this reason, a large penalty parameter λ is less harmful.*

We show the equivalence of the primal and the mixed elasticity problem in the following:

Proposition 9 (Equivalence of primal and mixed problem formulation)**.**
The primal linear elasticity problem

$$2\mu(g(\tilde{\varphi})E_{lin}(u), E_{lin}(w)) + \lambda(g(\tilde{\varphi})\nabla \cdot u, \nabla \cdot w) = 0 \quad w \in \mathcal{V}, \tag{5.3}$$

and the elasticity problem in mixed form

$$\begin{aligned} 2\mu(g(\tilde{\varphi})E_{lin}(u), E_{lin}(w)) + (g(\tilde{\varphi})p, \nabla \cdot w) = 0 \quad \forall w \in \mathcal{V}, \\ (g(\tilde{\varphi})\nabla \cdot u, q) - \frac{1}{\lambda}(g(\tilde{\varphi})p, q) = 0 \quad \forall q \in \mathcal{U}, \end{aligned} \tag{5.4}$$

are equivalent problem formulations.

Proof Let u, p be solutions of the mixed form. It means there exists a $\lambda \in \mathbb{R}^+$ such that Equation (5.4) is fulfilled. It holds

$$g(\tilde{\varphi})\nabla \cdot u, q) = \frac{1}{\lambda}(g(\tilde{\varphi})p, q) \quad \forall q \in \mathcal{U},$$

which is equivalent to

$$\lambda(g(\tilde{\varphi})\nabla \cdot u, q) = (g(\tilde{\varphi})p, q).$$

For $w \in \mathcal{V}$ it holds $\nabla \cdot w \in \mathcal{U}$. With $q = \nabla \cdot w$, it follows

$$\lambda(g(\tilde{\varphi})\nabla \cdot u, \nabla \cdot w) = (g(\tilde{\varphi})p, \nabla \cdot w) = (g(\tilde{\varphi})p, \nabla \cdot w).$$

Inserting this in the first equation of Equation (5.4) shows that u also solves:
Let $u \in \mathcal{V}$ be a solution of Equation (5.3), then it holds:

$$2\mu(g(\tilde{\varphi})E_{\text{lin}}(u), E_{\text{lin}}(w)) + \lambda(g(\tilde{\varphi})\nabla \cdot u, \nabla \cdot w) = 0 \quad \forall w \in \mathcal{V}.$$

To show the other direction, we define $p \in \mathcal{U}$ with $p \coloneqq \lambda(\nabla \cdot u)$. It follows

$$\begin{aligned} 2\mu(g(\tilde{\varphi})E_{\text{lin}}(u), E_{\text{lin}}(w)) + (g(\tilde{\varphi})p, \nabla \cdot w) = 0 \quad \forall w \in \mathcal{V}, \\ (g(\tilde{\varphi})\lambda\nabla \cdot u - p, q) = 0 \quad \forall q \in \mathcal{U}. \end{aligned}$$

This is equivalent to

$$(g(\tilde{\varphi})\nabla \cdot u, q) - \frac{1}{\lambda}(g(\tilde{\varphi})p, q) = 0 \quad \forall q \in \mathcal{U},$$

which shows the equivalence of Equations (5.3) and (5.4). □

To derive the linear elasticity problem in mixed form, we assume $\tilde{\varphi}$ to be given and ignored the phase-field inequality. Going back to the (coupled) phase-field fracture problem, we formulate the phase-field model with a mixed form of the u-equation:

Formulation 11 (Phase-field fracture problem in weak and mixed form)**.**

Given the initial data $\varphi^{n-1}, \varphi^{n-2} \in \mathcal{K}$. Find $u \in \mathcal{V} + \{u_D\}$, $p \in \mathcal{U}$ and $\varphi \in \mathcal{K}$, such that

$$2\mu\left(g(\tilde{\varphi})E_{lin}(u), E_{lin}(w)\right) + \left(g(\tilde{\varphi})\nabla \cdot w, p\right) = 0 \quad \forall w \in \mathcal{V},$$

$$\left(g(\tilde{\varphi})\nabla \cdot u, q\right) - \frac{1}{\lambda}\left(g(\tilde{\varphi})p, q\right) = 0 \quad \forall q \in \mathcal{U},$$

$$\begin{aligned}(1-\kappa)\left(\varphi\ 2\mu E_{lin}(u) : E_{lin}(u), \psi - \varphi\right) + (1-\kappa)\left(\varphi\lambda\nabla \cdot u\mathbb{1} : E_{lin}(u), \psi - \varphi\right) \\ + G_C\left(-\frac{1}{\epsilon}(1-\varphi), \psi - \varphi\right) + G_C\epsilon\left(\nabla\varphi, \nabla(\psi - \varphi)\right) \geq 0 \quad \forall \psi \in \mathcal{K}.\end{aligned}$$

As in Chapter 4, we give the problem formulation in mixed form also for pressurized fractures.

Formulation 12 (Phase-field fracture problem in weak and mixed form, pressure driven)**.**
Let $\rho \in L^\infty(\Omega)$ be given. Given the initial data $\varphi^{n-1}, \varphi^{n-2} \in \mathcal{K}$. Find $u \in \mathcal{V} + \{u_D\}$, $p \in \mathcal{U}$ and $\varphi \in \mathcal{K}$, such that

$$\begin{aligned}\Big(g(\tilde{\varphi}))\sigma(u,p)\,, E_{lin}(w)\Big) + (\tilde{\varphi}^2\rho, \nabla \cdot w) = 0 \quad \forall w \in \mathcal{V}, \\ g(\tilde{\varphi})(\nabla \cdot u, q) - g(\tilde{\varphi})(\frac{1}{\lambda}p, q) = 0 \quad \forall q \in \mathcal{U}, \\ (1-\kappa)(\varphi\sigma(u,p) : E_{lin}(u), \psi - \varphi) + 2(\varphi\rho\nabla \cdot u, \psi - \varphi) \\ + G_C\Big(-\frac{1}{\epsilon}(1-\varphi, \psi - \varphi) + \epsilon(\nabla\varphi, \nabla(\psi - \varphi))\Big) \geq 0 \quad \forall \psi \in \mathcal{K},\end{aligned}$$

with the Cauchy stress tensor defined pressure-dependent as $\sigma(u,p) \coloneqq 2\mu E_{lin}(u) + p\mathbb{1}$.

Combined with stress splitting from Section 4.7, the problem in mixed form for pressurized fractures is stated as:

Formulation 13 (Phase-field fracture problem in weak and mixed form with stress splitting, pressure driven)**.**
Let $\rho \in L^\infty(\Omega)$ be given. Given the initial data $\varphi^{n-1}, \varphi^{n-2} \in \mathcal{K}$. Find $u \in \mathcal{V} + \{u_D\}$, $p \in \mathcal{U}$ and $\varphi \in \mathcal{K}$ such that

$$\begin{aligned}g(\tilde{\varphi})\left(\sigma^+(u,p), E_{lin}(w)\right) + \left(\sigma^-(u,p), E_{lin}(w)\right) + (\tilde{\varphi}^2\rho, \nabla \cdot w) = 0 \quad \forall\ w \in \mathcal{V}, \\ g(\tilde{\varphi})\left(\nabla \cdot u, q\right) - \frac{1}{\lambda}(g(\tilde{\varphi})p, q) = 0 \quad \forall\ q \in \mathcal{U}, \\ (1-\kappa)\left(\varphi\sigma^+(u,p) : E_{lin}(u), \psi - \varphi\right) + 2(\varphi\rho\nabla \cdot u, \psi - \varphi) \\ + \frac{G_C}{\pi}\left(-\frac{1}{\epsilon}\varphi, \psi - \varphi\right) + \frac{G_C}{\pi}\epsilon\left(\nabla\varphi, \nabla(\psi - \varphi)\right) \geq 0 \quad \forall\ \psi \in \mathcal{K},\end{aligned}$$

where

$$g(\varphi)\sigma(u,p)^+ + \sigma^-(u,p) = \sigma(u,p).$$

The definitions of $\sigma(u,p)^+$ and $\sigma(u,p)^-$ depend on the chosen stress splitting.

For Miehe's splitting approach, we define the positive part of the pressure $p^+ \in L^2(\Omega)$ as $p^+ \coloneqq$

$\max\{p, 0\}$, such that the tensile and compressive parts of the strain tensor are reformulated to:

$$\sigma^+_{\text{Miehe}}(u,p) \coloneqq 2\mu E^+_{\text{lin}}(u) + p^+ \mathbb{1},$$
$$\sigma^-_{\text{Miehe}}(u,p) \coloneqq 2\mu \left(E_{\text{lin}}(u) - E^+_{\text{lin}}(u)\right) + \left(p - p^+\right) \mathbb{1}.$$

If the stress splitting approach according to Amor et al. [7] is considered, the stress tensor $\sigma(u,p)$ is split into:

$$\sigma^+_{\text{Amor}}(u,p) \coloneqq \mu \max\left\{0, \operatorname{tr}\left(E^+_{\text{lin}}(u)\right)\right\} \mathbb{1} + 2\mu \left(E^+_{\text{lin}}(u) - \frac{1}{3}\operatorname{tr}\left(E^+_{\text{lin}}(u)\right) \mathbb{1}\right) + p^+ \mathbb{1},$$
$$\sigma^-_{\text{Amor}}(u,p) \coloneqq \mu \left(\operatorname{tr}\left(E^+_{\text{lin}}(u)\right) - \max\left\{0, \operatorname{tr}\left(E^+_{\text{lin}}(u)\right)\right\}\right) \mathbb{1} + (p - p^+)\mathbb{1}.$$

Remark 20 (Block entries for different energy functionals)**.** *In Section 4.6, three energy functional are proposed: AT_2, AT_1, and Wu's functional. In Chapter 5, we use AT_2. The corresponding block entries of the Jacobian for the finite element discretization are given for the three energy functionals and two stress splitting schemes in Appendix B.*

5.3 Well-posedness of the mixed problem formulation

According to Hadamard [83], a given problem is well-posed if it is uniquely solvable and has a stable solution. Considering the primal phase-field fracture problem and decoupling the elasticity equation from the phase-field inequality in Section 5.1 yields two linear equations. We applied the Lax-Milgram lemma [185, 13] for the existence and uniqueness of a solution. Similarly, we discuss the well-posedness of the proposed phase-field fracture problem in mixed form in Formulation 11 from Section 5.2. The final result of this section is Theorem 5.

Remark 21 (Similarity to Stokes problem)**.** *The elasticity equation in mixed form has a saddle point structure with a penalty term, which allows reusing established results for the Stokes problem [39]. The similarity to Stokes-type problems is further used in Chapter 6, deriving a robust and efficient preconditioner.*

We start with the phase-field fracture problem in mixed form from Formulation 11 (Section 5.2): Let $\tilde{\varphi} \in \mathcal{K}$ be given. Find $u \in \mathcal{V} + \{u_D\}$, $p \in \mathcal{U}$ and $\varphi \in \mathcal{K}$ such that

$$2\mu \left(g(\tilde{\varphi}) E_{\text{lin}}(u), E_{\text{lin}}(w)\right) + \left(g(\tilde{\varphi}) \nabla \cdot w, p\right) = 0 \quad \forall w \in \mathcal{V},$$
$$\left(g(\tilde{\varphi}) \nabla \cdot u, q\right) - \frac{1}{\lambda} \left(g(\tilde{\varphi}) p, q\right) = 0 \quad \forall q \in \mathcal{U},$$
$$(1-\kappa) \left(\varphi\, 2\mu E_{\text{lin}}(u) : E_{\text{lin}}(u), \psi - \varphi\right) + (1-\kappa) \left(\varphi \lambda \nabla \cdot u \mathbb{1} : E_{\text{lin}}(u), \psi - \varphi\right)$$
$$+ G_C \left(-\frac{1}{\epsilon}(1-\varphi), \psi - \varphi\right) + G_C \epsilon \left(\nabla\varphi, \nabla(\psi - \varphi)\right) \geq 0 \quad \forall \psi \in \mathcal{K},$$

and we restrict ourselves to the elasticity part of the CVIS:

$$2\mu\left(g(\tilde{\varphi})E_{\text{lin}}(u), E_{\text{lin}}(w)\right) + \left(g(\tilde{\varphi})\nabla\cdot w, p\right) = 0 \quad \forall w \in \mathcal{V},$$
$$\left(g(\tilde{\varphi})\nabla\cdot u, q\right) - \frac{1}{\lambda}\left(g(\tilde{\varphi})p, q\right) = 0 \quad \forall q \in \mathcal{U}.$$

Further, we assume the phase-field variables $\tilde{\varphi}$ to be a given coefficient with sufficient regularity. We define the symmetric bilinear form

$$a_{\tilde{\varphi}}(u, w) \coloneqq \left(g(\tilde{\varphi})2\mu E_{\text{lin}}(u), E_{\text{lin}}(w)\right), \tag{5.5}$$

and further introduce the bilinear forms

$$\begin{aligned} b_{\tilde{\varphi}}(w, p) &\coloneqq \left(g(\tilde{\varphi})\nabla\cdot w, p\right), \\ c_{\tilde{\varphi}}(p, q) &\coloneqq \left(g(\tilde{\varphi})p, q\right), \end{aligned} \tag{5.6}$$

and general (sufficient regular) right hand sides l_1 and l_2. For the estimates of continuity and coercivity, we emphasize that $g(\varphi)$ enters, which is different from the proof of Proposition 7. First, we assume κ to be small but constant. For $c_{\tilde{\varphi}}(p, q)$ we define a norm $|q|_c \coloneqq c_{\tilde{\varphi}}(q, q)^{\frac{1}{2}}$. Because $a_{\tilde{\varphi}}(u, w) = a_{\tilde{\varphi}}(w, u)$ and $c_{\tilde{\varphi}}(p, q) = c_{\tilde{\varphi}}(q, p)$, the bilinear forms $a(\cdot,\cdot)$ and $c(\cdot,\cdot)$ are symmetric. The quadratic form $(g(\varphi)$ $E_{\text{lin}}(u)$, $E_{\text{lin}}(w))$ is coercive on the whole space, and the penalty term can be seen as a regular perturbation [39]. We get the following form based on the definitions in Equations (5.5) and (5.6).

Formulation 14 (Elasticity problem in mixed form)**.** *Given the initial data $\varphi^{n-1}, \varphi^{n-2} \in \mathcal{K}$. Find $(u, p) \in \mathcal{V} \times \mathcal{U}$ such that*

$$2\mu a_{\tilde{\varphi}}(u, w) + b_{\tilde{\varphi}}(w, p) = l_1 \quad \forall w \in \mathcal{V},$$
$$b_{\tilde{\varphi}}(u, q) - \frac{1}{\lambda}c_{\tilde{\varphi}}(p, q) = l_2 \quad \forall q \in \mathcal{U}.$$

We define a bilinear form $A_{\tilde{\varphi}}$ summing up the single terms:

$$A_{\tilde{\varphi}}(u, p; w, q) \coloneqq 2\mu a_{\tilde{\varphi}}(u, w) + b_{\tilde{\varphi}}(w, p) + b_{\tilde{\varphi}}(u, q) - \frac{1}{\lambda}c_{\tilde{\varphi}}(p, q), \tag{5.7}$$

and the right hand side $l \coloneqq l_1 + l_2$. The natural norm for a saddle point problem with a penalty term is given by

$$|\!|\!|(w, q)|\!|\!| \coloneqq \|w\|_{\mathcal{V}} + \|q\|_{\mathcal{U}} + \frac{1}{\lambda}|q|_c. \tag{5.8}$$

Remark 22 (Assumptions on κ and φ)**.** *As discussed in Remark 18 (Section 5.1), we assume φ to be fixed and given and κ to be small but constant. We are aware that a small κ has an impact on the coercivity of the bilinear form $A_{\tilde{\varphi}}(u, p; w, q)$ defined in Equation (5.7).*

In the following, we prove the well-posedness of Formulation 14, including a λ-independent stability estimate. In the following, we use three theorems, from Bartels [21, Theorem 6.3 and 6.4] and Braess [39, Theorem 4.13], which are given first.

Theorem 2 (Brezzi's splitting theorem according to Bartels [21]). *Assume $\mathcal{V}$ and $\mathcal{U}$ Hilbert spaces (with dual spaces $\mathcal{V}^*$ and $\mathcal{U}^*$, respectively), $a_{\tilde{\varphi}} : \mathcal{V} \times \mathcal{V} \to \mathbb{R}$ be a symmetric, bounded, and positive semi-definite bilinear form, and $b_{\tilde{\varphi}} : \mathcal{V} \times \mathcal{U} \to \mathbb{R}$ a bounded bilinear form. Then, the operator*

$$L : \mathcal{V} \times \mathcal{U} \to \mathcal{V}^* \times \mathcal{U}^*, \quad (u, p) \mapsto (a_{\tilde{\varphi}}(u, \cdot) + b_{\tilde{\varphi}}(\cdot, p), b_{\tilde{\varphi}}(u, \cdot))$$

is an isomorphism, i.e., a saddle point problem of the form:
Finding $(u, p) \in \mathcal{V} \times \mathcal{U}$ such that

$$\begin{aligned} a_{\tilde{\varphi}}(u, p) + b_{\tilde{\varphi}}(w, p) &= f(w), \quad \forall w \in \mathcal{V}, \\ b_{\tilde{\varphi}}(u, q) &= g(q), \quad \forall q \in \mathcal{U}, \end{aligned}$$

is uniquely solvable if

a) the bilinear form $a_{\tilde{\varphi}}(\cdot, \cdot)$ is coercive on $\ker(B)$, where $B : \mathcal{V} \to \mathcal{U}^*$, i.e., there exists an $\alpha > 0$ such that

$$a_{\tilde{\varphi}}(w, w) \geq \alpha \|w\|_{\mathcal{V}}^2 \quad \forall w \in \ker(B),$$

b) and the bilinear form $b_{\tilde{\varphi}}(\cdot, \cdot)$ satisfies an inf-sup condition, i.e., there exists $\beta > 0$ such that

$$\inf_{q \in \mathcal{U}} \sup_{w \in \mathcal{V}} \frac{b_{\tilde{\varphi}}(w, q)}{\|w\|_{\mathcal{V}} \|q\|_{\mathcal{U}}} \geq \beta.$$

The inf-sup or Ladyzhenskaya–Babuška–Brezzi (LBB) condition is a sufficient condition for a saddle point problem to have a unique solution that depends continuously on the input data; in some sense, it substitutes coercivity conditions for the bilinear forms [43]. To show the inf-sup stability of the saddle point problem with a penalty term, we use Theorem 4.13 from Braess [39], which is stated as follows:

Theorem 3 (Inf-sup for saddle point problem with a penalty term according to Braess [38, 39]). *Suppose the hypotheses of Theorem 2 be fulfilled and that $a_{\tilde{\varphi}}(\cdot, \cdot)$ is elliptic on $\mathcal{V}$. Then the mapping L as defined by the saddle point problem with a penalty term from Formulation 14 satisfies the following inf-sup condition:*

$$\inf_{(u,p) \in \mathcal{V} \times \mathcal{U}} \sup_{(w,q) \in \mathcal{V} \times \mathcal{U}} \frac{A_{\tilde{\varphi}}(u, p; w, q)}{|\!|\!| (u, p) |\!|\!| \cdot |\!|\!| (w, q) |\!|\!|} \geq \gamma > 0, \quad \forall\, 0 \leq \frac{1}{\lambda} \leq 1,$$

where γ is independent of λ. The natural norm $|\!|\!| (\cdot, \cdot) |\!|\!|$ is defined in Equation (5.8).

Further, we use a generalized version of the Lax-Milgram Lemma 1.

Theorem 4 (Generalized Lax-Milgram according to Bartels [21]). *Assume that $X = \mathcal{V} \times \mathcal{U}$. The linear operator $L : X \to X^*$ is an isomorphism if and only if the associated bilinear form $A_{\tilde{\varphi}}(\cdot, \cdot; \cdot, \cdot)$ (defined in Equation (5.7)) with right hand side $l(\cdot, \cdot)$, defined as*

$$A_{\tilde{\varphi}}(u, p; w, q) = l(w, q),$$

is bounded, satisfies an inf-sup condition, and is nondegenerated, i.e.,

a) there exists a constant $c_A \geq 0$ *such that*

$$|A_{\tilde{\varphi}}(u,p;w,q)| \leq c_A |\!|\!| (u,p) |\!|\!| \, |\!|\!| (w,q) |\!|\!|,$$

with the norm defined in Equation (5.8).

b) there exists a constant $\gamma > 0$ *such that*

$$\inf_{(u,p)\in\mathcal{V}\times\mathcal{U}} \sup_{(w,q)\in\mathcal{V}\times\mathcal{U}} \frac{A_{\tilde{\varphi}}(u,p;w,q)}{|\!|\!| (u,p) |\!|\!| \cdot |\!|\!| (w,q) |\!|\!|} \geq \gamma,$$

c) and for all $(w,q) \in \mathcal{V}\times\mathcal{U}$ *there exist a pair* $(u,p) \in \mathcal{V}\times\mathcal{U}$ *with* $A_{\tilde{\varphi}}(u,p;w,q) \neq 0$ *(nondegeneracy).*

Further, if $A_{\tilde{\varphi}}(\cdot,\cdot;\cdot,\cdot)$ *is symmetric, then the inf-sup condition implies nondegeneracy.*

For Theorem 3, the assumptions and the statements *a)* and *b)* of Brezzi's splitting Theorem 2 have to be satisfied: the bilinear form $a_{\tilde{\varphi}}(u,w)$ has to be symmetric, bounded and positive semi-definite, which is given via the symmetric definition in Equation (5.5), and the proof of boundedness and ellipticity of $a_{\tilde{\varphi}}(u,w)$ on the whole space from Section 5.1. Further, $b_{\tilde{\varphi}}(u,q)$ has to be bounded and should fulfill an inf-sup condition. We start with the boundedness of $b_{\tilde{\varphi}}(u,q)$:

Proof (Boundedness of $b_{\tilde{\varphi}}(u,q)$)

$$\begin{aligned} b_{\tilde{\varphi}}(u,q) &= \Big| \int_\Omega (\nabla\cdot u) q \, dx \Big| \leq \int_\Omega |(\nabla\cdot u) q| \, dx \\ &= \|(\nabla\cdot u) q\|_{L^1(\Omega)} \leq \|\nabla\cdot u\|_{\mathrm{L}^2(\Omega)} \|q\|_{\mathrm{L}^2(\Omega)}\| \\ &\leq \|\nabla u\|_{L^2(\Omega)} \|q\|_{L^2(\Omega)} \leq \|u\|_{H^1_0(\Omega)} \|q\|_{L^2(\Omega)}. \end{aligned}$$

□

Next, we proof, that $b_{\tilde{\varphi}}(\cdot,\cdot)$ is inf-sup stable:

Proof (Inf-sup for $b_{\tilde{\varphi}}(\cdot,\cdot)$) According to Girault and Raviart [78] one can show that for given $q \in U$ there exists $\tilde{w} \in \mathcal{V}$ such that $\nabla\cdot\tilde{w} = q$ and

$$\|\tilde{w}\|_{\mathcal{V}} \leq c \|q\|_{\mathcal{U}}, \tag{5.9}$$

with a positive constant $c > 0$. It holds

$$\begin{aligned} \sup_{w\in\mathcal{V}} \frac{b_{\tilde{\varphi}}(w,q)}{\|w\|_{\mathcal{V}}} &= \sup_{w\in\mathcal{V}} \frac{(\nabla\cdot w, q)}{\|w\|_{\mathcal{V}}} \\ &\geq \frac{(\nabla\cdot w, q)}{\|w\|_{\mathcal{V}}} = \frac{(q,q)}{\|w\|_{\mathcal{V}}}, \quad \text{for } \nabla\cdot w = q \\ &= \frac{\|q\|^2_{\mathcal{U}}}{\|w\|_{\mathcal{V}}} \geq \frac{1}{c}\|q\|_{\mathcal{U}}. \end{aligned}$$

Since we chose $q \in \mathcal{U}$ arbitrarily plus Equation (5.9), it follows

$$\inf_{q\in\mathcal{U}} \sup_{w\in\mathcal{V}} \frac{b(w,q)}{\|w\|_{\mathcal{V}}\|q\|_{\mathcal{U}}} \geq \frac{1}{c} =: \beta_b.$$

□

Lemma 5. *Let the assumptions of Theorem 2 be given. If it holds*

$$\frac{2\mu a_{\tilde{\varphi}}(u,u)}{\|u\|_{\mathcal{V}}} + \sup_{q\in\mathcal{U}} \frac{b_{\tilde{\varphi}}(u,q)}{\|q\|_{\mathcal{U}} + \frac{1}{\lambda}|q|_c} \geq \alpha\|u\|_{\mathcal{V}}, \quad \textit{for some } \alpha > 0, \tag{5.10}$$

or

$$\sup_{(w,q)\in\mathcal{V}\times\mathcal{W}} \frac{A_{\tilde{\varphi}}(u,0;w,q)}{|\!|\!|(w,q)|\!|\!|} \geq \tilde{\alpha}\|u\|_{\mathcal{V}} \quad \textit{with some } \tilde{\alpha} > 0, \tag{5.11}$$

then the inf-sup condition of Theorem 3 follows.

Proof (of Lemma 5) First, the equivalence of Equations (5.10) and (5.11) is shown. Then, we prove the inf-sup condition using the two equivalent expressions.
The inequality in Equation (5.10) can be derived via Equation (5.11) because it holds

$$\begin{aligned}\alpha\|u\|_{\mathcal{V}} \leq \frac{2\mu a_{\tilde{\varphi}}(u,u)}{\|u\|_{\mathcal{V}}} + \sup_{q\in\mathcal{U}} \frac{b_{\tilde{\varphi}}(u,q)}{\|q\|_{\mathcal{U}} + \frac{1}{\lambda}|q|_c} &= \frac{A_{\tilde{\varphi}}(u,0;u,0)}{|\!|\!|(u,0)|\!|\!|} + \sup_{q\in\mathcal{U}} \frac{A_{\tilde{\varphi}}(u,0;0,q)}{|\!|\!|(0,q)|\!|\!|} \\ &\leq 2 \sup_{(w,q)\in\mathcal{V}\times\mathcal{U}} \frac{A_{\tilde{\varphi}}(u,0;w,q)}{|\!|\!|(w,q)|\!|\!|}.\end{aligned}$$

Here, the definition of $A_{\tilde{\varphi}}(\cdot,\cdot;\cdot,\cdot)$ from Equation (5.7) is used.
Assuming $\tilde{\alpha} \geq \frac{\alpha}{2}$ implies that Equation (5.10) results from Equation (5.11). Now, the other direction is proven. By Cauchy Schwarz inequality for the definite form $a_{\tilde{\varphi}}(\cdot,\cdot)$, it holds $a_{\tilde{\varphi}}(u,w)^2 \leq a_{\tilde{\varphi}}(u,u)a_{\tilde{\varphi}}(w,w)$, which allows the following estimate:

$$\begin{aligned}\tilde{\alpha}\|u\|_{\mathcal{V}} &\leq \sup_{(w,q)\in\mathcal{V}\times\mathcal{U}} \frac{A_{\tilde{\varphi}}(u,0;w,q)}{|\!|\!|(w,q)|\!|\!|} \leq \sup_{(w,q)\in\mathcal{V}\times\mathcal{U}} \frac{2\mu a_{\tilde{\varphi}}(u,w)}{|\!|\!|(w,q)|\!|\!|} + \sup_{(w,q)\in\mathcal{V}\times\mathcal{U}} \frac{b_{\tilde{\varphi}}(u,q)}{|\!|\!|(w,q)|\!|\!|} \\ &= \sup_{w\in\mathcal{V}} \frac{2\mu a_{\tilde{\varphi}}(u,w)}{\|w\|_{\mathcal{V}}} + \sup_{q\in\mathcal{U}} \frac{b_{\tilde{\varphi}}(u,q)}{|\!|\!|(0,q)|\!|\!|} \leq \sup_{w\in\mathcal{V}} \frac{(2\mu a_{\tilde{\varphi}}(u,u))^{1/2} a_{\tilde{\varphi}}(w,w)^{\frac{1}{2}}}{\|w\|_{\mathcal{V}}} + \sup_{q\in\mathcal{U}} \frac{b_{\tilde{\varphi}}(u,q)}{|\!|\!|(0,q)|\!|\!|} \\ &\leq sup_{w\in\mathcal{V}} \frac{2\mu\|a\|a_{\tilde{\varphi}}}{\|w\|_{\mathcal{V}}} + \sup_{q\in\mathcal{U}} \frac{b_{\tilde{\varphi}}(u,q)}{|\!|\!|(0,q)|\!|\!|} \\ &\leq \left[\sup_{(u,w)\in\mathcal{V}\times\mathcal{V}} \frac{a_{\tilde{\varphi}}(u,w)}{\|u\|_{\mathcal{V}}\|w\|_{\mathcal{V}}}\right]^{\frac{1}{2}} a_{\tilde{\varphi}}(u,u)^{\frac{1}{2}} + \sup_{q\in\mathcal{U}} \frac{b_{\tilde{\varphi}}(u,q)}{|\!|\!|(0,q)|\!|\!|},\end{aligned}$$

where the sup-norm $||a||$ is defined as:

$$||a|| \coloneqq \sup_{(u,w)} \frac{a_{\tilde{\varphi}}(u,w)}{\|u\|_{\mathcal{V}}\|w\|_{\mathcal{V}}}.$$

In the first estimate, the Cauchy-Schwarz inequality from Lemma 3 is used. In the last step, with $x \leq y + z \Rightarrow x \leq 2y + z^2/x$ from [39] we get Equation 5.11. the equivalence is shown.
Next, utilizing the equivalent statements, we prove that the inf-sup condition from Theorem 3 follows: Assume $(u,p) \in \mathcal{V} \times \mathcal{U}$. For a better overview, we define

$$\text{SUP} \coloneqq \sup_{(w,q)\in\mathcal{V}\times\mathcal{U}} \frac{A_{\tilde{\varphi}}(u,p;w,q)}{|\!|\!|(w,q)|\!|\!|}. \tag{5.12}$$

Via the estimate

$$A_{\tilde{\varphi}}(u,p;u,-p) = 2\mu a_{\tilde{\varphi}}(u,u) + \frac{1}{\lambda}c_{\tilde{\varphi}}(p,p) \geq \frac{1}{\lambda}c_{\tilde{\varphi}}(p,p) = \frac{1}{\lambda}|p|_c^2,$$

it follows that

$$\frac{1}{\sqrt{\lambda}}|p|_c \leq \frac{A_{\tilde{\varphi}}(u,p;u,-p)}{|\!|\!|(u,p)|\!|\!|} \frac{|\!|\!|(u,p)|\!|\!|}{\frac{1}{\sqrt{\lambda}}|p|_c} \leq \frac{|\!|\!|(u,p)|\!|\!|}{\frac{1}{\sqrt{\lambda}}|p|_c}\ \text{SUP}. \tag{5.13}$$

In the last step the estimate is given via the SUP-norm defined in Equation (5.12). The inf-sup condition of $b_{\tilde{\varphi}}(w,q)$ is stated as

$$\inf_{q\in\mathcal{U}} \sup_{w\in\mathcal{V}} \frac{b_{\tilde{\varphi}}(w,q)}{\|w\|_{\mathcal{V}}\|q\|_{\mathcal{U}}} \geq \beta, \quad \beta > 0, \tag{5.14}$$

which provides:

$$\begin{aligned}
\beta\|p\|_{\mathcal{U}} \leq\ & \sup_{w\in\mathcal{V}} \frac{b_{\tilde{\varphi}}(w,p)}{\|w\|_{\mathcal{V}}} = \sup_{w\in\mathcal{V}} \frac{A_{\tilde{\varphi}}(u,p;w,0) - 2\mu a_{\tilde{\varphi}}(u,w)}{\|w\|_{\mathcal{V}}} \\
\leq\ & \sup_{w\in\mathcal{V}} \frac{A_{\tilde{\varphi}}(u,p;w,0)}{\|w\|_{\mathcal{V}}} + \sup_{w\in\mathcal{V}} \frac{|2\mu a_{\tilde{\varphi}}(u,w)|}{\|u\|_{\mathcal{V}}\|w\|_{\mathcal{V}}}||u||_{\mathcal{V}} \\
\leq\ & \text{SUP} + 2\mu\|a\|\|u\|_{\mathcal{V}}.
\end{aligned} \tag{5.15}$$

Via the estimate in Equation (5.11) it follows

$$\begin{aligned}
\tilde{\alpha}\|u\|_{\mathcal{V}} &\leq \frac{2\mu a_{\tilde{\varphi}}(u,u)}{\|u\|_{\mathcal{V}}} + \sup_{q\in\mathcal{U}} \frac{b_{\tilde{\varphi}}(u,q)}{\|q\|_{\mathcal{U}} + \frac{1}{\lambda}|q|_c} \\
&\leq \frac{|\!|\!|(u,p)|\!|\!|}{\|u\|_{\mathcal{V}}}\ \mathrm{SUP} + \sup_{q\in\mathcal{U}} \frac{A_{\tilde{\varphi}}(u,p;0,q)}{|\!|\!|(0,q)|\!|\!|} + \sup_{q\in\mathcal{U}} \frac{\frac{1}{\lambda}c_{\tilde{\varphi}}(p,q)}{|\!|\!|(0,q)|\!|\!|} \\
&\leq \frac{|\!|\!|(u,p)|\!|\!|}{\|u\|_{\mathcal{V}}}\ \mathrm{SUP} + \mathrm{SUP} + \sup_{q\in\mathcal{U}} \frac{\frac{1}{\lambda}c_{\tilde{\varphi}}(p,q)}{\|q\|_{\mathcal{U}} + \frac{1}{\lambda}|q|_c} \\
&\leq \frac{|\!|\!|(u,p)|\!|\!|}{\|u\|_{\mathcal{V}}}\ \mathrm{SUP} + \mathrm{SUP} + \sup_{q\in\mathcal{U}} \frac{\frac{1}{\lambda}c_{\tilde{\varphi}}(p,q)}{\frac{1}{\lambda}|q|_c} \\
&\leq \frac{|\!|\!|(u,p)|\!|\!|}{\|u\|_{\mathcal{V}}}\ \mathrm{SUP} + \mathrm{SUP} + \sup_{q\in\mathcal{U}} \frac{\frac{1}{\sqrt{\lambda}}c_{\tilde{\varphi}}(p,p)^{\frac{1}{2}}c_{\tilde{\varphi}}(q,q)^{\frac{1}{2}}}{|q|_c} \\
&\leq \frac{|\!|\!|(u,p)|\!|\!|}{\|u\|_{\mathcal{V}}}\ \mathrm{SUP} + \mathrm{SUP} + \frac{1}{\sqrt{\lambda}}|p|_c.
\end{aligned} \tag{5.16}$$

Here, the definition of $A_{\tilde{\varphi}}(\cdot,\cdot;\cdot,\cdot)$, the triangle inequality, and the Cauchy-Schwarz inequality from Lemma 3 are used.
For the next step, we use Lemma 4, which states that:

$$r \leq \frac{s^2}{r} + t \quad \Rightarrow\ r \leq s + t \quad \text{for } r,s,t \in \mathbb{R}^+.$$

From Equation (5.16) we consider two cases on the following:

$$\begin{aligned}
&i) \quad \frac{1}{\sqrt{\lambda}}|p|_c \leq \frac{1}{2}\tilde{\alpha}\|u\|_{\mathcal{V}}, \\
&ii) \quad \frac{1}{\sqrt{\lambda}}|p|_c > \frac{1}{2}\tilde{\alpha}\|u\|_{\mathcal{V}},
\end{aligned}$$

and show that for both cases inf-sup estimates for $A_{\tilde{\varphi}}(u,p;w,q)$ can be found:

i) We assume that

$$\frac{1}{\sqrt{\lambda}}|p|_c \leq \frac{1}{2}\tilde{\alpha}\|u\|_{\mathcal{V}}.$$

From Equation (5.16) it holds

$$\tilde{\alpha}\|u\|_{\mathcal{V}} \leq \frac{|\!|\!|(u,p)|\!|\!|}{\|u\|_{\mathcal{V}}}\ \mathrm{SUP} + \mathrm{SUP} + \frac{1}{\sqrt{\lambda}}|p|_c,$$

which is equivalent to

$$\tilde{\alpha}\|u\|_{\mathcal{V}} - \frac{1}{\sqrt{\lambda}}|p|_c \leq \mathrm{SUP}\ \left(\frac{\|u\|_{\mathcal{V}} + \|p\|_{\mathcal{U}} + \frac{1}{\sqrt{\lambda}}|p|_c}{\|u\|_{\mathcal{V}}} + 1\right).$$

And we can follow

$$\frac{1}{2}\tilde{\alpha}\|u\|_{\mathcal{V}} \leq \text{SUP}\ \left(\frac{\|u\|_{\mathcal{V}} + \|p\|_{\mathcal{U}} + \frac{1}{\sqrt{\lambda}}|p|_c}{\|u\|_{\mathcal{V}}} + 1\right).$$

Via Equation (5.15) we achieve further

$$\frac{1}{2}\tilde{\alpha}\|u\|_{\mathcal{V}} \leq \text{SUP}\ \left(\frac{\|u\|_{\mathcal{V}} + \|p\|_{\mathcal{U}} + \frac{1}{\sqrt{\lambda}}|p|_c}{\|u\|_{\mathcal{V}}} + 1\right) \leq \text{SUP}\ \left(2 + \frac{\frac{1}{\beta}\text{SUP}}{\|u\|_{\mathcal{V}}} + \frac{2\mu\|a\|}{\beta} + \frac{1}{2}\tilde{\alpha}\right),$$

which is equivalent to

$$\|u\|_{\mathcal{V}} \leq \text{SUP}\ \left(\frac{4}{\tilde{\alpha}} + \frac{\frac{2}{\tilde{\alpha}\beta}\text{SUP}}{\|u\|_{\mathcal{V}}} + \frac{4\mu\|a\|}{\tilde{\alpha}\beta} + 1\right).$$

In a next step we use Lemma 4 with

$$r = \|u\|_{\mathcal{V}}, \quad s = \sqrt{\frac{2}{\tilde{\alpha}\beta}\text{SUP}}, \quad t = \text{SUP}\ \frac{4}{\tilde{\alpha}} + \text{SUP}\ \frac{4\mu\|a\|}{\tilde{\alpha}\beta} + \text{SUP}.$$

Thus we obtain

$$\|u\|_{\mathcal{V}} \leq \text{SUP}\left(\frac{4}{\tilde{\alpha}} + \sqrt{\frac{2}{\tilde{\alpha}\beta}} + \frac{4\mu\|a\|}{\tilde{\alpha}\beta} + 1\right).$$

Bounds for the other norms are derived via Equation (5.15) and Lemma 4:

$$\|u\|_{\mathcal{V}} + \|p\|_{\mathcal{U}} + \frac{1}{\sqrt{\lambda}}|p|_c \leq \text{SUP}\left(\frac{4}{\tilde{\alpha}} + \sqrt{\frac{2}{\tilde{\alpha}\beta}} + \frac{4\mu\|a\|}{\tilde{\alpha}\beta} + 1\right) + \frac{1}{\beta}\left(\text{SUP}\ + 2\mu\|a\|\|u\|_{\mathcal{V}}\right) + \frac{1}{2}\tilde{\alpha}\|u\|_{\mathcal{V}}.$$

Further, via the definition of the natural norm and the estimate from the proof of Lemma 5, we get

$$\begin{aligned}
|\!|\!|(u,p)|\!|\!| &\leq \text{SUP}\left(\frac{4}{\tilde{\alpha}} + \sqrt{\frac{2}{\tilde{\alpha}\beta}} + \frac{4\mu\|a\|}{\tilde{\alpha}\beta} + 1\right) + \frac{1}{\beta}\text{SUP}\ + \frac{2\mu}{\beta}\|a\|\|u\|_{\mathcal{V}} + \frac{1}{2}\sup_{(w,q)\in\mathcal{V}\times\mathcal{W}}\frac{A(u,0;w,q)}{|\!|\!|(w,q)|\!|\!|} \\
&\leq \text{SUP}\left(\frac{4}{\tilde{\alpha}} + \sqrt{\frac{2}{\tilde{\alpha}\beta}} + \frac{4\mu\|a\|}{\tilde{\alpha}\beta} + 1\right) + \frac{1}{\beta}\text{SUP} \\
&+ \frac{2\mu}{\beta}\|a\|\frac{1}{\tilde{\alpha}}\sup_{(w,q)\in\mathcal{V}\times\mathcal{W}}\frac{A(u,0;w,q)}{|\!|\!|(w,q)|\!|\!|} + \frac{1}{2}\sup_{(w,q)\in\mathcal{V}\times\mathcal{W}}\frac{A(u,0;w,q)}{|\!|\!|(w,q)|\!|\!|} \\
&\leq \text{SUP}\left(\frac{4}{\tilde{\alpha}} + \sqrt{\frac{2}{\tilde{\alpha}\beta}} + \frac{4\mu\|a\|}{\tilde{\alpha}\beta} + 1\right) + \frac{1}{\beta}\text{SUP}\ + \frac{2\mu}{\beta\tilde{\alpha}}\|a\|\text{SUP}\ + \frac{1}{2}\text{SUP} \\
&= \left(\frac{4}{\tilde{\alpha}} + \sqrt{\frac{2}{\tilde{\alpha}\beta}} + \frac{4\mu\|a\|}{\tilde{\alpha}\beta} + 1 + \frac{1}{\beta} + \frac{2\mu}{\beta\tilde{\alpha}}\|a\| + \frac{1}{2}\right)\text{SUP} \\
&= \left(\frac{4}{\tilde{\alpha}} + \sqrt{\frac{2}{\tilde{\alpha}\beta}} + \frac{6\mu\|a\|}{\tilde{\alpha}\beta} + \frac{3}{2} + \frac{1}{\beta}\right)\text{SUP}.
\end{aligned}$$

It yields

$$\frac{1}{\tilde{\gamma}} \leq \mathrm{SUP}\ \frac{1}{|||(u,p)|||} = \sup_{(w,q)\in\mathcal{V}\times\mathcal{U}} \frac{A_{\tilde{\varphi}}(u,p;w,q)}{|||(w,q)|||\,|||(u,p)|||}.$$

Here, we defined a constant $\tilde{\gamma} > 0$. In the last step, the definition of SUP from Equation (5.12) is applied. Because $(u,p) \in \mathcal{V}\times\mathcal{U}$ is chosen arbitrarily, it holds

$$\frac{1}{\tilde{\gamma}} \leq \inf_{(u,p)\in\mathcal{V}\times\mathcal{U}} \sup_{(w,q)\in\mathcal{V}\times\mathcal{U}} \frac{A_{\tilde{\varphi}}(u,p;w,q)}{|||(w,q)|||\,|||(u,p)|||}.$$

With $\tilde{\gamma} > 0$ and $\gamma = \frac{1}{\tilde{\gamma}}$, the condition is fulfilled.

ii) As the second case, we consider

$$\frac{1}{\sqrt{\lambda}}|p|_c > \frac{1}{2}\tilde{\alpha}\|u\|_{\mathcal{V}}. \tag{5.17}$$

First, via Equations (5.15) and (5.17) it follows

$$\|p\|_{\mathcal{U}} \leq \frac{1}{\beta}\mathrm{SUP}\ + \frac{4\mu\|a\|}{\tilde{\alpha}\beta}\frac{1}{\sqrt{\lambda}}|p|_c. \tag{5.18}$$

Using Equations (5.13) and (5.18) in the second step, and the assumption from Equation (5.17), we conclude with Lemma 4 that

$$\begin{aligned}
\frac{1}{\sqrt{\lambda}}|p|_c &\leq \mathrm{SUP}\ \frac{\|u\|_{\mathcal{V}} + \|p\|_{\mathcal{U}} + \frac{1}{\sqrt{\lambda}}|p|_c}{\frac{1}{\sqrt{\lambda}}|p|_c} \\
&\leq \mathrm{SUP}\ \left(\frac{\|u\|_{\mathcal{V}}}{\frac{1}{\sqrt{\lambda}}|p|_c} + \frac{\frac{1}{\beta}\mathrm{SUP}}{\frac{1}{\sqrt{\lambda}}|p|_c} + \frac{4\mu\|a\|\frac{1}{\sqrt{\lambda}}|p|_c}{\tilde{\alpha}\beta\frac{1}{\sqrt{\lambda}}|p|_c} + 1\right) \\
&\leq \mathrm{SUP}\ \left(\frac{2}{\tilde{\alpha}} + \frac{\frac{1}{\beta}\mathrm{SUP}}{\frac{1}{\sqrt{\lambda}}|p|_c} + \frac{4\mu\|a\|}{\tilde{\alpha}\beta} + 1\right) \\
&= \mathrm{SUP}\ \left(\frac{2}{\tilde{\alpha}} + \frac{4\mu\|a\|}{\tilde{\alpha}\beta} + 1\right) + \frac{\frac{1}{\beta}\mathrm{SUP}^2}{\frac{1}{\sqrt{\lambda}}|p|_c} \\
&\leq \mathrm{SUP}\ \left(\frac{2}{\tilde{\alpha}} + \frac{4\mu\|a\|}{\tilde{\alpha}\beta} + 1\right) + \sqrt{\frac{1}{\beta}}\mathrm{SUP} \\
&= \left(1 + \frac{2}{\tilde{\alpha}} + \frac{1}{\sqrt{\beta}} + \frac{4\mu\|a\|}{\tilde{\alpha}\beta}\right)\ \mathrm{SUP}.
\end{aligned} \tag{5.19}$$

We give the bounds for the other norms derived using Equations (5.13), (5.15), (5.16) and the

results from Lemma 4.

$$\|p\|_{\mathcal{U}} + \frac{1}{\sqrt{\lambda}}|p|_c \leq \text{SUP}\ \frac{1}{\beta} + \frac{4\mu\|a\|}{\tilde{\alpha}\beta}\frac{1}{\sqrt{\lambda}}|p|_c + \text{SUP}\ \left(1 + \frac{2}{\tilde{\alpha}} + \frac{1}{\beta} + \frac{4\mu\|a\|}{\tilde{\alpha}\beta}\right)$$
$$= \text{SUP}\ \left(\frac{1}{\beta} + 1 + \frac{2}{\tilde{\alpha}} + \frac{2}{\beta} + \frac{4\mu\|a\|}{\tilde{\alpha}\beta}\right) + \frac{4\mu\|a\|}{\tilde{\alpha}\beta}\frac{1}{\sqrt{\lambda}}|p|_c.$$

This is equivalent to

$$\|u\|_{\mathcal{V}} + \|p\|_{\mathcal{U}} + \frac{1}{\sqrt{\lambda}}|p|_c \leq \text{SUP}\ \left(\frac{1}{\beta} + 1 + \frac{2}{\tilde{\alpha}} + \frac{1}{\beta} + \frac{4\mu\|a\|}{\tilde{\alpha}\beta}\right) + \frac{4\mu\|a\|}{\tilde{\alpha}\beta}\frac{1}{\sqrt{\lambda}}|p|_c + \frac{2}{\tilde{\alpha}}\frac{1}{\sqrt{\lambda}}|p|_c$$
$$= \text{SUP}\ \left(\frac{1}{\beta} + 1 + \frac{2}{\tilde{\alpha}} + \frac{1}{\beta} + \frac{4\mu\|a\|}{\tilde{\alpha}\beta}\right) + \left(\frac{4\mu\|a\|}{\tilde{\alpha}\beta} + \frac{2}{\tilde{\alpha}}\right)\frac{1}{\sqrt{\lambda}}|p|_c.$$

Finally it holds

$$|||(u,p)||| \leq \text{SUP}\ \left(\frac{1}{\beta} + 1 + \frac{2}{\tilde{\alpha}} + \frac{1}{\beta} + \frac{4\mu\|a\|}{\tilde{\alpha}\beta}\right) + \left(\frac{4\mu\|a\|}{\tilde{\alpha}\beta} + \frac{2}{\tilde{\alpha}}\right)\left(1 + \frac{2}{\tilde{\alpha}} + \frac{1}{\sqrt{\beta}} + \frac{4\mu\|a\|}{\tilde{\alpha}\beta}\right)\text{SUP}$$
$$= \text{SUP}\ \left(\left(\frac{1}{\beta} + 1 + \frac{2}{\tilde{\alpha}} + \frac{1}{\beta} + \frac{2\|a\|}{\tilde{\alpha}\beta}\right) + \left(\frac{2\|a\|}{\tilde{\alpha}\beta} + \frac{2}{\tilde{\alpha}}\right)\left(1 + \frac{2}{\tilde{\alpha}} + \frac{1}{\sqrt{\beta}} + \frac{2\|a\|}{\tilde{\alpha}\beta}\right)\right)$$
$$= \text{SUP}\ (\tilde{\gamma}_1 + \tilde{\gamma}_2),$$

which can be summarized as one constant $\tilde{\gamma} \coloneqq \tilde{\gamma}_1 + \tilde{\gamma}_2$. We conclude

$$\frac{1}{\tilde{\gamma}} \leq \text{SUP}\ \frac{1}{|||(u,p)|||} = \sup_{(w,q)\in\mathcal{V}\times\mathcal{U}} \frac{A_{\tilde{\varphi}}(u,p;w,q)}{|||(w,q)|||\,|||(u,p)|||}.$$

Because $\tilde{\gamma} > 0$ and $(u,p) \in \mathcal{V}\times\mathcal{U}$ were chosen arbitrarily, the inf-sup condition is fulfilled with $\gamma = \frac{1}{\tilde{\gamma}}$ as in Case 1, which shows Lemma 5.

□

Proof (of Theorem 3) The coercivity on $\mathcal{V}$ with

$$a_{\tilde{\varphi}}(u,u) \geq \alpha\|u\|_{\mathcal{V}}^2,$$

allows justifying Equation (5.10). In Lemma 5, two equivalent statements were given, which proves Theorem 3. □

Theorem 5 (Well-posedness of the elasticity problem in mixed form)**.** *If the assumptions of Brezzi's splitting theorem 2 are fulfilled, and $a_{\tilde{\varphi}}(\cdot,\cdot)$ is elliptic on $\mathcal{V}$, then Formulation 14 is a well-posed problem satisfying the following inf-sup condition:*

$$\inf_{(u,p)\in\mathcal{V}\times\mathcal{U}} \sup_{(w,q)\in\mathcal{V}\times\mathcal{U}} \frac{A_{\tilde{\varphi}}(u,p;w,q)}{|||(u,p)|||\,|||(w,q)|||} \geq \gamma > 0, \quad \forall\ 0 \leq \frac{1}{\lambda} \leq 1,$$

where γ is independent of λ.

PROOF The inf-sup stability is proven in Theorem 3. For the existence and uniqueness of a solution of the inf-sup stable problem Formulation 14, we use the generalized Lax-Milgram Theorem 4. Condition b) in Theorem 4 is fulfilled via Theorem 3 for the bilinear form $A_{\tilde{\varphi}}(u,p;w,q)$. Further, the bilinear form $A_{\tilde{\varphi}}(u,p;w,q)$ defined in Equation (5.7) is symmetric, which implies c) from Theorem 4. From the assumption from Brezzi's splitting theorem, we fulfill a) from Theorem 4 aside from the boundedness of $c_{\tilde{\varphi}}(p,q)$, which is proven in the following:
By using the Cauchy-Schwarz inequality from Lemma 3, we get

$$|c_{\tilde{\varphi}}(p,q)| = \left|\int_\Omega pq\,dx\right| \leq \int_\Omega |pq|\,dx \leq \left(\int_\Omega |p|^2\,dx\right)^{\frac{1}{2}} \left(\int_\Omega |q|^2\,dx\right)^{\frac{1}{2}} = \|p\|_{\mathcal{U}}\|q\|_{\mathcal{U}}.$$

□

Remark 23 (Well-posedness with restrictions)**.** *With the help of Brezzi's splitting theorem and a generalized Lax-Milgram theorem, we could prove the existence, uniqueness, and an inf-sup condition independent of $\lambda > 0$ for the mixed elasticity problem from Formulation 14. The statement is restricted to the assumptions that φ and κ are given and constant.*

The proof of a stable problem formulation allows formulating a stable discrete problem formulation of Formulation 10. The discretized system reads:

Formulation 15 (Linear elasticity in weak and mixed form, discretized)**.** *Given the initial data $\varphi_h^{n-1}, \varphi_h^{n-2} \in \mathcal{K}_h$. Find $u_h \in \mathcal{V}_h \subset \mathcal{V}$ and $p_h \in \mathcal{U}_h \subset \mathcal{U}$ such that*

$$\begin{aligned} 2\mu\left(g(\tilde{\varphi})E_{lin}(u_h), E_{lin}(w)\right) + \left(g(\tilde{\varphi})p_h, \nabla\cdot w\right) &= 0 \quad \forall w \in \mathcal{V}_h, \\ \left(g(\tilde{\varphi})\nabla\cdot u_h, q\right) - \frac{1}{\lambda}\left(g(\tilde{\varphi})p_h, q\right) &= 0 \quad \forall q \in \mathcal{U}_h. \end{aligned}$$

We discretize the PDE system with stable Taylor-Hood elements of the type $Q_2^c Q_1^c$ for the pair (u,p). For the discretization of φ we also use bilinear Q_1^c finite elements.

Proposition 10 (Stable Taylor-Hood elements)**.** *We still assume $\varphi \neq 0$ and $\kappa > 0$ small and fix. Taylor-Hood-elements of the type $Q_2^c Q_1^c$ fulfill a discrete inf-sup or Babuska-Brezzi-condition [14, 44]*

$$\min_{q_h \in \mathcal{U}_h}\left\{\max_{w_h \in \mathcal{V}_h} \frac{(q_h, g(\tilde{\varphi})\nabla\cdot w_h)}{\|q_h\|\,\|\nabla w_h\|}\right\} \geq \gamma_h \geq \gamma > 0,$$

with a stability constant γ_h, which has to be greater than the stability constant γ on the continuous level.

PROOF For the proof we refer to Verfürth [170]. □

5.4 Numerical studies on locking observed in a hanging block

To study locking, we consider a hanging block, see Figure 5.1, similar to [101] and increase the Lamé coefficient λ while $\mu = 1.0$ is constant. The computations are based on Formulation 5.3 and the AT_2

functional from Section 4.6.1. The discretization and numerical solving of the problem are given in Chapter 3. As established in Section 5.1, for large λ, Céa's lemma is not reliable. Because we do

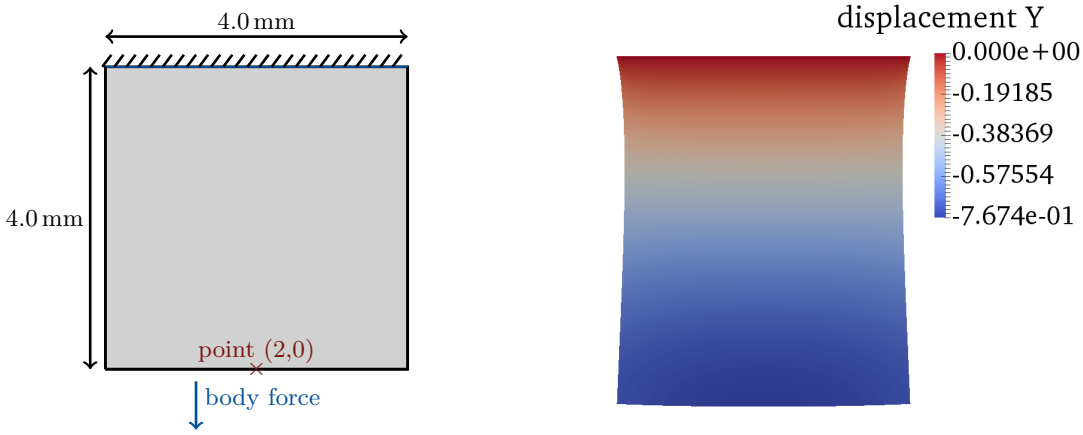

Figure 5.1: Left: geometry and boundary conditions of a hanging block. Two-dimensional square of length 4.0 mm. A body force $f = -10^{-4}\,\mathrm{N/mm^2}$ is applied to the hanging block. The block is fixed on the top boundary. Point evaluation for u_x in $(2, 0)$ on the bottom boundary of the block. Right: solution of the displacement in the y-direction of a hanging block for $\nu = 0.25$.

not have a fracture, the phase-field inequality does not play a role. We compare results based on Formulation 3, and our newly developed mixed problem Formulation 11. For the primal formulation, usually $Q_1^c Q_1^c$ elements are used for (u, φ). For the mixed form, we use $Q_2^c Q_1^c$ Taylor-Hood elements for the pair (u, p) and Q_1^c elements for the phase-field variable φ, denoted as $Q_2^c Q_1^c Q_1^c$. For a fair comparison of the problem sizes, we further run tests based on the primal form with $Q_2^c Q_1^c$ elements. The total numbers of dof are given for all tests in the legend of Figure 5.2.

In Figure 5.2, the maximal displacement in a certain point $(2, 0)$ (marked in Figure 5.1) is given as positive values (even if we have negative displacements). For four refinement levels of uniform refined meshes, three computations are conducted for seven different settings of λ: for the primal form with $Q_1^c Q_1^c$ and $Q_2^c Q_1^c$ elements, and for the mixed form with $Q_2^c Q_1^c Q_1^c$ elements. The Lamé coefficient λ is $\lambda = 1, 10, 100, 1\,000, 10\,000, 100\,000, 1\,000\,000$, while $\mu = 1.0$ is fixed. For the computations based on Formulation 11, convergence of the maximal displacement can be observed with increasing λ towards a value of around 0.5, while the computations based on Formulation 3 underestimate the displacement value. The results become more accurate for finer meshes and $Q_2^c Q_1^c$ elements. The computed displacement in a certain point $(2, 0)$ in the y-direction naturally decreases with a higher Poisson ratio due to the higher stiffness of the material. The proposed study confirms the observations from Section 5.1, where we explained locking effects. Further examples, studies, and theoretical aspects on locking phenomena in the literature can be found, e.g., in [121, 15, 65, 23].

5.5 First numerical results for crack propagation based on the mixed model

In this section, we present the first numerical results based on a test case with a propagating fracture, and reference values from the literature for $\nu = 0.3$. Employing Formulation 11 from Section 5.2, we

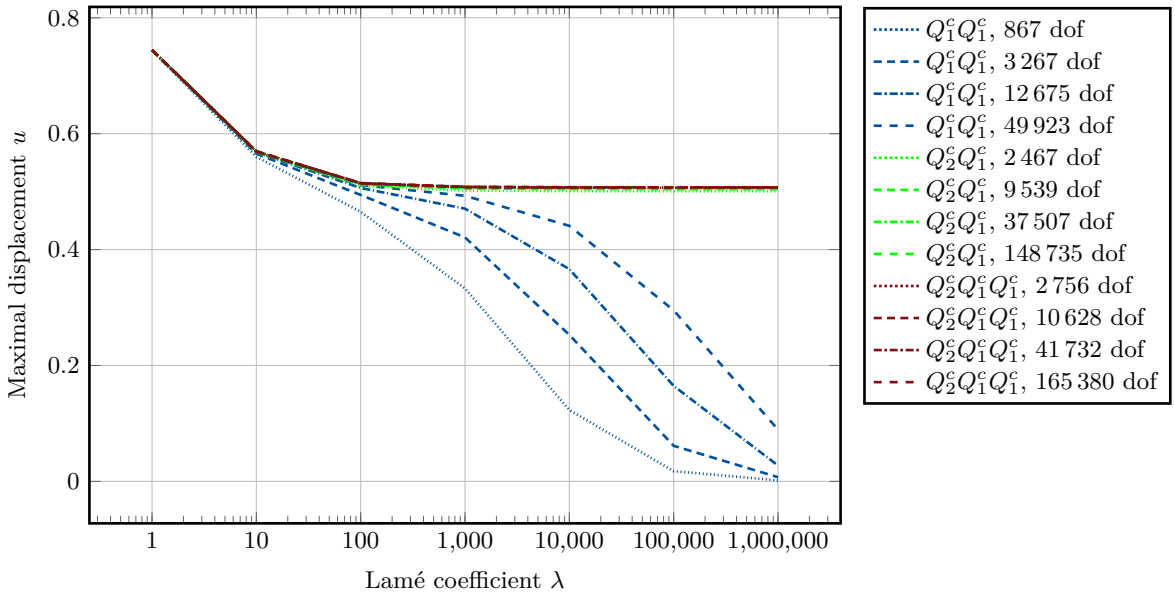

Figure 5.2: Maximal displacement values u_y in the point $(2, 0)$ given for the hanging block test for different finite elements on uniform refined meshes based on the primal Formulation 3 ($Q_1^cQ_1^c$ and $Q_2^cQ_1^c$) and mixed problem Formulation 11 ($Q_2^cQ_1^cQ_1^c$).

conduct three studies[2] for the single-edge notched shear test proposed in Section 4.7.3:

- Study 1: comparison of low-order and higher-order finite elements
- Study 2: mesh refinement studies
- Study 3: varying Poisson's ratio

The programming code of the numerical tests in this section is built on Example 8 of the instationary PDE Examples in the open-source library DOpElib [62, 79]. DOpElib, in turn, is based on the deal.II finite element library [9, 18].

Parameter	value
λ_0	$121.15\,\mathrm{kN/mm^2}$
μ_0	$80.77\,\mathrm{kN/mm^2}$
ν_0	0.3
G_C	$2.7\,\mathrm{N/mm}$
h_0	$0.044\,\mathrm{mm}$
ϵ_0	$2\,h_0$
δt	$10^{-4}\,\mathrm{s}$
κ	10^{-10}

Table 5.1: Settings of material and numerical parameters for the single-edge notched pure shear test.

[2]Results of Section 5.5 are published in [128].

5.5.1 Comparison of low order and higher-order finite elements

In the first set of computations, we concentrate on a comparison of bilinear and biquadratic finite elements. Such studies improve retracing the behavior of the numerical solution because we need higher-order finite elements when discretizing our proposed mixed formulation with Taylor-Hood elements. For this reason, we first use the primal Formulation 3 from Section 4.2 and employ two finite element combinations. We list the setting of the material and numerical parameters in Table 5.1.
In the following, we consider three finite element settings as in the previous section:

- Formulation 3 from Section 4.2 with $Q_1^c Q_1^c$ elements for (u, φ)
- Formulation 3 from Section 4.2 with $Q_2^c Q_1^c$ elements for (u, φ)
- Formulation 11 from Section 5.2 with $Q_2^c Q_1^c Q_1^c$ elements for (u, p, φ)

The load-displacement curves in Figure 5.3 have a similar course for all finite element settings. The

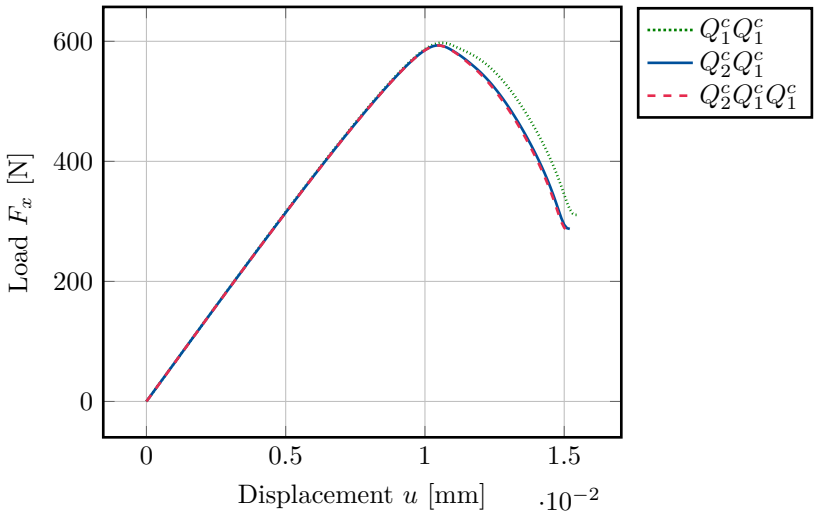

Figure 5.3: Load-displacement curves for the single-edge notched shear test with a uniform refined mesh for the primal formulation with $Q_1^c Q_1^c$ and $Q_2^c Q_1^c$ elements compared to the new mixed model $Q_2^c Q_1^c Q_1^c$. All computations with a mesh size of $h = 0.022\,\text{mm}$.

load-displacement curves for $\nu = 0.3$ based on Formulations 3 and 11 conform to the plots shown in the literature, e.g., [4] and [181]. The loading force increases until the critical energy release rate is reached and the material cracks. The crack propagation releases energy, and the loading force decreases after a certain maximal point until the material is broken at the bottom left corner; to remember the expected crack path behavior of the pure shear test, see Figure 3.2 on the right side.

5.5.2 Spatial mesh refinement studies

Mesh refinement studies are performed with a varying mesh size parameter h. The load-displacement curves in Figure 5.4 are based on Formulation 11 with $Q_2^c Q_1^c Q_1^c$ elements. In the refinement studies, we notice that we vary the discretization parameter h while the bandwidth of the transition zone ϵ is fixed via $\epsilon_0 = 2\,h_0$. Here, h_0 corresponds to the mesh size of the coarsest mesh. The only study

where we vary ϵ proportionally to the currently chosen h is depicted in Figure 5.5 to see the difference to Figure 5.4. In Figure 5.4, we see the course of the load-displacement curves with different levels of global refinement and fixed bandwidth ϵ. Besides the first test with $h = 0.044\,\text{mm}$, the load-displacement curves are similar. Figure 5.5 contains the load-displacement curves of the single-edge

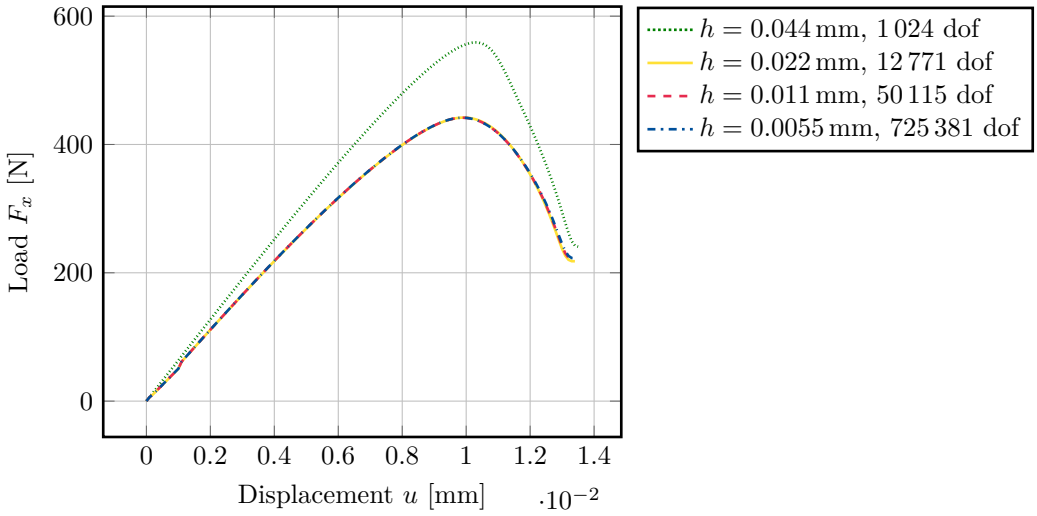

Figure 5.4: Load-displacement curves for the single-edge notched shear test with four different uniformly refined meshes. Based on Formulation 11 with $Q_2^c Q_1^c Q_1^c$ elements for (u, p, φ). Poisson's ratio is $\nu = 0.3$. The bandwidth ϵ is fixed by $\epsilon = \epsilon_0 = 0.088\,\text{mm}$.

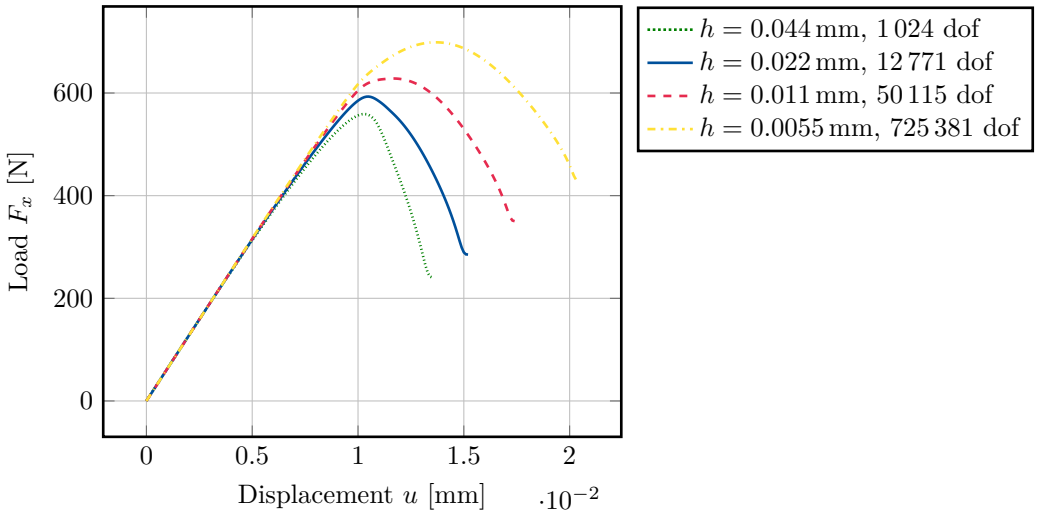

Figure 5.5: Load-displacement curves for the single-edge notched shear test with four different uniformly refined meshes. Based on Formulation 11 with $Q_2^c Q_1^c Q_1^c$ elements for (u, p, φ). Poisson's ratio $\nu = 0.3$. $\epsilon = 2\,h$ depending on the current mesh size.

notched shear test with different choices of h, and depending on the current uniformly refined mesh via the relation $\epsilon = 2\,h$. This sensitivity of the curves in Figure 5.5 also observed Heister et al. [87].

5.5.3 Variations in Poisson's ratio

We turn our attention to increasing Poisson ratios. To this end, our newly developed mixed phase-field system (Formulation 11) becomes crucial. The relevant load-displacement curves are given in the following for Poisson ratios from 0.3 to 0.4999. We discuss the numerical results via load-displacement curves and illustrations of the crack path of the phase-field function at specific time steps with large Lamé coefficient λ.

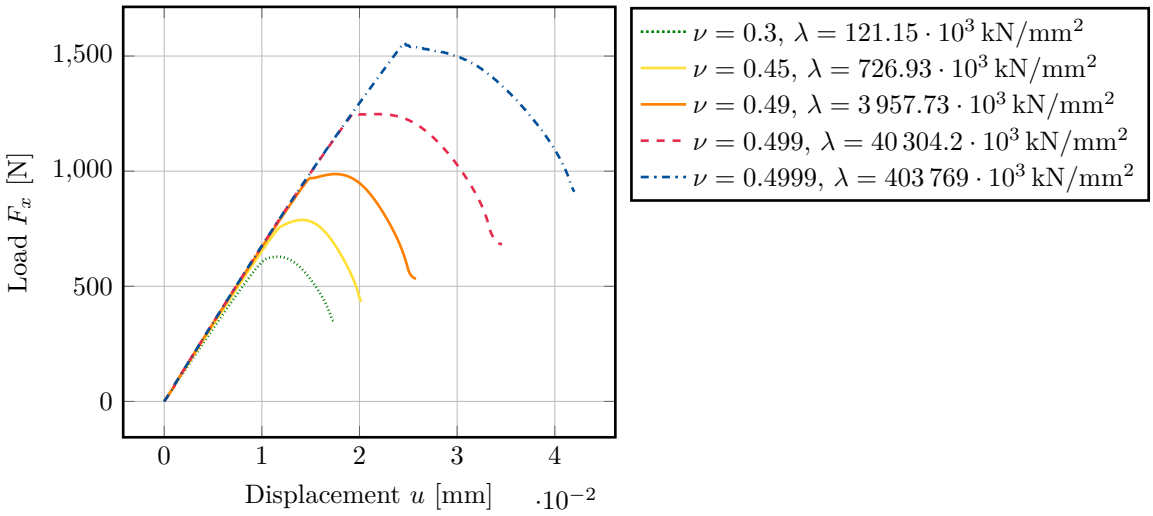

Figure 5.6: Load-displacement curves for the single-edge notched shear test with $h = 0.011\,\text{mm}$ (50 115 dof), different Poisson ratios and λ while $\mu = 80.77 \cdot 10^3\,\text{kN/mm}^2$. Based on Formulation 11 with $Q_2^c Q_1^c Q_1^c$ elements for (u, p, φ).

Figure 5.6 displays the load-displacement curves with different Poisson ratios ν. With an increasing ν, the loading values generally seem to be higher. The curves have a sharper maximal loading, and the crack progresses later. The more incompressible a solid is, the more robust it appears to be against displacement forces.

Figure 5.7 presents plots of the phase-field function at specific time steps with an increasing Poisson ratio ($\nu = 0.3, \nu = 0.49$, and $\nu = 0.4999$ from left to right). The propagation of the crack starts later with an increasing Lamé coefficient λ. For $\nu = 0.4999$, the loading of 0.03 mm (0.03 s) does not suffice that the crack tends to the bottom left corner. For this reason, in Figure 5.8 on the left, the phase-field function at later time steps is depicted for $\nu = 0.499$ and $\nu = 0.4999$. Further, plots of the corresponding pressure field in Figure 5.8 on the right in the same two time steps allow observing the nearly incompressible behavior with $\nu = 0.4999$.

In all studies within the single-edge notched pure shear test, the load-displacement curves and the behavior of the phase-field function, the same pattern could be observed: the higher ν, the later the crack propagation starts.

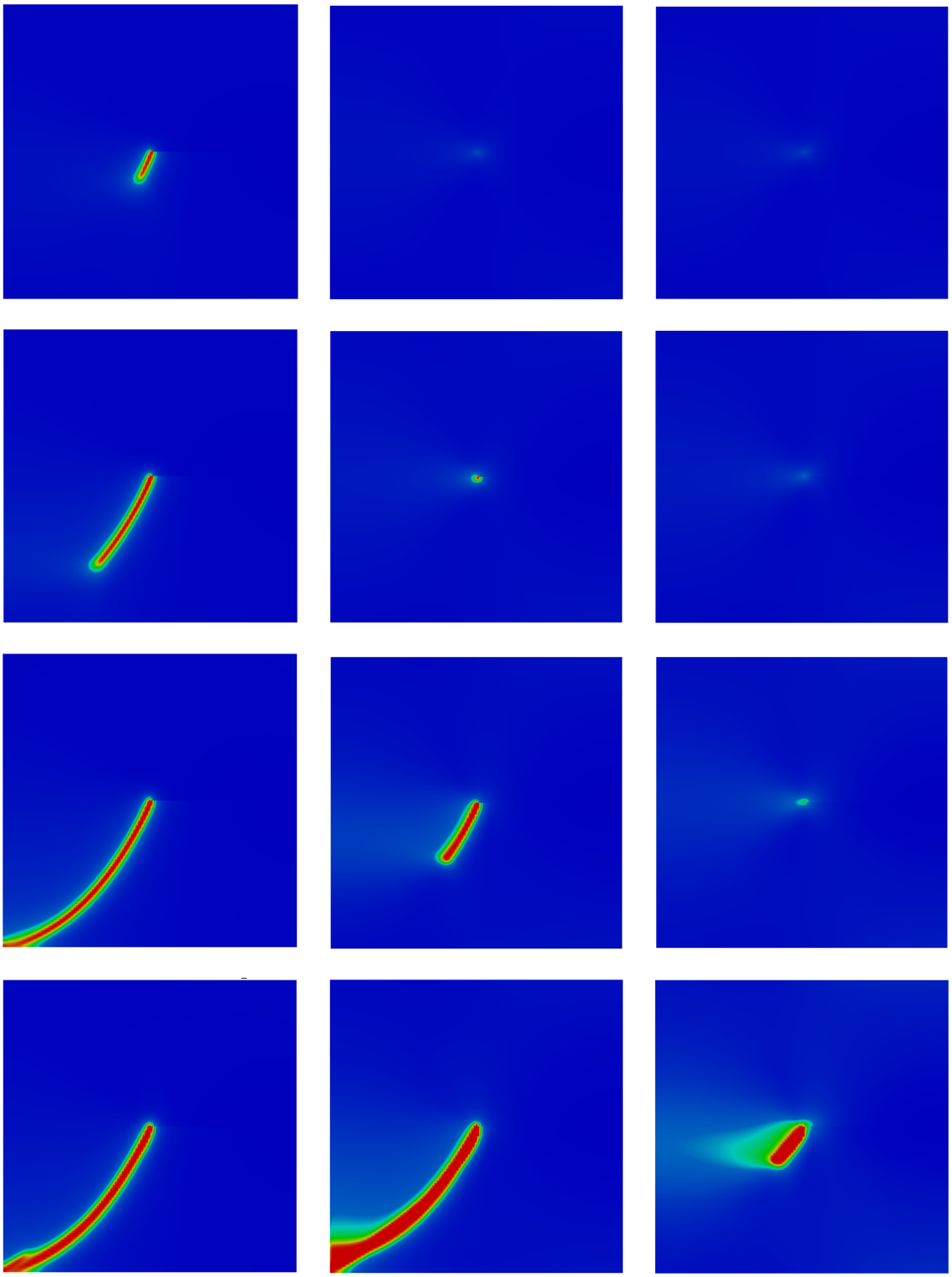

Figure 5.7: Phase-field function, from red-broken to blue-unbroken, with loading $u_y = 0.012, 0.015, 0.02$, and $0.03\,\text{mm}$ from top to bottom line, and for $\nu = 0.30$ (left), for $\nu = 0.49$ (middle) and for $\nu = 0.4999$ (right) with $h = 0.011\,\text{mm}$.

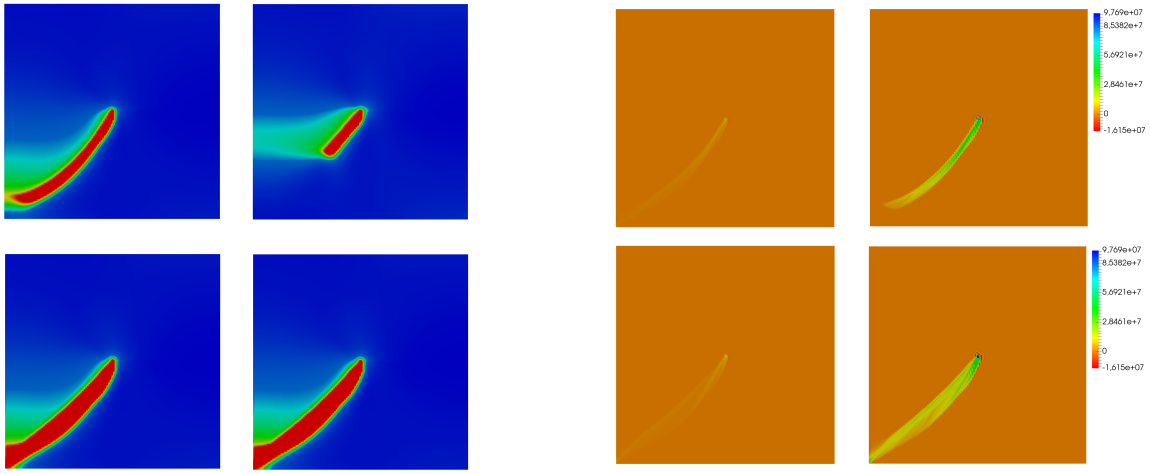

Figure 5.8: Phase-field function (left) and pressure field (right) with loading $u_y = 0.033$ and $u_y = 0.042\,\text{mm}$ from top to bottom line and for $\nu = 0.499$ (left) and for $\nu = 0.4999$ (right) with $h = 0.011\,\text{mm}$.

5.6 Modification in the model for a natural pressure field

With the help of the newly developed phase-field fracture model in mixed form, we could see that computing fracture simulation in nearly incompressible solids is possible; see Section 5.5. In Figure 5.8, we observe high pressure values inside the propagating crack and a wider crack for higher Poisson ratios. Since benchmark results on nearly incompressible solids are rarely available, we cannot verify or evaluate the experiences within the single-edge notched shear test and changed material parameters. In 2019, when the author of this thesis started to collaborate with the DIK, the main intention was to improve the understanding, how crack propagation in nearly incompressible solids behaves and how the new mixed model performs for a nearly incompressible real-world application. A detailed answer to that question is given for punctured EPDM strips in Chapter 7. For now, we figure out an essential modification in the model formulation which allows natural pressure solutions for higher Poisson ratios.

We consider modifications of the derived pressure equation from the mixed Formulation 11 for a more natural pressure field over the specimen with zero pressure values in the crack. Three possible formulations of the pressure equation from Formulation 11 are given as follows:

a) The incompressibility condition separated from the mixed problem formulation states

$$(g(\tilde{\varphi})\nabla \cdot u, q) - \left(g(\tilde{\varphi})\frac{1}{\lambda}p, q\right) = 0, \tag{5.20}$$

which is the original derivation from the primal problem. For $\lambda \to \infty$, the second term vanishes and $\nabla \cdot u = 0$ is fulfilled. Further, and more relevant for now, in the crack with $\varphi = 0$ and $g(\varphi) = \kappa$, we have

$$(\kappa\nabla \cdot u, q) - \left(\frac{\kappa}{\lambda}p, q\right) = 0 \quad \Leftrightarrow \quad (\kappa\nabla \cdot u, q) = \left(\frac{\kappa}{\lambda}p, q\right).$$

Here, for high Poisson ratios, the pressure values are expected to be large, especially in the transition zone of the fracture. It leads to an unrealistic crack behavior, as seen in Figure 5.8,

and justifies the maximal pressure values in the origin of the propagating fracture where $\varphi = 0$. High Poisson ratios even strengthen the effect that the pressure function balances κ and λ.

b) To avoid incompressibility in the broken part of the domain, we considered as the second option a λ-dependent incompressibilty condition, such that

$$(g(\tilde{\varphi})\nabla \cdot u, q) - \left(g(\tilde{\varphi})\frac{1}{\varphi\lambda + (1-\varphi)\lambda_{\text{comp}}}p, q\right) = 0. \tag{5.21}$$

For the considered test case $\lambda_{\text{comp}} = 1.83031\,\text{N/mm}^2$, the material differs regarding the stiffness with a Poisson ratio of $\nu = 0.3$ in the inner crack. It yields a linear decrease of λ from the crack boundary to the inner of the crack, which could fasten the crack growth. Further, it does not allow having an empty crack, but it changes the material's stiffness over the crack.

c) As a third option, we propose the following:

$$(g(\varphi)\nabla \cdot u, q) - (\frac{1}{\lambda}p, q) = 0, \tag{5.22}$$

which would yield for $\varphi = 0$:

$$(\kappa\nabla \cdot u, q) - \left(\frac{1}{\lambda}p, q\right) = 0 \quad \Rightarrow p \to 0 \quad \text{for } \lambda \to \infty.$$

This formulation allows small pressure values where $\varphi = 0$ even for high Poisson ratios and small κ, which is desired. Further, we preserve the symmetry of the inner saddle point problem with penalty term.

To compare the numerical results based on the three proposed formulations for the pressure equation in Equations (5.20), (5.21), and (5.22), we consider a two-dimensional rectangle similar to the proposed geometry from Chapter 7. We consider a strip of length 28 mm and width 20 mm. The strip is fixed on the top boundary and stretched on the bottom boundary downwards via quasi-time-dependent Dirichlet boundary conditions. We have an initial crack with $\varphi = 0$ on the left side of size 1 mm on a height of 6 mm measured from the bottom boundary. We use three levels of adaptive refinement via the predictor-corrector scheme from Section 3.3.1 with $\epsilon = 4\,h$. The material parameters are stated as $G_C = 0.97\,\text{N/mm}$, $\lambda = 60\,\text{N/mm}^2$, $\mu = 1.22\,\text{N/mm}^2$ and $\nu = 0.49$ (nearly incompressible). In Figure 5.9, we present snapshots of the phase-field solution after total failure and the pressure field before the material is broken to observe the pressure field behavior. The three proposed formulations for the pressure equation are used for simulating crack propagation in the strip from the left to the right boundary. In the first row, snapshots of the phase-field solution are given. Below, the pressure field is given. The pressure field in the first snapshot based on Equation (5.20) has maximal values on the crack boundary close to the initial slit, similar to Figure 5.8 from Section 5.5.3. In addition, the phase-field solution shows a wide crack compared to the other results on the same mesh, which is also similar to Figure 5.8. In the pressure field of the second snapshot based on Equation (5.21), the highest pressure values are in the initial crack, even if the material is broken. The shape and width of the corresponding phase-field function in the middle are more natural than on the left side. In the snapshots on the right in Figure 5.9, the phase-field and pressure field based on the mixed problem formulation with the pressure equation from Equation (5.22) are given. We point out that

the pressure field is intentionally given earlier in quasi-time to see the pressure values in front of the crack tip. We have zero pressure values in the crack, and the maximal values are located where the crack propagates.

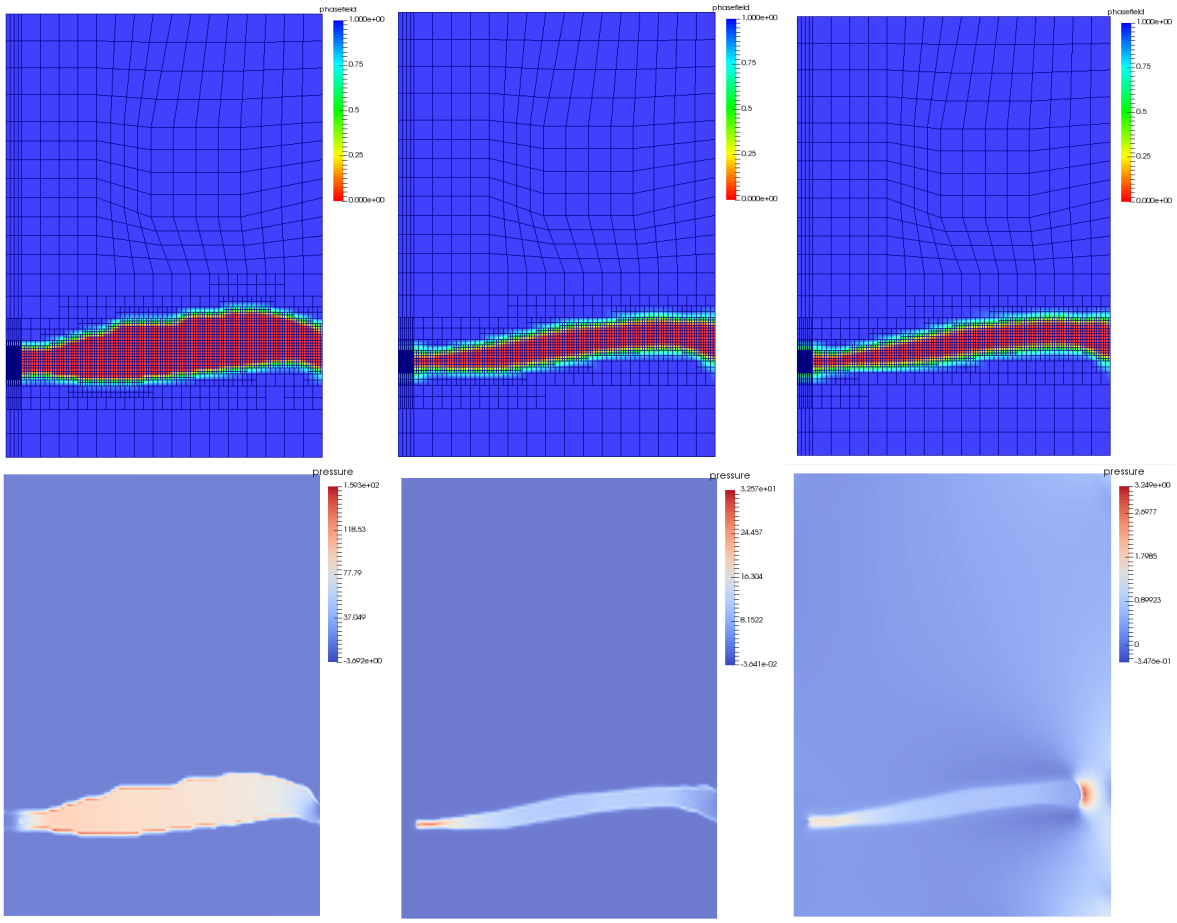

Figure 5.9: Snapshots of the phase-field solution after total failure (first row) and pressure field (second row) in rubber-like strips compared with a given notch at 6 mm and non-homogeneous Dirichlet boundary conditions. From left to right, the three proposed options to handle the incompressible solid behavior in the crack are given: on the left $\nu = 0.49$ in the whole domain, in the middle small λ in the crack domain, and on the right, the degradation function $g(\varphi)$ just weights the divergence term. The last column looks the most natural, with the highest pressure values in front of the crack tip.

We assume that Equation (5.22) is the most natural approach to have an empty crack without retroactive effects of the pressure solution on the phase-field and the crack behavior. We conclude the section with the new model formulations using Equation (5.22) as the pressure equation.

Formulation 16 (Modified mixed phase-field fracture formulation)**.** *Be* $\tilde{\varphi} := \tilde{\varphi}(\varphi^{n-1}, \varphi^{n-2})$*. Let the solutions of the previous incremental steps* $\varphi^{n-1}, \varphi^{n-2} \in \mathcal{K}$ *be given. Find* $u := u^n \in \{u_D + \mathcal{V}\}$,

$p := p^n \in \mathcal{U}$ and $\varphi := \varphi^n \in \mathcal{K}$ for the incremental steps $n = 1, 2, \ldots, N$ such that

$$
\begin{aligned}
(g(\tilde{\varphi})\sigma(u,p), E_{lin}(w)) &= 0 \quad \forall\ w \in \mathcal{V},\\
(g(\tilde{\varphi})\nabla\cdot u, q) - \frac{1}{\lambda}(p,q) &= 0 \quad \forall\ q \in \mathcal{U},\\
(1-\kappa)\,(\varphi\sigma(u,p) : E_{lin}(u), \psi-\varphi) + G_C\left(-\frac{1}{\epsilon}\varphi, \psi-\varphi\right)&\\
+ G_C\epsilon\,(\nabla\varphi, \nabla(\psi-\varphi)) &\geq 0 \quad \forall\ \psi \in \mathcal{K}.
\end{aligned}
$$

Also for pressurized fracture, we modify the incremental model problem.

Formulation 17 (Modified mixed phase-field fracture formulation, pressurized)**.** *Let $\rho \in L^\infty(\Omega)$ be given. Be $\tilde{\varphi} := \tilde{\varphi}(\varphi^{n-1}, \varphi^{n-2})$. Let the solutions of the previous incremental steps $\varphi^{n-1}, \varphi^{n-2} \in \mathcal{K}$ be given. Find $u := u^n \in \{u_D + \mathcal{V}\}$, $p := p^n \in \mathcal{U}$ and $\varphi := \varphi^n \in \mathcal{K}$ for the incremental steps $n = 1, 2, \ldots, N$ such that*

$$
\begin{aligned}
(g(\tilde{\varphi})\sigma(u,p), E_{lin}(w)) + (\tilde{\varphi}^2\rho, \nabla\cdot w) &= 0 \quad \forall\ w \in \mathcal{V},\\
(g(\tilde{\varphi})\nabla\cdot u, q) - \frac{1}{\lambda}(p,q) &= 0 \quad \forall\ q \in \mathcal{U},\\
(1-\kappa)\,(\varphi\sigma(u,p) : E_{lin}(u), \psi-\varphi)\, 2(\varphi\rho\nabla\cdot u, \psi-\varphi)&\\
+G_C\left(-\frac{1}{\epsilon}\varphi, \psi-\varphi\right) + G_C\epsilon\,(\nabla\varphi, \nabla(\psi-\varphi)) &\geq 0 \quad \forall\ \psi \in \mathcal{K}.
\end{aligned}
$$

Conclusions of the chapter

We derived quasi-static phase-field fracture modeling in mixed form to avoid locking effects in solids with high Poisson ratios. For the elasticity problem in mixed form, we proved an inf-sup condition independent of λ, and further, the well-posedness of the partial problem stated in Theorem 5. We discretized the pair (u, p) from the mixed elasticity problem with $Q_2^c Q_1^c$ elements. First numerical results were presented in Sections 5.4 and 5.5. For a natural pressure field solution, we modified the pressure equation, properly achieving zero pressure values inside the crack.

Based on the new model formulation in mixed form (Formulations 16 and 17, the following two chapters have different subjects: Chapter 7 contains a detailed description of conducted experiments in punctured rubber strips and fracture simulations based on the newly developed and modified phase-field fracture model in mixed form.

Chapter 6 focuses on solving the linear system arising in each Newton step. As a linear solver for the discretized mixed problem with three components, we used a sparse direct solver provided by UMFPACK [60, 59]. Chapter 6 presents a robust and efficient linear solver to increase computational efficiency. We precondition the solver GMRES with a Schur-type preconditioner. With the help of five numerical tests, we check the robustness of the solver.

Chapter 6

A robust & efficient linear solver

In this chapter, we develop a physics-based Schur-type preconditioner for robust and efficient solving of the mixed phase-field fracture model (Formulations 16 and 17 from Section 5.6). Our mixed model from Chapter 5 is a CVIS with three unknowns, which increases the overall workload compared to the primal phase-field fracture model from Chapter 4. Up to this chapter, we use a direct linear solver from UMFPACK [60, 59] provided in deal.II [9], to solve the linear system in each Newton step. The software library deal.II [9] offers scalable parallel algorithms for finite element computations [17]. Further, functionalities from other libraries can be used, such as Trilinos [90, 91], including the ML package [168, 74]. Direct solvers are robust, but iterative linear solvers are more attractive concerning memory, parallelization, and computational effort. Because the reliability of iterative techniques depends much more on the quality of the preconditioner than on the particular Krylov solver [148], efficient preconditioning at this point is an indispensable tool. We use GMRES as a linear solver preconditioned with the conjugate gradient method (CG) and algebraic multigrid (AMG) from the ML package.
First, in Section 6.1, we introduce a block diagonal preconditioner from Heister and Wick [88, 89] as a benchmark solver for the primal phase-field fracture problem. In Section 6.2, a robust iterative solver[1] for the mixed problem formulation from Chapter 5 is derived leveraging the saddle-point structure of the inner elasticity problem in mixed form with a physics-based preconditioner. Section 6.3 presents numerical results of five examples in two dimensions to confirm the robustness of the solver concerning the Poisson ratio, the discretization and regularization parameters.

6.1 Block-diagonal preconditioner of the primal problem

As a first preconditioner, we employ the block-diagonal preconditioner from Heister and Wick [88, 89] for the extrapolated primal phase-field fracture problem from Formulation 3 (Section 4.2). The primal

[1] The derivation of the Schur-type preconditioner and its basic implementation was developed mainly during a research stay of the author in February 2020 in the group of Prof. Dr. Timo Heister at Clemson University, SC, USA.

problem formulation has the following block structure:

$$\mathcal{M}_{\text{primal}} = \begin{pmatrix} M^{uu} & M^{u\varphi} \\ M^{\varphi u} & M^{\varphi\varphi} \end{pmatrix} = \begin{pmatrix} g(\tilde{\varphi})A_u & 0 \\ E & L \end{pmatrix},$$

where A_u is the mass matrix of the displacements, E contains the coupling terms of u and φ, and L is a Laplacian-like matrix of the phase-field function φ. We use the linear-in-time extrapolation with $\tilde{\varphi} := \tilde{\varphi}(\varphi^{n-1}, \varphi^{n-2})$ from Section 3.1.1. For the definition of the block entries of the primal problem formulation, we refer to Equation (3.7). As a preconditioning matrix, the following diagonal matrix is used:

$$P_{\text{primal}} := \begin{pmatrix} P^{uu} & P^{u\varphi} \\ P^{\varphi u} & P^{\varphi\varphi} \end{pmatrix} = \begin{pmatrix} g(\tilde{\varphi})A_u & 0 \\ 0 & L \end{pmatrix},$$

where

$$\begin{aligned} g(\tilde{\varphi})A_{u_{i,j}} &= (g(\tilde{\varphi})\sigma(\chi_j^u), E_{\text{lin}}(\chi_i^u)), \\ L_{i,j} &= (1-\kappa)(\chi_j^\varphi \sigma(u) : E_{\text{lin}}(u), \chi_i^\varphi) + 2\rho(\chi_j^\varphi \nabla \cdot u, \chi_i^\varphi) \\ &\quad + G_C \left(\frac{1}{\epsilon}(\chi_j^\varphi, \chi_i^\varphi) + \epsilon(\nabla\chi_j^\varphi, \nabla\chi_i^\varphi) \right), \end{aligned} \tag{6.1}$$

with ansatz functions $(\chi_j^u, \chi_j^\varphi) \in \mathcal{V}_h \times \mathcal{W}_h$ and test functions $(\chi_i^u, \chi_i^\varphi) \in \mathcal{V}_h \times \mathcal{K}_h$ for $i, j = 1, \dots, N$ with N total nodes. For right preconditioning of the linear system $\mathcal{M}\delta U = F$, the inverse of P_{primal} is given as:

$$P_{\text{primal}}^{-1} = \begin{pmatrix} (g(\tilde{\varphi})A_u)^{-1} & 0 \\ 0 & L^{-1} \end{pmatrix}.$$

The diagonal blocks correspond to the linear elasticity problem and a mixture of a Laplacian and mass-matrix of the phase-field [88]. The blocks $(g(\tilde{\varphi})A_u)^{-1}$ and L^{-1} are approximated with a single v-cycle of AMG, which is provided as part of the ML package [168, 74] of the Trilinos library [90, 91]. This approach has been tested in various numerical simulations; see [88, 184, 89, 98]. It serves to compare linear iteration numbers with the new solver for the mixed model presented in the next section.

Remark 24 (Matrix-free geometric multigrid solver for primal problem)**.** *Jodlbauer et al. [99, 98] recently developed a matrix-free geometric multigrid preconditioner for the primal phase-field fracture problem. The matrix-free approach allows overcoming the substantial memory requirements of standard, sparse matrix-based methods, particularly for high-order polynomial shape functions.*

6.2 Schur-type preconditioner of the mixed problem

Instead of solving the arising linear system in each Newton step directly we apply right preconditioning to reduce the condition number of the system matrix $\mathcal{M}$. A linear system $\mathcal{M}\delta U = F$ is called right

preconditioned with P^{-1}, if we substitute $\delta U = P^{-1}\vec{x}$, solve

$$\mathcal{M}P^{-1}\vec{x} = F,$$

and compute the solution vector δU via $\delta U = P^{-1}\vec{x}$. For fast convergence of GMRES, the condition number of $(\mathcal{M}P^{-1})$ should be smaller than the condition number of $\mathcal{M}$. With GMRES, the residual is minimized in each iteration over an increasing subspace. Further, the condition number of $(\mathcal{M}P^{-1})$ should be independent of discretization and regularization parameters.

6.2.1 Preconditioning the (3×3) linear system

The system matrix $\mathcal{M}_{\text{mixed}}$ of the mixed phase-field fracture from the modified mixed problem Formulation 16 or Formulation 17 (Section 5.6) has the following block structure[2]:

$$\mathcal{M}_{\text{mixed}} = \begin{pmatrix} M^{uu} & M^{up} & M^{u\varphi} \\ M^{pu} & M^{pp} & M^{p\varphi} \\ M^{\varphi u} & M^{\varphi p} & M^{\varphi\varphi} \end{pmatrix} = \begin{pmatrix} g(\tilde{\varphi})A_u & g(\tilde{\varphi})B^T & 0 \\ g(\tilde{\varphi})B & -\frac{1}{\lambda}M_p & 0 \\ E & F & L \end{pmatrix}, \tag{6.2}$$

where block A_u is the mass matrix of the displacements, B and B^T are symmetric off-diagonal blocks coupling u and p, and M_p is the mass matrix of the pressure variable. The blocks E, F and L from Equation (6.2) consist of the entries from the phase-field equation, where L is Laplacian-like. For the definition of the entries of the blocks A_u, M_p, E, F, and L, we refer to Appendix B, where the blocks correspond to M^{uu}, M^{pp}, $M^{\varphi u}$, $M^{\varphi p}$, and $M^{\varphi\varphi}$, respectively. If we reduce the (3×3) system from Equation (6.2) to the elasticity blocks, the saddle point structure is apparent:

$$\mathcal{M}_{(2\times2)} = \begin{pmatrix} g(\tilde{\varphi})A_u & g(\tilde{\varphi})B^T \\ g(\tilde{\varphi})B & -\frac{1}{\lambda}M_p \end{pmatrix}. \tag{6.3}$$

For this saddle-point problem with a penalty term, we use a block triangular preconditioner [25], first considered by Bramble and Pasciak in 1988 [42], and frequently used for Stokes-type problems [56] and the Oseen equations [104], where mesh-independent convergence can be observed. The non-symmetric block triangular matrix has the following form for preconditioning $\mathcal{M}_{(2\times2)}$:

$$P_{(2\times2)} = \begin{pmatrix} P^{uu} & P^{up} \\ P^{pu} & P^{pp} \end{pmatrix} = \begin{pmatrix} g(\tilde{\varphi})A_u & g(\tilde{\varphi})B^T \\ 0 & S_{(2\times2)} \end{pmatrix}, \tag{6.4}$$

where S is the Schur complement block exactly defined as

$$S_{(2\times2)} = -\frac{1}{\lambda}M_p - g(\tilde{\varphi})B^T \cdot [g(\tilde{\varphi})A_u]^{-1} \cdot g(\tilde{\varphi})B. \tag{6.5}$$

The implemented Schur complement is not build up with an expensive matrix-matrix multiplication. Instead, the fully dense inverse matrix (of a sparse matrix) is approximated properly; see Section 6.2.2 for further details. With the help of the preconditioning block matrix $P_{(2\times2)}$, the system matrix

[2] Parts of this section are accepted as a PAMM proceeding from the GAMM annual meeting, 2021 [86].

$\mathcal{M}_{(2\times2)}$ can be decomposed into a lower and an upper triangular matrix

$$\begin{aligned}\mathcal{M}_{(2\times2)} = \begin{pmatrix} g(\tilde{\varphi})A_u & g(\tilde{\varphi})B^T \\ g(\tilde{\varphi})B & -\frac{1}{\lambda}M_p \end{pmatrix} &= \begin{pmatrix} I & 0 \\ g(\tilde{\varphi})B(g(\tilde{\varphi})A_u)^{-1} & I \end{pmatrix} \begin{pmatrix} g(\tilde{\varphi})A_u & g(\tilde{\varphi})B^T \\ 0 & S_{(2\times2)} \end{pmatrix} \\ &= \begin{pmatrix} I & 0 \\ B(A_u)^{-1} & I \end{pmatrix} \begin{pmatrix} g(\tilde{\varphi})A_u & g(\tilde{\varphi})B^T \\ 0 & S_{(2\times2)} \end{pmatrix} \\ &= L_{(2\times2)} \cdot P_{(2\times2)}.\end{aligned} \tag{6.6}$$

It follows

$$\mathcal{M}_{(2\times2)} \cdot P^{-1}_{(2\times2)} = L_{(2\times2)},$$

where $L_{(2\times2)}$ is a well-conditioned (only one distinct eigenvalue equal to one [56]) lower triangular matrix, for which a method like GMRES would converge in at most two steps [25] if we assume an exact inverse $P^{-1}_{(2\times2)}$. According to Verfürth [170], for inf-sup stable discretizations of the linear elasticity problem, the Schur-complement is spectrally equivalent to the mass matrix, which yields

$$\hat{S}^{-1}_{(2\times2)} \coloneqq -\left(\left(\frac{1}{\lambda} + \frac{g(\tilde{\varphi})}{2\mu}\right) M_p\right)^{-1}. \tag{6.7}$$

Inverting the block matrix $P_{(2\times2)}$ with the simplified Schur block $\hat{S}^{-1}_{(2\times2)}$ yields the preconditioning matrix of the elasticity problem in mixed form:

$$\begin{aligned}\hat{P}^{-1}_{(2\times2)} &\coloneqq \begin{pmatrix} (g(\tilde{\varphi})A_u)^{-1} & -(g(\tilde{\varphi})A_u)^{-1} g(\tilde{\varphi})B^T \hat{S}^{-1}_{(2\times2)} \\ 0 & \hat{S}^{-1}_{(2\times2)} \end{pmatrix} \\ &= \begin{pmatrix} (g(\tilde{\varphi})A_u)^{-1} & -(A_u)^{-1} B^T \hat{S}^{-1}_{(2\times2)} \\ 0 & \hat{S}^{-1}_{(2\times2)} \end{pmatrix}.\end{aligned} \tag{6.8}$$

Wee need the inverses of the Laplacian-like matrix $(g(\tilde{\varphi})A_u)^{-1}$ and the Schur complement matrix $\hat{S}^{-1}_{(2\times2)}$ in the block preconditioning matrix $\hat{P}^{-1}_{(2\times2)}$.

Remark 25 (Differences to Stokes-type problems)**.** *Commonly, this Schur complement approach is used for Stokes-type problems and incompressible fluid dynamics, see, e.g. [148, 63]. Even if the elasticity part of the considered phase-field fracture problem has a similar saddle-point structure, aside from the phase-field function, material and regularization parameters complicate the situation: $\lambda \to \infty$ leads to a purely κ-dependent block $\hat{S}^{-1}_{(2\times2)}$, and $\kappa \to 0$ increases the condition number of the block $(g(\tilde{\varphi})A_u)^{-1}$ in the crack, where $\varphi = 0$.*

In the following, we transfer the idea of preconditioning with a Schur-type block matrix to the (3×3) system matrix $\mathcal{M}_{\text{mixed}}$ from Equation (6.2).

As a preconditioning matrix for $\mathcal{M}_{\text{mixed}}$, we define:

$$P_{\text{mixed}} = \begin{pmatrix} P^{uu} & P^{up} & P^{u\varphi} \\ P^{pu} & P^{pp} & P^{p\varphi} \\ P^{\varphi u} & P^{\varphi p} & P^{\varphi\varphi} \end{pmatrix} = \begin{pmatrix} g(\tilde{\varphi})A_u & g(\tilde{\varphi})B^T & 0 \\ 0 & S & 0 \\ 0 & 0 & L \end{pmatrix},$$

such that

$$\begin{aligned} \mathcal{M}_{\text{mixed}} &= \begin{pmatrix} g(\tilde{\varphi})A_u & g(\tilde{\varphi})B^T & 0 \\ g(\tilde{\varphi})B & -\frac{1}{\lambda}M_p & 0 \\ E & F & L \end{pmatrix} \\ &= \begin{pmatrix} I & 0 & 0 \\ B(g(\tilde{\varphi})A_u)^{-1} & I & 0 \\ E(g(\tilde{\varphi})A_u)^{-1} & -E(g(\tilde{\varphi})A_u)^{-1}B^T S^{-1} + FS^{-1} & I \end{pmatrix} \begin{pmatrix} g(\tilde{\varphi})A_u & g(\tilde{\varphi})B^T & 0 \\ 0 & S & 0 \\ 0 & 0 & L \end{pmatrix} \\ &= L_{(3\times 3)} \cdot P_{(3\times 3)}, \end{aligned}$$

where the Schur complement is defined in Equation (6.5). As for the reduced (2×2) system from Equation (6.6), we could decompose the system matrix $\mathcal{M}_{\text{mixed}}$ into a lower and an upper triangular matrix. The block L is a Laplacian-like block matrix of the phase-field transferred to a weighted mass matrix for $\epsilon \to 0$; see Equation (6.1). We ignore the coupling terms E and F of displacements and pressure with the phase-field variable in the preconditioning block matrix. As for the (2×2) problem, we reduce the inverse of the Schur complement $\hat{S}$ to a mass matrix of the pressure field as follows:

$$\hat{P}^{-1}_{\text{mixed}} = \begin{pmatrix} (g(\tilde{\varphi})A_u)^{-1} & -A_u^{-1}B^T\hat{S}^{-1} & 0 \\ 0 & \hat{S}^{-1} & 0 \\ 0 & 0 & L^{-1} \end{pmatrix},$$

with

$$\hat{S}^{-1} = -\left(\left(\frac{1}{\lambda} + \frac{g(\tilde{\varphi})}{2\mu}\right) M_p\right)^{-1}.$$

According to Silvester and Wathen [154], the chosen approximation $\hat{S}^{-1}$ via a mass matrix of the pressure field is spectrally equivalent to the exact definition of S^{-1} from Equation (6.5). For the incompressible limit $\nu = 0.5$, the Schur complement approximation remains

$$\hat{S}^{-1} = -\left(\frac{g(\tilde{\varphi})}{2\mu}M_p\right)^{-1} = -\frac{2\mu}{g(\tilde{\varphi})}\left(M_p\right)^{-1}.$$

With a spectrally equivalent approximation of S^{-1}, respectively, the condition number of $\mathcal{M}\hat{P}^{-1}_{\text{mixed}}$ can be assumed to be independent of h. Assembling $\hat{P}^{-1}_{\text{mixed}}$ requires the inverses of the blocks A_u^{-1}, $\hat{S}^{-1}$, and L^{-1}. In the following section, we propose proper preconditioning schemes for approximations of the three inverses, and the algorithm for building the preconditioner $\hat{P}^{-1}_{\text{mixed}}$.

6.2.2 Preconditioning algorithm

We have to approximate the exact inverses of A_u, $\hat{S}$ and L properly. In the construction of the approximations, it is essential to realize that iterative solvers do not need an element-by-element representation of the preconditioner but only the results of a matrix-vector product [110]. We approximate the blocks L^{-1} and $\hat{S}^{-1}$ in $\hat{P}^{-1}_{\text{mixed}}$ by one v-cycle of AMG. Multigrid methods can allow mesh-independent convergence [82], which remains unclear for our system with various limiting processes.
This section focus on the preconditioning algorithm for the GMRES solver which allows solving a system $\mathcal{M}\delta U = F$ with right preconditioning. We focus on the matrix-vector multiplication $\hat{P}^{-1}_{\text{mixed}}\vec{x}$ with $\vec{x} = (x_u, x_p, x_{\tilde{\varphi}})^T$ given as

$$\begin{aligned}\hat{P}^{-1}_{\text{mixed}}\vec{x} &= \begin{pmatrix} (g(\tilde{\varphi})A_u)^{-1} & -(g(\tilde{\varphi})A_u)^{-1}g(\tilde{\varphi})B^T\hat{S}^{-1} & 0 \\ 0 & \hat{S}^{-1} & 0 \\ 0 & 0 & L^{-1} \end{pmatrix} \begin{pmatrix} x_u \\ x_p \\ x_\varphi \end{pmatrix} \\ &= \begin{pmatrix} (g(\tilde{\varphi})A_u)^{-1}x_u - (g(\tilde{\varphi})A_u)^{-1}g(\tilde{\varphi})B^T\hat{S}^{-1}x_p \\ \hat{S}^{-1}x_p \\ L^{-1}x_\varphi \end{pmatrix}. \end{aligned} \tag{6.9}$$

The resulting vector in Equation (6.9) is built up step by step in the implementation. The key point is to recognize that we do not need the actual elements of the matrix $\hat{P}^{-1}_{\text{mixed}}$. In deal.II [9, 11], the matrices and preconditioners given to solver classes need a `vmult()` member function [61]. In the following algorithm, we list the solving steps with right preconditioning. The matrix-vector product to build $\hat{P}^{-1}_{\text{mixed}}\vec{x}$, is done in the member function `vmult()` in a solver class.

Algorithm 5 (Evaluation of $\hat{P}^{-1}_{\text{mixed}}\vec{x}$)**.**

1. *Approximate* $\hat{S}^{-1}$ *via AMG and compute* $q \coloneqq \hat{S}^{-1}x_p$*;*
2. *Compute* $r \coloneqq x_u - g(\tilde{\varphi})B^T q$*;*
3. *Approximate* $(g(\tilde{\varphi})A_u)^{-1}$ *via CG preconditioned with AMG and compute* $s \coloneqq (g(\tilde{\varphi})A_u)^{-1}r$*;*
4. *Approximate* L^{-1} *via AMG and compute* $t \coloneqq L^{-1}x_\varphi$*.*

We evaluated the expression $(g(\tilde{\varphi})A_u)^{-1}g(\tilde{\varphi})B^T\hat{S}^{-1}$ from right to left to avoid matrix-matrix products. Later, in Figures 6.7 and 6.11, Step 1 from Algorithm 5 is modified such that the approximation of $\hat{S}^{-1}$ is also computed via a CG solver preconditioned with one v-cycle AMG.
For the used solvers GMRES CG, and AMG from the ML package [168, 74] of the Trilinos library [90, 91], the following tolerances are chosen:

- GMRES with a relative tolerance of 10^{-5} and maximal 700 iterations;
- CG with a relative tolerance of 10^{-6} and maximal 200 iterations.

Recall that the linear system is solved at each step of Newton's method with an absolute tolerance of 10^{-7}. We use four CPUs on a single machine with four E7 v3 CPUs for all computations. The following section shows numerical results based on the new preconditioner for the mixed phase-field fracture problem for simulating fractures in compressible and incompressible solids efficiently.

6.3 Numerical results

This section substantiates the proposed iterative solver by five numerical test configurations in two spatial dimensions. To facilitate the readability of the tables from the next sections, we give an overview, how to read them. For the five tests, we conduct numerical studies with different emphases: we investigate robustness in h, κ, λ, ϵ, we use different models ('primal' from Chapter 4 versus 'mixed' from Chapter 5) and different finite element discretizations. In the top row of each table, we summarize the key aspect of the current numerical study: the name of the example, the observed task, the modeling, and – if required – further test-specific settings. The white rows in the tables correspond to results based on the primal phase-field fracture model and the solver from Section 6.1 or to reference values. The colored rows belong to computations based on the mixed model and $Q_2^c Q_1^c Q_1^c$ for $\nu = 0.2$ (yellow), $\nu = 0.4999$ (blue) and $\nu = 0.5$ (red). Green rows mark computations with stabilized equal-order elements for $\nu = 0.2$, pink rows are used for $\nu = 0.5$ and $\epsilon = 2\,h$ (otherwise ϵ is fixed). Further, it holds; the stronger the color, the finer the mesh.
The five test configurations with attributes are given in the following:

1. Section 6.3.1: a hanging block similar to [101] for $\nu = 0.2, 0.4999$ and 0.5, uniform mesh refinement, mixed ($Q_2^c Q_1^c Q_1^c$) versus primal ($Q_2^c Q_1^c$), ϵ fixed, $\kappa = 10^{-8}$;

2. Section 6.3.2: a hanging block with an initial slit for $\nu = 0.2, 0.4999$ and 0.5, uniform mesh refinement, mixed ($Q_2^c Q_1^c Q_1^c$) versus primal ($Q_2^c Q_1^c$), ϵ fixed and $\epsilon = 2\,h$, $\kappa = 10^{-2}, 10^{-5}, 10^{-8}$;

3. Section 6.3.3: Sneddon's test [155, 156] for $\nu = 0.2, 0.4999$ and 0.5, uniform mesh refinement, mixed ($Q_2^c Q_1^c Q_1^c$ and $Q_1^c Q_1^{\text{stab}} Q_1^c$), ϵ fixed and $\epsilon = 2\,h$, $\kappa = 10^{-2}, 10^{-8}$;

4. Section 6.3.4: Sneddon's test layered [22] for $\nu = 0.2, 0.4999$ and 0.5 in the inner domain, adaptive mesh refinement (geometric), mixed ($Q_2^c Q_1^c Q_1^c$ and $Q_1^c Q_1^{\text{stab}} Q_1^c$), $\epsilon = h$, $\kappa = 10^{-2}, 10^{-8}$;

5. Section 6.3.5: single-edge notched tension test for $\nu = 0.3, 0.45$, and 0.49, adaptive mesh refinement (predictor-corrector scheme), mixed ($Q_2^c Q_1^c Q_1^c$), $\epsilon = 4\,h$, $\kappa = 10^{-8}$.

With the help of numerical studies, we check the robustness of the new Schur-type preconditioner via evaluating the required number of linear iterations for different mesh sizes, Poisson ratios, κ, and different finite element discretizations. Besides, we discuss challenges and point out difficulties.

Remark 26 (Model problem 'primal' versus 'mixed')**.** *The results marked with 'primal' are based on Formulation 3 from Section 4.2 and solved with the block preconditioner from Section 6.1. All numerical tests of the hanging block, hanging block with slit, and single-edge notched shear test with the attribute 'mixed' are based on Formulation 16, and the 'mixed' numerical tests of Sneddon's test configurations (pressurized fracture) are based on Formulation 17, both from Section 5.6. We use the AT_2 functional and no stress splitting in the current chapter.*

6.3.1 Hanging block

As a first stationary test, we consider a hanging block similar to [101], where a constant body force is given. We used this test configuration already in Section 5.4 tests on locking effects. A square of length 4.0 mm is fixed on the top boundary, and the body is deformed by the acting force, as displayed in Figure 6.1. As material parameters, we determine $G_C = 50.0\,\text{N/mm}$, Young's modulus

$E = 10^{-3}$ MPa, and μ and λ depend on the chosen Poisson ratio. This example allows testing the robustness of the preconditioned linear solver for the elasticity problem in mixed form without any fracture ($\varphi = 1$ on the whole domain).

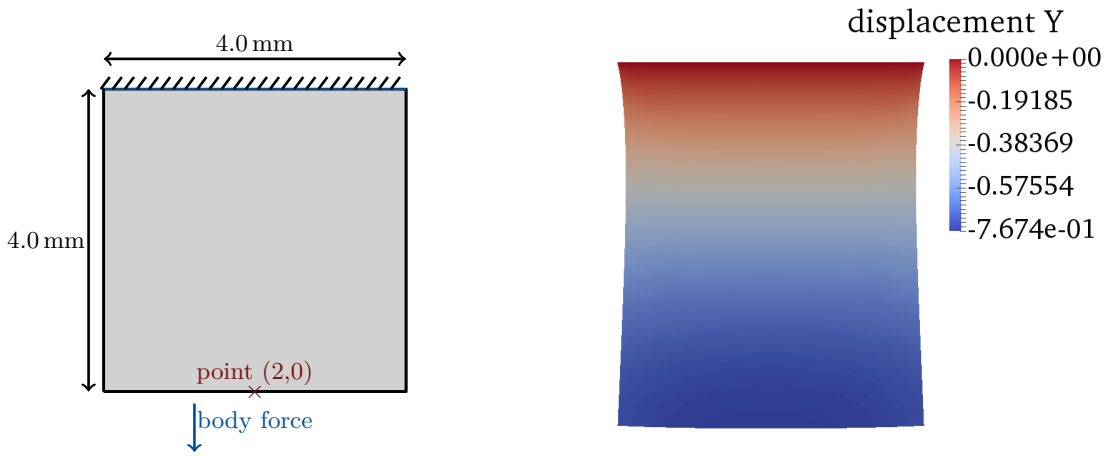

Figure 6.1: Left: geometry and boundary conditions of a hanging block. Right: displacement solution in the y-direction of a hanging block for $\nu = 0.2$ and the finest computation from Table 6.1. Applied force $f = -10^{-4}$ N/mm^2.

As a quantity of interest, the displacement in the point $(2, 0)$ in the y-direction is evaluated and denoted as $u_y(2, 0)$ in Table 6.1. In Table 6.1, the numerical results for a hanging black are given. We confirm the robustness of the linear solver (column labeled with ⌀lin) for different uniform refinement levels. For this study, the crack width ϵ is fixed (which is not relevant for this test case), and we refine the mesh size h for three Poisson ratios $\nu = 0.2, 0.4999$, and $\nu = 0.5$ (incompressible limit). In yellow, blue, and red, we depict the results for the mixed problem, for three Poisson ratios, respectively, and $Q_2^c Q_1^c Q_1^c$ elements for (u, p, φ). In the non-colored rows, the results based on the primal Formulation 3 from Section 4.2, and the preconditioner proposed in Section 6.1, are given for comparison. There, $Q_2^c Q_1^c$ elements are used for (u, φ) for a fairer comparison between the two models (problem size and discretization). In short notation, we use 'primal' and 'mixed' for the two models from Chapters 4 and 5, respectively. Naturally, we do not get results with the primal problem formulation for the incompressible limit. The listed linear and CG iterations values are average values for the second and last computed quasi-time step. The number of Newton/Active set steps (#AS) is also listed for the last computed step. In total, two quasi-time steps are computed. We observe a stable number of three Newton iterations. Further, the number of CG iterations (⌀CG) for approximating $(g(\tilde{\varphi})A_u)^{-1}$ increases with an increasing problem size (#dof) due to AMG not being h-independent. The results in the linear solver (GMRES, denoted as ⌀lin) are promising for the three considered Poisson ratios with less than nine iterations on average per Newton/AS step. We confirm robustness in h of the linear solver for all three settings of ν, which also implies the robustness in λ. In the last column of Table 6.1, the computed maximal displacement in the lowest point $(2, 0)$ in the y-direction is naturally decreasing with a higher Poisson ratio.

Hanging block: robustness in h and λ; mixed versus primal; $\kappa = 10^{-8}$									
model	FE	ν	h	ϵ	#dof	∅lin	∅CG	#AS	$u_y(2,0)$
mixed	$Q_2^cQ_1^cQ_1^c$	0.2	0.353	0.707	2 756	5	17	3	-0.7673
mixed	$Q_2^cQ_1^cQ_1^c$	0.2	0.176	0.707	10 628	5	19	3	-0.7674
mixed	$Q_2^cQ_1^cQ_1^c$	0.2	0.088	0.707	41 732	6	25	3	-0.7674
mixed	$Q_2^cQ_1^cQ_1^c$	0.2	0.044	0.707	165 380	6	30	4	-0.7674
mixed	$Q_2^cQ_1^cQ_1^c$	0.2	0.022	0.707	658 436	5	37	3	-0.7674
mixed	$Q_2^cQ_1^cQ_1^c$	0.2	0.011	0.707	2 627 588	6	64	3	-0.7674
primal [87]	$Q_2^cQ_1^c$	0.2	0.353	0.707	2 467	1	-	3	-0.7673
primal [87]	$Q_2^cQ_1^c$	0.2	0.176	0.707	9 539	1	-	3	-0.7674
primal [87]	$Q_2^cQ_1^c$	0.2	0.088	0.707	37 507	5	-	3	-0.7674
primal [87]	$Q_2^cQ_1^c$	0.2	0.044	0.707	148 739	5	-	3	-0.7674
primal [87]	$Q_2^cQ_1^c$	0.2	0.022	0.707	592 387	5	-	3	-0.7674
primal [87]	$Q_2^cQ_1^c$	0.2	0.011	0.707	2 364 419	6	-	3	-0.7674
mixed	$Q_2^cQ_1^cQ_1^c$	0.4999	0.353	0.707	2 756	6	16	3	-0.5068
mixed	$Q_2^cQ_1^cQ_1^c$	0.4999	0.176	0.707	10 628	6	17	3	-0.5073
mixed	$Q_2^cQ_1^cQ_1^c$	0.4999	0.088	0.707	41 732	8	24	3	-0.5075
mixed	$Q_2^cQ_1^cQ_1^c$	0.4999	0.044	0.707	165 380	8	28	3	-0.5076
mixed	$Q_2^cQ_1^cQ_1^c$	0.4999	0.022	0.707	658 436	8	40	3	-0.5077
mixed	$Q_2^cQ_1^cQ_1^c$	0.4999	0.011	0.707	2 627 588	8	63	3	-0.5077
primal [87]	$Q_2^cQ_1^c$	0.4999	0.353	0.707	2 467	1	-	3	-0.5008
primal [87]	$Q_2^cQ_1^c$	0.4999	0.176	0.707	9 539	1	-	3	-0.5046
primal [87]	$Q_2^cQ_1^c$	0.4999	0.088	0.707	37 507	5	-	3	-0.5063
primal [87]	$Q_2^cQ_1^c$	0.4999	0.044	0.707	148 739	5	-	3	-0.5071
primal [87]	$Q_2^cQ_1^c$	0.4999	0.022	0.707	592 387	5	-	3	-0.5075
primal [87]	$Q_2^cQ_1^c$	0.4999	0.011	0.707	2 364 419	6	-	3	-0.5076
mixed	$Q_2^cQ_1^cQ_1^c$	0.5	0.353	0.707	2 756	4	16	3	-0.5066
mixed	$Q_2^cQ_1^cQ_1^c$	0.5	0.176	0.707	10 628	4	18	3	-0.5071
mixed	$Q_2^cQ_1^cQ_1^c$	0.5	0.088	0.707	41 732	7	24	3	-0.5074
mixed	$Q_2^cQ_1^cQ_1^c$	0.5	0.044	0.707	165 380	6	27	3	-0.5075
mixed	$Q_2^cQ_1^cQ_1^c$	0.5	0.022	0.707	658 436	6	40	3	-0.5075
mixed	$Q_2^cQ_1^cQ_1^c$	0.5	0.011	0.707	2 627 588	6	63	3	-0.5076

Table 6.1: Hanging block similar to [101] for $\nu = 0.2, 0.4999$ and 0.5, uniform mesh refinement, mixed ($Q_2^cQ_1^cQ_1^c$) versus primal ($Q_2^cQ_1^c$), ϵ fixed, $\kappa = 10^{-8}$. Problem size in #dof, average number of linear GMRES iterations (∅lin) per Newton/active set (AS) step, the average number of inner CG iterations (∅CG) per linear iteration, number of Newton/AS (#AS), and goal functional displacement in a certain point ($u_y(2,0)$ in mm). Applied force $f = -10^{-4}\,\mathrm{N/mm^2}$.

6.3.2 Hanging block with initial slit

As the second test configuration, we modify the hanging block test from the previous section such that we have an initial geometrical slit of length 2.0 mm with an interpolated initial condition $\varphi = 0$ in the crack; see Figure 6.2. The force acting on the hanging block is reduced to $f = -8.0 \cdot 10^{-7}\,\mathrm{N/mm^2}$. In Figure 6.2 on the right, the solution of the phase-field function is given on the deformed block for

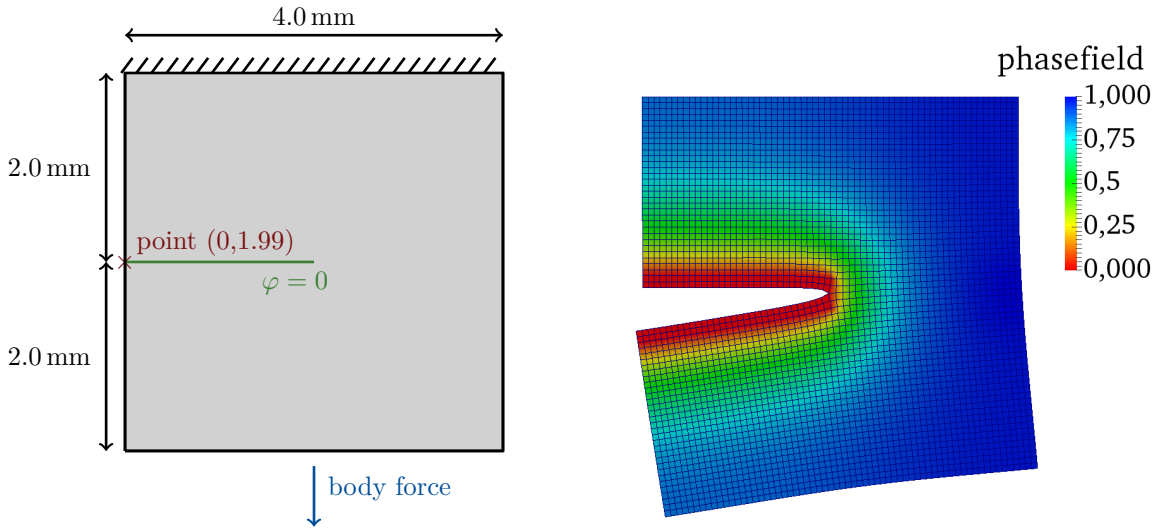

Figure 6.2: Left: geometry and boundary conditions of a hanging block with a slit. Right: deformed geometry with phase-field solution; 41 924 dof. In the geometrically pre-refined slit we interpolate $\varphi = 0$ as an initial condition. No propagating crack. Applied force $f = -8.0 \cdot 10^{-7}\,\mathrm{N/mm^2}$.

$\nu = 0.2$ on a uniform refined mesh with 41 924 dof. We evaluate the displacement in the y-direction in a certain point $(0, 1.99)$ on the lower opening crack lip.
Tables 6.2 and 6.3 show analogously to Table 6.1 the iteration numbers of numerical tests for the hanging block with a slit, based on the preconditioned linear solver for the mixed and primal problem formulation for three Poisson ratios ν, and h refinement. Here, we use $\kappa = 10^{-2}$ to avoid observed effects for small κ on the CG solver for the block $(g(\tilde{\varphi})A_u)^{-1}$. For the incompressible limit $\nu = 0.5$, Table 6.3 presents the results for ϵ fixed, and further in the pink rows, results for $\epsilon = 2\,h$ are listed. The nearly constant number of GMRES iterations confirms the robustness in ϵ for $\nu = 0.5$, tested for the hanging block with a slit on five levels of uniform refined meshes; see the last five rows in Table 6.3.

Remark 27 (High iteration number in the primal-dual active set method)**.** *In Table 6.3 in the pink rows, many active set/Newton iterations are required for $\epsilon \to 0$. Here, not the Poisson ratio is responsible, but the refinement in h and ϵ. For finer meshes with small ϵ, the active set algorithm oscillates between a certain non-equal number of active nodes from the constraint. This effect leads to high total Newton iterations, even if the Newton algorithm converges.*

To check the impact of κ, we conduct tests with three mesh refinements, three Poisson ratios ν, and three settings of $\kappa = 10^{-2}, 10^{-5}, 10^{-8}$. We focus on the impact of κ on the number of inner CG iterations. In Table 6.4, slightly more linear iterations are required for finer meshes and higher Poisson ratios, but independent of κ. The number of linear iterations on average per Newton step has an upper bound of 12 iterations. The number of CG iterations does not depend significantly on

Hanging block slit: robustness in h and λ; mixed versus primal; $\kappa = 10^{-2}$									
model	FE	ν	h	ϵ	#dof	∅lin	∅CG	#AS	$u_y(0, 1.99)$
mixed	$Q_2^cQ_1^cQ_1^c$	0.2	0.353	0.707	2 804	4	24	3	-0.3871
mixed	$Q_2^cQ_1^cQ_1^c$	0.2	0.176	0.707	10 724	4	25	3	-0.5189
mixed	$Q_2^cQ_1^cQ_1^c$	0.2	0.088	0.707	41 924	10	32	32	-0.4919
mixed	$Q_2^cQ_1^cQ_1^c$	0.2	0.044	0.707	165 764	4	36	31	-0.0825
mixed	$Q_2^cQ_1^cQ_1^c$	0.2	0.022	0.707	659 204	8	50	53	-0.0824
mixed	$Q_2^cQ_1^cQ_1^c$	0.2	0.011	0.707	2 629 124	8	79	38	-0.0815
primal [87]	$Q_2^cQ_1^c$	0.2	0.353	0.707	2 507	1	-	3	-0.3368
primal [87]	$Q_2^cQ_1^c$	0.2	0.176	0.707	9 619	1	-	3	-0.4479
primal [87]	$Q_2^cQ_1^c$	0.2	0.088	0.707	37 667	5	-	5	-0.4434
primal [87]	$Q_2^cQ_1^c$	0.2	0.044	0.707	149 059	5	-	38	-0.0818
primal [87]	$Q_2^cQ_1^c$	0.2	0.022	0.707	593 027	7	-	35	-0.0820
primal [87]	$Q_2^cQ_1^c$	0.2	0.011	0.707	2 365 699	8	-	35	-0.0810
mixed	$Q_2^cQ_1^cQ_1^c$	0.4999	0.353	0.707	2 804	10	24	3	-0.2181
mixed	$Q_2^cQ_1^cQ_1^c$	0.4999	0.176	0.707	10 724	9	25	3	-0.2869
mixed	$Q_2^cQ_1^cQ_1^c$	0.4999	0.088	0.707	41 924	6	32	29	-0.1295
mixed	$Q_2^cQ_1^cQ_1^c$	0.4999	0.044	0.707	165 764	7	38	36	-0.0576
mixed	$Q_2^cQ_1^cQ_1^c$	0.4999	0.022	0.707	659 204	10	52	38	-0.0585
mixed	$Q_2^cQ_1^cQ_1^c$	0.4999	0.011	0.707	2 629 124	11	80	41	-0.0578
primal [87]	$Q_2^cQ_1^c$	0.4999	0.353	0.707	2 507	1	-	3	-0.2077
primal [87]	$Q_2^cQ_1^c$	0.4999	0.176	0.707	9 619	1	-	3	-0.2788
primal [87]	$Q_2^cQ_1^c$	0.4999	0.088	0.707	37 667	4	-	4	-0.2789
primal [87]	$Q_2^cQ_1^c$	0.4999	0.044	0.707	149 059	5	-	31	-0.0587
primal [87]	$Q_2^cQ_1^c$	0.4999	0.022	0.707	593 027	7	-	31	-0.0583
primal [87]	$Q_2^cQ_1^c$	0.4999	0.011	0.707	2 365 699	8	-	34	-0.5076

Table 6.2: A hanging block with an initial slit for $\nu = 0.2$ and $\nu = 0.4999$, uniform mesh refinement, mixed ($Q_2^cQ_1^cQ_1^c$) versus primal ($Q_2^cQ_1^c$), ϵ fixed, $\kappa = 10^{-2}$. Problem size in #dof, average number of linear GMRES iterations (∅lin) per Newton/active set (AS) step, the average number of inner CG iterations (∅CG) per linear iteration, number of Newton/AS (#AS), and goal functional displacement in a certain point ($u_y(0, 1.99)$). Applied force $f = -8 \cdot 10^{-7}\,\mathrm{N/mm^2}$.

Hanging block slit: robustness in h, λ and ϵ for $\nu = 0.5$; mixed; $\kappa = 10^{-2}$									
model	FE	ν	h	ϵ	#dof	∅lin	∅CG	#AS	$u_y(0, 1.99)$
mixed	$Q_2^c Q_1^c Q_1^c$	0.5	0.353	0.707	2 804	9	23	3	-0.0578
mixed	$Q_2^c Q_1^c Q_1^c$	0.5	0.176	0.707	10 724	9	24	3	-0.2835
mixed	$Q_2^c Q_1^c Q_1^c$	0.5	0.088	0.707	41 924	7	32	33	-0.0955
mixed	$Q_2^c Q_1^c Q_1^c$	0.5	0.044	0.707	165 764	6	37	38	-0.0584
mixed	$Q_2^c Q_1^c Q_1^c$	0.5	0.022	0.707	658 436	9	53	36	-0.0583
mixed	$Q_2^c Q_1^c Q_1^c$	0.5	0.011	0.707	2 629 124	11	80	39	-0.0579
mixed	$Q_2^c Q_1^c Q_1^c$	0.5	0.353	0.707	2 804	9	23	3	-0.2166
mixed	$Q_2^c Q_1^c Q_1^c$	0.5	0.176	0.353	10 724	7	25	4	-0.1033
mixed	$Q_2^c Q_1^c Q_1^c$	0.5	0.088	0.176	41 924	6	30	14	-0.0701
mixed	$Q_2^c Q_1^c Q_1^c$	0.5	0.044	0.088	165 764	5	36	109	-0.0572
mixed	$Q_2^c Q_1^c Q_1^c$	0.5	0.022	0.044	658 436	7	40	805	-0.0516

Table 6.3: A hanging block with an initial slit for $\nu = 0.5$, uniform mesh refinement, mixed ($Q_2^c Q_1^c Q_1^c$) versus primal ($Q_2^c Q_1^c$), ϵ fixed and $\epsilon = 2\,h$, $\kappa = 10^{-2}$. Problem size in #dof, average number of linear GMRES iterations (∅lin) per Newton/active set (AS) step, the average number of inner CG iterations (∅CG) per linear iteration, number of Newton/AS (#AS), and goal functional displacement in a certain point ($u_y(0, 1.99)$). Applied force $f = -8 \cdot 10^{-7}\,\mathrm{N/mm^2}$.

the size of κ for this test setup. Further, the required CG iterations seem to be independent of λ but sensitive to the mesh size. Aside from the robustness in h and λ, we confirm the robustness in κ for the hanging block test with a slit.

6.3.3 Sneddon's pressure-driven cavity

As a third example, we consider a benchmark test [153] (already described in Section 4.5), which is motivated by the book of Sneddon [155] and Sneddon and Lowengrub [156]. We restrict ourselves to a 1d fracture C on a 2d domain $\Omega = (-10, 10)^2$ as depicted on the left in Figure 6.3 (same as Figure 4.2). In this domain, an initial crack with length $2l_0 = 2.0$ and thickness h of two cells is prescribed with the help of the phase-field function φ, i.e., $\varphi = 0$ in the crack and $\varphi = 1$ elsewhere. As boundary conditions, the displacements u are set to zero on $\partial\Omega$. We use homogeneous Neumann conditions for the phase-field variable, i.e., $\epsilon \partial_n \varphi = 0$ on $\partial\Omega$. The driving force is given by a constant pressure $\rho = 10^{-3}\,\mathrm{Pa}$ in the interior of the crack. An overview of the parameter setting is given in Figure 6.3 on the right.

Two quantities of interest are discussed, similar to Section 4.5: the crack opening displacement (COD) and the total crack volume (TCV). The analytical solution (from [156]) can be computed via

$$\mathrm{COD}_{\mathrm{ref}} = 2\frac{p l_0}{E'}\left(1 - \frac{x^2}{l_0^2}\right)^{\frac{1}{2}}, \tag{6.10}$$

where $E' \coloneqq \frac{E}{1-\nu^2}$, E is the Young modulus and ν is the Poisson ratio. The TCV can be computed numerically with

$$\mathrm{TCV} = \int_\Omega u(x, y) \cdot \nabla\varphi(x, y) d(x, y).$$

Hanging block slit: robustness in κ; mixed					
h	κ	ν	⌀lin	⌀CG	#AS
0.044	10^{-2}	0.2	4	36	31
0.044	10^{-5}	0.2	5	37	33
0.044	10^{-8}	0.2	4	37	32
0.044	10^{-2}	0.4999	6	38	36
0.044	10^{-5}	0.4999	5	38	33
0.044	10^{-8}	0.4999	5	39	35
0.044	10^{-2}	0.5	6	38	38
0.044	10^{-5}	0.5	5	39	35
0.044	10^{-8}	0.5	6	38	37
0.022	10^{-2}	0.2	5	37	3
0.022	10^{-5}	0.2	7	51	34
0.022	10^{-8}	0.2	7	50	35
0.022	10^{-2}	0.4999	8	40	3
0.022	10^{-5}	0.4999	9	52	35
0.022	10^{-8}	0.4999	9	52	39
0.022	10^{-2}	0.5	9	53	36
0.022	10^{-5}	0.5	8	52	33
0.022	10^{-8}	0.5	9	52	53
0.011	10^{-2}	0.2	8	79	38
0.011	10^{-5}	0.2	9	69	37
0.011	10^{-8}	0.2	9	69	36
0.011	10^{-2}	0.4999	8	80	34
0.011	10^{-5}	0.4999	11	69	37
0.011	10^{-8}	0.4999	11	70	35
0.011	10^{-2}	0.5	11	80	39
0.011	10^{-5}	0.5	10	69	35
0.011	10^{-8}	0.5	12	70	41

Table 6.4: Hanging block with initial geometrical and phase-field slit. Study for $Q_2^c Q_1^c Q_1^c$ with three uniform refinement levels, $\epsilon = 0.707\,\text{mm}$ fixed, and 165 380 dof on three settings of $\kappa = 10^{-2}, 10^{-5}, 10^{-8}$ to understand the sensitivity of the inner CG solver for $(A_u)^{-1}$. Average number of linear GMRES iterations (⌀lin) per Newton/active set (AS) step, the average number of inner CG iterations (⌀CG) per linear iteration, number of Newton/AS (#AS). Applied force $f = -8 \cdot 10^{-7}\,\text{N/mm}^2$.

ν	COD_{max} (reference)	TCV_{2d} (reference)
0.2	1.9200×10^{-3}	6.03186×10^{-3}
0.4999	1.5001×10^{-3}	4.71302×10^{-3}
0.5	1.5000×10^{-3}	4.71239×10^{-3}

Table 6.5: Manufactured reference values of the crack opening displacement (COD_{max}) and the total crack volume (TCV_{2d}) from [153], and given in Equation (6.10) for an infinite domain.

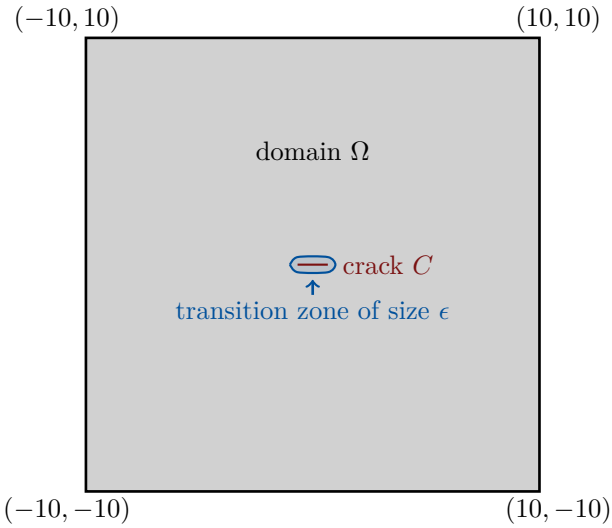

Parameter	value
Ω	$(-10, 10)^2$
h	test-dependent
l_0	1.0
G_C	1.0 kN/mm
E	1.0MPa
μ	0.42 N/mm^2
λ	test-dependent
ν	$0.2, 0.4999, 0.5$
ρ	10^{-3} Pa

Figure 6.3: Left: geometry of the two-dimensional Sneddon's test in 2d. Domain of size $(-10, 10)^2$ with a pressurized fracture. Right: setting of material and numerical parameters for Sneddon's benchmark test.

The analytical solution (from [156]) is given by

$$\mathrm{TCV}_{\mathrm{ref}} = \frac{2\pi p l_0^2}{E'}.$$

In Table 6.5, the manufactured reference values (on an infinite domain) of COD and TCV are given for the three considered Poisson ratios.

To reduce the computational workload, and as an alternative to $Q_2^c Q_1^c Q_1^c$ finite elements, we use equal-order finite elements. For a stable formulation with equal-order elements, we stabilize the elasticity problem in mixed form mainly with an h-dependent Laplacian term $(\nabla p, \nabla q)$. The idea of a consistent stabilization is that the additional terms vanish if we insert the continuous solution $U := (u, p, \varphi)^T$, which is well-known for incompressible fluid flow; see for example [151, Chapter 3] or [141, Chapter 6.2]. It yields full Galerkin orthogonality. Standard literature on streamline upwind/Petrov Galerkin formulations is given, e.g., by Brooks and Hughes [46], and Texduyar et al. [165]. The elasticity problem in mixed form consistently stabilized is given in the following:

Formulation 18 (Consistent stabilization for equal-order discretization, pressure-driven)**.**
Let $\rho \in L^\infty(\Omega)$ be given. Given the initial data $\varphi^{n-1}, \varphi^{n-2} \in \mathcal{K}$. Find $u := u^n \in \mathcal{V}$, $p := p^n \in \mathcal{U}$ and

$\varphi := \varphi^n \in \mathcal{K}$ for incremental steps $n = 1, 2, \ldots, N$ with $\{u, p, \varphi\} \in \mathcal{V} \times \mathcal{U} \times \mathcal{K}$ such that

$$(g(\tilde{\varphi})\sigma(u,p), E_{lin}(w)) + (\tilde{\varphi}^2\rho, \nabla \cdot w) = 0 \quad \forall w \in \mathcal{V},$$

$$g(\tilde{\varphi})(\nabla \cdot u, q) - \frac{1}{\lambda}(p,q) - \alpha h^2(\nabla p, \nabla q) - \alpha h^2(2\mu g(\tilde{\varphi})E_{lin}(u) : E_{lin}(u), \nabla q) = 0 \quad \forall q \in \mathcal{U},$$

$$\begin{aligned}(1-\kappa)(\varphi\sigma(u,p) : E_{lin}(u), \psi - \varphi) + 2(\varphi\rho\nabla \cdot u, \psi - \varphi) \\ + G_C\Big(-\frac{1}{\epsilon}(1-\varphi, \psi-\varphi) + \epsilon(\nabla\varphi, \nabla(\psi-\varphi))\Big) \geq 0 \quad \forall \psi \in \mathcal{K},\end{aligned}$$

where h is the cell-diameter, ρ is the given pressure for Sneddon's test, and $\alpha > 0$ has to be chosen properly. We chose $\alpha = 1$.

The corresponding block entries of the Jacobian based on Formulation 18 are given in Appendix B.1.

Table 6.6 shows the numerical results on uniformly refined meshes for Sneddon's test for $Q_2^c Q_1^c Q_1^c$ and stabilized equal-order elements ($Q_1^c Q_1^{\text{stab}} Q_1^c$).
In Table 6.6, for $\kappa = 10^{-8}$, the average number of CG iterations increases with a decreasing mesh size. We observe an increase in the CG iteration numbers in particular for the incompressible limit $\nu = 0.5$ and finer meshes, where we finally do not get convergence in the solver for smaller h. Already for $\nu = 0.4999$ and a problem size of less than 300 000 dof, the average number of CG iterations is above 100.

Remark 28 (Difficulties considering small κ)**.** *In Table 6.6, compared to Table 6.8, we can evaluate the impact of the setting of κ. We compute Sneddon's test for different mesh sizes h, fixed bandwidth ϵ, for three Poisson ratios $\nu = 0.2, 0.4999$, and $\nu = 0.5$, and for three sizes of $\kappa = 10^{-2}, \kappa = 10^{-5}, \kappa = 10^{-8}$. Values towards 1 for κ are critical, but from a numerical perspective, we use high values for κ to understand large numbers of CG iteration numbers approximating the ill-conditioned matrix block $(g(\tilde{\varphi})A_u)^{-1}$, where $\varphi = 0$. The number of required iterations for this test case depends on the size of κ. Further, we observe an increased number of CG iterations for high Poisson ratios. The number of GMRES and AS iterations do not differ significantly for different κ.*

To retrace the mentioned difficulties from Remark 28 we consider the preconditioning matrix with limiting values for κ and λ: $\kappa \to 0$, and $\lambda \to \infty$. This would yield the following block behavior in the crack nodes where $\varphi = 0$:

$$\hat{P}^{-1}_{\text{mixed}} = \begin{pmatrix} (g(\tilde{\varphi})A_u)^{-1} & -A_u^{-1}B^T\hat{S}^{-1} & 0 \\ 0 & \hat{S}^{-1} & 0 \\ 0 & 0 & L^{-1} \end{pmatrix} = \begin{pmatrix} \to\infty & -A_u^{-1}B^T\hat{S}^{-1} & 0 \\ 0 & \to\infty & 0 \\ 0 & 0 & L^{-1} \end{pmatrix}.$$

If we consider an incompressible solid and sufficiently small κ, we do have a critical block $(g(\tilde{\varphi})A_u^{-1}$, and an ill-conditioned Schur-complement block. This observation is confirmed by the numerical results from Table 6.7, where a CG solver preconditioned with AMG is used to approximate $\hat{S}^{-1}$. The numerical results in Table 6.7 are based on the same tests as in Table 6.6 but for $\nu = 0.4999$ and $\nu = 0.5$. The number of linear iterations is moderate, and maximum six CG iterations are needed for $\hat{S}^{-1}$.

Sneddon's test: robustness in h, λ, ϵ; $\kappa = 10^{-8}$; mixed									
FE	ν	h	ϵ	#dof	∅lin	∅CG	#AS	$\text{COD}_{\max}$	TCV
$Q_2^c Q_1^c Q_1^c$	0.2	0.707	1.414	16 484	3	26	4	0.00282	0.0240
$Q_2^c Q_1^c Q_1^c$	0.2	0.353	1.414	64 964	6	28	6	0.00270	0.0189
$Q_2^c Q_1^c Q_1^c$	0.2	0.176	1.414	257 924	9	35	4	0.00260	0.0164
$Q_2^c Q_1^c Q_1^c$	0.2	0.088	1.414	1 027 844	12	31	5	0.00252	0.0150
$Q_1^c Q_1^{\text{stab}} Q_1^c$	0.2	0.707	1.414	6 724	6	8	2	0.00280	0.0235
$Q_1^c Q_1^{\text{stab}} Q_1^c$	0.2	0.353	1.414	26 244	8	9	3	0.00269	0.0188
$Q_1^c Q_1^{\text{stab}} Q_1^c$	0.2	0.176	1.414	103 684	9	11	3	0.00260	0.0164
$Q_1^c Q_1^{\text{stab}} Q_1^c$	0.2	0.088	1.414	412 164	9	12	5	0.00252	0.0150
ref. [156]	0.2							0.0019200	0.00603
$Q_2^c Q_1^c Q_1^c$	0.4999	0.707	1.414	16 484	3	31	6	3.0383e-05	0.000257
$Q_2^c Q_1^c Q_1^c$	0.4999	0.353	1.414	64 964	7	46	8	3.6024e-05	0.000254
$Q_2^c Q_1^c Q_1^c$	0.4999	0.176	1.414	257 924	6	107	39	3.9899e-05	0.000252
$Q_2^c Q_1^c Q_1^c$	0.4999	0.088	1.414	1 027 844	5	57	24	4.2265e-05	0.000250
ref. [156]	0.4999							0.0015001	0.004713
$Q_2^c Q_1^c Q_1^c$	0.5	0.707	1.414	16 484	3	31	3	2.9937e-20	7.1504e-20
$Q_2^c Q_1^c Q_1^c$	0.5	0.353	1.414	64 964	6	25	2	1.3258e-19	2.3835e-19
$Q_2^c Q_1^c Q_1^c$	0.5	0.176	1.414	257 924	5	59	7	1.9309e-19	7.8981e-19
$Q_2^c Q_1^c Q_1^c$	0.5	0.088	1.414	1 027 844	-	-	-	-	-
$Q_2^c Q_1^c Q_1^c$	0.5	0.707	1.414	16 484	11	37	3	2.4585e-15	1.2562e-14
$Q_2^c Q_1^c Q_1^c$	0.5	0.353	0.707	64 964	6	32	3	2.3632e-18	1.0069e-17
$Q_2^c Q_1^c Q_1^c$	0.5	0.176	0.353	257 924	10	30	3	6.5953e-18	1.4749e-16
$Q_2^c Q_1^c Q_1^c$	0.5	0.088	0.176	1 027 844	14	38	3	1.2397e-18	2.6778e-18
ref. [156]	0.5							0.0015000	0.0047124

Table 6.6: Sneddon's pressure-driven cavity in 2d. Average number of linear GMRES iterations (∅lin) per Newton step, the average number of CG iterations (∅CG) per linear iteration, number of Newton/AS steps (#AS). Based on the newly developed mixed model $Q_2^c Q_1^c Q_1^c$ (or $Q_1^c Q_1^{\text{stab}} Q_1^c$) elements for different problem sizes and setting of the length scale parameter ϵ for three Poisson ratios. Quantities of interest: $\text{COD}_{\max}$ and TCV. $\kappa = 10^{-8}$. Uniform refined meshes.

Sneddon's test: robustness in h, λ, ϵ; $\kappa = 10^{-8}$; mixed; CG+AMG for $\hat{S}^{-1}$								
FE	ν	h	ϵ	#dof	∅lin	∅CG $(g(\tilde{\varphi})A_u)^{-1}$	∅CG $\hat{S}^{-1}$	#AS
$Q_2^c Q_1^c Q_1^c$	0.4999	0.707	1.414	16 484	3	26	1	3
$Q_2^c Q_1^c Q_1^c$	0.4999	0.353	1.414	64 964	8	56	6	8
$Q_2^c Q_1^c Q_1^c$	0.4999	0.176	1.414	257 924	6	106	6	38
$Q_2^c Q_1^c Q_1^c$	0.4999	0.088	1.414	1 027 844	6	42	6	69
$Q_2^c Q_1^c Q_1^c$	0.5	0.707	1.414	16 484	10	36	1	3
$Q_2^c Q_1^c Q_1^c$	0.5	0.353	1.414	64 964	6	26	6	8
$Q_2^c Q_1^c Q_1^c$	0.5	0.176	1.414	257 924	6	63	6	37
$Q_2^c Q_1^c Q_1^c$	0.5	0.088	1.414	1 027 844	7	41	6	101

Table 6.7: Sneddon's pressure-driven cavity in 2d. Average number of linear GMRES iterations (∅lin) per Newton step, the average number of CG iterations (∅CG) per linear iteration, CG plus AMG is used for $(g(\tilde{\varphi})A_u)^{-1}$ and $\hat{S}^{-1}$, number of Newton/AS steps (#AS). Based on the newly developed mixed model $Q_2^c Q_1^c Q_1^c$ elements for different problem sizes and setting of the length scale parameter ϵ for two Poisson ratios. Uniform refined meshes.

In Tables 6.6, 6.7 and 6.8, considering the quantities of interest $\mathrm{COD}_{\max}$ and TCV, they get vanishingly small for high Poisson ratios. In incompressible solids, a closed domain does not change its volume; the opening of the initial crack in the interior of the domain is avoided. For $\nu = 0.2$, the quantities of interest are acceptable compared to the reference values from Table 6.5. Also for $\nu = 0.2$, since all computations are conducted with uniformly refined meshes, moderate problem sizes, and fixed ϵ, we cannot expect excellent results in the quantities of interest.

Sneddon's test: robustness in h, λ, ϵ; $\kappa = 10^{-2}$; mixed									
FE	ν	h	ϵ	#dof	⌀lin	⌀CG	#AS	$\mathrm{COD}_{\max}$	TCV
$Q_2^c Q_1^c Q_1^c$	0.2	0.707	1.414	16 484	2	16	4	0.00248	0.0224
$Q_2^c Q_1^c Q_1^c$	0.2	0.353	1.414	64 964	8	18	4	0.00227	0.0173
$Q_2^c Q_1^c Q_1^c$	0.2	0.176	1.414	257 924	9	18	15	0.00206	0.0145
$Q_2^c Q_1^c Q_1^c$	0.2	0.088	1.414	1 027 844	15	28	5	0.00190	0.0129
$Q_1^c Q_1^{\mathrm{stab}} Q_1^c$	0.2	0.707	1.414	6 724	6	8	2	0.00245	0.0221
$Q_1^c Q_1^{\mathrm{stab}} Q_1^c$	0.2	0.353	1.414	26 244	8	9	2	0.00224	0.0171
$Q_1^c Q_1^{\mathrm{stab}} Q_1^c$	0.2	0.176	1.414	103 684	9	10	6	0.00205	0.0144
$Q_1^c Q_1^{\mathrm{stab}} Q_1^c$	0.2	0.088	1.414	412 164	9	12	8	0.00190	0.0129
ref. [156]	0.2							0.0019200	0.0060
$Q_2^c Q_1^c Q_1^c$	0.4999	0.707	1.414	16 484	13	16	3	3.0833e-05	0.000269
$Q_2^c Q_1^c Q_1^c$	0.4999	0.353	1.414	64 964	8	18	14	3.1739e-05	0.000242
$Q_2^c Q_1^c Q_1^c$	0.4999	0.176	1.414	257 924	6	18	93	3.3667e-05	0.000224
$Q_2^c Q_1^c Q_1^c$	0.4999	0.088	1.414	1 027 844	7	26	65	3.4560e-05	0.000216
ref. [156]	0.4999							0.0015001	0.004713
$Q_2^c Q_1^c Q_1^c$	0.5	0.707	1.414	16 484	9	14	3	1.7339e-19	5.8895e-19
$Q_2^c Q_1^c Q_1^c$	0.5	0.353	1.414	64 964	9	18	14	2.3734e-19	5.6268e-18
$Q_2^c Q_1^c Q_1^c$	0.5	0.176	1.414	257 924	11	18	14	5.6547e-20	6.0823e-18
$Q_2^c Q_1^c Q_1^c$	0.5	0.088	1.414	1 027 844	5	26	39	7.7351e-19	2.2733e-17
$Q_2^c Q_1^c Q_1^c$	0.5	0.707	1.414	16 484	9	14	3	1.5881e-19	5.8895e-19
$Q_2^c Q_1^c Q_1^c$	0.5	0.353	0.707	64 964	6	17	3	1.9290e-19	1.8057e-18
$Q_2^c Q_1^c Q_1^c$	0.5	0.176	0.353	257 924	6	18	3	4.1847e-19	2.1156e-18
$Q_2^c Q_1^c Q_1^c$	0.5	0.088	0.176	1 027 844	10	26	3	2.4801e-18	9.5514e-18
ref. [156]	0.5							0.0015000	0.0047124

Table 6.8: Sneddon's pressure-driven cavity. Average number of linear GMRES iterations (⌀lin) per Newton step, average number of CG iterations (⌀CG) per linear iteration, average number of Newton/AS steps (#AS). Based on the newly developed mixed model $Q_2^c Q_1^c Q_1^c$ (or stabilized $Q_1^c Q_1^c Q_1^c$) elements for different problem sizes and setting of the length scale parameter ϵ for three Poisson ratios. Quantities of interest: $\mathrm{COD}_{\max}$ and TCV. $\kappa = 10^{-2}$. Uniform refined meshes.

In Table 6.8, the same computations are conducted as in Table 6.6 and Table 6.7 for $\kappa = 10^{-2}$ to discuss the statement of Remark 28. The COD values are close to the reference values. Here, a large regularization parameter $\kappa = 10^{-2}$ stabilizes the block $(g(\tilde{\varphi})A_u)^{-1}$. Further, the linear iterations are stable, and also the inner CG iterations are relatively constant. In the last four rows of Table 6.8, similar to Table 6.3, results of four tests with $\epsilon = 2\,h$ are listed to check the robustness in ϵ for $\nu = 0.5$, which can be confirmed for Sneddon's benchmark test.

6.3.4 Sneddon's pressure-driven cavity, layered

As a fourth test case, the pressure-driven cavity from [153] is modified similarly to [22]. We consider a two-dimensional domain $\Omega = (-20, 20)^2$. In contrast to the previous Sneddon test, a compressible layer of size 10 is added around the incompressible domain to allow deforming of the solid on a finite domain. So the Poisson ratio changes over the domain for the layered Sneddon test. We expect to get better results concerning COD and TCV on a finite domain compared to the reference values on an infinite domain. A sketch of the geometry is given in Figure 6.4 on the left. The setting of the material and numerical parameters is the same as in the previous section.

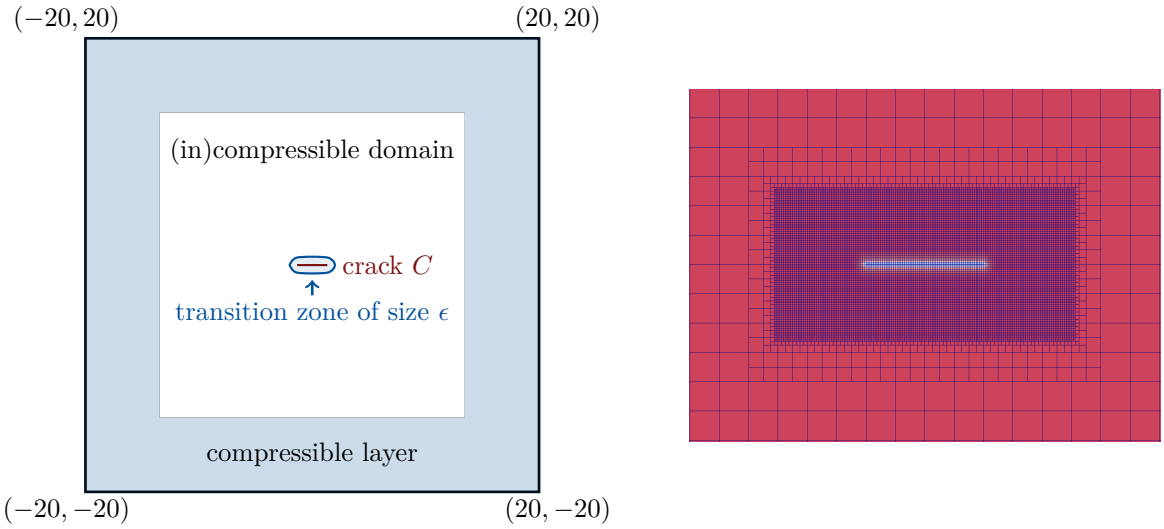

Figure 6.4: Left: geometry of the two-dimensional Sneddon's test with a compressible layer of size 10. Further, the inside of the initial crack is assumed to be compressible [22]. Right: Close zoom-in to the geometrically refined mesh around the crack, used in Table 6.10.

In Figure 6.4 on the right, a zoom-in snapshot of the inner domain is given to see the geometric refinement for the tests in Tables 6.9, 6.10, and 6.11. Aside from the adaptively refined mesh, we set $\epsilon = h$, depending on the current mesh size. The total numbers of dof (#dof) on Ω are listed in the numerical results in Tables 6.9 to 6.11.

In Table 6.9, the results for the Sneddon test in 2d with a compressible layer around a possibly incompressible domain are given for three Poisson ratios and adaptively refined meshes, with $\epsilon = h$, and $\kappa = 10^{-2}$. We choose $\kappa = 10^{-2}$ to avoid the effects of κ on the inner CG iterations. We observe with large κ that the computed quantities of interest COD_{max} and TCV are not converging with mesh refinement to the exact values from Table 6.5 because a large κ changes the material property. In Table 6.9, the numbers of GMRES iterations are moderate for $\nu = 0.2$. For higher Poisson ratios, we observe high linear iteration numbers. The incompressibility and the mesh adaptivity seem to significantly impact the linear solver. We observe the same effects for $\kappa = 10^{-8}$ in Table 6.10.

In Table 6.10, the numerical results of the same tests are given as in Table 6.9 for $\kappa = 10^{-8}$. Results for $\nu = 0.2$ and stabilized equal-order elements are added in green rows. For higher Poisson ratios, small κ, and stabilized equal-order elements, GMRES does not converge, as observed for the previous test; see Table 6.6. Analogously to Table 6.7, Table 6.11 contains the numerical results for the Sneddon

Sneddon layered adaptive: robustness in h, λ, ϵ; $\epsilon = h$ $\kappa = 10^{-2}$; mixed							
FE	ν	h	#dof	∅lin	#AS	$\text{COD}_{\max}$	TCV
$Q_2^c Q_1^c Q_1^c$	0.2	0.353	257 924	18	3	0.00214077	0.0097207
$Q_2^c Q_1^c Q_1^c$	0.2	0.176	263 604	25	4	0.00188194	0.0069353
$Q_2^c Q_1^c Q_1^c$	0.2	0.088	282 484	20	3	0.00163459	0.0055415
$Q_2^c Q_1^c Q_1^c$	0.2	0.044	350 804	17	3	0.00136002	0.0044906
$Q_2^c Q_1^c Q_1^c$	0.2	0.022	610 164	19	4	0.00104379	0.0034504
$Q_2^c Q_1^c Q_1^c$	0.2	0.011	1 620 244	24	6	0.00071731	0.0024168
$Q_2^c Q_1^c Q_1^c$	0.2	0.0055	5 606 324	28	6	0.00043963	0.0015294
ref. [156]	0.2					0.00192000	0.0060318
$Q_2^c Q_1^c Q_1^c$	0.4999	0.353	257 924	40	2	0.00205349	0.0108334
$Q_2^c Q_1^c Q_1^c$	0.4999	0.176	263 604	52	2	0.00168136	0.0069892
$Q_2^c Q_1^c Q_1^c$	0.4999	0.088	282 484	58	3	0.00143863	0.0052347
$Q_2^c Q_1^c Q_1^c$	0.4999	0.044	350 804	58	3	0.00122931	0.0041947
$Q_2^c Q_1^c Q_1^c$	0.4999	0.022	610 164	62	4	0.00099810	0.0033284
$Q_2^c Q_1^c Q_1^c$	0.4999	0.011	1 620 244	150	4	0.00073786	0.0024681
$Q_2^c Q_1^c Q_1^c$	0.4999	0.0055	5 606 324	318	7	0.00048545	0.0016595
ref. [156]	0.4999					0.00150019	0.0047130
$Q_2^c Q_1^c Q_1^c$	0.5	0.353	257 924	40	2	0.00205332	0.0108334
$Q_2^c Q_1^c Q_1^c$	0.5	0.176	263 604	52	2	0.00168117	0.0069889
$Q_2^c Q_1^c Q_1^c$	0.5	0.088	282 484	59	3	0.00143847	0.0052343
$Q_2^c Q_1^c Q_1^c$	0.5	0.044	350 804	57	4	0.00122920	0.0041944
$Q_2^c Q_1^c Q_1^c$	0.5	0.022	610 164	65	4	0.00099804	0.0033282
$Q_2^c Q_1^c Q_1^c$	0.5	0.011	1 620 244	155	4	0.00073784	0.0024681
$Q_2^c Q_1^c Q_1^c$	0.5	0.0055	5 606 324	271	7	0.00048545	0.0016595
ref. [156]	0.5					0.00150000	0.0047124

Table 6.9: Sneddon's pressure-driven cavity layered. Average number of linear GMRES iterations (∅lin) per Newton step, number of Newton/AS steps (#AS). Computations based on the newly developed mixed model with $Q_2^c Q_1^c Q_1^c$ elements for different problem size, $\epsilon = h$ for three Poisson ratios. Quantities of interest: $\text{COD}_{\max}$ and TCV. $\kappa = 10^{-2}$. Geometrically refined mesh in the area around the crack zone as depicted in Figure 6.4.

Sneddon layered adaptive: robustness in h, λ, ϵ; $\epsilon = h$, $\kappa = 10^{-8}$; mixed							
FE(u,p,φ)	ν	h	#dof	⌀lin	#AS	$\text{COD}_{\max}$	TCV
$Q_2^cQ_1^cQ_1^c$	0.2	0.353	257 924	10	3	0.00242526	0.0107193
$Q_2^cQ_1^cQ_1^c$	0.2	0.176	263 604	20	3	0.00221789	0.0080340
$Q_2^cQ_1^cQ_1^c$	0.2	0.088	282 484	18	3	0.00208683	0.0069646
$Q_2^cQ_1^cQ_1^c$	0.2	0.044	350 804	29	6	0.00200814	0.0064862
$Q_2^cQ_1^cQ_1^c$	0.2	0.022	610 164	26	4	0.00196329	0.0062530
$Q_2^cQ_1^cQ_1^c$	0.2	0.011	1 620 244	32	3	0.00193890	0.0061344
$Q_2^cQ_1^cQ_1^c$	0.2	0.0055	5 606 324	40	3	0.00192609	0.0060733
$Q_1^cQ_1^{\text{stab}}Q_1^c$	0.2	0.353	103 684	7	4	0.00242340	0.0105394
$Q_1^cQ_1^{\text{stab}}Q_1^c$	0.2	0.176	105 956	14	3	0.00221747	0.0079727
$Q_1^cQ_1^{\text{stab}}Q_1^c$	0.2	0.088	113 508	14	4	0.00208628	0.0069425
$Q_1^cQ_1^{\text{stab}}Q_1^c$	0.2	0.044	140 836	12	13	0.00200734	0.0064770
$Q_1^cQ_1^{\text{stab}}Q_1^c$	0.2	0.022	244 580	13	14	0.00196228	0.0062479
$Q_1^cQ_1^{\text{stab}}Q_1^c$	0.2	0.011	648 612	15	11	0.00193775	0.0061306
$Q_1^cQ_1^{\text{stab}}Q_1^c$	0.2	0.0055	2 243 044	23	31	0.00192485	0.0060698
ref. [156]	0.2					0.00192000	0.0060318
$Q_2^cQ_1^cQ_1^c$	0.4999	0.353	257 924	40	2	0.00223914	0.0116630
$Q_2^cQ_1^cQ_1^c$	0.4999	0.176	263 604	74	5	0.00187365	0.0077192
$Q_2^cQ_1^cQ_1^c$	0.4999	0.088	282 484	229	4	0.00168693	0.0060788
$Q_2^cQ_1^cQ_1^c$	0.4999	0.044	350 804	511	4	0.00159278	0.0053537
$Q_2^cQ_1^cQ_1^c$	0.4999	0.022	610 164	601	6	0.00154436	0.0050158
$Q_2^cQ_1^cQ_1^c$	0.4999	0.011	1 620 244	565	5	0.00151941	0.0048527
$Q_2^cQ_1^cQ_1^c$	0.4999	0.0055	5 606 324	641	5	0.00150668	0.00477248
ref. [156]	0.4999					0.00150019	0.0047130
$Q_2^cQ_1^cQ_1^c$	0.5	0.353	257 924	40	2	0.00223891	0.0116629
$Q_2^cQ_1^cQ_1^c$	0.5	0.176	263 604	73	5	0.00187338	0.0077187
$Q_2^cQ_1^cQ_1^c$	0.5	0.088	282 484	227	4	0.00168667	0.0060782
ref. [156]	0.5					0.00150000	0.0047124

Table 6.10: Sneddon's pressure-driven cavity layered. Average number of linear GMRES iterations (⌀lin) per Newton step, number of Newton/AS steps (#AS). Computations based on the newly developed mixed model with $Q_2^cQ_1^cQ_1^c$ (or $Q_1^cQ_1^{\text{stab}}Q_1^c$) elements for different problem size, $\epsilon = h$ for three Poisson ratios. Quantities of interest: $\text{COD}_{\max}$ and TCV. $\kappa = 10^{-8}$. Geometrically refined mesh in the area around the crack zone as depicted on the right in Figure 6.4.

test layered for high Poisson ratios and small κ. In contrast to Table 6.10, we approximate $\hat{S}^{-1}$ with a CG solver which is preconditioned with AMG.

Remark 29 (Difficulties with equal-order elements)**.** *We proposed a stabilized equal-order discretization in Formulation 18 of the mixed problem formulation, similar to the common use for the Navier-Stokes equations. The advantages would be having a reduced problem size, and secondly, the attraction of the simplicity of linear finite elements [63]. This approach is not advised for our mixed phase-field fracture framework combined with high Poisson ratios. For large λ, the naturally stabilizing mass term (p, q) becomes small or vanishes. Further, the stabilizing terms contain ∇p with mesh-dependent coefficients. But the pressure approximation in the crack region yields high gradients, which yields an 'over-stabilization'. We follow that consistent stabilization cannot be used in the current state. For this reason, Taylor-Hood finite elements are the choice to obtain stable solutions.*

Sneddon layered adaptive: robustness in h, λ, ϵ; $\epsilon = h$, $\kappa = 10^{-8}$; mixed; CG for two blocks							
FE(u, p, φ)	ν	h	#dof	⌀lin	#AS	$\text{COD}_{\max}$	TCV
$Q_2^c Q_1^c Q_1^c$	0.4999	0.353	257 924	40	2	0.00223914	0.0116630
$Q_2^c Q_1^c Q_1^c$	0.4999	0.176	263 604	70	4	0.00187365	0.0077192
$Q_2^c Q_1^c Q_1^c$	0.4999	0.088	282 484	165	4	0.00168693	0.0060788
$Q_2^c Q_1^c Q_1^c$	0.4999	0.044	350 804	153	4	0.00159278	0.0053537
$Q_2^c Q_1^c Q_1^c$	0.4999	0.022	610 164	145	5	0.00154436	0.0050158
$Q_2^c Q_1^c Q_1^c$	0.4999	0.011	1 620 244	139	5	0.00151941	0.0048527
$Q_2^c Q_1^c Q_1^c$	0.4999	0.0055	5 606 324	148	5	0.00150668	0.0047724
ref. [156]	0.4999					0.00150019	0.0047130
$Q_2^c Q_1^c Q_1^c$	0.5	0.353	257 924	40	2	0.00223891	0.0116629
$Q_2^c Q_1^c Q_1^c$	0.5	0.176	263 604	70	4	0.00187338	0.0077187
$Q_2^c Q_1^c Q_1^c$	0.5	0.088	282 484	200	4	0.00168667	0.0060782
$Q_2^c Q_1^c Q_1^c$	0.5	0.044	350 804	229	4	0.00159254	0.0060782
$Q_2^c Q_1^c Q_1^c$	0.5	0.022	610 164	238	7	0.00154414	0.0050151
$Q_2^c Q_1^c Q_1^c$	0.5	0.011	1 620 244	220	5	0.00151920	0.0048521
$Q_2^c Q_1^c Q_1^c$	0.5	0.0055	5 606 324	222	5	0.00150648	0.0047718
ref. [156]	0.5					0.00150000	0.0047124

Table 6.11: Sneddon's pressure-driven cavity layered with $Q_2^c Q_1^c Q_1^c$ elements and $\epsilon = h$. Average number of linear GMRES iterations (⌀lin) per Newton step, number of Newton/AS steps (#AS). CG plus AMG is used for $(g(\tilde{\varphi})A_u)^{-1}$ and $\hat{S}^{-1}$: the average number of CG iterations for $(g(\tilde{\varphi})A_u)^{-1}$ is 38 for $\nu = 0.4999$ and 36 for $\nu = 0.5$. The average number of CG iterations for $\hat{S}^{-1}$ is 8 for $\nu = 0.4999$ and 7 for $\nu = 0.5$. Computations based on the newly developed mixed model with $Q_2^c Q_1^c Q_1^c$ elements for different problem size, $\epsilon = h$ for three Poisson ratios. Quantities of interest: $\text{COD}_{\max}$ and TCV. $\kappa = 10^{-8}$. Geometrically refined mesh in the area around the crack zone as depicted on the right in Figure 6.4.

The results of $\text{COD}_{\max}$ and TCV in Tables 6.10 and 6.11 look promising for all three Poisson ratios. We stress that the number of Newton steps is relatively constant for the Taylor Hood elements, and increasing up to 31 steps for the stabilized Q_1^c elements. For $\nu = 0.5$ the solver does not converge with sufficiently small κ and $h \to 0$. An explanation is given in Remark 28 (Section 6.3.3). In Table 6.11 for high Poisson ratios, the modified approximation of $\hat{S}^{-1}$ changes the behavior of the linear solver. With a relative tolerance of 10^{-6} for the preconditioned CG solver for $(g(\tilde{\varphi})A_u)^{-1}$ and $\hat{S}^{-1}$, we observe that more GMRES iterations are required. The number of linear iterations is relatively high, but nearly constant for $\nu = 0.4999$ and $\nu = 0.5$. The number of linear iterations increases for higher Poisson ratios

with adaptive refined meshes and $\epsilon = h$. The results of $\text{COD}_{\max}$ and TCV match the manufactured reference values from Table 6.5.

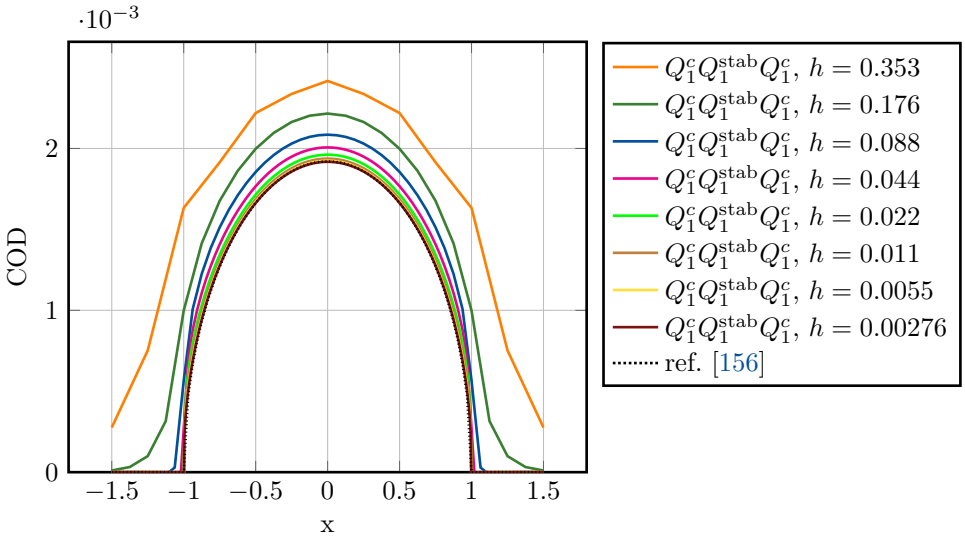

Figure 6.5: Crack opening displacements (COD) for various refinement levels for $Q_1^c Q_1^{\text{stab}} Q_1^c$ elements, geometrical refinement around the crack area and $\nu = 0.2$. Results from Table 6.10. COD computed from -1.5 to 1.5. Initial crack in $x \in [-1.0, 1.0]$.

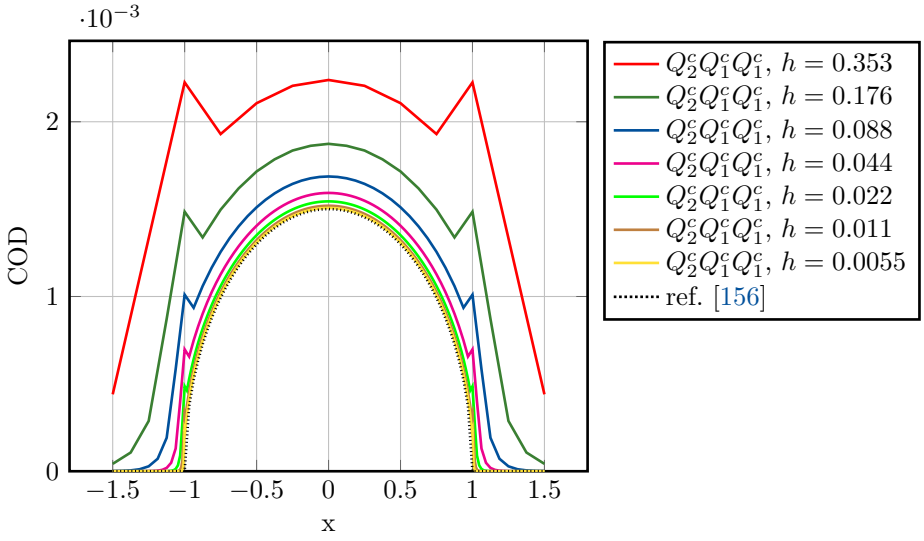

Figure 6.6: Crack opening displacements (COD) for various refinement levels for $Q_2^c Q_1^c Q_1^c$ elements, geometrical refinement around the crack area and $\nu = 0.4999$. Results from Table 6.10. COD computed from -1.5 to 1.5. Initial crack in $x \in [-1.0, 1.0]$.

In Figures 6.5, 6.6, and 6.7, the computed crack opening displacement (COD) values are given for $\nu = 0.2$ (with $Q_1^c Q_1^{\text{stab}}$), $\nu = 0.4999$ (with $Q_2^c Q_1^c Q_1^c$), and $\nu = 0.5$ (with $Q_2^c Q_1^c Q_1^c$ and CG solver for $\hat{S}^{-1}$). The maximal COD values ($x = 0$) are listed in Table 6.10, and in Table 6.11 for $\nu = 0.5$. The crack opening displacement curves converge to the corresponding reference curves with an increasing

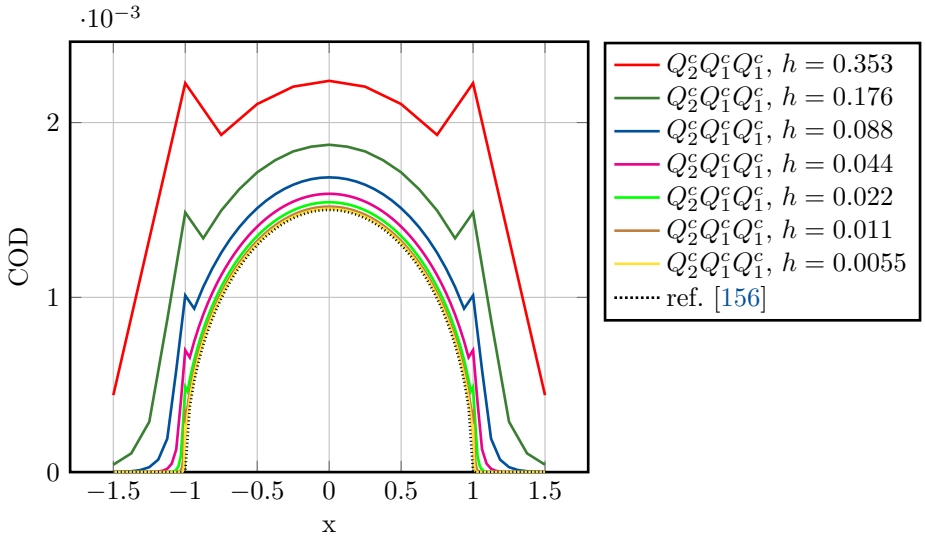

Figure 6.7: Crack opening displacements (COD) for various refinement levels for $Q_2^c Q_1^c Q_1^c$ elements, geometrical refinement around the crack area and $\nu = 0.5$. Results from Table 6.11. COD computed from -1.5 to 1.5. Initial crack in $x \in [-1.0, 1.0]$.

number of geometric refinement steps for all three chosen Poisson ratios in Figures 6.5, 6.6, and 6.7. In Figure 6.8, the solutions of u_x, u_y, p, and φ are presented as zoom-in snapshots for $\nu = 0.5$ with a compressible layer, based on Table 6.11. Especially the pressure field (upper left snapshot) is expected to have zero values in the interior of the crack and the maximal values in the crack tip on the left and the right of the pre-defined initial crack. Further, in Figure 6.8, the mesh on the finest refinement level is given on the bottom left. On the bottom right, the crack zone is shown, on which the computed solutions are presented above to get an impression of the mesh size around the fracture.

6.3.5 Single edge notched pure tension test

As the last example, we use the single-edge notched tension test from Miehe et al. [130], similar to Section 4.6.4 testing with three Poisson ratios. We use the predictor-corrector scheme from Section 5.5.2 for two steps of adaptive mesh refinement on four times uniformly refined mesh with a phase-field threshold of 0.5. The parameter setting is the same as in Section 4.6.4, but we use the mixed problem formulation and discretization from Chapter 3 and vary the Poisson ratio; see Table 6.12.

ν	μ	λ	#dofs
0.3	$80.77 \cdot 10^3$	$121.15 \cdot 10^3$	19 584
0.45	$80.77 \cdot 10^3$	$726.93 \cdot 10^3$	19 704
0.49	$80.77 \cdot 10^3$	$3957.73 \cdot 10^3$	19 498

Table 6.12: Parameter setting for three tests with different Poisson's ratios for the single-edge notched tension test with $\kappa = 10^{-8}$, and $\epsilon = 4\,h$. The maximal number of dof (#dofs) is given in the last column for the test cases. For all tests, four uniform ($h = 0.011$) and two adaptive refinement steps are conducted with a phase-field threshold of 0.5 for predictor-corrector.

We consider the bulk and crack energy as two further numerical quantities of interest. The bulk energy

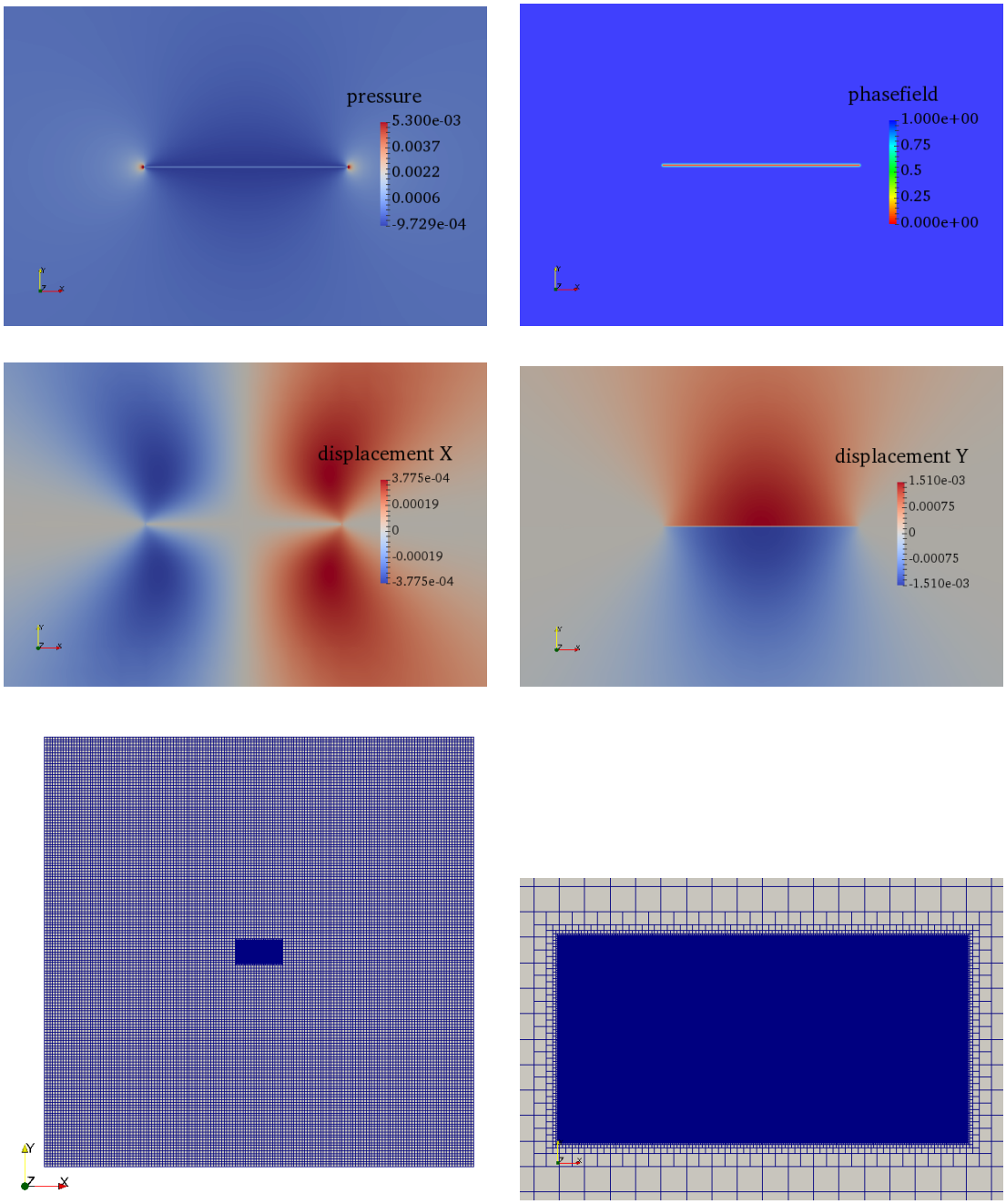

Figure 6.8: Sneddon 2d layered. Upper four snapshots: zoom-in solutions from left to right, and top to bottom: the pressure field, the phase-field, the displacement in the x-direction and the displacement in the y-direction. The solutions are for $\nu = 0.5$ from Table 6.11 on the finest level with $Q_2^c Q_1^c Q_1^c$ elements. The solutions fit the reference values from [22]. Lower two snapshots show on the left the whole domain $(-20, 20)^2$ with the adaptively refined mesh in the last refinement step. On the bottom right, a zoom-in snapshot of the crack zone is given on the domain, where the upper snapshots are taken.

E_B can be computed via

$$E_B(u,\varphi) = \int_\Omega (g(\tilde{\varphi})\psi(E_{\text{lin}}(u))\,\mathrm{d}(x,y),$$

where the strain energy functional is defined as

$$\psi(E_{\text{lin}}(u)) \coloneqq \mu\,\mathrm{tr}\left(E_{\text{lin}}(u)^2\right) + \frac{1}{2}\lambda\,\mathrm{tr}\left(E_{\text{lin}}(u)\right)^2.$$

Here, no manufactured reference values are provided and we only present values computed numerically. Further, we compute the crack energy E_C via

$$E_C(u,\varphi) = \frac{G_C}{2}\int_\Omega \left(\frac{(\varphi-1)^2}{\epsilon} + \epsilon|\nabla\varphi|^2\right)\mathrm{d}(x,y). \tag{6.11}$$

Again, no manufactured reference values are provided. At least for $\nu = 0.3$, we can compare our results for E_B and E_C with reference values from the literature, e.g., [3, 128]. In Figures 6.9, 6.10, and 6.11, on the left side, the bulk and the crack energy are plotted versus the incremental step number. On the right of Figures 6.9 to 6.11, the average number of linear iterations and the number of Newton/AS steps are plotted. The number of linear iterations behaves differently for $\nu = 0.3$ from the results for higher Poisson ratios. While for $\nu = 0.3$, in Figure 6.9 on the right, the linear iterations decrease if the crack starts propagating, in Figures 6.10 and 6.11, the linear iterations increase up to an average of more than 70 iterations at the end of the crack simulations.

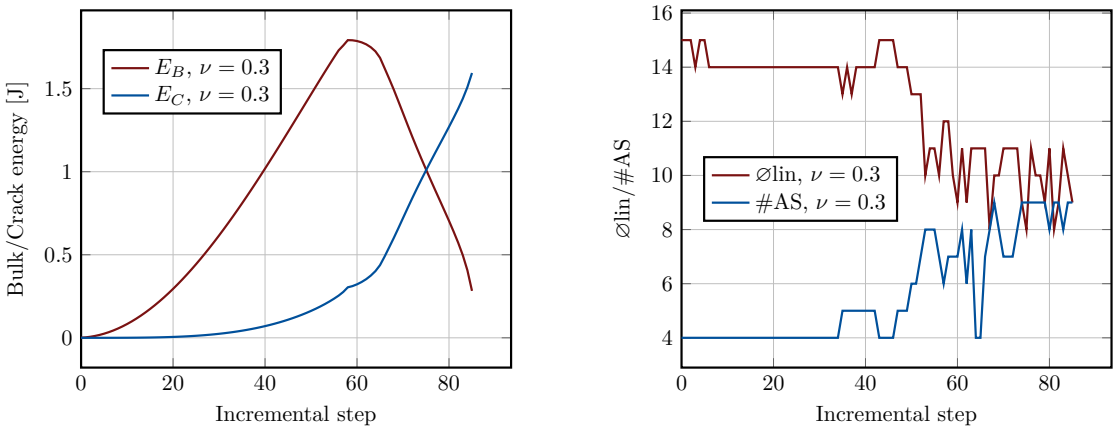

Figure 6.9: Left: bulk (E_B) and crack energy (E_C) for the single-edge notched tension test, AT_2 functional, adaptive refined meshes. The incremental step size was 10^{-4} s for the first 58 steps and reduced to 10^{-5} s. Right: number of linear iterations on average per Newton step (∅lin), and number of active set/Newton steps (#AS) against the incremental steps. The crack starts propagating at incremental step 66, mesh refinement starts at step 57. $\nu = 0.3$.

In Figure 6.13, snapshots of the pressure field and phase-field are given for $\nu = 0.49$, where – to the author's knowledge – no reference values are available in the literature. The crack paths look similar as for $\nu = 0.3$, but a slight asymmetry is visible in the crack path. We decided to present the crack path during the simulation to depict the pressure field with the maximal value in front of the crack tip while the pressure values in the crack are zero.
The computed bulk and crack energies in Figures 6.9, and 6.10 fit well to results in the literature,

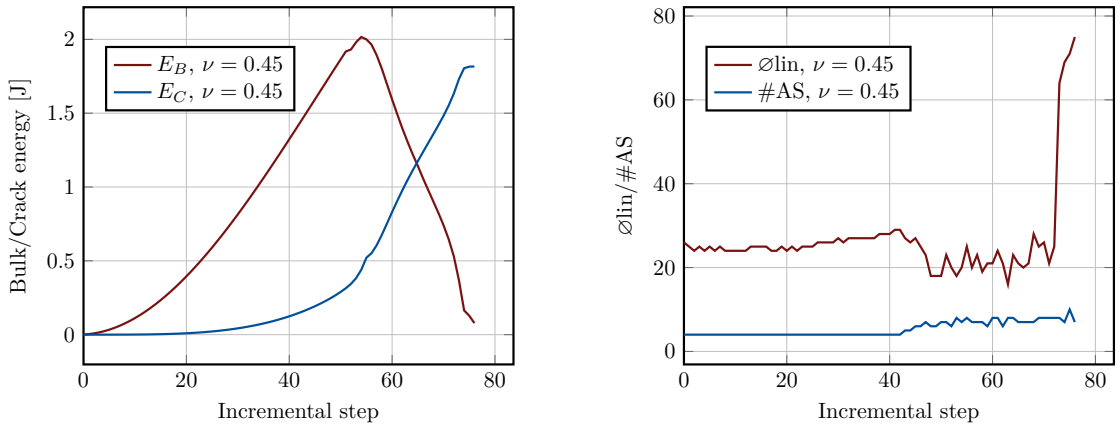

Figure 6.10: Left: bulk (E_B) and crack energy (E_C) for the single-edge notched tension test, AT_2 functional, adaptive refined meshes. The incremental step size was 10^{-4} s for the first 55 steps and reduced to 10^{-5} s. Right: number of linear iterations on average per Newton step (⌀lin), and number of active set/Newton steps (#AS) against the incremental steps. The crack starts propagating at incremental step 56, mesh refinement starts at step 52. $\nu = 0.45$.

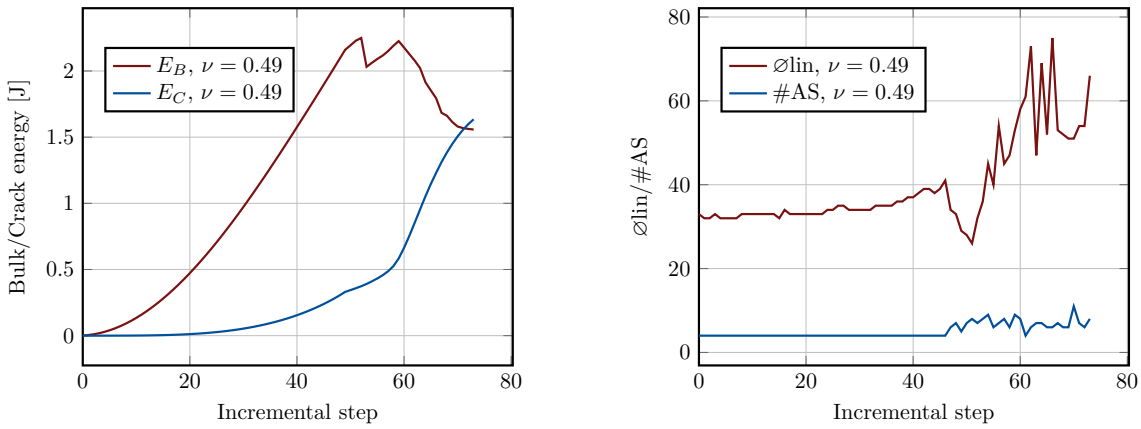

Figure 6.11: Left: bulk (E_B) and crack energy (E_C) for the single-edge notched tension test, AT_2 functional, adaptive refined meshes. The incremental step size was 10^{-4} s for the first 48 steps and reduced to 10^{-5} s. Right: number of linear iterations on average per Newton step (⌀lin), and number of active set/Newton steps (#AS) against the incremental steps. The crack starts propagating at incremental step 60, mesh refinement starts at step 52. $\nu = 0.49$.

e.g., [87]. The bulk energy increases until the critical energy release rate is reached, and the crack energy increases when the crack propagates while the bulk energy releases. Also, in Figure 6.11, the bulk and crack energy curves fit the observed crack pattern in Figure 6.14. For $\nu = 0.49$ with snapshots of the solutions at two certain incremental steps in Figure 6.14, no comparable results in the literature are available. The crack pattern differs from the snapshots for smaller Poisson ratios. We observe that the crack has an orientation to the upper left corner, and a second crack develops from the singularity in the corner, where non-homogeneous Dirichlet boundary conditions and Neumann boundary conditions meet.

In Figure 6.12, the pressure and phase-field solution is given for $\nu = 0.3$ after total failure. The crack propagates from the center of the geometry to the left boundary, as we expect it. Further, one can see a pure zero pressure field after total failure.

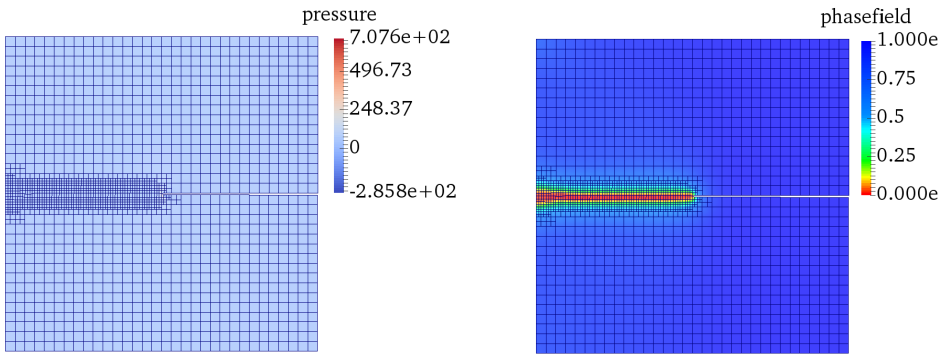

Figure 6.12: Snapshots of the solution for the single-edge notched tension test with $\nu = 0.3$. Adaptive mesh refinement with predictor-corrector. Pressure field (left) and phase-field (right) on deformed two-dimensional domain in incremental steps 88, which is the last computed step.

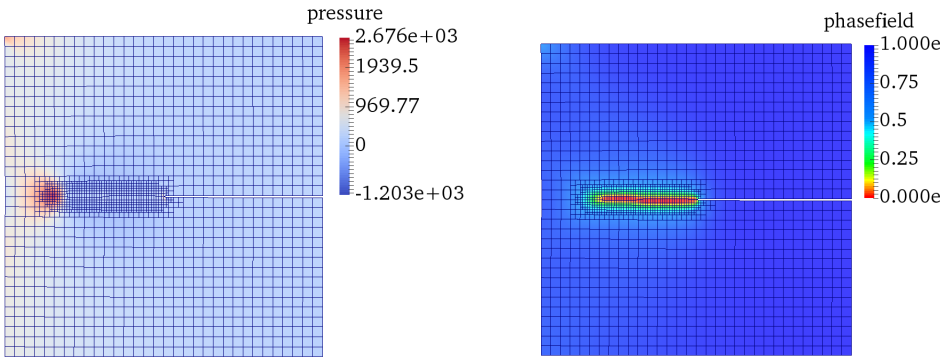

Figure 6.13: Snapshots of the solution for the single-edge notched tension test with $\nu = 0.45$. Adaptive mesh refinement with predictor-corrector. Pressure field (left) and phase-field (right) on deformed two-dimensional domain in incremental step 70, where the crack propagates as in Figure 6.12.

Remark 30 (Pressure field in the inside of the crack)**.** *In Figure 6.14, the crack is as sharp as for smaller Poisson ratios and the inside of the crack has zero pressure values. In contrast to the results in Figure 5.8, the pressure solution is more realistic. In Figure 5.8, the pressure fields for high Poisson ratios were given for the single-edge notched shear test, which assumes different boundary conditions,*

but the geometry and parameter setting are the same. The crack in Figure 6.14 has an adequate size regarding the mesh size and bandwidth, but no artificially wide crack resulting from high pressure values in the interior of the crack. The reason is a small change in the problem formulation, allowing zero pressure values in the crack; see Section 5.6 for further details.

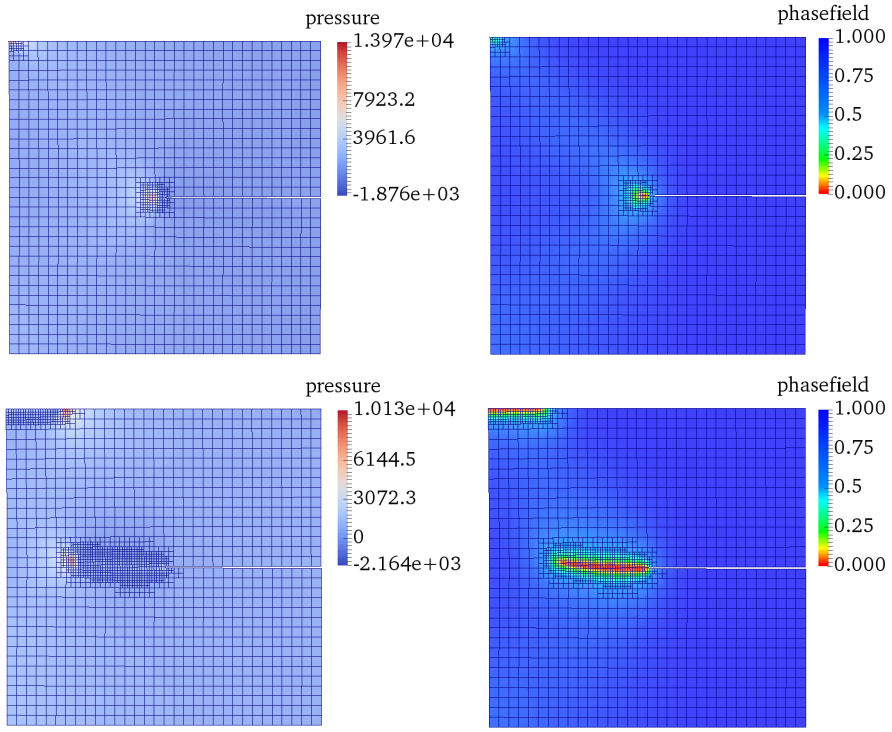

Figure 6.14: Snapshots of the solution for the single-edge notched tension test with $\nu = 0.49$. Adaptive mesh refinement with predictor-corrector. Pressure field (left) and phase-field (right) on deformed two-dimensional domain at two incremental steps, where the crack starts propagating (first row) and in the last computed step (second row).

Conclusions of the chapter

We conducted numerical tests for five test configurations for different Poisson ratios up to the incompressible limit. For the first two test cases, hanging block and hanging block with a slit, we confirmed the robustness and efficiency of the physics-based preconditioner, discretized with $Q_2^c Q_1^c Q_1^c$ finite elements. An impact of κ on the number of CG iterations (preconditioned with AMG) could be explicitly seen for Sneddon's test case and $\kappa = 10^{-8}$. For the stabilized equal-order discretization with $Q_1^c Q_1^{\text{stab}} Q_1^c$ elements, the numerical results look promising for the compressible parameter setting tested for both proposed Sneddon tests and the single-edge notched shear test.

The next chapter focuses on a practical application of the developed mixed model from Chapter 5: At the DIK, punctured EPDM strips were elongated until total failure, and the crack behavior was retraced with a Digital Image Correlation system (DIC) for qualitative measurement data. The following chapter aims a detailed description of the conducted experiments and a critical comparison of experimental and numerical results for validating our newly developed mixed phase-field fracture model for fractures in nearly incompressible solids as EPDM.

Chapter 7

Simulating fractures in punctured EPDM strips

In this chapter[1], we present crack propagation experiments evaluated by Digital Image Correlation (DIC) for a carbon black-filled ethylene propylene diene monomer rubber (EPDM). Our primary focus is the crack evolution in one-sided notched EPDM strips containing a circular hole and stretched until total failure. A picture of the experimental setup is given in Figure 7.1. Using the experimentally

Figure 7.1: Experimental setup: punctured EPDM strip fixed via bulges on the top, and bottom boundary. The specimen has a small given notch on the left side and a (originally) circular hole. The strip is elongated on the bottom boundary until total failure.

identified material parameters, we apply the newly established mixed phase-field fracture model from Section 5.6 to simulate crack propagation in punctured EPDM strips. To discuss agreements and point out challenges, we compare the crack paths, the maximal force response, the traverse displacement at

[1] Parts of this chapter are published in [123].

the crack start, and the force-displacement curves of the experimental and numerical results. While often in the published literature, models are developed and discussed on a purely theoretical basis, e.g., [117], or historical data, e.g., [114, 162], we check our mixed phase-field fracture model against a systematically conducted experimental series. Therefore, a technically used EPDM compound is characterized for its mechanical and fracture properties, described in Sections 7.1 and 7.2. Being well aware of geometric and material nonlinearities dealing with rubber and high strains, we neglect those effects focusing on the modeling approach and the qualitative comparison to the experiments. We present the crack path results from the experiments in Section 7.3. The corresponding results from numerical simulations are given in Section 7.4. The last Section 7.5 picks up on the topic of Sections 4.6 and 4.7: we investigate the dependency of the crack paths in punctured EPDM strips on the chosen energy functional and Cauchy stress splitting.

7.1 Material compounding and sample preparation

For the experimental study[2] a sulphur crosslinked EPDM (Keltan 2450) filled with 60 phr carbon black N550 is used. The EPDM mixture, see Table 7.1, is prepared on a 5.0-liter mixer adding the ingredients step-wise. The crosslinking agent and catalysts are admixed at a roller at 60°C. The samples, 2 mm thick specimens for all experiments, are compression moulded at 170°C for six minutes, corresponding to "t_{90}" plus two minutes of a corresponding vulcameter test. If required for the experiments, we pierce notches and circular inclusions in the specimens after vulcanisation.

Remark 31 (EPDM and rubbers)**.** *In the experimental context, we add some comments on the properties of rubber from Schaefer [149]. Rubber is an elastic and viscous material that allows wide usage in many different fields. In the frame of this thesis, we focus on vulcanized rubber because unvulcanized rubber would start to flow after a while. Sometimes rubber is meant to be natural rubber, so elastomer is used instead of rubber. EPDM is a special kind of vulcanized elastomer.*

Ingredients	EPDM	Carbon black N550	PEG-4000	Oil	Zinc oxid	Stearic acid	Sulphur	TBBS	TBzTD
Phr	100	60	5.0	5.0	5.0	3.0	0.7	1.0	3.5
Admixed at	Mixer						Roller		
Admixed after min	0	2/3@1 1/3@2	2m30	1	2m30	1	1	1	1

Table 7.1: Recipe of the investigated EPDM mixture (phr $\widehat{=}$ parts per hundred parts of rubber related to mass parts).

7.2 Parameter identification

We identify the material parameters via experiments with the help of DIC. Subsequently, we present first numerical test results in Section 7.2.3 to identify a proper value of the critical energy release rate

[2]The experiments and corresponding material parameter evaluations from Sections 7.1, 7.2, and 7.3, were conducted at and from the Deutsches Institut für Kautschuktechnologie e.V. (DIK) within the department 'Simulation and Continuum Mechanics'. We identified an interesting and challenging test setup that results in this chapter's experiments within the collaboration. In the first months, the essential task was communicating about the compounding, geometry, and behavior of EPDM. I thank Dr. Nils Hendrik Kröger and Andreas Fehse for their time until achieving a clear description of the experiments and a fair comparison between experiments and simulations.

G_C via available load-displacement curves from the experiments.

7.2.1 Elastic constants

The mechanical material properties are determined on a ZWICK Universal test machine in four loading modes - uniaxial, planar (pure shear), biaxial tension, and confined (volumetric) compression. The tests are conducted with an (initial) strain rate of approximately 50 % per minute and a pre-force of 1 N; see Figure 7.2 (black line). The later defined material model uses a linear elastic approach such that the minor nonlinear behavior has to be estimated by, e.g., the average behavior until a certain strain, a lower or upper bound, or alternative with an estimate for Young's modulus consistent with the Neo Hooke model (estimate holds for the initial stiffness, therefore one possibility for an upper bound definition), see Figure 7.2 (gray line for 'up to 150 % estimate' and green line for 'Neo Hooke estimate'). The bulk modulus is derived by volumetric compression experiments within the constant response region of 1 000 to 2 000 N, see Figure 7.3. For parameter identification is we use a minimization for the least square sum of the absolute errors between experiment and prediction, considering the varying strain range. The resulting parameters are depicted in Table 7.2. The estimation of linear material behavior might deviate for strains under 50% but is a solid assumption for higher strains appearing in the later crack path experiments for this particular EPDM.

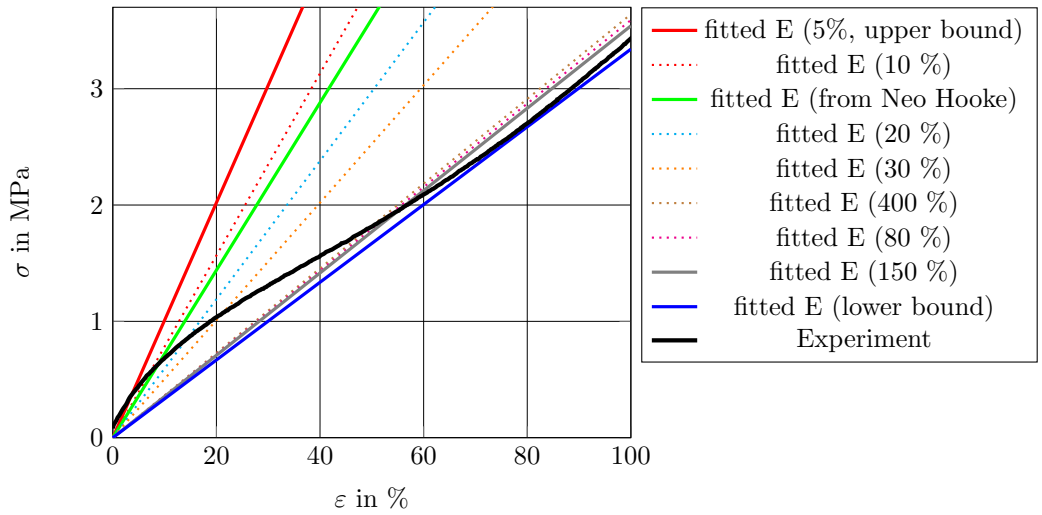

Figure 7.2: Uniaxial tension test (stress σ versus strain ϵ) and prediction of the elastic behavior based on parameter identifications of the elastic moduli related to specific fitting strain ranges.

To emphasize the relations between the already used Lamé coefficients λ and μ, the Poisson ratio ν, and the Young modulus E given from the experiments [52], we give the formulas for λ and μ depending on ν and E:

$$\lambda(E,\nu) = \frac{E\nu}{(1+\nu)(1-2\nu)}, \quad \mu(E,\nu) = \frac{E}{2(1+\nu)}.$$

Remark 32. *In the numerical implementation in deal.II [9] derived from the framework pfm-cracks [89], we have λ and μ as input variables. From the experiments we have the bulk modulus K and Young's*

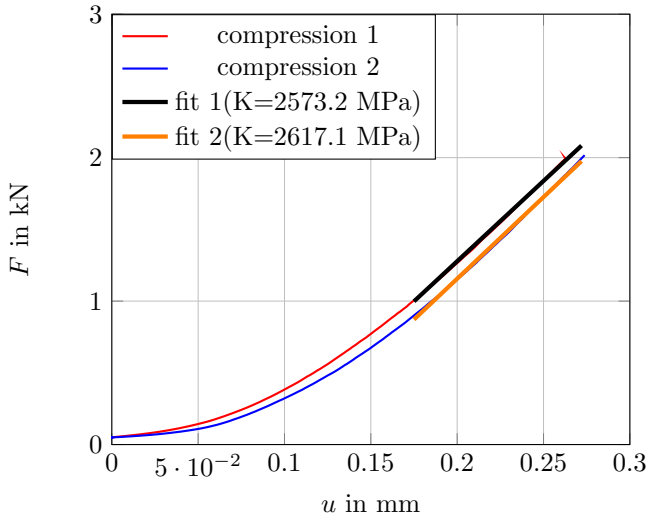

Figure 7.3: Volumetric compression test and estimation of the bulk modulus by a linear fit in the range between 1 and 2 kN. The force F and displacement u are depicted in sense of compression, compared to tension the sign would switch. We refer to [75, 142] for details on the experimental setup.

modulus E.

Parameter	upper	Neo Hooke	10	20	80	150	400	lower
E [MPa]	10.1	7.20	7.83	5.95	3.59	3.54	3.64	3.34
K [MPa]	2 595	2 595	2 595	2 595	2 595	2 595	2 595	2 595
λ [MPa]	2 592.75	2 593.40	2 593.26	2 593.68	2 594.20	2 594.21	2 594.19	2 594.26
μ [MPa]	3.37	2.40	2.61	1.98	1.20	1.18	1.21	1.11
ν	0.49978	0.49985	0.49983	0.49987	0.49992	0.49992	0.49992	0.49993

Table 7.2: Young's modulus E, bulk modulus K, Lamé coefficients λ and μ and Poisson ratio ν for different identification variants of E (upper and lower bound, resp. results for parameter fit up to $X\%$ of strain, and estimated by Neo Hookean model); see Figures 7.2 and 7.3. Parameters set in light blue are used in the simulations from Section 7.4.

7.2.2 Critical energy release rate

We use pure shear tests to determine the (critical) energy release rate G_C. The specimens have a length of 196 mm, a height of 28 mm, and a thickness of 1.8 mm. A ZWICK 1445 universal test machine was used for the tests. The traverse velocity is chosen to be 200 mm/min. Two tests are conducted: standard pure shear tests until the break and pure shear tests with notched samples. The notched sample has an initial crack l_0 of 47 mm. In the second case, we apply a square pattern to the specimen such that a DIC recording can follow the crack growth; see Figure 7.5 on the lower right. The crack growth is correlated with the recorded force-displacement curves. The resulting force-displacement and crack growth curves are shown in Figure 7.4. We determine the critical (strain) energy release rate based on the data using the following formula from [147, 146]:

$$G_C = -\frac{\partial U}{\partial A}\bigg|_\alpha = -\frac{dU}{dA}\bigg|_\alpha .$$

Here, U is the stored elastic energy, and dU is the difference between the sample with and without a crack, see [147, 146] for further details. With F_w and u_w being the force-displacement data of the sample without a crack, F_c and u_c being the data of the sample with a crack, and α as the stretch, dU reads as

$$dU = \int_\alpha F_w du_w - \int_\alpha F_c du_c.$$

The crack area dA depends on the specimen thickness t and the crack length $l_0 + l$. Here, l_0 is the initial crack length of 47 mm and l is the length of the growing crack [147, 146]:

$$dA = (l_0 + l) \cdot t.$$

From the experimental results, we approximate the stationary value of the critical strain energy release rate G_C by 17.0 N/mm, see Figure 7.5. The result coincides in general with literature results, e. g. [145] for carbon black-filled styrene-butadiene rubber. Already in the 60s, Rivlin and Thomas [143] presented characteristic energy for thin natural rubber strips with a cut and identified the critical energy between 10.0 and 20.0 N/mm.

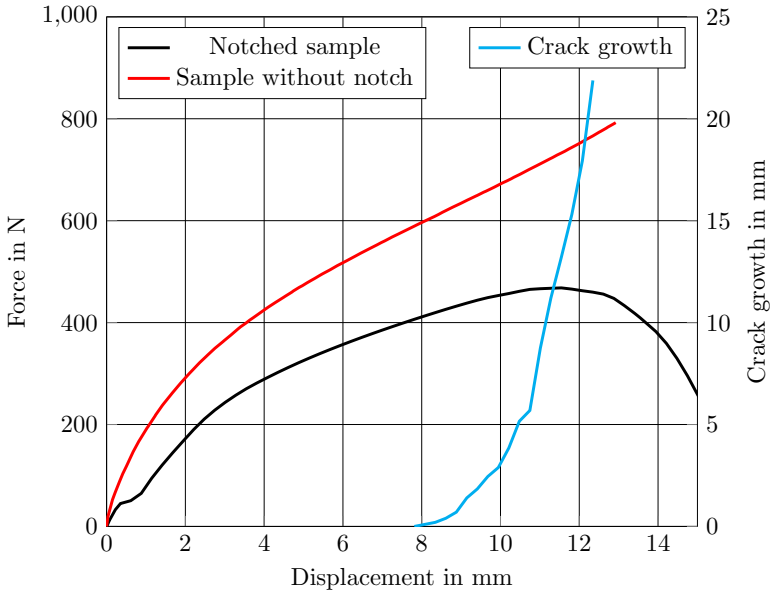

Figure 7.4: Force-displacement curves (displacement u in the y-direction measured on the top boundary versus force F_y) for a notched sample and a sample without a notch. The crack growth evaluated from DIC from Figure 7.5 is given depending on the displacement is plotted in blue.

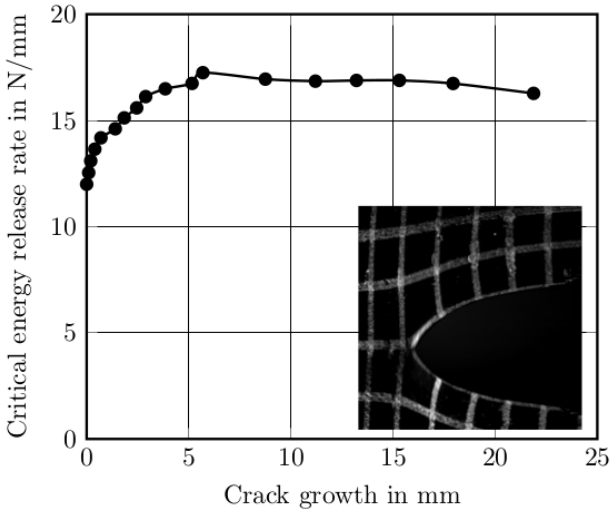

Figure 7.5: Estimated (critical) strain energy release rate G_C versus the crack length of a single-edge notched pure shear tension test. The average value in the stable crack growth region after 5.0 mm crack length is approximately 17.0 N/mm.

7.2.3 Numerical studies on the critical energy release rate

This section tracks the discussions we had at that time in parameter identification. While the team of Dr. Nils Hendrik Kröger at the DIK conducted the first experiments and evaluated the pure shear tests for parameter identification, we started the first numerical tests with the Lamé coefficients as input parameters, but not yet with the critical energy release rate G_C computed from the experiments as explained above, according to Klüppel et al. [105]. At that time, the load-displacement curves for four to six conducted experiments per notch height were available, which we used for a first comparison (see Figure 7.9 in Section 7.3).

Remark 33 (Reference to numerical solving in Section 7.4)**.** *For information on the used model, numerical solving, and computing of the loading forces for comparison of simulation and experiment, we refer to Section 7.4 and Chapter 3. In each Newton/active-set step, the linear system is solved with a direct solver from UMFPACK [60, 59] (as in all numerical results apart from Chapter 7).*

Figure 7.6 (black lines) displays the load-displacement curves of five punctured EPDM strips with a notch height of 18 mm. At the beginning of the load-displacement curves, one can see the nonlinear behavior of the material, not represented by the linear elasticity model, though. The numerical tests are displayed in colored curves for two parameter settings (150% fit and Neo Hookean) for three values for G_C to identify a first approximative value of the critical energy release rate G_C.
In particular, the pink curve with test name '$G_C = 18.0$ N/mm, 150 % fit' coincides with 'experiment 2' in the first maximum value when the crack propagates from the initial slit to the hole. Even if the load-displacement curves of experiments and simulations in Figure 7.6 differ mainly in the displacement value at total failure and maximal loading, two points can be captured: With $G_C = 18.0$ N/mm, the maximal displacement is relatively close to the experimentally achieved maximal displacements. Secondly, for all load-displacement curves in Figure 7.6, two loading peaks are similar and close to reality: the first one, when the crack starts propagating from the initial slit, the second one when the

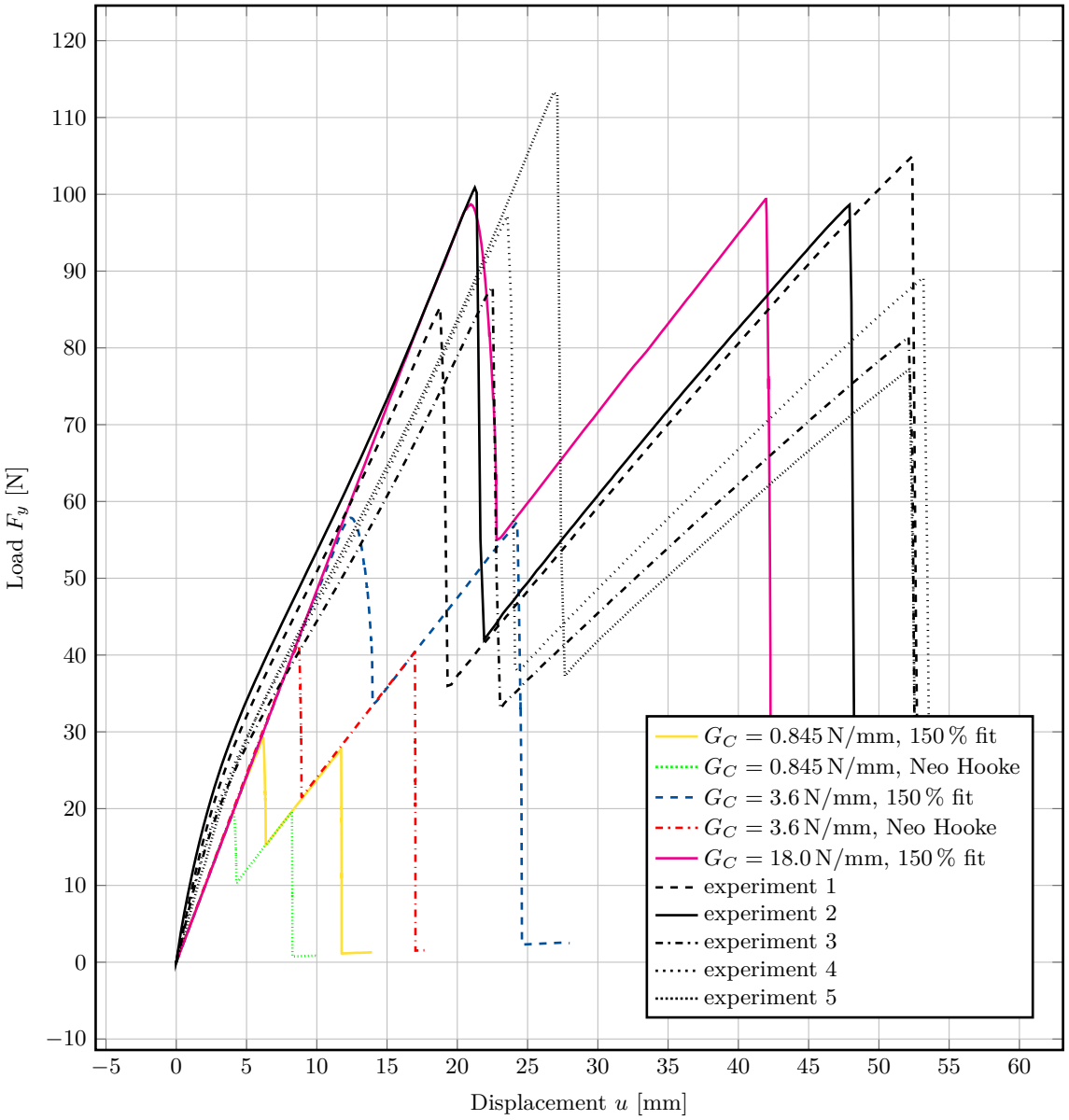

Figure 7.6: Load-displacement curves for the EPDM benchmark test with a notch at 18 mm and adaptively refined meshes. Here, the load-displacement curves are compared for three settings of the critical energy release rate $G_C = 0.845, 3.6, 18.0\,\mathrm{N/mm}$ with the experimental data (five experiments). Load measured on the top boundary.

crack propagates from the deformed inclusion to the right boundary until total failure. Aside from the main deficit using a linear elasticity model for nonlinear material behavior, a further reason could be the coarse finite element mesh used for the experiments (two steps of adaptive mesh refinements are used on a relatively coarse starting mesh).

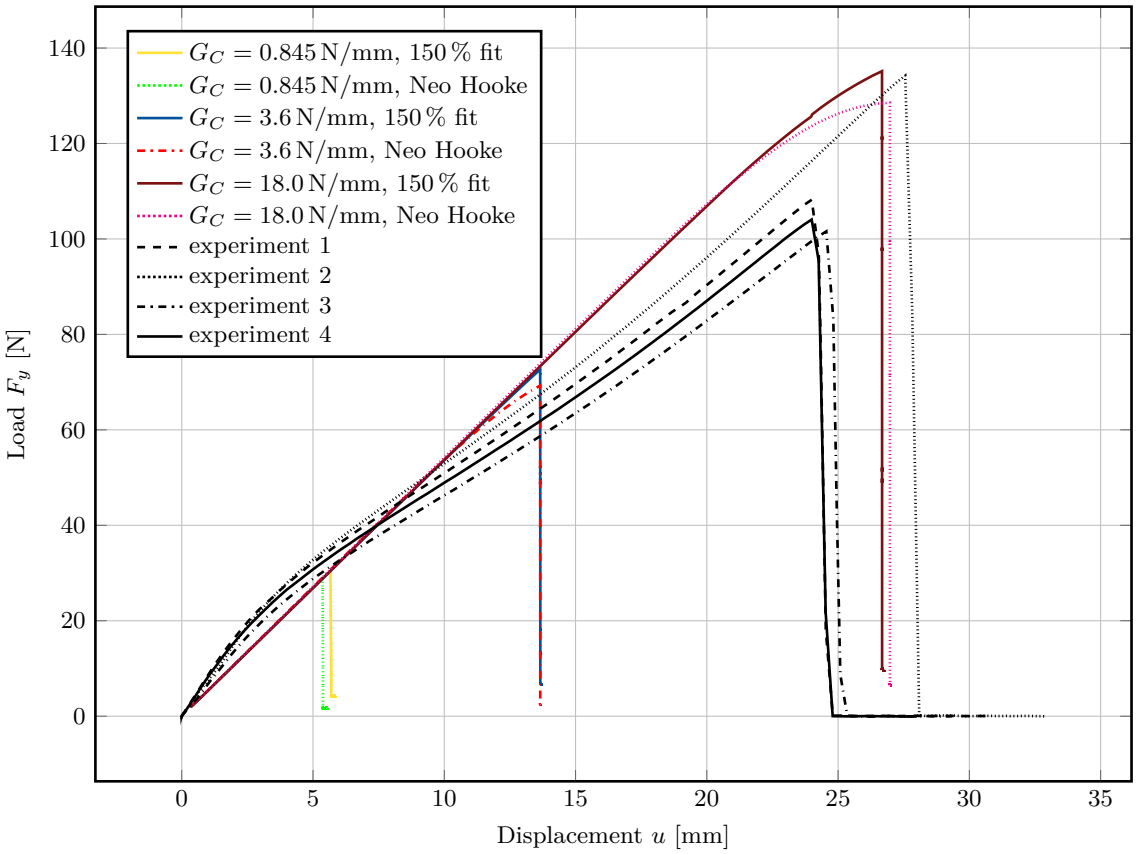

Figure 7.7: Load-displacement curves for the EPDM benchmark test with notch at 6 mm and adaptively refined meshes. Here, the load-displacement curves are compared for three settings of the critical energy release rate $G_C = 0.845, 3.6, 18.0\,\mathrm{N/mm}$ with the experimental data (four experiments). Load measured on the top boundary.

In Figure 7.7, the load-displacement curves are given by experimental data (black lines) and numerical computations (colored lines) for the tests with a notch height of 6 mm. in the numerical results, this test configuration is the only one of five notch heights where the crack path does not lead into the circular inclusion, which is also visible in the general shape of the load-displacement curves; see Section 7.3 for further details on the crack path behavior. Once the critical energy release rate is reached, and the crack starts propagating from the initial slit, the loading decreases towards zero (total failure). The reached maximal displacement of the simulations is close to the maximal displacement of the experiments for $G_C = 18.0\,\mathrm{N/mm}$ in Figure 7.7. Observing the pink and dark-red curves for both parameter settings and $G_C = 18.0\,\mathrm{N/mm}$, due to the linear behavior at the beginning of the load-displacement curves, the maximal value is larger than in the experiments, but the displacement values are similar at the crack starting point. From the results for $G_C = 18.0\,\mathrm{N/mm}$, we further deduce that the critical energy release rate should be slightly smaller than $G_C = 18.0\,\mathrm{N/mm}$, computed in

Section 7.2.2.

Remark 34 (Quasi-time steps)**.** *We assume that a significant part of the errors in the maximal loading and displacement in Figures 7.6 and 7.7 stems from the quasi-static model. Fractures in punctured EPDM rubber propagate fast (broken within approximately* 0.1 s*), which is challenging to capture with a quasi-static model. Dynamic phase-field fracture model could allow investigating the stated hypothesis.*

Remark 35 (Constant G_C)**.** *In the frame of this thesis, G_C is assumed to be constant during the simulations. Some measurements and considerations give evidence to suggest that this is not the case in reality. The critical energy release rate – the required force when the material starts to crack – depends on the material's temperature, which can be assumed to be 5-10 degrees Celsius higher in the crack tip. Further comments on this topic (thermo-elasticity) are given in Chapter 8 in the future tasks.*

7.3 Crack path experiments

In order to investigate the crack path behavior, punctured strips are elongated with 200 mm/min (related to traverse velocity) in a ZWICK Universal test machine until total failure, as seen in Figure 7.1 and in the following Figure 7.8.

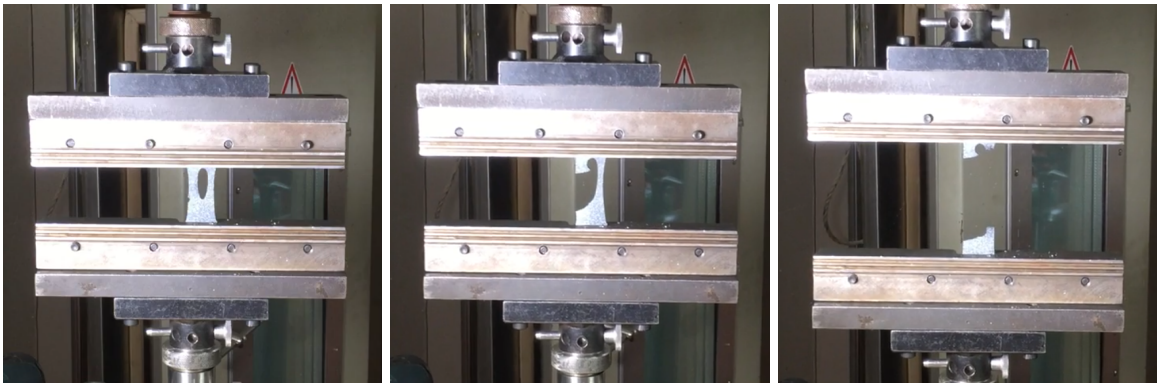

Figure 7.8: Snapshots of the experimental setup during stretching one of the punctured EPDM strips with a notch height of 12 mm until total failure in a ZWICK Universal test machine at the DIK.

An inhomogeneous forming strain and stress field during the experiment is introduced by a circular hole of 8 mm diameter in the upper right part of the strip; see Figure 7.14. A similar experimental setup was proposed and investigated by Ozelo et al. [137].
Variations of the experiments are realized by varying the position of the given notch on the left side with a length of 1 mm at 6, 10, 12, 14, and 18 mm height (from the bottom boundary). In all experiments, the hole has an impact on the crack path. While for 6 and 10 mm, the crack is diverted towards the hole but propagates below the hole towards the right edge, for 12, 14, and 18 mm the crack propagates into the hole, and grows further nearly at the middle right interior edge of the hole towards the boundary edge of the specimen; see Figures 7.9 and 7.10. Comparing the start of the propagating fracture, the notch height only has a minor influence on the force response. Although the distance between the initial notch and the circular hole is the shortest for the 14 mm test, the resistance is strong. We do not observe a clear trend between initial notch position and the start of the

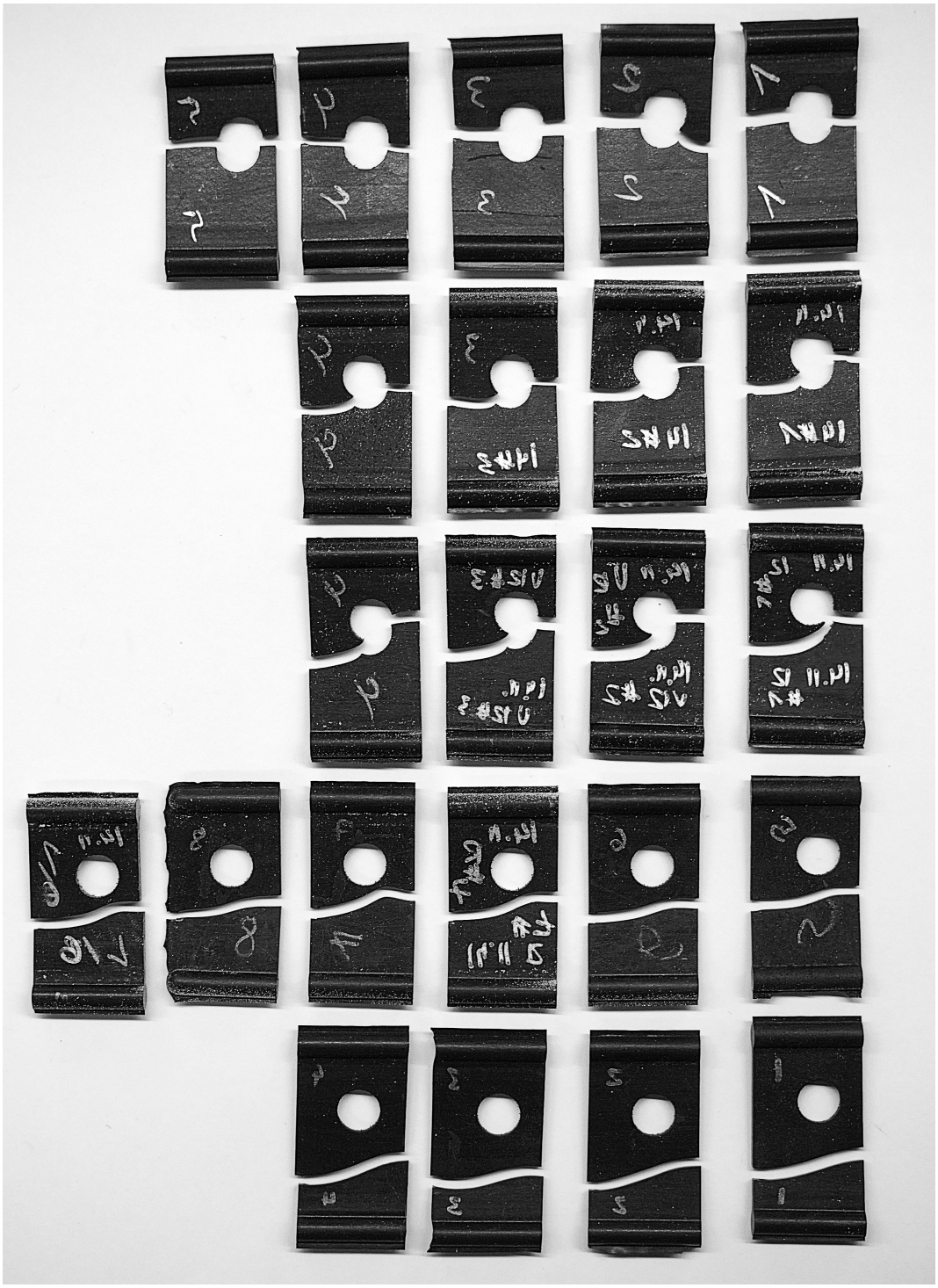

Figure 7.9: Overview of the executed tests concerning tracking of the crack paths, backside of tested punctured strips, with an initially given notch of 1 mm length and 18, 14, 12, 10, and 6 mm notch height (top to bottom).

force drop in the global displacement in Figure 7.13. The deviation in the (starting) crack behavior between the same experiments is typical for carbon black-filled rubbers. Despite the deviations in the force drop, the crack path is stable within the group of the same experiments for one notch height; see Figure 7.10.

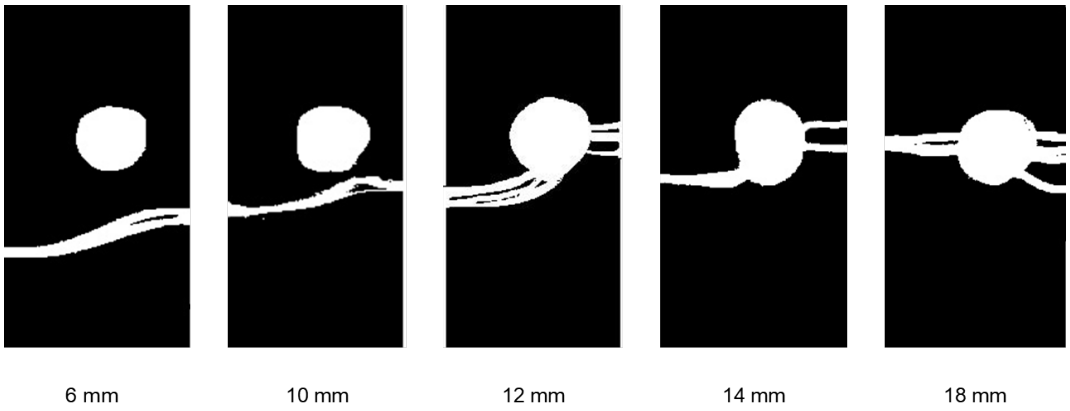

Figure 7.10: Evaluation of the averaged crack paths (4 to 6 experiments in Figure 7.9) of the tested punctured EPDM strips with given notches at the height of $6, 10, 12, 14$, and $18\,\text{mm}$ measured from the bottom boundary above the bottom bulges (left to right).

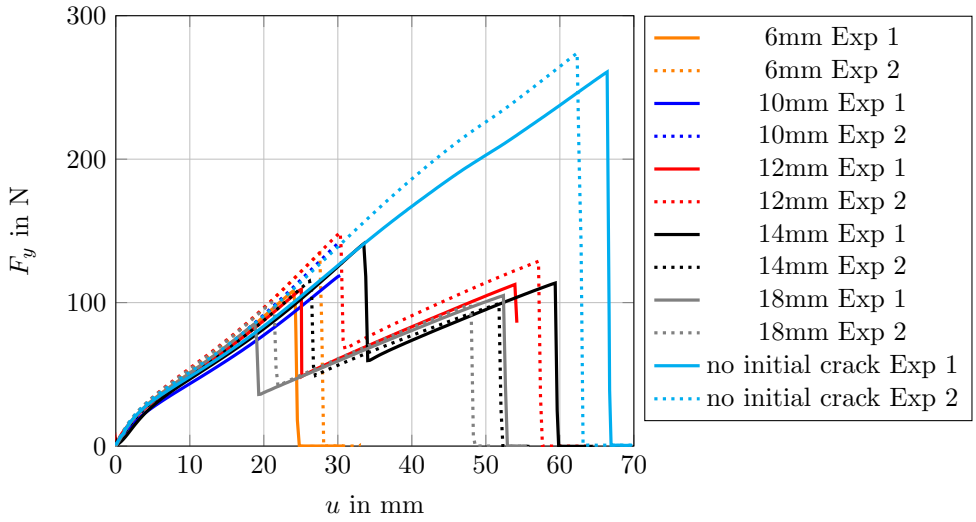

Figure 7.11: Two force-displacement curves for each notch height and test runs without an initial notch. Force response F_y versus the traverse displacement u measured in the y-direction on the top boundary of the EPDM strips.

In Figure 7.12, the maximal loading forces at the crack start are given for the experiments on punctured strips with different notch heights compared to the numerical results for each test. Concerning the experiments, we see a fully evolved crack to the opposite edge (6 and 10 mm) respectively or an evolved crack to the hole (12, 14, and 18 mm) in Figures 7.9, 7.10, and 7.11. In red (left bar) and blue (right bar) in Figure 7.12, the numerical results for the force maximum are plotted, based on the two colored parameter settings from Table 7.2 for the notch heights of 6 to 18mm.

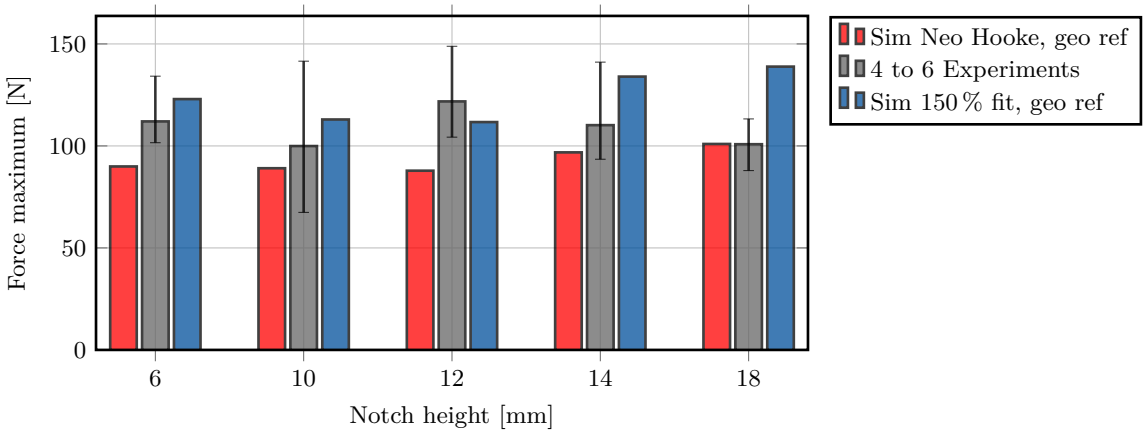

Figure 7.12: Maximal loading force F_y at the crack start measured on the top boundary, of experiments and finite element simulations. In gray (middle bar for each test), the averaged force maximum of 4 to 6 experiments in dependence of traverse displacement. The numerically achieved force maxima are given in red and blue (left and right for each notch height).

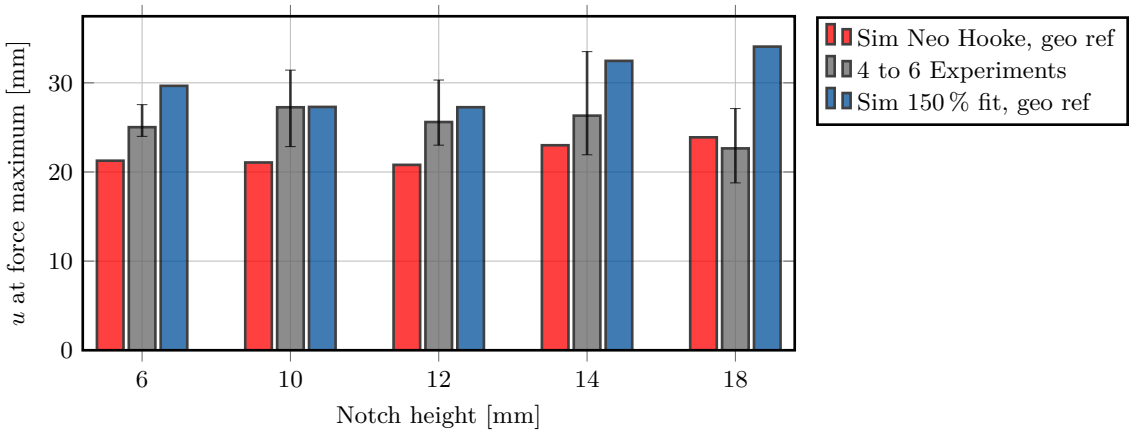

Figure 7.13: Traverse displacement u in the y-direction at the first force maximum of experiments and finite element simulations. In gray (middle bar), the average displacement of (4 to 6) experiments, in red and blue (left and right bar for each notch height), the numerically achieved displacements at the first force maximum are given.

In Figure 7.13, we present the experimental and numerical results of the traverse displacement at the first force maximum from Figure 7.12. The grey bars in the middle give the experimental weighted results, including the natural scattering of the experiments. In red (left bar) and blue (right bar), the results for the maximal displacement at the force maximum are plotted based on the parameter settings from Table 7.2.

7.4 Numerical simulations of punctured EPDM strips

We use the model from Chapter 5 based on Wu's functional (Section 4.6.3) and Amor's split (Section 4.7.2) for simulating crack propagation in punctured EPDM strips. The presented model in Section 5.2 builds the basis to simulate cracks in nearly incompressible solids with the help of a stable problem formulation in mixed form and discretized with Taylor-Hood elements ($Q_2^c Q_1^c Q_1^c$) from Section 3.2.3.
We start with the Euler-Lagrange equations in incremental form. Then, a detailed spatial convergence study is presented for the EPDM test with a notch height of 6 mm. Further, we compare the crack paths of simulation and experiments for the two chosen parameter settings from Table 7.2. Finally, we conclude the section with a discussion on the experimental and numerical results.

7.4.1 Phase-field fracture model in mixed form for EPDM

We combine Formulation 11 from Section 5.2 with Wu's energy functional definition from Equation (4.19) and Amor's volumetric-deviatoric splitting approach from Section 4.7.2. From that, our newly introduced mixed phase-field fracture problem based on Wu's energy functional and strain energy splitting of Amor et al. [7] in incremental form is given as:

Formulation 19 (Mixed phase-field formulation)**.** *Let the solutions of the previous incremental steps $\varphi^{n-1}, \varphi^{n-2} \in \mathcal{K}$ be given. Find $u := u^n \in \{u_D + \mathcal{V}\}$, $p := p^n \in \mathcal{U}$ and $\varphi := \varphi^n \in \mathcal{K}$ for the incremental steps $n = 1, 2, \ldots, N$ such that*

$$
\begin{aligned}
g(\tilde{\varphi})\left(\sigma^+(u,p), E_{lin}(w)\right) + \left(\sigma^-(u,p), E_{lin}(w)\right) &= 0 \quad \forall\ w \in \mathcal{V}, \\
g(\tilde{\varphi})\left(\nabla \cdot u, q\right) - \frac{1}{\lambda}(p,q) &= 0 \quad \forall\ q \in \mathcal{U}, \\
(1-\kappa)\left(\varphi\sigma^+(u,p) : E_{lin}(u), \psi - \varphi\right) + \frac{2G_C}{\pi}\left(-\frac{1}{\epsilon}\varphi, \psi - \varphi\right) & \\
+\frac{2G_C}{\pi}\epsilon\left(\nabla\varphi, \nabla(\psi - \varphi)\right) &\geq 0 \quad \forall\ \psi \in \mathcal{K},
\end{aligned}
$$

with Amor's splitting approach depending on u and p:

$$
\begin{aligned}
\sigma^+(u,p) &:= \mu \max\left\{0, tr\left(E_{lin}^+(u)\right)\right\} \mathbb{1} + 2\mu\left(E_{lin}^+(u) - \frac{1}{3} tr\left(E_{lin}^+(u)\right)\mathbb{1}\right) + p^+\mathbb{1}, \\
\sigma^-(u,p) &:= \mu\left(tr\left(E_{lin}^+(u)\right) - \max\left\{0, tr\left(E_{lin}^+(u)\right)\right\}\right)\mathbb{1} + (p - p^+)\mathbb{1}.
\end{aligned}
\tag{7.1}
$$

The block entries of the model formulation based on Wu's functional and Amor's splitting are given in Appendix B.7.

For the numerical simulation of the crack propagation in punctured strips in a two-dimensional setup with the help of the phase-field fracture model from Section 5.2, we reduce the geometry to the area of interest between the bulges on the bottom and top part, where the specimens are fixed. The geometry is given in Figure 7.14.

Remark 36 (Inclusions and phase-field)**.** *Considering holes in a material combined with phase-field fracture modeling is a challenging task; see Section 7.5, or [192, Section 8.2] and [129], for examples and further comments on the difficulty of inclusions.*

We determine homogeneous Dirichlet boundary conditions $u_y = 0$ on the top boundary, and the strips are fixed in the horizontal direction on the top, and bottom boundary with $u_x = 0$. The following boundary condition characterizes the loading force on the bottom boundary Γ_{force} in the y-direction:

$$u_y = -t \cdot 200\,\text{mm/min}, \quad \text{for } t \in I := [0; \text{total failure}], \tag{7.2}$$

where t denotes the total time. In a quasi-static context, the time interval I is divided into incremental steps of size δt. Further, the phase-field is fixed via $\varphi = 0$ in the given notch as an initial boundary condition. We decided to handle the given notch on the left side of size 1 mm with an initial condition $\varphi = 0$ such that the material is broken in the notch area. In addition, we describe the initial crack geometrically by doubling the dof on the respective faces similar to Wick [182, Section 5.1.]. This allows the material to open in the notch, and the maximal stress is obtained in the notch tip, which imitates the observed opening of the notch in running experiments.

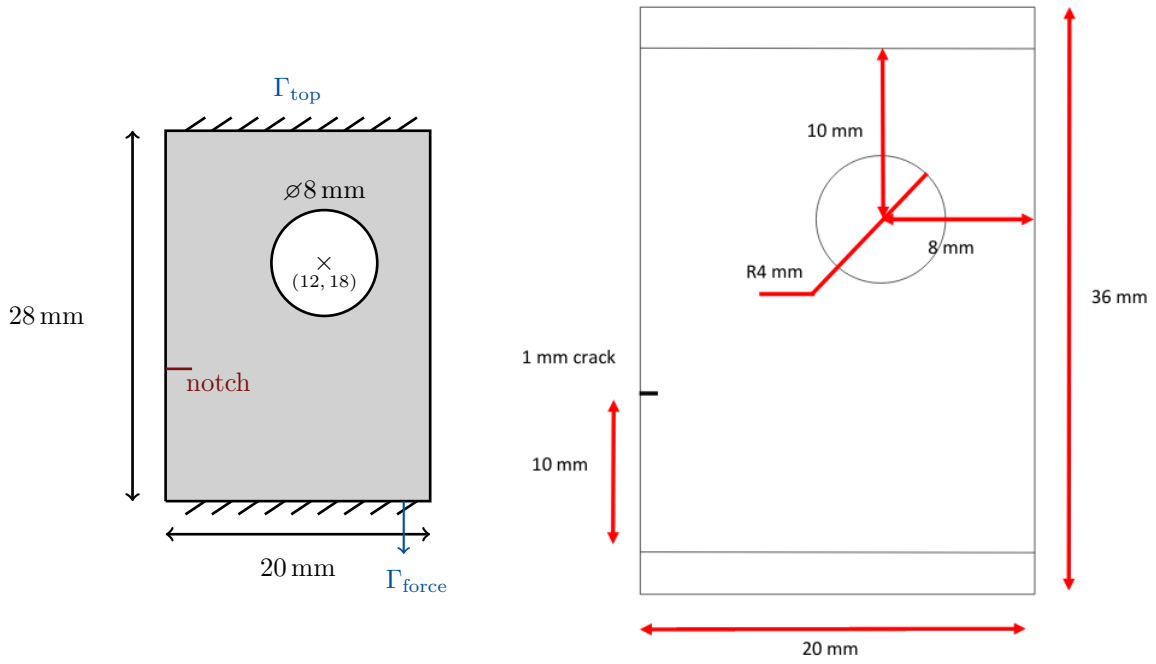

Figure 7.14: Left: geometry and boundary conditions of punctured EPDM strips for numerical simulations. Load force on Γ_{force} defined in Equation (7.2). Right: geometry of punctured EPDM strips produced at the DIK. The specimens have a thickness of 1.8 mm and the bulges on the top and the bottom of the specimen are of size 2.0 mm, which are not taken into account in the numerical simulation.

Parameter	description	value
h	discretization parameter (coarsest)	0.3 mm
# ref	number of adaptive refinement steps	0 to 3
ϵ	bandwidth	$2\,h$
δt	incremental step size	10^{-2} s
κ	regularization parameter	$0.01h$
	phase-field threshold for refinement	0.7

Table 7.3: Numerical parameters for the phase-field fracture simulation of punctured EPDM strips. Parameters '# ref' and the threshold for predictor-corrector are required for the adaptive test runs in Section 7.4.2. The numerical parameters $h, \epsilon, \delta t$ and κ are valid for all numerical test runs.

The numerical parameters are listed in Table 7.3. The setting of the numerical parameters in Table 7.3 applies for all numerical results considering the spatial convergence study with the 6 mm test using adaptive refinement. The incremental step size δt and the size of κ are the same for all numerical tests. Related to the material parameter setting, we choose two setups. The colored material parameters in Table 7.2 reflect the parameter settings based on two different assumptions for a linear stress-strain relation: Young's modulus is estimated via a Neo Hookean model and a fit of 150 % of the strain. In all following numerical results and especially in the figures of this section, the material parameters' setting differs via naming it '150 % fit' or 'Neo Hooke'. The bulk modulus $K = 2\,595$ MPa listed in Table 7.2 is specified via an averaged value of fitted values. The critical energy release rate is adopted from Section 7.2.2 with $G_C = 17.0$ N/mm. We use the experimentally determined critical energy, not the fitting on force-displacement one from Section 7.2.3.

Remark 37 (Plane stress)**.** *We stress that it is sufficient to assume plane stress since the experimental specimens are thin, which justifies two-dimensional numerical simulations.*

7.4.2 Spatial convergence study

To study spatial convergence of the finite element simulation, we start with tests for one of the five test setups: the given notch is at the height of 6 mm, where experimentally we do not expect the crack propagating towards the hole but in an 'S'-curve from left to right. For this example, we conduct four tests on a global pre-refined mesh with a discretization parameter $h_{\text{start}} = 0.3$ mm and three tests with one to three adaptive refinement steps. The numerical results are given in Figure 7.4.2. The number of dof for all conducted test runs of spatial convergence are listed in Table 7.4. While refining the area around the crack adaptively with the help of the predictor-corrector scheme from [87] (Section 3.3.1), which decreases h locally, the length scale parameter ϵ is fixed. Consequently, for all computations considered in Figure 7.15, it holds $\epsilon = 0.6$ mm. To get an idea how the predictor-corrector scheme works within the propagating fracture, we depict the meshes at five certain loading points for one test (6 mm, Neo Hooke, hole) in Figure 7.16.

Besides spatial convergence, we want to avoid locking effects that could arise in the mesh around the circular hole. The test with a notch at 6 mm height gives a crack path away from the hole, even if the inclusion impacts the crack pattern. The refinement series is conducted for both material parameter settings (Neo Hooke and 150 % strain fit) without an inclusion.

In total, we observe three points in Figure 7.15:

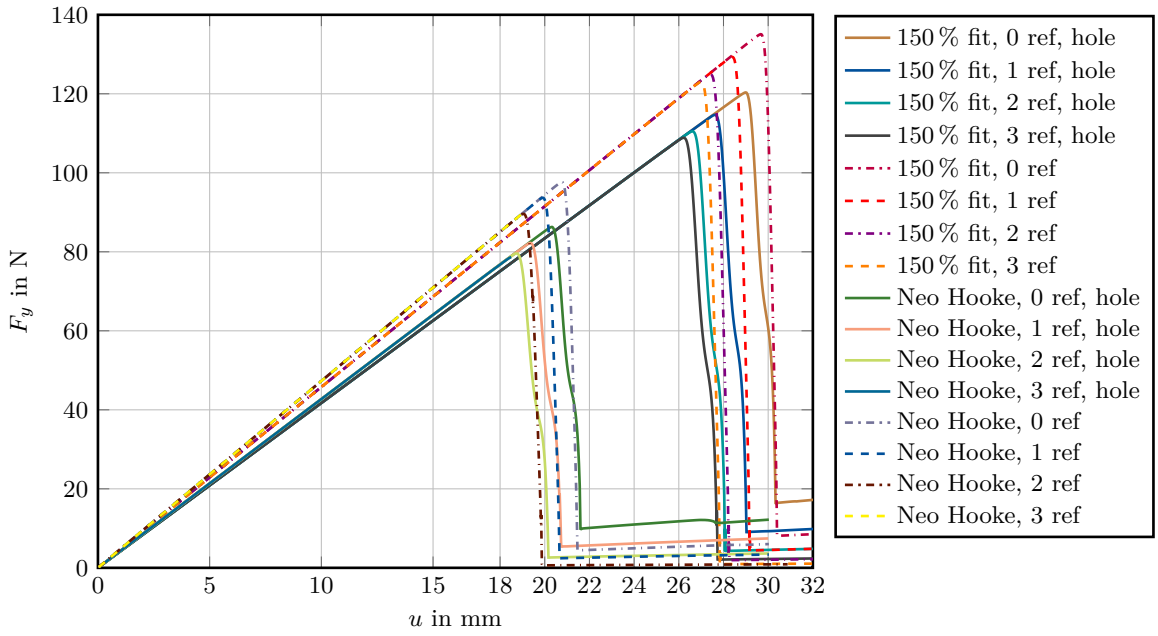

Figure 7.15: Numerical refinement study: force-displacement curves (displacement u in the y-direction versus force F_y) for the EPDM benchmark test based on the material parameters of Table 7.2 (150 % fit of strain) compared the material parameters of Table 7.2 with a notch at 6 mm, $h_{\text{start}} = 0.3$ and $\epsilon = 2h_{\text{start}} = 0.6$ mm fixed. $G_C = 17.0\,\text{N/mm}$. The computation of the force response F_y on the top boundary is defined in Equation (4.21) in Section 4.6.4.

- We compare the results based on the Neo Hookean material parameters from Table 7.2 with the computation based on the 150 % strain fit assumption;
- We present the numerical results based on the geometry in Figure 7.14 with a given notch and a circular hole in the upper right part of the strips compared to results based on the same geometry with a given notch but without a hole. The results in Figure 7.15 based on the punctured strips are marked with the attribute 'hole' in the legend;
- The third point discussed in Figure 7.15 is spatial convergence of the force-displacement curves with an increasing number of adaptive refinement steps, while the crack width ϵ is fixed as in Table 7.3 even if h is getting smaller in the crack area. In the legend of Figure 7.15 the number of refinement steps ('# ref') is given for each force-displacement curve.

The increase of the force response based on the punctured strips is lower than without a circular inclusion. From this, one could follow that the inclusion makes the material more elastic and decreases the material stiffness. We observe a significant difference between the force-displacement curves of the tests based on the 150 % fit or Neo Hookean material parameters. All Neo Hookean tests have a lower maximal force, leading to a smaller displacement when the crack starts propagating (see Figures 7.12 and 7.13). In Figure 7.15, we observe spatial convergence within tests from 0 to 3 adaptive refinement steps.
In Figure 7.17, the numerically and the experimentally achieved force-displacement curves have a similar course. To retrace the differences in the load-displacement curves while the crack propagates,

Test description	#dof u	(#dof p) = (#dof φ)
150 % fit & Neo Hooke, 0 ref, hole	49 984	6 352
150 % fit, 1 ref, hole	65 284	8 277
150 % fit, 2 ref, hole	117 400	14 815
150 % fit, 3 ref, hole	304 786	38 288
150 % fit, 0 ref	51 906	6 577
150 % fit, 1 ref	70 376	8 898
150 % fit, 2 ref	135 220	17 028
150 % fit, 3 ref	369 498	46 359
Neo Hooke, 1 ref, hole	65 420	8 294
Neo Hooke, 2 ref, hole	119 396	15 067
Neo Hooke, 3 ref, hole (Fig. 7.16)	293 572	36 880
Neo Hooke, 0 ref	51 906	6 577
Neo Hooke, 1 ref	70 446	8 907
Neo Hooke, 2 ref	136 742	17 308
Neo Hooke, 3 ref	371 840	46 650
Figure 7.19	237 436	29 877
Figure 7.20	391 656	49 192
Figure 7.21	427 932	53 731
Figure 7.22	437 544	54 934
Figure 7.23	581 724	72 979

Table 7.4: Degrees of freedom (#dof) for all numerical test runs with a notch height 6 mm from Figure 7.15, and the Figures 7.19 to 7.23 for the displacement u (Q_2^c elements) and the pressure variable p (Q_1^c elements), which has the same number of dof as the phase-field variable φ (Q_1^c elements). The number of dof for the test with adaptive predictor corrector mesh refinement from Figure 7.15 are given for the mesh at total failure in the last computed incremental step.

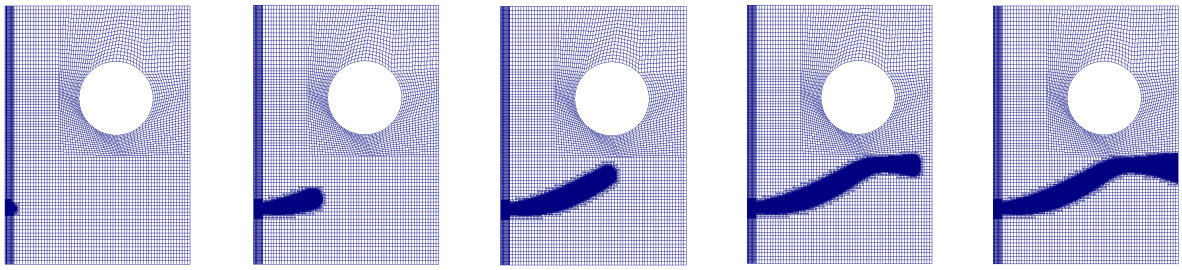

Figure 7.16: Adaptively refined meshes at five specific time points for the numerical simulation based on the Neo Hookean material parameter setting from Table 7.2 and three steps of adaptive refinement steps via the predictor-corrector scheme from [87]; see the blue-green curve in Figure 7.15 ('Neo Hooke, 3 ref, hole'). In the last snapshot, the mesh has 293 572 dof for the solid displacements and 36 880 dof for the pressure and the phase-field variable.

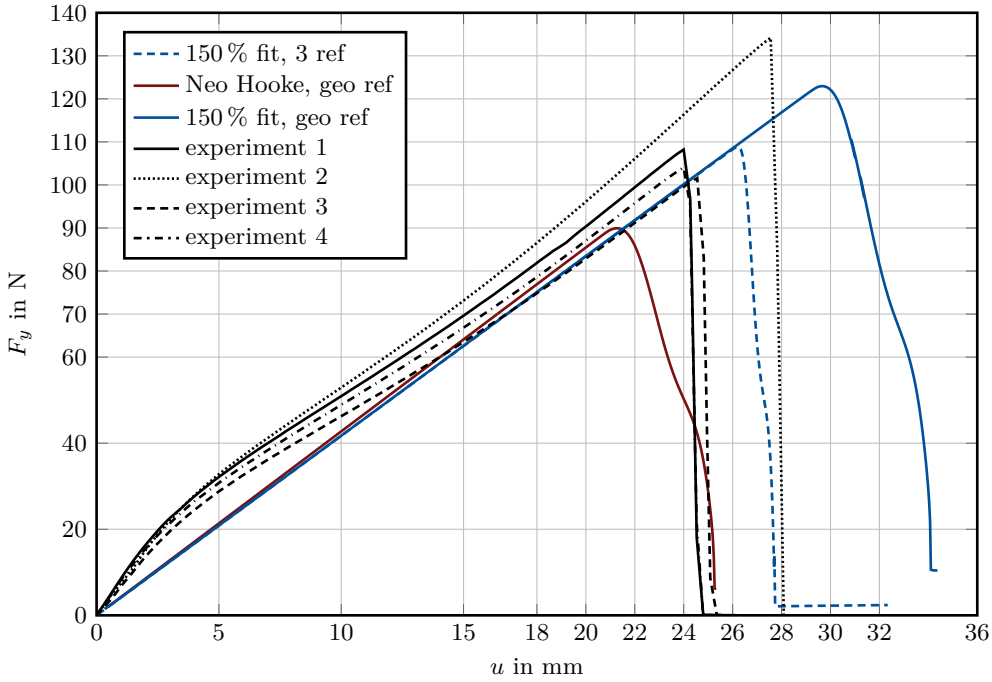

Figure 7.17: Comparison of the force-displacement curves (displacement u in the y-direction versus force F_y) for the samples with a notch at 6 mm height (experiments 1 to 4 versus simulations).

in Figure 7.18, snapshots of the phase-field function are given on the deformed domain (u_x and u_y) at specific displacements applied on the bottom boundary to see the difference between the Neo Hookean and the 150 % fit setting. We notice that the material cracks earlier with the Neo Hookean parameter setting from Table 7.2. In addition, the material starts inverting, which is a non-physical effect because of missing contact conditions.

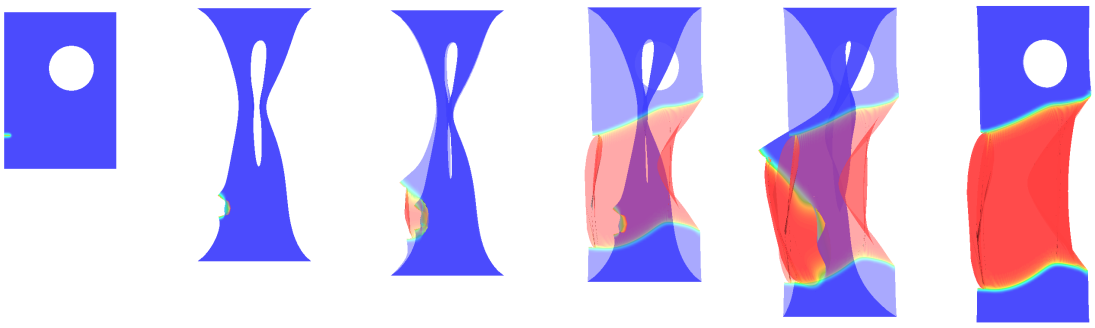

Figure 7.18: FEM simulation via mixed phase-field fracture modeling of crack propagation in punctured EPDM strips based on the material parameters of Table 7.2 for Neo Hooke (transparent) and 150 % fit (strong color) with a given notch at 6.0 mm and 0 mm, 17 mm, 19 mm, 20 mm, 27 mm and 28 mm y-displacement on the bottom boundary from left to right.

Here, not just the results on the finest mesh 'Neo Hooke, 3 ref' and '150 % fit, 3 ref' from Figure 7.15 are given in Figure 7.17, but also the results from a second test run, where we geometrically pre-

refined two times the area from 2 mm below the notch until 1 mm above the circular hole in addition to a globally pre-refined mesh with cell diameter $h = 0.3$. See Figure 7.23, for the finite element mesh used for the dashed and colored force-displacement curves given in Figure 7.17. The force-displacement curves from the simulations computed on the geometrically pre-refined meshes yield better results compared to the experiments than the results based on adaptively refined meshes and fixed bandwidth ϵ. The observed mesh-sensitivity of phase-field fracture models is widely discussed in the literature, e.g., in [4, 128, 87, 124, 182]. Further, we indicate that the length scale ϵ, the relation ϵ-h, and the incremental step size δt can impact the accurate shape of the force-displacement curves.

7.4.3 Crack paths comparison

Figures 7.19 to 7.23 show the phase-field functions for five notch heights compared to the experimental crack paths after total failure. The finite element meshes are geometrically pre-refined, including the hole and the given notch. The used numbers of dof in Figures 7.19 to 7.23 are listed in the lower part of Table 7.4. For the tests with a given notch at 18 mm, 14 mm, 12 mm and 6 mm, the crack paths of the simulation coincide sufficiently with the average crack paths from four to six conducted experiments in Figures 7.19, 7.20, 7.21, and 7.23. Furthermore, the numerically achieved crack paths for the two parameter settings 'Neo Hooke' and '150% fit' are similar for all five tests with different notch heights. The location and angle from where the crack passes the circular inclusion varies slightly; see e.g., Figure 7.21. In Figure 7.22, snapshots of the phase-field function for both parameter settings are given for the test with a notch at 10 mm. In the experiments for this test case, the crack propagates close to the hole but not into the hole. Compare also Figure 7.9 for the 10mm test (second row from the bottom), especially the first, third, and fourth test specimen, where the crack propagates close to the hole. The phase-field fracture simulation shows a fracture path similar to those of the 14 and 18mm tests. One reason could be that the crack width ϵ is, from a numerical point of view, not small enough to allow cracks close to the boundary of the hole without cracking into it.

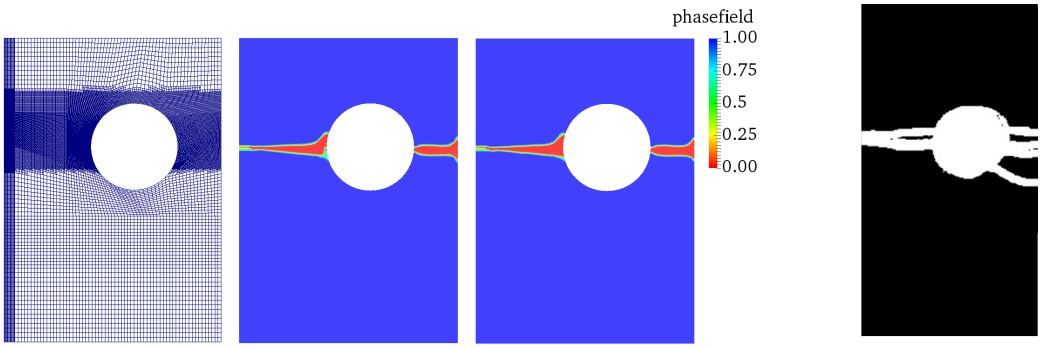

Figure 7.19: Snapshots of the phase-field function after total failure compared to the experimental results for the samples with a notch at 18 mm height. From left to right: the geometrically pre-refined mesh, the phase-field function based on the Neo Hookean parameter setting from Table 7.2, the phase-field function based on the 150 % strain fit parameter setting from Table 7.2, the experimental results from 5 executed experiments.

In the numerical results in Figure 7.19 to 7.22, we observe that the location where the crack propagates from the hole to the right boundary of the EPDM strips is in the middle of the hole and goes straight to the right (shortest way for the crack). In the experiments the angles and paths of the crack paths on the right of the hole vary a lot; see, for example, Figure 7.19.

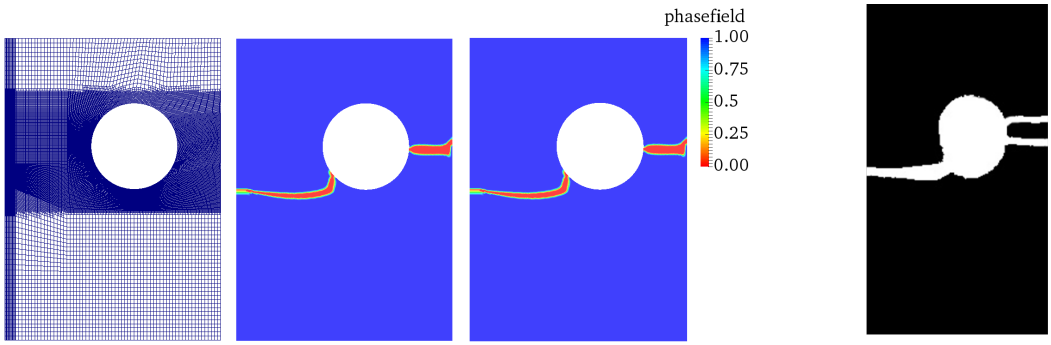

Figure 7.20: Snapshots of the phase-field function after total failure compared to the experimental results for the samples with a notch at 14 mm height. From left to right: the geometrically pre-refined mesh, the phase-field function based on the Neo Hookean parameter setting from Table 7.2, the phase-field function based on the 150 % strain fit parameter setting from Table 7.2, the experimental results from 4 executed experiments.

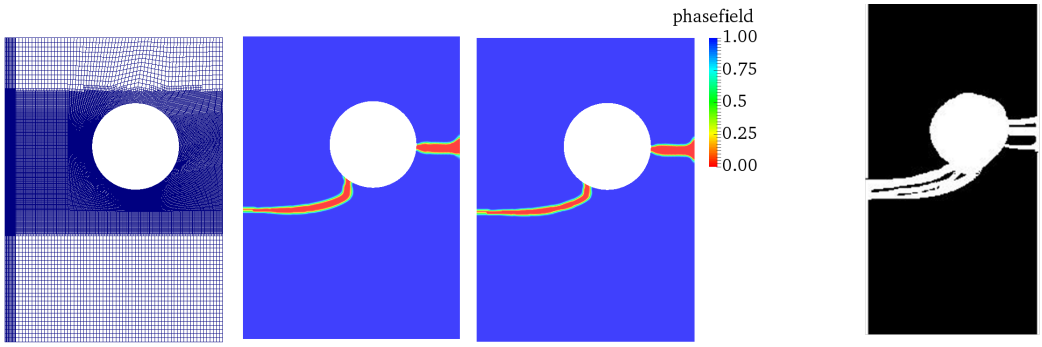

Figure 7.21: Snapshots of the phase-field function after total failure compared to the experimental results for the samples with a notch at 12 mm height. From left to right: the geometrically pre-refined mesh, the phase-field function based on the Neo Hookean parameter setting from Table 7.2, the phase-field function based on the 150 % strain fit parameter setting from Table 7.2, the experimental results from 4 executed experiments.

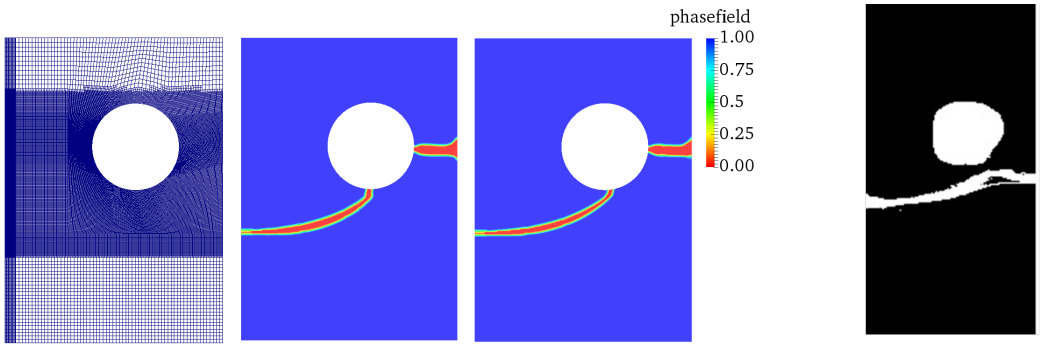

Figure 7.22: Snapshots of the phase-field function after total failure compared to the experimental results for the samples with a notch at 10 mm height. From left to right: the geometrically pre-refined mesh, the phase-field function based on the Neo Hookean parameter setting from Table 7.2, the phase-field function based on the 150 % strain fit parameter setting from Table 7.2, the experimental results from 6 executed experiments.

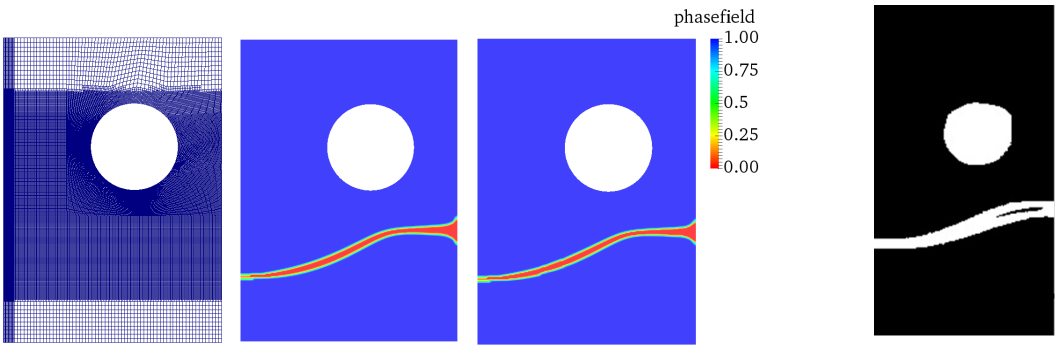

Figure 7.23: Snapshots of the phase-field function after total failure compared to the experimental results for the samples with a notch at 6 mm height. From left to right: the geometrically pre-refined mesh, the phase-field function based on the Neo Hookean parameter setting from Table 7.2, the phase-field based on the 150 % strain fit parameter setting from Table 7.2, the experimental results from 4 executed experiments.

7.4.4 Discussion of experimental and numerical results

Despite the assumed simplifications related to geometrical and material nonlinearities, our mixed model can capture the behavior qualitatively and quantitatively while interpreting the mechanical model variations as lower and upper estimates; see Figures 7.12 and 7.13. The experimental data related to the tracking of the crack paths and the respective numerical simulations suggest a clear dependency on the initial crack position, which the numerical simulations confirm. In the bottom row in Figure 7.9 and in Figure 7.23, even for an initial crack near the lower boundary (6 mm) far from the hole, the impact of the inhomogeneous stress/strain field is still apparent. The crack starts perpendicularly to the direction of tension on the right side (here: backside), but is diverted upwards later on and returns to a perpendicular path in the end. This effect is observed in the experimental data till initial cracks with a notch height of 10 mm. The path is diverted downwards at the end of the crack path for specimens marked with #7 in Figure 7.9 (second row from below, third specimen from the left). In the finite element simulation, the crack path within the 10 mm test differs such that the crack propagates into the hole, as seen in the 12, 14, and 18 mm tests. For initial cracks at 12, and 14 mm height, the path proceeds in a curved shape into the hole and continues perpendicular on the other side. At 18 mm height, approximately on the position of the circle's center, the initial crack propagates directly perpendicular into the hole and propagates likewise on the other side until complete rupture. The same can be observed in the numerical results for the tests with a notch height of 12, 14, and 18 mm. Evaluating the statistics of the experiments, repeatability is given. The repetitions of the tests indicate that minor variations, e.g., small changes in the initial crack length or its angle, have small effects on the general crack path. Although dealing with a carbon black-filled rubber, no bifurcations in the crack paths for the EPDM compound were observed. Due to the high variation in the onset of total failure in the experiments, the calibration of related phase-field parameters might be tricky in the future.

7.5 Numerical studies on the impact of energy functional and stress split

Our choice of the energy functional and the strain energy splitting in Section 7.4.3 is deliberately fitted to the experiments proposed in this chapter. We made the experience that even with a given notch, the crack starts propagating from the circular hole in the interior of the EPDM strip and propagates simultaneously to the left and right, if the mixed phase-field fracture model is based on an Ambrosio-Tortorelli functional [5, 6] (AT_1 or AT_2, see [163] for a comparison of AT_1 and AT_2 considering crack nucleation) and the elastic energy splitting approach of Miehe [130]. This high sensitivity around the inclusion also for a small incremental step size δt and proper adaptive refinement schemes led us to the energy functional of Wu [189] and Amor's volumetric-deviatoric energy splitting [7]. For example by Wu et al. [192], a pre-cracked sample with two holes is presented in a compressible solid. Besides the fact that different crack path results are presented depending on the mesh, the boundary conditions, initial conditions, and the underlying phase-field model, inclusions are an additional challenge [192, Section 8.2]. Other references on computing and discussing crack propagation in solids with inclusions are, e.g., [197, 12, 120, 113].

Related to the first studies on different functional and stress splitting approaches, in Sections 4.6.4 and 4.7.3, in this section, we conduct numerical studies based on the mixed problem formulation and for simulating cracks in punctured EPDM strips to retrace our choice of functional and splitting for punctured EPDM strips[3].

Three energy functionals and two(commonly used) stress splitting approaches were proposed in Sections 4.6 and 4.7. This leads to six possible combinations of energy functionals and splitting approaches. For the mixed problem formulation from Formulation 19 (Section 7.4.1) and in the context of experiments with punctured EPDM strips, we briefly repeat the energy functionals and stress splitting schemes depending on u, p, and φ. The AT_2 functional is defined as

$$\begin{aligned} \mathrm{AT}_2: \quad E_\epsilon(u,p,\varphi) \coloneqq & \int_\Omega \frac{g(\varphi)}{2}\sigma(u,p) : E_{\mathrm{lin}}(u)\,dx \\ & + \int_\Omega \frac{G_C}{2}\frac{(1-\varphi)^2}{\epsilon}\,dx + \int_\Omega \frac{G_C}{2}\epsilon|\nabla\varphi|^2\,dx. \end{aligned} \tag{7.3}$$

The block entries of the Jacobian based on the Euler-Lagrange equations derived from the AT_2 functional, are given in Appendix B.2 and B.5 with Miehe and Amor splitting, respectively.

The AT_1 functional is defined as

$$\begin{aligned} \mathrm{AT}_1: \quad E_\epsilon(u,p,\varphi) \coloneqq & \int_\Omega \frac{g(\varphi)}{2}\sigma(u,p) : E_{\mathrm{lin}}(u)\,dx \\ & + \int_\Omega \frac{3G_C}{8}\frac{1-\varphi}{\epsilon}\,dx + \int_\Omega \frac{3G_C}{8}\epsilon|\nabla\varphi|^2\,dx. \end{aligned} \tag{7.4}$$

Wu's energy functional in Equation (4.19) uses a combination of a linear and a quadratic part in the crack energy term, which has the advantage of finite support for a localized phase-field [189].

The block entries of the Jacobian based on the Euler-Lagrange equations derived from the AT_1 func-

[3] Results of this section are published in [127].

tional, are given in Appendix B.3 and B.6 with Miehe and Amor splitting, respectively.
We refer to Wu [189] for a unified phase-field fracture model with the energy functional

$$\begin{aligned} \text{Wu}: \quad E_\epsilon(u,p,\varphi) \coloneqq & \int_\Omega \frac{g(\varphi)}{2}\sigma(u,p) : E_{\text{lin}}(u)\, dx \\ & + \int_\Omega \frac{G_C}{\pi}\frac{2(1-\varphi)-(1-\varphi)^2}{\epsilon}\, dx + \int_\Omega \frac{G_C}{\pi}\epsilon|\nabla\varphi|^2\, dx. \end{aligned} \tag{7.5}$$

The block entries of the Jacobian based on the Euler-Lagrange equations derived from Wu's functional, are given in Appendix B.4 and B.7 with Miehe and Amor splitting, respectively.
In the model formulations from Equations (7.3), (7.4), and (7.5), we do not distinguish between fracture behavior in tension and compression. The most popular approaches of stress splitting are given by Miehe et al. [130, 132] and Amor et al. [7]; see Section 4.7 for further details. From [130, 132], proposed in Section 4.7.1, we differentiate between compressive and tensile loading. The tensile and compressive parts of the strain tensor can be defined with Miehe's split [130, 132] as:

$$\begin{aligned} \sigma^+_{\text{Miehe}}(u,p) &\coloneqq 2\mu E^+_{\text{lin}}(u) + p^+\mathbb{1}, \\ \sigma^-_{\text{Miehe}}(u,p) &\coloneqq 2\mu\left(E_{\text{lin}}(u) - E^+_{\text{lin}}(u)\right) + \left(p - p^+\right)\mathbb{1}. \end{aligned} \tag{7.6}$$

Amor et al. [7] proposed a volumetric-deviatoric decomposition of the elastic energy density: (same definition as in Equation (7.1)):

$$\begin{aligned} \sigma^+_{\text{Amor}}(u,p) &\coloneqq \mu \max\left\{0, \text{tr}\left(E^+_{\text{lin}}(u)\right)\right\}\mathbb{1} + 2\mu\left(E^+_{\text{lin}}(u) - \frac{1}{3}\text{tr}\left(E^+_{\text{lin}}(u)\right)\mathbb{1}\right) + p^+\mathbb{1}, \\ \sigma^-_{\text{Amor}}(u,p) &\coloneqq \mu\left(\text{tr}\left(E^+_{\text{lin}}(u)\right) - \max\left\{0, \text{tr}\left(E^+_{\text{lin}}(u)\right)\right\}\right)\mathbb{1} + (p-p^+)\mathbb{1}. \end{aligned} \tag{7.7}$$

Via

$$g(\varphi)\sigma(u,p) = g(\varphi)\sigma^+(u,p) + \sigma^-(u,p),$$

the energy functionals from Equations (7.3), (7.4), and (7.5) could be reformulated, such that we end up with six combinations of functional and splitting definition resulting six phase-field fracture models for incompressible solids. In the following, we present the numerically achieved crack paths for these six models.

Remark 38 (Description of the mixed models)**.** *Implicitly in the current section, the six developed phase-field fracture models are given. In Section 5.6, we derived the final incremental Formulations 16 and 17 based on the AT_2 functional and no Cauchy stress split. In Formulation 19 from Section 7.4.1, we presented the model in mixed form based on Wu's functional and Amor's splitting scheme, which is chosen as the best fitting model for fractures in punctured EPDM strips. The block entries of the discrete systems of all six models are given in Appendix B, which can be of interest for implementing of the models.*

The test setup and the geometry remains the same as in Section 7.4. The numerical parameters for the numerical studies of this section are given in Table 7.5. In the frame of this study, we assume to have

Poisson ratio $\nu = 0.49$ and a critical energy release rate $G_c = 0.97\,\mathrm{N/mm}$ (to reduce the simulation run-time for this study). For adaptively refined meshes, we use three steps with the predictor-corrector scheme on a uniform mesh according to [87] with a threshold of 0.5 for the phase-field variable; see Section 3.3.1.

Parameter	description	value
λ	Lamé's first parameter	$60\,\mathrm{N/mm^2}$
μ	shear modulus	$1.22\,\mathrm{N/mm^2}$
ν	Poisson's ratio	0.49
G_C	critical energy release rate	$0.97\,\mathrm{N/mm}$
ϵ	bandwidth	$3\,h$
δt	incremental step size	$10^{-3}\,\mathrm{s}$
κ	regularization parameter	$0.01\,h$

Table 7.5: Material and numerical parameters for results presented in Figures 7.24 to 7.29.

In Figures 7.24 to 7.29, the numerically achieved crack paths are presented for five initial notch heights from 6 to 18 mm from the bottom boundary compared to the experimentally observed crack paths (see Figure 7.9). Further, in the six Figures 7.24 to 7.29, the crack paths results differ due to energy functionals and stress splitting approaches.

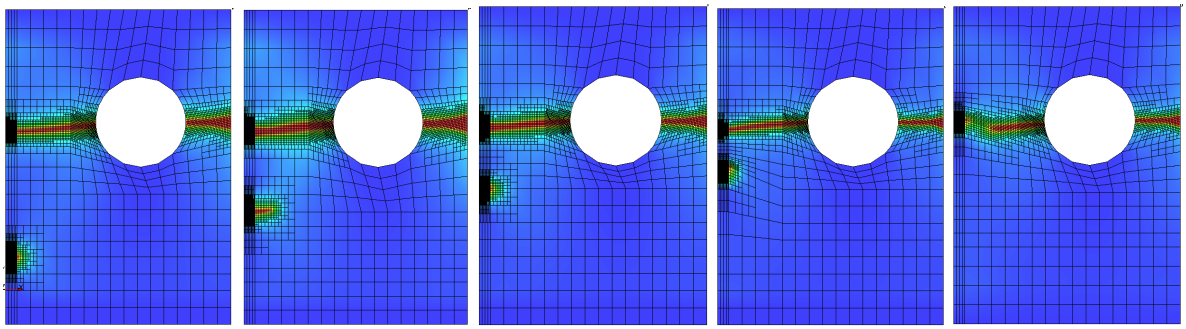

Figure 7.24: Snapshots of the phase-field solution (from blue - unbroken to red - broken) in punctured EPDM strips based on AT_2 functional from Equation (7.3) and Miehe splitting from Equation (7.6) with a given notch at $6, 10, 12, 14$ and $18\,\mathrm{mm}$ from left to right.

The crack path results based on the AT_2 functional from Equation (4.17) for both stress splitting approaches have a more smeared crack zone compared to the other energy functionals. In other, words, the AT_2 functional with a quadratic term has a less steep gradient in the phase-field function than AT_1 or Wu's approach. Aside from this, for all five notch heights in Figures 7.24 and 7.25, the crack starts propagating from the hole to the left and right. The crack paths in Figures 7.26 and 7.27 have a thinner zone where the phase-field variable φ has values between 0 and 1, which means the AT_1 functional allows a sharper crack area. Aside from the third test in Figure 7.26 and the fourth in Figure 7.27, the computed crack paths do not match the experimentally achieved crack paths from Figure 7.9. A high sensitivity around the circular hole is observed for all AT_2 and AT_1 tests.
Based on Wu's functional and Miehe's split, the crack paths for all five test configurations match with the experiments in Figure 7.28, but we can not achieve convergence of the nonlinear solver within 100 Newton steps for the first two tests with a notch height of 6 and 10 mm at the time point of

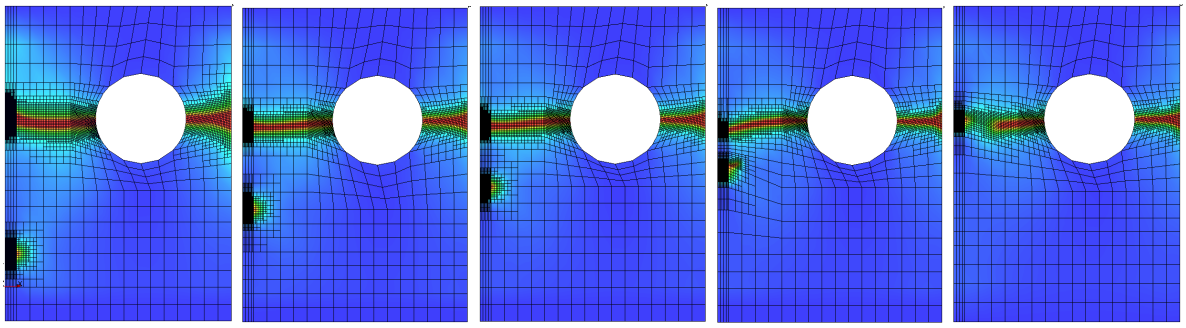

Figure 7.25: Snapshots of the phase-field solution (from blue - unbroken to red - broken) in punctured EPDM strips based on AT_2 functional from Equation (7.3) and Amor splitting from Equation (7.7) with a given notch at $6, 10, 12, 14$ and $18\,\text{mm}$ from left to right.

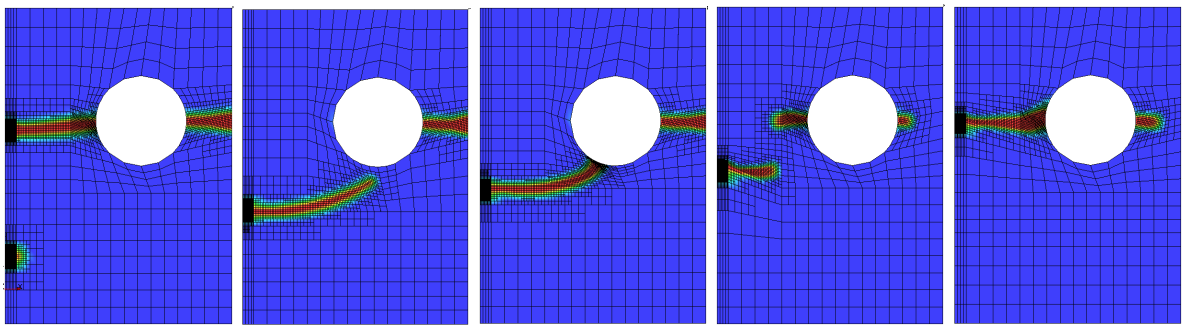

Figure 7.26: Snapshots of the phase-field solution (from blue - unbroken to red - broken) in punctured EPDM strips based on AT_1 functional from Equation (7.4) and Miehe splitting from Equation (7.6) with a given notch at $6, 10, 12, 14$ and $18\,\text{mm}$ from left to right.

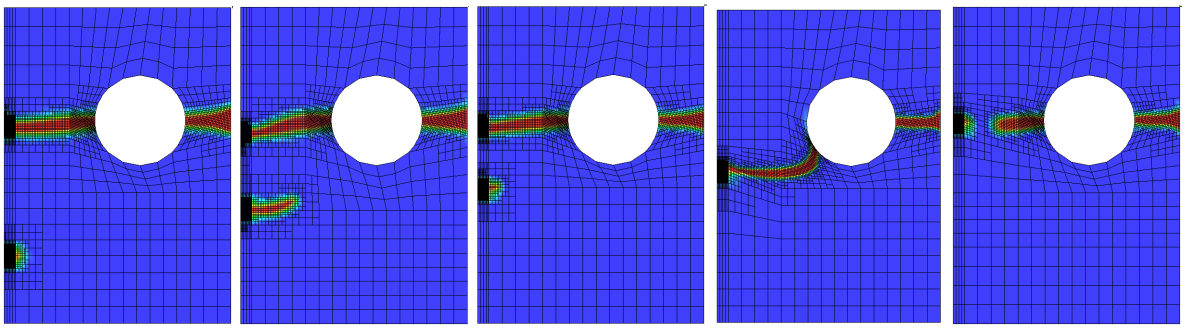

Figure 7.27: Snapshots of the phase-field solution (from blue - unbroken to red - broken) in punctured EPDM strips based on AT_1 functional from Equation (7.4) and Amor splitting from Equation (7.7) with a given notch at $6, 10, 12, 14$ and $18\,\text{mm}$ from left to right.

the displayed snapshots. A reason could be the observed sensitivity on the incremental step size or the mesh size around the inclusion. In Figure 7.29, the crack paths for all five test cases behave similarly to the experimentally observed crack paths. It can be inferred that the Wu functional with Amor splitting fits best to this experimental setup and possibly more general to configurations with holes [192].

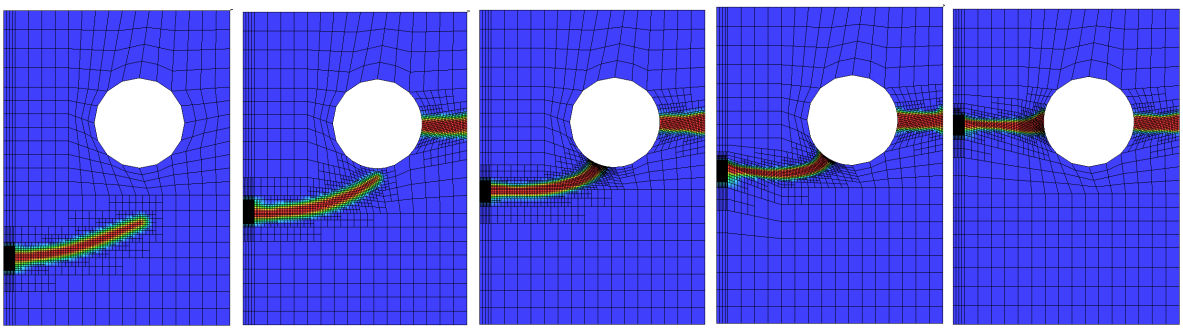

Figure 7.28: Snapshots of the phase-field solution (from blue - unbroken to red - broken) in punctured EPDM strips based on Wu's energy functional from Equation (7.5) and Miehe splitting from Equation (7.6) with a given notch at 6, 10, 12, 14 and 18 mm from left to right.

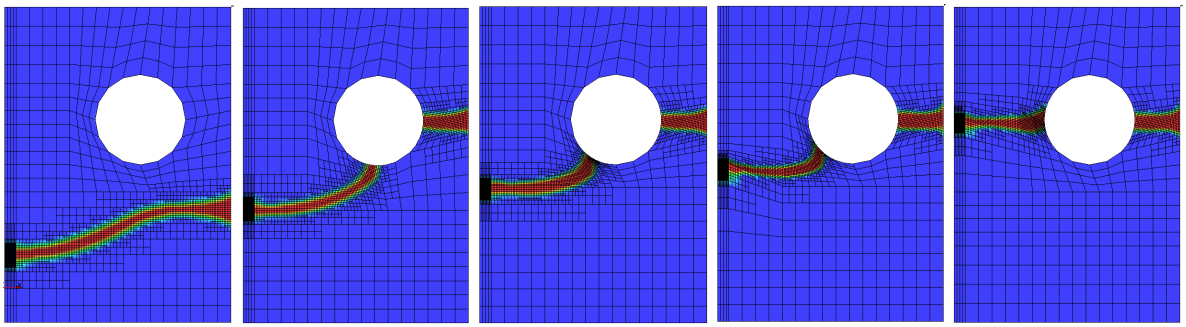

Figure 7.29: Snapshots of the phase-field solution (from blue - unbroken to red - broken) in punctured EPDM strips based on Wu's energy functional from Equation (7.5) and Amor splitting from Equation (7.7) with a given notch at 6, 10, 12, 14 and 18 mm from left to right.

Conclusions of the chapter

In Sections 7.1 and 7.2 we determined the material compounding, the mechanical properties, and the (critical) strain energy release rate via digital image correlation (DIC) for a carbon-black-filled EPDM rubber. The DIK provided a reliable and profound database for crack propagation experiments concerning technically used EPDM to validate fracture models for (carbon black) filled (synthetic) elastomers. We proposed the newly developed quasi-static mixed phase-field fracture model based on Wu's model [189] and Amor's strain energy split [7] for incompressible solids, derived from Chapter 5. We substantiated the new model with satisfactorily numerical simulations of crack propagation in punctured EPDM strips in Section 7.4. Even though we used a quasi-static model with the assumption of linear elasticity, the crack paths of the numerical simulations were promising compared to the qualitative experimental data. Due to the complexity of the experimental setup and our newly developed mixed phase-field fracture model, such comparisons are a major effort, and our modeling

approach yields upper and lower estimates of the fracture behavior in EPDM. The following last chapter concludes the main results of this thesis. Therein, future and open tasks are given.

Chapter 8

Conclusions & outlook

In the thesis at hand, we rose to the challenge of phase-field fracture modeling and reliable numerical simulation of fractures in compressible and incompressible solids – motivated by the interest of industry and other sciences that either depend on the predictability of material behavior or whose future research can base on our fundamental research. We summarize the main results concerning modeling, solving, and validation in the following.

Derived from a primal phase-field fracture model, we developed a phase-field fracture model in mixed form to overcome locking effects arising for high Poisson ratios. We proved the inf-sup stability of the mixed model's elasticity part and discretized it with Taylor-Hood elements (Chapter 5). The mixed phase-field fracture problem is coupled and nonlinear variational system (CVIS) with an additional time-dependent irreversibility constraint. In the frame of this thesis, we avoided the nonlinearity with the help of extrapolation in the phase-field function φ, and solved the inequality constraint with a primal-dual active set method. Our numerical results are based on the mixed form for well-known benchmark examples and high Poisson ratios and support our approach. For a natural behavior of the pressure field, we modified the added pressure equation to get an empty crack without impacting pressure values from inside.

We designed a robust and efficient linear solver for the (3×3) block system to reduce the computational workload, memory, and run-time (Chapter 6). For the linear solver (GMRES), we developed a physics-based Schur-type block preconditioner. We partly derived it from Stokes-type problems, where we consider the block containing the incompressibility ($\lambda \to \infty$) as a perturbation or penalty term. With one v-cycle of AMG or a CG solver, we approximated the three inverse blocks in the preconditioning matrix. We implemented the new solver in deal.II [9] derived from the parallel-adaptive framework *pfm-cracks* [89]. Based on five benchmark examples, we confirmed the robustness of the linear solver in the discretization parameter h and the crack width ϵ. In particular, the numerical results for a modified stationary benchmark test with analytical reference values up to the incompressible limit approve our preconditioner and model concerning iteration numbers and computed quantities of interest.

Finally, we could validate the new model with the help of qualitative measurements in punctured EPDM strips with an initial notch stretched until total failure (Chapter 7). For the experimental measurement data yielding a well-defined test setup, identified parameters with Digital Image Correlation, and data on specific quantities of interest, we collaborated with the Deutsches Institut für Kautschuktechnologie e.V. The crack paths, the maximal loading force, and the traverse displacement

from experiments and numerical simulations behaved similarly.
We conclude the thesis by proposing future tasks in the following:

Complementarity system for realizing the crack irreversibility constraint
We proposed an attractive alternative for the irreversibility constraint briefly in Section 3.2.5, where the inequality is resolved with a Lagrange multiplier embedded in the discrete system. This approach has the advantage of resolving the constraint more accurately and without additional iterations for the constraint. In the case of our mixed model, we would get a (4×4) block system with unknowns (u, p, φ, ζ). One future task could be to work further on complementarity systems and to consider efficient solving of the resulting linear system of increased dimension. The implementation of the complementarity system is available open-source for the primal phase-field fracture problem with three components in Example 8, 10, and 11 of the instationary PDE Examples of DOpElib [62, 79]. The implementation of the mixed phase-field fracture problem with four components is given in Example 12 of the same package for a pressurized fracture example.

Domain decomposition for efficient solving
The robustness of our preconditioned linear solver becomes critical in κ and λ if both are tending to their limits: $\lambda \to \infty$ and $\kappa \to 0$. For small κ, we noticed in the modeling of phase-field fracture that we have coercivity loss in the elasticity equations leading to an ill-conditioned problem. A solution could be an overlapping domain-decomposition method with the broken and the unbroken domains, which overlap in the transition zone where $0 < \varphi < 1$. Classic literature on domain decomposition is given by Quarteroni and Valli [140], Toselli and Widlund [167], and Smith et al. [19]. An additive-Schwarz method could overcome the ill-conditioned problem in the crack nodes; see e.g., Beuchler and Nepomnyaschikh [26]. Ideally, such a solver could avoid the observed sensitivities triggered by the material and regularization parameters ϵ, λ, and κ. Splitting the system's stiffness into two sub-problems could increase the efficiency of the computations.

High-performance computing
Another aspect is parallel computing. In Chapter 6, we used four CPUs (on a single machine with four E7 v3 CPUs). As a future task, parallel studies could be conducted similar to Jodlbauer et al. [98], investigating scalability, speed up, and efficiency regarding the detected difficulties considering small κ, small h, and large λ.

Computations in 3d
As we considered in this thesis, the third dimension is neglectable for benchmark tests and thin strips, and 2d computations are justifiable (Chapter 7). In the future, 3d computations could be caught up for broader usage of the new model and to evaluate the performance of the designed linear solver in higher dimensions.

Nonlinear modeling for EPDM including viscoelasticity and temperature effects
Our mixed model could capture crack propagation behavior in EPDM qualitatively and quantitatively despite the assumed simplifications related to geometrical and material nonlinearities. To simulate fractures in punctured EPDM strips, we used a quasi-static model assuming linear elasticity, small deformations, a constant critical energy release rate, and constant temperature. Considering the

highly nonlinear behavior of filled rubbers in cyclic applications, nonlinear geometrical and material effects could be addressed in the future. Further, viscoelasticity, temperature effects due to energy dissipation, static hysteresis, and permanent deformations become more relevant within cyclic dynamic loading. Carleo et al. [50] benchmarked several models to describe those effects; see Plagge et al. [139]. Prospectively, the combination of sophisticated mechanical material models and phase-field fracture for describing crack propagation in rubbers seems promising. We would be specifically interested in combining the developed mixed form with models on fractured thermo-elastic solids [131, 16, 37, 122, 150], dynamic fracture [36, 30, 122, 179, 198], and hyperelastic fracture [92]. A prototype system of a dynamic thermo-elastic phase-field configuration for incompressible solids could read:
Let $\Omega \subset \mathbb{R}^d, d = 2, 3$ be a domain and $I := (0, T)$ be a time interval with end time $T > 0$. Find vector-valued displacements $u : \Omega \times I \to \mathbb{R}^d$, a scalar-valued pressure $p : \Omega \times I \to \mathbb{R}$, a phase-field indicator function $\varphi : \Omega \times I \to [0, 1]$, and a temperature $\tau : \Omega \times I \to \mathbb{R}$ such that

$$
\begin{aligned}
\partial_t^2 u - \nabla \cdot (g(\varphi)\sigma(u, p, \tau)) = 0 \quad &\text{in } \Omega \times I, \\
g(\varphi)\nabla \cdot u - \frac{1}{\lambda} p = 0 \quad &\text{in } \Omega \times I, \\
\partial_t \varphi + \varphi(1-\kappa)(\sigma(u, p, \tau) : \nabla u) + \frac{G_C}{\epsilon}(1-\varphi) - G_C \epsilon \Delta \varphi \leq 0 \quad &\text{in } \Omega \times I, \\
\partial_t \varphi \leq 0 \quad &\text{in } \Omega \times I, \\
(\partial_t \varphi + \varphi(1-\kappa)(\sigma(u, p, \tau) : \nabla u) + \frac{G_C}{\epsilon}(1-\varphi) - G_C \epsilon \Delta \varphi) \cdot \partial_t \varphi = 0 \quad &\text{in } \Omega \times I, \\
\partial_t \tau - \nabla \cdot (\gamma \nabla \tau) = f \quad &\text{in } \Omega \times I,
\end{aligned}
$$

plus initial and boundary conditions. Here, $g(\varphi)$ is the degradation function, γ is the thermal conductivity, and f is the heat source term. The form of the solid stress tensor $\sigma(u, p, \tau)$ depends on the (nonlinear) material model, see e.g., [131, 122, 150]. Recent work on this topic of thermo-viscoelasticity with a similar phase-field fracture model, but different finite element discretization, is given by Arash et al. [8]. For large deformation and simulating the failure of viscoelastic elastomers, see Brighenti et al. [45].

Appendix A

Proof of Γ-convergence in 1d

We prove for the 1d case that the energy functional defined as

$$E_\epsilon(u,\varphi) = \frac{1}{2}\int_\Omega \left([(1-\kappa)\varphi^2 + \kappa](2\mu+\lambda)|\nabla u|^2 + \rho\ \varphi\nabla u \right) dx + \frac{1}{2}G_C \int_\Omega \left(\frac{1}{\epsilon}(1-\varphi)^2 + \epsilon|\nabla\varphi|^2 \right) dx,$$

is a valid choice as an approximation of the Ambrosio-Tortorelli functional [5, 6]

$$E_T(u,C) = \frac{1}{2}\int_\Omega \left((2\mu+\lambda)|\nabla u|^2 + \rho\nabla u \right) dx + G_C \#(S(u)).$$

The theorem of Γ-convergence was given in Theorem 1 in Section 4.4 and is repeated in the following for completeness.

Theorem 6 (Γ-convergence)**.** *The regularized functional $G_j : L^1(\Omega)\times L^1(\Omega) \to \mathbb{R}\cup\{\infty\}$, defined by*

$$G_j(u,\varphi) = \begin{cases} E_{\epsilon_j}(u_j,\varphi_j) & \text{if } (u_j,\varphi_j) \in H^1(\Omega)\times\mathcal{K}, \\ +\infty & \text{otherwise,} \end{cases}$$

Γ-converges, as

$$\epsilon_j \to 0^+ \text{ for } j\to\infty \text{ and } \kappa = o(\epsilon_j),$$

to the functional $G : L^1(\Omega)\times L^1(\Omega)\to\mathbb{R}\cup\{\infty\}$, given by

$$G(u,\varphi) = \begin{cases} E_T(u) & \text{if } \varphi = 1 \quad \text{a.e. and } u \in PH^1(\Omega), \\ +\infty & \text{otherwise.} \end{cases}$$

Furthermore, if (u_j,φ_j) is a minimizer of G_j, then (u_j,φ_j) (possibly a subsequence) converges to a minimizer of G.

Proof In *Part 2* of the proof of Theorem 1, we use the following lemma:

Lemma 6. *If (ϵ_j) is a sequence of positive numbers converging to 0 and*

$$\sup_j E_{\epsilon_j}(u, \varphi_j) < \infty, \quad j \to \infty,$$

then there exists a subsequence of (φ_j) converging in $L^1(\Omega)$ to some function $\varphi \in PC(\Omega)$ which satisfies $\varphi \in Z = \{v \in PC(\Omega) |\ v = 1$ a.e. in $\Omega\}$. Further, for every $\eta > 0$ there exists a finite set $S = S_\eta$ such that

$$\left|\max_I \varphi_j - \min_I \varphi_j\right| \leq \eta$$

on each fixed compact subset I of $\Omega \setminus S$.

The proof of Lemma 6 can be found in [41, Lemma 6.2].

Part 1: We prove the lower semicontinuity inequality

$$G(u, \varphi) \leq \liminf_{j\to\infty} G_j(u_j, \varphi_j).$$

Let be

$$\epsilon_j \to 0^+, \quad u_j \to u \text{ in } L^1(\Omega), \quad \varphi_j \to \varphi \text{ in } L^1(\Omega),$$

as $j \to \infty$. Further, we set $\kappa = \kappa_j = o(\epsilon_j)$. Up to subsequences we can assume

$$u_j \to u \quad \text{a.e. in } \Omega, \quad \varphi_j \to \varphi \quad \text{a.e. in } \Omega,$$

and

$$\lim_{j\to\infty} G_j(u, \varphi) = C < +\infty. \tag{A.1}$$

In the first step, we prove that $\varphi_j \to 1$ in $L^2(\Omega)$. This property is useful in a later step. For this, the possible negativity of the pressure terms needs to be handled using Young's inequality. For arbitrary $\delta > 0$ it holds

$$\begin{aligned}
&\frac{1}{2}\int_\Omega [(1-\kappa_j)\varphi_j^2 + \kappa_j](2\mu+\lambda)|\nabla u_j|^2 + \rho\varphi_j \nabla u_j \, dx \\
&\qquad \geq \int_\Omega \frac{1}{2}(1-\kappa_j)\varphi_j^2(2\mu+\lambda)|\nabla u_j|^2 \, dx - \int_\Omega \left(\frac{1}{2\delta}|\rho|^2 + \frac{\delta}{2}|\varphi_j \nabla u_j|^2\right) dx \\
&\qquad \geq \left(\frac{1}{2}(1-\kappa_j) - \frac{\delta}{2}\right)(2\mu+\lambda)\,\|\varphi_j \nabla u_j\|^2_{L^2(\Omega)} - \frac{1}{2\delta}\,\|\rho\|^2_{L^2(\Omega)}\,.
\end{aligned} \tag{A.2}$$

Choosing $\delta < (1-\kappa_j)$ leads to

$$\begin{aligned}
\liminf_{j\to\infty} \frac{1}{2} G_C \int_\Omega \frac{1}{\epsilon_j}(1-\varphi_j)^2 \, dx \leq \liminf_{j\to\infty} &\left(\frac{1}{2}(1-\kappa_j) - \frac{\delta}{2}\right)(2\mu+\lambda)\,\|\varphi_j \nabla u_j\|^2_{L^2(\Omega)} \\
&+ \frac{1}{2} G_C \int_\Omega \frac{1}{\epsilon_j}(1-\varphi_j)^2 + \epsilon_j |\nabla \varphi_j|^2 \, dx.
\end{aligned}$$

Using Equation (A.1) and Equation (A.2) yields

$$\begin{aligned}
&\liminf_{j\to\infty} \frac{1}{2} G_C \int_\Omega \frac{1}{\epsilon_j}(1-\varphi_j)^2\,dx \\
&\quad\le \liminf_{j\to\infty} \frac{1}{2}\int_\Omega [(1-\kappa_j)\varphi_j^2+\kappa_j](2\mu+\lambda)|\nabla u_j|^2 + \rho\varphi_j \nabla u_j\,dx + \frac{1}{2\delta}\|\rho\|^2_{L^2(\Omega)} \\
&\qquad + \frac{1}{2} G_C \int_\Omega \frac{1}{\epsilon_j}(1-\varphi_j)^2 + \epsilon_j |\nabla\varphi_j|^2\,dx \\
&\quad\le \liminf_{j\to\infty} G_j(u_j,\varphi_j) + \frac{1}{2\delta}\|\rho\|^2_{L^2(\Omega)} \le C + \frac{1}{2\delta}\|\rho\|^2_{L^2(\Omega)} =: \tilde{C}.
\end{aligned}$$

Multiplying with $\frac{2\epsilon_j}{G_C} > 0$ yields

$$\liminf_{j\to\infty} \int_\Omega (1-\varphi_j)^2\,dx \le \liminf_{j\to\infty} \frac{2\epsilon_j}{G_C}\tilde{C}.$$

With Fatou's Lemma we get

$$\int_\Omega (1-\varphi)^2\,dx \le \liminf_{j\to\infty} \int_\Omega (1-\varphi_j)^2\,dx,$$

and obtain

$$\int_\Omega (1-\varphi)^2\,dx \le \liminf_{j\to\infty} \frac{2\epsilon_j}{G_C}\tilde{C} = 0.$$

Hence, $\varphi = 1$ almost everywhere in Ω and $\|\varphi_j - 1\|_{L^2(\Omega)} \to 0$ as $j \to \infty$ and therefore

$$\varphi_j \to 1 \text{ in } L^2(\Omega).$$

In a next step, we prove that $u \in H^1(I)$ for $I \subset \Omega \setminus S(u)$. Since $\varphi_j \to \varphi = 1$ almost everywhere, it follows from Lemma 6 that a finite set S exists such that for every fixed open set I compactly embedded in $\Omega \setminus S$ it holds $\frac{1}{2} < \varphi_j < \frac{3}{2}$ on I. For every such fixed I, it can be assumed without restrictions that $u \in L^1(I)$. Further, it follows from the estimate

$$\frac{1}{2}(2\mu+\lambda)\sup_j \int_I |\nabla u_j|^2 \le \sup_j \int_\Omega [(1-\kappa_j)\varphi_j^2+\kappa_j](2\mu+\lambda)|\nabla u_j|^2\,dx < +\infty,$$

that

$$\|\nabla u_j\|^2_{L^2(I)} < +\infty.$$

Thus, since $H^1(I)$ is reflexive, ∇u_j yields a subsequence ∇u_{j_k} which converges weakly in $H^1(I)$. Without loss of generality we can set $j = j_k$. With $\varphi_j \to 1$ in $L^2(I)$ and $u_j \rightharpoonup u$ in $H^1(I)$ it follows

$$\begin{aligned}
\int_I |\nabla u|^2 dx \;&\le\; \liminf_{j\to\infty} \int_I [(1-\kappa_j)\varphi_j^2+\kappa_j](2\mu+\lambda)|\nabla u_j|^2 dx \\
&\overset{I\subset\Omega}{\le} \liminf_{j\to\infty} \int_\Omega [(1-\kappa_j)\varphi_j^2+\kappa_j](2\mu+\lambda)|\nabla u_j|^2 dx < +\infty.
\end{aligned} \tag{A.3}$$

Hence $u \in H^1(I)$ and since this estimate is independent of I, even $u \in PH^1(\Omega)$ and $S(u) \subset S$. In the following, we show that the lower semicontinuity inequality is independent of the pressure term. At first, subtracting the pressure term of G_j from G (with the integral over I) leads to

$$\int_I \rho \nabla u \, dx - \int_I \rho \varphi_j \nabla u_j \, dx = \int_I \rho (\nabla u - \varphi_j \nabla u_j) \, dx.$$

Since $\varphi = 1$ almost everywhere, it holds

$$\begin{aligned} \Big| \int_I \rho \nabla u - \varphi_j \nabla u_j \, dx \Big| \leq & \Big| \int_I \rho \, (\nabla u - \nabla u_j) \, dx \Big| + \Big| \int_I (\rho - \varphi_j) \nabla u_j \, dx \Big| \\ & \leq \Big| \int_I \rho \, (\nabla u - \nabla u_j) \, dx \Big| + \|\rho - \varphi_j\| \|\nabla u_j\|. \end{aligned} \tag{A.4}$$

Thus

$$\begin{aligned} \liminf_{j \to \infty} \Big| \int_I \rho \nabla u - \varphi_j \nabla u_j \, dx \Big| &\leq \liminf_{j \to \infty} \rho \bigg(\int_I |\varphi| \big| \nabla u - \nabla u_j \big| \, dx + ||\nabla u_j||_{L^2(I)} ||\varphi - \varphi_j||_{L^2(I)} \bigg) \\ &= \rho \bigg(\liminf_{j \to \infty} \int_I |\varphi| \big| \nabla u - \nabla u_j \big| \, dx + \liminf_{j \to \infty} ||\nabla u_j||_{L^2(I)} ||\varphi - \varphi_j||_{L^2(I)} \bigg) \\ &= \rho \, (0 + 0) = 0. \end{aligned}$$

Hence,

$$\liminf_{j \to \infty} \int_I \rho \varphi_j \nabla u_j \, dx = \int_I \rho \nabla u \, dx. \tag{A.5}$$

To estimate the bulk energy term, we assume $t \in S(u)$. Then t_j^1, t_j^2, s_j exist such that $t_j^1 < s < t_j^2$ with

$$\begin{aligned} \lim_{j \to \infty} t_j^1 = \lim_{j \to \infty} t_j^2 = \lim_{j \to \infty} s_j = t, \\ \lim_{j \to \infty} \varphi_j(t_j^1) = \lim_{j \to \infty} \varphi_j(t_j^2) = 1, \\ \lim_{j \to \infty} \varphi_j(s_j) = 0. \end{aligned}$$

Otherwise, a neighbourhood I of t would exist such that $u \in H^1(I)$ and $t \notin S(u)$. A particular case of Young's inequality, which states $x^2 + y^2 \geq 2xy$, leads to

$$\int_{t_j^1}^{s_j} \left(\frac{1}{\epsilon} (1 - \varphi_j)^2 + \epsilon |\nabla \varphi_j|^2 \right) dt \geq 2 \int_{t_j^1}^{s_j} \left(\sqrt{\frac{1}{\epsilon}} (1 - \varphi_j) \sqrt{\epsilon} |\nabla \varphi_j| \right) dt \geq \left| 2 \int_{t_j^1}^{s_j} (1 - \varphi_j) \nabla \varphi_j \, dt \right|.$$

Application of the substitution rule yields

$$\int_{t_j^1}^{s_j} \left(\frac{1}{\epsilon} (1 - \varphi_j)^2 + \epsilon |\nabla \varphi_j|^2 \right) dt \geq 2 \left| \int_{\varphi(t_j^1)}^{\varphi(s_j)} (1 - s) \, ds \right|.$$

The estimate of the second integral follows the same idea. Thus

$$\liminf_{j\to\infty} \int_{t_j^1}^{s_j} \left(\frac{1}{\epsilon}(1-\varphi_j)^2 + \epsilon|\nabla\varphi_j|^2\right) dt \geq \liminf_{j\to\infty} 2\left|\int_{\varphi(t_j^1)}^{\varphi(s_j)} (1-s)\, ds\right| = 2\int_0^1 (1-s)\, ds = 1,$$

and

$$\liminf_{j\to\infty} \int_{s_j}^{t_j^2} \left(\frac{1}{\epsilon}(1-\varphi_j)^2 + \epsilon|\nabla\varphi_j|^2\right) dt \geq \liminf_{j\to\infty} 2\left|\int_{\varphi(s_j)}^{\varphi(t_j^2)} (1-s)\, ds\right| \geq 2\int_0^1 (1-s)\, ds = 1.$$

We repeat the argument for all $t_i \in S(u)$ yielding

$$\begin{aligned}\sum_{t_i\in S(u)} \liminf_{j\to\infty} \frac{G_C}{2}\left[\int_{t_{i,j}^1}^{s_{i,j}} \left(\frac{1}{\epsilon}(1-\varphi_j)^2 + \epsilon|\nabla\varphi_j|^2\right) dt + \int_{s_{i,j}}^{t_{i,j}^2} \left(\frac{1}{\epsilon}(1-\varphi_j)^2 + \epsilon|\nabla\varphi_j|^2\right) dt\right] \\ \geq \frac{G_C}{2}\sum_{t_i\in S(u)} (1+1) = \#G_C(S(u)),\end{aligned} \tag{A.6}$$

and taking into account the arbitrariness of I in Equation (A.3), it holds that

$$\liminf_{j\to\infty} \frac{1}{2} G_C \int_\Omega \left(\frac{1}{\epsilon_j}(1-\varphi_j)^2 + \epsilon_j|\nabla\varphi_j|^2\right) dx$$

is equal to Equation (A.6) since it vanishes on all intervals $[t_{i,j}^2, t_{i+1,j}^1]$ because of $\varphi_j \to 1$ on $I \subset \Omega \setminus S(u)$. Thus

$$G_C \#(S(u)) \leq \liminf_{j\to\infty} \frac{1}{2} G_C \int_\Omega \left(\frac{1}{\epsilon_j}(1-\varphi)^2 + \epsilon_j|\nabla\varphi_j|^2\right) dx.$$

It remains to expand Equation (A.5) on the whole domain Ω using the same arguments as in Equation (A.6). Let $t_i \in S(u)$ and $t_{i,j}^1$ and $t_{i,j}^2$ be defined as before. Then, Equation (A.3) and Equation (A.5) with $I_i = (t_{i-1,j}^2, t_{i,j}^1)$ as depicted in Figure A.1

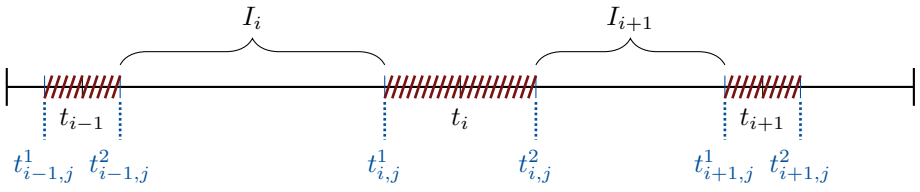

Figure A.1: Visualization of I_i.

lead to

$$\begin{aligned}\frac{1}{2}\int_\Omega (2\mu+\lambda)|\nabla u|^2+\rho\nabla u\,dx &= \lim_{j\to\infty}\sum_{t_i\in S(u)}\frac{1}{2}\int_{I_i}(2\mu+\lambda)|\nabla u|^2+\rho\nabla u\,dx\\ &\le \liminf_{j\to\infty}\sum_{t_i\in S(u)}\frac{1}{2}\int_{I_i}[(1-\kappa_j)\varphi_j^2+\kappa_j](2\mu+\lambda)|\nabla u_j|^2+\rho\varphi_j\nabla u_j\,dx\\ &\le \liminf_{j\to\infty}\frac{1}{2}\int_{\Omega}[(1-\kappa_j)\varphi_j^2+\kappa_j](2\mu+\lambda)|\nabla u_j|^2+\rho\varphi_j\nabla u_j\,dx\\ &\quad -\liminf_{j\to\infty}\sum_{t_i\in S(u)}\int_{t_j^1}^{t_j^2}[(1-\kappa_j)\varphi_j^2+\kappa_j](2\mu+\lambda)|\nabla u_j|^2+\rho\varphi_j\nabla u_j\,dx.\end{aligned}$$

The last subtraction is necessary since the red parts in Figure A.1 are not included in $\bigcup I_i$. Due to $(u_j,\varphi_j)\in H^1(\Omega;\mathbb{R}^2)$, ρ being constant and $\lim_{j\to\infty}t_j^1=\lim_{j\to\infty}t_j^2=t$ it holds

$$-\liminf_{j\to\infty}\sum_{t_i\in S(u)}\int_{t_j^1}^{t_j^2}[(1-\kappa_j)\varphi_j^2+\kappa_j](2\mu+\lambda)|\nabla u_j|^2+\rho\varphi_j\nabla u_j\,dx=0.$$

To sum up, the two major estimates, which were shown, are

$$\frac{1}{2}\int_\Omega (2\mu+\lambda)|\nabla u|^2+\rho\nabla u\,dx\le\liminf_{j\to\infty}\frac{1}{2}\int_{\Omega}[(1-\kappa_j)\varphi_j^2+\kappa_j](2\mu+\lambda)|\nabla u_j|^2+\rho\varphi_j\nabla u_j\,dx,\tag{A.7}$$

and

$$G_C\#(S(u))\le\liminf_{j\to\infty}\frac{1}{2}G_C\int_\Omega(\frac{1}{\epsilon_j}(1-\varphi)^2+\epsilon_j|\nabla\varphi_j|^2)\,dx.\tag{A.8}$$

These two inequalities give us the lower semicontinuity inequality:

$$G(u,\varphi)\le\liminf_{j\to\infty}G_j(u_j,\varphi_j).$$

Part 2: The second part proves the upper semicontinuity inequality:

$$G(u,\varphi)\ge\limsup_{j\to\infty}G_j(u_j,\varphi_j).\tag{A.9}$$

The idea is to construct recovery sequences for $u\in PH^1(\Omega)$ and $\varphi=1$ almost everywhere; see Figure A.2.

It suffices considering the case $\Omega=(-1,1)$ with $S(u)=\{0\}$. For a general case with finitely many jump discontinuities, we can scale Ω and repeat similar steps for every jump point. Let be $\kappa=\kappa_j=\mathcal{O}(\epsilon_j)$. Set $\xi_j=\mathcal{O}(\epsilon_j)$ and let $u_j\in H^1(\Omega)$ with $u_j(t)=u(t)$ if $|t|>\xi_j$. For $|t|\le\xi_j$, u_j is Lagrange-interpolated linearly with $-\xi_j$ and ξ_j as grid points. The Lagrange-polynomials are given by

$$L_0^{(1)}(t)=\frac{t-\xi_j}{-\xi_j-\xi_j}=\frac{t-\xi_j}{-2\xi_j},\quad L_1^{(1)}(t)=\frac{t-(-\xi_j)}{\xi_j-(-\xi_j)}=\frac{t+\xi_j}{2\xi_j}.$$

The interpolation is then given by

$$\begin{aligned} u_j|_{[-\xi_j,\xi_j]} &= u(-\xi_j)\frac{t-\xi_j}{-2\xi_j} + u(\xi_j)\frac{t+\xi_j}{2\xi_j} \\ &= u(-\xi_j)\frac{\xi_j - t}{2\xi_j} + u(\xi_j)\frac{t+\xi_j}{2\xi_j} \\ &= \frac{u(-\xi_j)\xi_j - u(-\xi_j)t + u(\xi_j)t + u(\xi_j)\xi_j}{2\xi_j} \\ &= \frac{\xi_j(u(-\xi_j)+u(\xi_j)) + t(u(\xi_j)-u(-\xi_j))}{2\xi_j} \\ &= \frac{u(\xi_j)-u(-\xi_j)}{2\xi_j}\cdot t + \frac{u(\xi_j)+u(-\xi_j)}{2}, \end{aligned}$$

such that u_j is given by

$$u_j(t) \coloneqq \begin{cases} \frac{u(\xi_j)-u(-\xi_j)}{2\xi_j}\cdot t + \frac{u(\xi_j)+u(-\xi_j)}{2} & \text{if } |t| \le \xi_j \\ u & \text{if } |t| > \xi_j. \end{cases}$$

Since it obviously holds $u_j \to u$ in $L^1(\Omega)$, all the deductions from *Part 1* hold as well.
The construction of φ_j proceeds as follows. With fixed $\eta > 0$, let $T > 0$ and $\bar{\varphi} \in H^1(0,T)$ be such that $\bar{\varphi}(0) = 0$, $\bar{\varphi}(0) = 1$, $0 \le \bar{\varphi} \le 1$ and

$$\int_0^T (1-\bar{\varphi})^2 + |\nabla\bar{\varphi}|^2 dt \le 1 + \eta. \tag{A.10}$$

Define

$$\varphi_j(t) \coloneqq \begin{cases} 0 & \text{if } |t| \le \xi_j \\ \bar{\varphi}\left(\frac{|t|-\xi_j}{\epsilon_j}\right) & \text{if } \xi_j < |t| < \xi_j + \epsilon_j T \\ 1 & \text{if } |t| \ge \xi_j + \epsilon_j T. \end{cases}$$

Since $\xi_j \to 0$ as $j \to \infty$ it holds

$$\lim_{j\to\infty} \{t \in \mathbb{R} : |t| \le \xi_j\} = \{0\},$$

thus $0 \le \varphi_j \le 1$ and $\varphi_j \to 1$ a.e. in Ω.

We show Equation (A.9) proving the following three inequalities:

$$\limsup_{j\to\infty} \frac{1}{2}\int_\Omega [(1-\kappa_j)\varphi_j^2 + \kappa_j](2\mu+\lambda)|\nabla u_j|^2\, dx \le \frac{1}{2}\int_\Omega (2\mu+\lambda)|\nabla u|^2\, dx, \tag{A.11}$$

$$\limsup_{j\to\infty} \frac{1}{2}\int_\Omega \rho\varphi_j \nabla u_j\, dx \le \frac{1}{2}\int_\Omega \rho\nabla u\, dx, \tag{A.12}$$

$$\limsup_{j\to\infty} \frac{1}{2} G_C \int_\Omega \left(\frac{1}{\epsilon_j}(1-\varphi_j)^2 + \epsilon_j|\nabla\varphi_j|^2\right) dx \le G_C \#(S(u)). \tag{A.13}$$

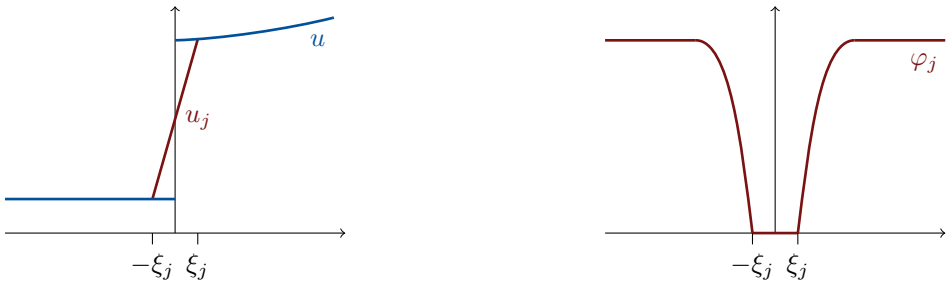

Figure A.2: Visualization of the recovery sequences u_j and φ_j; similar to [41].

Starting with Equation (A.11), the left-hand side can be estimated by

$$\begin{aligned}
&\limsup_{j\to\infty} \frac{1}{2}\int_\Omega [(1-\kappa_j)\varphi_j^2+\kappa_j](2\mu+\lambda)|\nabla u_j|^2\,dx \\
&\qquad = \limsup_{j\to\infty} \frac{1}{2}\int_{-1}^{-\xi_j-\epsilon_j T} [(1-\kappa_j)\varphi_j^2+\kappa_j](2\mu+\lambda)|\nabla u_j|^2\,dx \\
&\qquad\quad + \limsup_{j\to\infty} \frac{1}{2}\int_{-\xi_j-\epsilon_j T}^{-\xi_j} [(1-\kappa_j)\varphi_j^2+\kappa_j](2\mu+\lambda)|\nabla u_j|^2\,dx \\
&\qquad\quad + \limsup_{j\to\infty} \frac{1}{2}\int_{-\xi_j}^{\xi_j} [(1-\kappa_j)\varphi_j^2+\kappa_j](2\mu+\lambda)|\nabla u_j|^2\,dx \\
&\qquad\quad + \limsup_{j\to\infty} \frac{1}{2}\int_{\xi_j}^{\xi_j+\epsilon_j T} [(1-\kappa_j)\varphi_j^2+\kappa_j](2\mu+\lambda)|\nabla u_j|^2\,dx \\
&\qquad\quad + \limsup_{j\to\infty} \frac{1}{2}\int_{\xi_j+\epsilon_j T}^{1} [(1-\kappa_j)\varphi_j^2+\kappa_j](2\mu+\lambda)|\nabla u_j|^2\,dx.
\end{aligned}$$

Inserting the definitions of φ_j and u_j yields

$$\begin{aligned}
\limsup_{j\to\infty} \frac{1}{2}\int_\Omega [(1-\kappa_j)\varphi_j^2+\kappa_j](2\mu+\lambda)|\nabla u_j|^2\,dx &= \limsup_{j\to\infty} \frac{1}{2}\int_{-1}^{-\xi_j-\epsilon_j T} (2\mu+\lambda)|\nabla u|^2\,dx \\
&\quad + \limsup_{j\to\infty} \frac{1}{2}\int_{-\xi_j-\epsilon_j T}^{-\xi_j} [(1-\kappa_j)\varphi_j^2+\kappa_j](2\mu+\lambda)|\nabla u|^2\,dx \\
&\quad + \limsup_{j\to\infty} \frac{1}{2}\int_{-\xi_j}^{\xi_j} \kappa_j(2\mu+\lambda)|\nabla u_j|^2\,dx \\
&\quad + \limsup_{j\to\infty} \frac{1}{2}\int_{\xi_j}^{\xi_j+\epsilon_j T} [(1-\kappa_j)\varphi_j^2+\kappa_j](2\mu+\lambda)|\nabla u|^2\,dx \\
&\quad + \limsup_{j\to\infty} \frac{1}{2}\int_{\xi_j+\epsilon_j T}^{1} (2\mu+\lambda)|\nabla u|^2\,dx.
\end{aligned}$$

Due to $\epsilon_j \to 0$ and $[(1-\kappa_j)\varphi_j^2 + \kappa_j] \to \varphi_j^2 \leq 1$ as $j \to \infty$, it holds

$$\limsup_{j\to\infty} \frac{1}{2} \int_{-\xi_j-\epsilon_j T}^{-\xi_j} [(1-\kappa_j)\varphi_j^2 + \kappa_j](2\mu+\lambda)|\nabla u|^2 \, dx = 0,$$
$$\limsup_{j\to\infty} \frac{1}{2} \int_{\xi_j}^{\xi_j+\epsilon_j T} [(1-\kappa_j)\varphi_j^2 + \kappa_j](2\mu+\lambda)|\nabla u|^2 \, dx = 0.$$

Since u_j is linear on $[-\xi_j, \xi_j]$, the integral over this interval is given as

$$\begin{aligned}
\limsup_{j\to\infty} \frac{1}{2} \int_{-\xi_j}^{\xi_j} \kappa_j |\nabla u_j|^2 \, dx &= \limsup_{j\to\infty} \frac{1}{2} \int_{-\xi_j}^{\xi_j} \kappa_j \left| \frac{u(\xi_j) - u(-\xi_j)}{2\xi_j} \right|^2 dx \\
&= \limsup_{j\to\infty} \frac{1}{2} \int_{-\xi_j}^{\xi_j} \kappa_j \frac{(u(\xi_j) - u(-\xi_j))^2}{4\xi_j^2} \, dx \\
&= \limsup_{j\to\infty} \frac{1}{2} \left[\kappa_j \frac{(u(\xi_j) - u(-\xi_j))^2}{4\xi_j^2} x \right]_{-\xi_j}^{\xi_j} \\
&= \limsup_{j\to\infty} \kappa_j \frac{(u(\xi_j) - u(-\xi_j))^2}{4\xi_j} \\
&= \limsup_{j\to\infty} \frac{1}{4} \frac{\kappa_j}{\sqrt{\kappa_j \epsilon_j}} (u(\xi_j) - u(-\xi_j))^2 \\
&= \limsup_{j\to\infty} \frac{1}{4} \frac{\sqrt{\kappa_j}}{\sqrt{\epsilon_j}} (u(\xi_j) - u(-\xi_j))^2 = 0.
\end{aligned}$$

Hence

$$\begin{aligned}
\limsup_{j\to\infty} \frac{1}{2} \int_\Omega [(1-\kappa_j)\varphi_j^2 + \kappa_j](2\mu+\lambda)|\nabla u_j|^2 \, dx &= \limsup_{j\to\infty} \frac{1}{2} \int_{-1}^{-\xi_j-\epsilon_j T} (2\mu+\lambda)|\nabla u|^2 \, dx \\
+ \limsup_{j\to\infty} \frac{1}{2} \int_{\xi_j+\epsilon_j T}^{1} (2\mu+\lambda)|\nabla u|^2 \, dx &\leq \frac{1}{2} \int_\Omega (2\mu+\lambda)|\nabla u|^2 \, dx,
\end{aligned}$$

and the first Equation (A.11), given by

$$\limsup_{j\to\infty} \frac{1}{2} \int_\Omega [(1-\kappa_j)\varphi_j^2 + \kappa_j](2\mu+\lambda)|\nabla u_j|^2 \, dx \leq \frac{1}{2} \int_\Omega (2\mu+\lambda)|\nabla u|^2 \, dx,$$

is proven.

For Equation (A.12), we have to show that $\varphi_j \to 1$ in $L^2(-\xi_j - \epsilon_j T, \xi_j + \epsilon_j T)$. We observe by

construction of φ_j that

$$\begin{aligned}
||\varphi_j - 1||^2_{L^2(-\xi_j-\epsilon_j T,\xi_j+\epsilon_j T)} &= \int_{-\xi_j-\epsilon_j T}^{-\xi_j} (\varphi_j - 1)^2\,dt + \int_{-\xi_j}^{\xi_j} (\varphi_j - 1)^2\,dt + \int_{\xi_j}^{\xi_j+\epsilon_j T} (\varphi_j - 1)^2\,dt \\
&= \int_{-\xi_j-\epsilon_j T}^{-\xi_j} \left[\bar{\varphi}\left(\frac{-t-\xi_j}{\epsilon_j}\right) - 1\right]^2 dt + \int_{-\xi_j}^{\xi_j} (0-1)^2\,dt \\
&\quad + \int_{\xi_j}^{\xi_j+\epsilon_j T} \left[\bar{\varphi}\left(\frac{t-\xi_j}{\epsilon_j}\right) - 1\right]^2 dt \\
&= \int_{-\xi_j-\epsilon_j T}^{-\xi_j} \left[\bar{\varphi}\left(\frac{-t-\xi_j}{\epsilon_j}\right) - 1\right]^2 dt + \int_{-\xi_j}^{\xi_j} 1\,dt \\
&+ \int_{\xi_j}^{\xi_j+\epsilon_j T} \left[\bar{\varphi}\left(\frac{t-\xi_j}{\epsilon_j}\right) - 1\right]^2 dt.
\end{aligned}$$

Now, we consider the substitution

$$s = \frac{|t| - \xi_j}{\epsilon_j} \text{ with } ds = \frac{dt}{\epsilon_j}. \tag{A.14}$$

Since $s(\xi_j) = s(-\xi_j) = 0$ and $s(\xi_j + \epsilon_j T) = s(-\xi_j - \epsilon_j T) = T$, it follows

$$\begin{aligned}
||\varphi_j - 1||^2_{L^2(-\xi_j-\epsilon_j T,\xi_j+\epsilon_j T)} &= 2\int_0^T \epsilon_j \left(\bar{\varphi}(s) - 1\right)^2 ds + \int_{-\xi_j}^{\xi_j} 1\,dt \\
&\leq 2\int_0^T \epsilon_j \left(\bar{\varphi}(s) - 1\right)^2 + \epsilon_j |\nabla\bar{\varphi}(s)|^2 ds + \int_{-\xi_j}^{\xi_j} 1\,dt.
\end{aligned}$$

This can be estimated via Equation (A.10) such that

$$||\varphi_j - 1||^2_{L^2(-\xi_j-\epsilon_j T,\xi_j+\epsilon_j T)} \leq 2\epsilon_j(1+\eta) + 2\xi_j.$$

The right-hand side tends to 0 as $j \to \infty$. Hence, it holds true that $\varphi_j \to 1$ in $L^2(-\xi_j - \epsilon_j T, \xi_j + \epsilon_j T)$. This is used to estimate the pressure terms restricted to $(-\xi_j - \epsilon_j T, \xi_j + \epsilon_j T)$. The Hölder inequality leads to

$$\begin{aligned}
\int_{-\xi_j-\epsilon_j T}^{\xi_j+\epsilon_j T} \rho\varphi_j \nabla u\,dx &\leq \int_{-\xi_j-\epsilon_j T}^{\xi_j+\epsilon_j T} |\rho\varphi_j \nabla u|\,dx \\
&\leq \rho||\nabla u||_{L^2(-\xi_j-\epsilon_j T,\xi_j+\epsilon_j T)}||\varphi_j - 1||_{L^2(-\xi_j-\epsilon_j T,\xi_j+\epsilon_j T)} \overset{j\to\infty}{\longrightarrow} 0.
\end{aligned} \tag{A.15}$$

Since $\varphi_j = 0$ on $[-\xi_j, \xi_j]$ and $u_j = u$ on $\Omega \setminus [-\xi_j, \xi_j]$, Equation (A.12) can be handled as follows:

$$\begin{aligned}
\frac{1}{2}\int_\Omega \rho\varphi_j \nabla u_j\,dx &= \frac{1}{2}\int_\Omega \rho\varphi_j \nabla u\,dx \\
&= \frac{1}{2}\int_{-1}^{-\xi_j-\epsilon_j T} \rho\varphi_j \nabla u\,dx + \frac{1}{2}\int_{-\xi_j-\epsilon_j T}^{\xi_j+\epsilon_j T} \rho\varphi_j \nabla u\,dx + \frac{1}{2}\int_{\xi_j+\epsilon_j T}^{1} \rho\varphi_j \nabla u\,dx.
\end{aligned}$$

Applying the $\limsup_{j\to\infty}$ together with Equation (A.15) yields

$$\limsup_{j\to\infty} \frac{1}{2} \int_{-\xi_j-\epsilon_j T}^{\xi_j+\epsilon_j T} \rho\varphi_j \nabla u \, dx = 0$$

and since $\varphi_j \to 1$ and $\varphi_j = 1$ it finally holds

$$\begin{aligned}\limsup_{j\to\infty} \frac{1}{2} \int_{\Omega} \rho\varphi_j \nabla u_j \, dx &= \limsup_{j\to\infty} \frac{1}{2} \int_{-1}^{-\xi_j-\epsilon_j T} \rho\varphi_j \nabla u \, dx + \limsup_{j\to\infty} \frac{1}{2} \int_{\xi_j+\epsilon_j T}^{1} \rho\varphi_j \nabla u \, dx \\ &\leq \frac{1}{2} \int_{\Omega} \rho \nabla u \, dx.\end{aligned}$$

Thus, Equation (A.12) given by

$$\limsup_{j\to\infty} \frac{1}{2} \int_{\Omega} \rho\varphi_j \nabla u_j \, dx \leq \frac{1}{2} \int_{\Omega} \rho \nabla u \, dx,$$

is proven.

The last inequality to show is Equation (A.13). The monotony of the integral and $|\nabla\varphi_j|^2 \geq 0$ yield

$$\begin{aligned}\frac{1}{2}G_C\int_\Omega\left(\frac{1}{\epsilon_j}(1-\varphi_j)^2+\epsilon_j|\nabla\varphi_j|^2\right)dx \leq \frac{1}{2}G_C\frac{1}{\epsilon_j}\int_\Omega\left((1-\varphi_j)^2+|\nabla\varphi_j|^2\right)dx \\ +\frac{1}{2}G_C\int_\Omega\epsilon_j|\nabla\varphi_j|^2\,dx.\end{aligned} \tag{A.16}$$

Splitting the first integral of the right-hand side gives further

$$\begin{aligned}\frac{1}{2}G_C\frac{1}{\epsilon_j}\int_\Omega\left((1-\varphi_j)^2+|\nabla\varphi_j|^2\right)dx &= \frac{1}{2}G_C\frac{1}{\epsilon_j}\int_{-1}^{-\xi_j-\epsilon_jT}\left((1-\varphi_j)^2+|\nabla\varphi_j|^2\right)dx \\ &+\frac{1}{2}G_C\frac{1}{\epsilon_j}\int_{-\xi_j-\epsilon_jT}^{-\xi_j}\left((1-\varphi_j)^2+|\nabla\varphi_j|^2\right)dx \\ &+\frac{1}{2}G_C\frac{1}{\epsilon_j}\int_{-\xi_j}^{\xi_j}\left((1-\varphi_j)^2+|\nabla\varphi_j|^2\right)dx \\ &+\frac{1}{2}G_C\frac{1}{\epsilon_j}\int_{\xi_j}^{\xi_j+\epsilon_jT}\left((1-\varphi_j)^2+|\nabla\varphi_j|^2\right)dx \\ &+\frac{1}{2}G_C\frac{1}{\epsilon_j}\int_{\xi_j+\epsilon_jT}^{1}\left((1-\varphi_j)^2+|\nabla\varphi_j|^2\right)dx.\end{aligned}$$

Since $\varphi_j = 1$ on $[-1,-\xi-\epsilon_jT]\cup[\xi+\epsilon_jT,1]$ and $\varphi_j = 0$ on $[-\xi,\xi]$ it holds

$$\begin{aligned}\frac{1}{2}G_C\frac{1}{\epsilon_j}\int_\Omega\left((1-\varphi_j)^2+|\nabla\varphi_j|^2\right)dx &= \frac{1}{2}G_C\frac{1}{\epsilon_j}\int_{-\xi_j-\epsilon_jT}^{-\xi_j}\left((1-\varphi_j)^2+|\nabla\varphi_j|^2\right)dx \\ &+\frac{1}{2}G_C\frac{1}{\epsilon_j}\int_{-\xi_j}^{\xi_j}1\,dx \\ &+\frac{1}{2}G_C\frac{1}{\epsilon_j}\int_{\xi_j}^{\xi_j+\epsilon_jT}\left((1-\varphi_j)^2+|\nabla\varphi_j|^2\right)dx.\end{aligned} \tag{A.17}$$

For clarity, the remaining integrals are estimated separately. Firstly,

$$\frac{1}{2}G_C\frac{1}{\epsilon_j}\int_{-\xi_j}^{\xi_j}1\,dx = \frac{1}{2}G_C\frac{1}{\epsilon_j}2\xi_j = G_C\frac{\xi_j}{\epsilon_j}.$$

Secondly,

$$\begin{aligned}\frac{1}{2}G_C\frac{1}{\epsilon_j}\int_{-\xi_j-\epsilon_jT}^{-\xi_j}\left((1-\varphi_j)^2+|\nabla\varphi_j|^2\right)dx &= \frac{1}{2}G_C\frac{1}{\epsilon_j}\int_{-\xi_j-\epsilon_jT}^{-\xi_j}\left((1-\varphi_j)^2+|\nabla\varphi_j|^2\right)dx \\ &= \frac{1}{2}G_C\frac{1}{\epsilon_j}\int_{-\xi_j-\epsilon_jT}^{-\xi_j}\left(\left(1-\bar{\varphi}\left(\frac{|x|-\xi_j}{\epsilon_j}\right)\right)^2\right. \\ &\quad\left.+\left|\nabla\bar{\varphi}\left(\frac{|x|-\xi_j}{\epsilon_j}\right)\right|^2\right)dx.\end{aligned} \tag{A.18}$$

Applying the substitution defined in Equation (A.14) reduces Equation (A.18) to

$$\frac{1}{2}G_C\frac{1}{\epsilon_j}\int_0^T \epsilon_j\left(1-\tilde{\varphi}\left(s\right)\right)^2+\left|\nabla\tilde{\varphi}\left(s\right)\right|^2\,dx=\frac{1}{2}G_C\int_0^T\left(1-\tilde{\varphi}\left(s\right)\right)^2+\left|\nabla\tilde{\varphi}\left(s\right)\right|^2\,dx.$$

Using Equation (A.10) yields

$$\frac{1}{2}G_C\int_0^T\left(1-\tilde{\varphi}\left(s\right)\right)^2+\left|\nabla\tilde{\varphi}\left(s\right)\right|^2\,dx\leq\frac{1}{2}G_C(1+\eta).$$

The estimation of the last integral in Equation (A.17)

$$\frac{1}{2}G_C\frac{1}{\epsilon_j}\int_{\xi_j}^{\xi_j+\epsilon_jT}\left((1-\varphi_j)^2+|\nabla\varphi_j|^2\right)\,dx,$$

works equal such that it is smaller than $\frac{1}{2}G_C(1+\eta)$ as well. This concludes to

$$\frac{1}{2}G_C\frac{1}{\epsilon_j}\int_\Omega\left((1-\varphi_j)^2+|\nabla\varphi_j|^2\right)\,dx\leq G_C\frac{\xi_j}{\epsilon_j}+G_C(1+\eta).$$

Going back to Equation (A.16) and applying the $\limsup_{j\to\infty}$ yields

$$\begin{aligned}\limsup_{j\to\infty}\frac{1}{2}G_C\int_\Omega\left(\frac{1}{\epsilon_j}(1-\varphi_j)^2+\epsilon_j|\nabla\varphi_j|^2\right)\,dx\leq\limsup_{j\to\infty}G_C\frac{\xi_j}{\epsilon_j}+G_C(1+\eta)\\+\limsup_{j\to\infty}\frac{1}{2}G_C\epsilon_j\int_\Omega|\nabla\varphi_j|^2\,dx.\end{aligned}$$

Due to the construction of φ_j it holds

$$\limsup_{j\to\infty}\epsilon_j\frac{1}{2}G_C\int_\Omega|\nabla\varphi_j|^2\,dx=0,$$

and further, since $\frac{\xi_j}{\epsilon_j}\to 0$ as $j\to\infty$, it follows

$$\limsup_{j\to\infty}G_C\frac{\xi_j}{\epsilon_j}+G_C(1+\eta)=G_C(1+\eta).$$

Since this holds for arbitrary $\eta>0$, $\eta\to 0$ we get Equation (A.13), given by

$$\limsup_{j\to\infty}\frac{1}{2}G_C\int_\Omega(\frac{1}{\epsilon_j}(1-\varphi_j)^2+\epsilon_j|\nabla\varphi_j|^2)\,dx\leq G_C\#(S(u)).$$

To sum up, Equation (A.11), Equation (A.12) and Equation (A.13)

$$\begin{aligned}\limsup_{j\to\infty}\frac{1}{2}\int_\Omega[(1-\kappa_j)\varphi_j^2+\kappa_j](2\mu+\lambda)|\nabla u_j|^2\,dx\leq\frac{1}{2}\int_\Omega(2\mu+\lambda)|\nabla u|^2\,dx,\\\limsup_{j\to\infty}\frac{1}{2}\int_\Omega\rho\varphi_j\nabla u_j\,dx\leq\frac{1}{2}\int_\Omega\rho\nabla u\,dx\end{aligned}$$

and

$$\limsup_{j\to\infty} \frac{1}{2} G_C \int_\Omega \left(\frac{1}{\epsilon_j}(1-\varphi_j)^2 + \epsilon_j |\nabla \varphi_j|^2\right) dx \leq G_C \#(S(u))$$

were shown. The combination yields the upper semi-continuity inequality

$$G(u,\varphi) \geq \limsup_{j\to\infty} G_j(u_j,\varphi_j).$$

Part 3: The result follows from [58, Corollary 7.20]. Under the assumption that there exists a sequence (u_j,φ_j), which minimizes G_j, and further, that $(u_j,\varphi_j) \to (u,\varphi)$ in $L^1(\Omega;\mathbb{R}^2)$ as $j\to\infty$,Dal Maso [58, Corollary 7.20] states that (u,φ) minimizes G. □

Appendix B

Block entries of discretized system

In the following, the block entries and residuals of all used problem formulations in mixed form are given. We use as ansatz functions $(\chi_j^u, \chi_j^p, \chi_j^\varphi) \in \mathcal{V}_h \times \mathcal{U}_h \times \mathcal{K}_h$ and test functions $(\chi_i^u, \chi_i^p, \chi_i^\varphi) \in \mathcal{V}_h \times \mathcal{U}_h \times \mathcal{K}_h$ for $i, j = 1, \dots, N$ with N total nodes. The discrete spaces are defined as

$$\begin{aligned}
\mathcal{V}_h &\coloneqq \{u_h \in H_0^1(\Omega; \mathbb{R}^2),\ u_h|_K \in (Q_2^c(K))^2\ \forall K \in \mathcal{T}_h\},\\
\mathcal{U}_h &\coloneqq \{p_h \in L^2(\Omega),\ p_h|_K \in Q_1^c(K) \quad \forall K \in \mathcal{T}_h\},\\
\mathcal{W}_h &\coloneqq \{\varphi_h \in H^1(\Omega),\ \varphi_h|_K \in Q_1^c(K)\ \forall K \in \mathcal{T}_h\}.
\end{aligned}$$

As proposed in Section 3.2.1, we define the block entries of the Jacobian $\mathcal{M}$ and the right hand side F consisting of the residuals of Newton's method:

$$\mathcal{M} = \begin{pmatrix} M^{uu} & M^{up} & M^{u\varphi} \\ M^{pu} & M^{pp} & M^{p\varphi} \\ M^{\varphi u} & M^{\varphi p} & M^{\varphi\varphi} \end{pmatrix}, \quad F = \begin{pmatrix} F^u \\ F^p \\ F^\varphi \end{pmatrix}.$$

In the definitions of the block entries we frequently use the following two identities for $u, w, \in \mathcal{V}_h$:

$$\begin{aligned}
(E_{\text{lin}}(u), \nabla w) &= (E_{\text{lin}}(u), E_{\text{lin}}(w)),\\
((\nabla \cdot u)\mathbb{1}, \nabla w) &= (\nabla \cdot u, \nabla \cdot w),
\end{aligned}$$

which can be seen easily using the definition of the linearized elasticity

$$E_{\text{lin}}(u) \coloneqq \frac{1}{2}(\nabla u + \nabla u^T).$$

Further, it holds for $p \in \mathcal{U}_h$ (in two dimensions x and y):

$$\begin{aligned}
p\mathbb{1} : E_{\text{lin}}(u) &= \begin{pmatrix} p & 0 \\ 0 & p \end{pmatrix} : \frac{1}{2}\left(\nabla u + \nabla u^T\right)\\
&= \begin{pmatrix} p & 0 \\ 0 & p \end{pmatrix} : \frac{1}{2}\begin{pmatrix} 2\partial_x u & \partial_y u_x + \partial_x u_y \\ \partial_x u_y + \partial_y u_x & 2\partial_y u_y \end{pmatrix} = p\ (\nabla \cdot u).
\end{aligned}$$

B.1 Mixed stabilized equal-order formulation based on AT_2, pressure driven

The block entries of the consistently stabilized equal-order Formulation 18 from Section 6.3.3 (Q_1^c elements for u, p, and φ), based on the AT_2 functional from Equation (7.3) and no splitting, are given as follows:

$$
\begin{aligned}
F_i^u &= (((1-\kappa)\tilde{\varphi}^2+\kappa)2\mu E_{\text{lin}}(u), E_{\text{lin}}(\chi_i^u)) + (((1-\kappa)\tilde{\varphi}^2+\kappa)p, \nabla\cdot\chi_i^u) + (\tilde{\varphi}^2\rho, \nabla\cdot\chi_i^u),\\
F_i^p &= ((1-\kappa)\tilde{\varphi}^2+\kappa)(\nabla\cdot u, \chi_i^p) - \alpha h^2(\nabla p, \nabla\chi_i^p) - \alpha h^2(2\mu((1-\kappa)\tilde{\varphi}^2+\kappa)E_{\text{lin}}(u) : E_{\text{lin}}(u), \nabla\chi_i^p),\\
F_i^\varphi &= (1-\kappa)(\varphi 2\mu E_{\text{lin}}(u) : E_{\text{lin}}(u), \chi_i^\varphi) + (1-\kappa)(\varphi(p\mathbb{1} : E_{\text{lin}}(u), \chi_i^\varphi),\\
&\quad + 2\rho(\varphi\nabla\cdot u, \chi_i^\varphi) + G_C\left(-\frac{1}{\epsilon}(1-\varphi, \chi_i^\varphi) + \epsilon(\nabla\varphi, \nabla\chi_i^\varphi)\right),
\end{aligned}
$$

$$
\begin{aligned}
M_{i,j}^{uu} &= (((1-\kappa)\tilde{\varphi}^2+\kappa)2\mu E_{\text{lin}}(\chi_j^u), E_{\text{lin}}(\chi_i^u)),\\
M_{i,j}^{pu} &= ((1-\kappa)\tilde{\varphi}^2+\kappa)(\nabla\cdot\chi_j^u, \chi_i^p)\\
&\quad - \alpha h^2(2\mu((1-\kappa)\tilde{\varphi}^2+\kappa)\left(E_{\text{lin}}(\chi_j^u) : E_{\text{lin}}(u) + E_{\text{lin}}(u) : E_{\text{lin}}(\chi_j^u), \nabla\chi_i^p\right),\\
M_{i,j}^{\varphi u} &= (1-\kappa)(\varphi 2\mu(E_{\text{lin}}(\chi_j^u) : E_{\text{lin}}(u) + E_{\text{lin}}(u) : E_{\text{lin}}(\chi_j^u)), \chi_i^\varphi) + 2\rho(\varphi\nabla\cdot\chi_j^u, \chi_i^\varphi),\\
M_{i,j}^{up} &= \left(((1-\kappa)\tilde{\varphi}^2+\kappa)\chi_j^p, \nabla\cdot\chi_i^u\right),\\
M_{i,j}^{pp} &= -\alpha h^2(\nabla\chi_j^p, \nabla\chi_i^p),\\
M_{i,j}^{\varphi p} &= (1-\kappa)(\varphi\chi_j^p\mathbb{1} : E_{\text{lin}}(u), \chi_i^\varphi),\\
M_{i,j}^{u\varphi} &= 0,\\
M_{i,j}^{p\varphi} &= 0,\\
M_{i,j}^{\varphi\varphi} &= (1-\kappa)(\chi_j^\varphi 2\mu E_{\text{lin}}(u) : E_{\text{lin}}(u), \chi_i^\varphi) + (1-\kappa)(\chi_j^\varphi(p\mathbb{1} : E_{\text{lin}}(u)), \chi_i^\varphi),\\
&\quad + 2\rho(\chi_j^\varphi\nabla\cdot u, \chi_i^\varphi) + G_C\left(\frac{1}{\epsilon}(\chi_j^\varphi, \chi_i^\varphi) + \epsilon(\nabla\chi_j^\varphi, \nabla\chi_i^\varphi)\right).
\end{aligned}
$$

B.2 Mixed model formulation based on AT_2 with Miehe's split, pressure driven

The block entries of the mixed Formulation 17 from Section 5.6, based on the AT_2 energy functional from Equation (7.3) and Miehe's split from Equation (7.6), are given as follows:

$$
\begin{aligned}
F_i^u &= ((1-\kappa)\tilde{\varphi}^2+\kappa)(2\mu E_{\text{lin}}^+(u)+p^+\mathbb{1}, E_{\text{lin}}(\chi_i^u)) \\
&\quad + (2\mu(E_{\text{lin}}(u)-E^+(u))+(p-p^+)\mathbb{1}, E_{\text{lin}}(\chi_i^u)) + (\tilde{\varphi}^2\rho, \nabla\cdot\chi_i^u), \\
F_i^p &= ((1-\kappa)\tilde{\varphi}^2+\kappa)(\nabla\cdot u, \chi_i^p) - \frac{1}{\lambda}(p,\chi_i^p), \\
F_i^\varphi &= (1-\kappa)(\varphi(2\mu E_{\text{lin}}^+(u)+p^+\mathbb{1}) : E_{\text{lin}}(u), \chi_i^\varphi) + 2\rho(\varphi\nabla\cdot u, \chi_i^\varphi) \\
&\quad + G_C(-\frac{1}{\epsilon}(1-\varphi), \chi_i^\varphi) + G_C\epsilon(\nabla\varphi, \nabla\chi_i^\varphi).
\end{aligned}
$$

$$
\begin{aligned}
M_{i,j}^{uu} &= (((1-\kappa)\tilde{\varphi}^2+\kappa)2\mu {E_{\text{lin}}^+}'(u,\chi_j^u), E_{\text{lin}}(\chi_i^u)) + (2\mu(E_{\text{lin}}(\chi_j^u)-E_{\text{lin}}^+(\chi_j^u)), E_{\text{lin}}(\chi_i^u)), \\
M_{i,j}^{pu} &= ((1-\kappa)\tilde{\varphi}^2+\kappa)(\nabla\cdot\chi_j^u, \chi_i^p), \\
M_{i,j}^{\varphi u} &= (1-\kappa)(2\mu\varphi E_{\text{lin}}^+(\chi_j^u) : E_{\text{lin}}(u), \chi_i^\varphi) + (1-\kappa)(2\mu\varphi E_{\text{lin}}^+(u) : E_{\text{lin}}(\chi_j^u), \chi_i^\varphi), \\
&\quad + (1-\kappa)(\varphi p^+\mathbb{1} : E_{\text{lin}}(\chi_i^u), \chi_i^\varphi) + 2\rho(\varphi\nabla\cdot\chi_j^u, \chi_i^\varphi), \\
M_{i,j}^{up} &= (((1-\kappa)\tilde{\varphi}^2+\kappa)\chi_j^{p,+}\mathbb{1}, E_{\text{lin}}(\chi_i^u)) + ((\chi_j^p-\chi_j^{p,+})\mathbb{1}, E_{\text{lin}}(\chi_i^u)), \\
M_{i,j}^{pp} &= -\frac{1}{\lambda}(\chi_j^p, \chi_i^p), \\
M_{i,j}^{\varphi p} &= (1-\kappa)(\varphi\chi_j^{p,+}\mathbb{1} : E_{\text{lin}}(u), \chi_i^\varphi), \\
M_{i,j}^{u\varphi} &= 0, \\
M_{i,j}^{p\varphi} &= 0, \\
M_{i,j}^{\varphi\varphi} &= (1-\kappa)(2\mu\chi_j^\varphi(E_{\text{lin}}^+(u) : E_{\text{lin}}(u)), \chi_i^\varphi) + (1-\kappa)(\chi_j^\varphi(p^+\mathbb{1}, E_{\text{lin}}(u)), \chi_i^\varphi) \\
&\quad + 2\rho(\chi_j^\varphi\nabla\cdot u, \chi_i^\varphi) + G_C\left(\frac{1}{\epsilon}(\chi_j^\varphi, \chi_i^\varphi) + \epsilon(\nabla\chi_j^\varphi, \nabla\chi_i^\varphi)\right).
\end{aligned}
$$

B.3 Mixed model formulation based on AT_1 with Miehe's split, pressure driven

The block entries of the mixed Formulation 17 from Section 5.6, based on the AT_1 energy functional from Equation (7.4) and Miehe's split from Equation (7.6), are given as follows:

$$
\begin{aligned}
F_i^u &= ((1-\kappa)\tilde{\varphi}^2+\kappa)(2\mu E_{\text{lin}}^+(u)+p^+\mathbb{1}, E_{\text{lin}}(\chi_i^u)) \\
&\quad + (2\mu(E_{\text{lin}}(u)-E^+(u))+(p-p^+)\mathbb{1}, E_{\text{lin}}(\chi_i^u)) + (\tilde{\varphi}^2\rho, \nabla\cdot\chi_i^u), \\
F_i^p &= ((1-\kappa)\tilde{\varphi}^2+\kappa)(\nabla\cdot u, \chi_i^p) - \frac{1}{\lambda}(p, \chi_i^p), \\
F_i^\varphi &= (1-\kappa)(\varphi(2\mu E_{\text{lin}}^+(u)+p^+\mathbb{1}) : E_{\text{lin}}(u), \chi_i^\varphi) + 2\rho(\varphi\nabla\cdot u, \chi_i^\varphi) \\
&\quad + G_C\left(-\frac{3}{8\epsilon}(1-\varphi), \chi_i^\varphi\right) + \frac{3}{4}G_C\epsilon(\nabla\varphi, \nabla\chi_i^\varphi).
\end{aligned}
$$

$$
\begin{aligned}
M_{i,j}^{uu} &= (((1-\kappa)\tilde{\varphi}^2+\kappa)2\mu {E_{\text{lin}}^+}'(u, \chi_j^u), E_{\text{lin}}(\chi_i^u)) + (2\mu(E_{\text{lin}}(\chi_j^u) - E_{\text{lin}}^+(\chi_j^u)), E_{\text{lin}}(\chi_i^u)), \\
M_{i,j}^{pu} &= (((1-\kappa)\tilde{\varphi}^2+\kappa)(\nabla\cdot\chi_j^u, \chi_i^p), \\
M_{i,j}^{\varphi u} &= (1-\kappa)(2\mu\varphi E_{\text{lin}}^+(\chi_j^u) : E_{\text{lin}}(u), \chi_i^\varphi) + (1-\kappa)(2\mu\varphi E_{\text{lin}}^+(u) : E_{\text{lin}}(\chi_j^u), \chi_i^\varphi) \\
&\quad + (1-\kappa)(\varphi p^+\mathbb{1} : E_{\text{lin}}(\chi_j^u), \chi_i^\varphi) + 2\rho(\varphi\nabla\cdot\chi_j^u, \chi_i^\varphi), \\
M_{i,j}^{up} &= (((1-\kappa)\tilde{\varphi}^2+\kappa)\chi_j^{p,+}\mathbb{1}, E_{\text{lin}}(\chi_i^u))) + ((\chi_j^p - \chi_j^{p,+})\mathbb{1}, E_{\text{lin}}(\chi_i^u)), \\
M_{i,j}^{pp} &= -\frac{1}{\lambda}(\chi_j^p, \chi_i^p), \\
M_{i,j}^{\varphi p} &= (1-\kappa)(\varphi\chi_j^{p,+}\mathbb{1} : E_{\text{lin}}(u), \chi_i^\varphi), \\
M_{i,j}^{u\varphi} &= 0, \\
M_{i,j}^{p\varphi} &= 0, \\
M_{i,j}^{\varphi\varphi} &= (1-\kappa)(2\mu\chi_j^\varphi(E_{\text{lin}}^+(u); E_{\text{lin}}(u)), \chi_i^\varphi) + (1-\kappa)\left(\chi_j^\varphi(p^+\mathbb{1}, E_{\text{lin}}(u)), \chi_i^\varphi\right) \\
&\quad + 2\rho(\chi_j^\varphi\nabla\cdot u, \chi_i^\varphi) + \frac{6}{8}G_C\epsilon(\nabla\chi_j^\varphi, \nabla\chi_i^\varphi).
\end{aligned}
$$

B.4 Mixed model formulation based on Wu's approach with Miehe's split, pressure driven

The block entries of the mixed Formulation 17 from Section 5.6, based on Wu's energy functional from Equation (7.5) and Miehe's split from Equation (7.6), are given as follows:

$$
\begin{aligned}
F_i^u &= ((1-\kappa)\tilde{\varphi}^2+\kappa)(2\mu E_{\text{lin}}^+(u)+p^+\mathbb{1}, E_{\text{lin}}(\chi_i^u)) \\
&\quad + (2\mu(E_{\text{lin}}(u)-E^+(u))+(p-p^+)\mathbb{1}, E_{\text{lin}}(\chi_i^u)) + (\tilde{\varphi}^2\rho, \nabla\cdot\chi_i^u), \\
F_i^p &= ((1-\kappa)\tilde{\varphi}^2+\kappa)(\nabla\cdot u, \chi_i^p) - \frac{1}{\lambda}(p, \chi_i^p), \\
F_i^\varphi &= (1-\kappa)(\varphi(2\mu E_{\text{lin}}^+(u)+p^+\mathbb{1}) : E_{\text{lin}}(u), \chi_i^\varphi) + 2\rho(\varphi\nabla\cdot u, \chi_i^\varphi) \\
&\quad + \ -G_C\frac{2}{\pi\epsilon}(1-\varphi, \chi_i^\varphi) + G_C\frac{2}{\pi}\epsilon(\nabla\varphi, \nabla\chi_i^\varphi).
\end{aligned}
$$

$$
\begin{aligned}
M_{i,j}^{uu} &= (((1-\kappa)\tilde{\varphi}^2+\kappa)2\mu {E_{\text{lin}}^+}'(u, \chi_j^u), E_{\text{lin}}(\chi_i^u)) + (2\mu(E_{\text{lin}}(\chi_j^u)-E_{\text{lin}}^+(\chi_j^u)), E_{\text{lin}}(\chi_i^u)), \\
M_{i,j}^{pu} &= ((1-\kappa)\tilde{\varphi}^2+\kappa)(\nabla\cdot\chi_j^u, \chi_i^p), \\
M_{i,j}^{\varphi u} &= (1-\kappa)(\varphi 2\mu(E_{\text{lin}}(\chi_j^u) : E_{\text{lin}}(u) + E_{\text{lin}}(u) : E_{\text{lin}}(\chi_j^u)), \chi_i^\varphi) + 2\rho(\varphi\nabla\cdot\chi_j^u, \chi_i^\varphi), \\
M_{i,j}^{up} &= (((1-\kappa)\tilde{\varphi}^2+\kappa)\chi_j^{p,+}\mathbb{1}, E_{\text{lin}}(\chi_i^u))) + ((\chi_j^p-\chi_j^{p,+})\mathbb{1}, E_{\text{lin}}(\chi_i^u)), \\
M_{i,j}^{pp} &= \ -\frac{1}{\lambda}(\chi_j^p, \chi_i^p), \\
M_{i,j}^{\varphi p} &= (1-\kappa)(\varphi\chi_j^{p,+}\mathbb{1} : E_{\text{lin}}(u), \chi_i^\varphi), \\
M_{i,j}^{u\varphi} &= 0, \\
M_{i,j}^{p\varphi} &= 0, \\
M_{i,j}^{\varphi\varphi} &= (1-\kappa)(2\mu\chi_j^\varphi(E_{\text{lin}}^+(u) : E_{\text{lin}}(u)), \chi_i^\varphi) + (1-\kappa)(\chi_j^\varphi(p^+\mathbb{1}, E_{\text{lin}}(u)), \chi_i^\varphi) \\
&\quad + 2\rho(\chi_j^\varphi\nabla\cdot u, \chi_i^\varphi) - G_C\frac{2}{\pi\epsilon}(\chi_j^\varphi, \chi_i^\varphi) + G_C\frac{2}{\pi}\epsilon(\nabla\chi_j^\varphi, \nabla\chi_i^\varphi).
\end{aligned}
$$

B.5 Mixed model formulation based on AT_2 with Amor's split, pressure driven

The block entries of the mixed Formulation 17 from Section 5.6, based on the AT_2 energy functional from Equation (7.3) and Amor's split from Equation (7.7), are given as follows:

$$
\begin{aligned}
F_i^u =& \left((1-\kappa)\tilde{\varphi}^2+\kappa\right)\left(\mu \max\left\{0, \operatorname{tr}\left(E_{\text{lin}}^+(u)\right)\right\}\mathbb{1} + 2\mu\left(E_{\text{lin}}^+(u) - \frac{1}{3}\operatorname{tr}\left(E_{\text{lin}}^+(u)\right)\mathbb{1}\right) + p^+\mathbb{1}, E_{\text{lin}}(\chi_i^u)\right)\\
&+ \left(\mu\left(\operatorname{tr}\left(E_{\text{lin}}^+(u)\right) - \max\left\{0, \operatorname{tr}\left(E_{\text{lin}}^+(u)\right)\right\}\right)\mathbb{1} + (p-p^+)\mathbb{1}, E_{\text{lin}}(\chi_i^u)\right) + (\tilde{\varphi}^2\rho, \nabla\cdot\chi_i^u),\\
F_i^p =& \left((1-\kappa)\tilde{\varphi}^2+\kappa\right)(\nabla\cdot u, \chi_i^p) - \frac{1}{\lambda}(p, \chi_i^p),\\
F_i^\varphi =& (1-\kappa)\left(\varphi\left(\mu\max\left\{0, \operatorname{tr}\left(E_{\text{lin}}^+(u)\right)\right\}\mathbb{1} + 2\mu\left(E_{\text{lin}}^+(u) - \frac{1}{3}\operatorname{tr}\left(E_{\text{lin}}^+(u)\right)\mathbb{1}\right) + p^+\mathbb{1}\right) : E_{\text{lin}}(u), \chi_i^\varphi\right)\\
&+2\rho(\varphi\nabla\cdot u, \chi_i^\varphi) + G_C\left(-\frac{1}{\epsilon}(1-\varphi), \chi_i^\varphi\right) + G_C\epsilon(\nabla\varphi, \nabla\chi_i^\varphi).
\end{aligned}
$$

$$
\begin{aligned}
M_{i,j}^{uu} =& \left((1-\kappa)\tilde{\varphi}^2+\kappa\right)\left(\mu\max\left\{0, \operatorname{tr}\left(E_{\text{lin}}^+(\chi_j^u)\right)\right\}\mathbb{1} + 2\mu\left(E_{\text{lin}}^+(\chi_j^u) - \frac{1}{3}\operatorname{tr}\left(E_{\text{lin}}^+(\chi_j^u)\right)\mathbb{1}\right), E_{\text{lin}}(\chi_i^u)\right)\\
&+ \left(\mu\left(\operatorname{tr}\left(E_{\text{lin}}^+(\chi_j^u)\right) - \max\left\{0, \operatorname{tr}\left(E_{\text{lin}}^+(\chi_j^u)\right)\right\}\right)\mathbb{1}, E_{\text{lin}}(\chi_i^u)\right),\\
M_{i,j}^{pu} =& \left((1-\kappa)\tilde{\varphi}^2+\kappa\right)(\nabla\cdot\chi_j^u, \chi_i^p),\\
M_{i,j}^{\varphi u} =& (1-\kappa)(\varphi\mu\max\left\{0, \operatorname{tr}\left(E_{\text{lin}}^+(\chi_j^u)\right)\right\}\mathbb{1} + 2\mu\left(E_{\text{lin}}^+(\chi_j^u) - \frac{1}{3}\operatorname{tr}\left(E_{\text{lin}}^+(\chi_j^u)\right)\mathbb{1}\right) : E_{\text{lin}}(u), \chi_i^\varphi)\\
&+ (1-\kappa)(\varphi\left(\mu\left(\operatorname{tr}\left(E_{\text{lin}}^+(u)\right) - \max\left\{0, \operatorname{tr}\left(E_{\text{lin}}^+(u)\right)\right\}\right)\mathbb{1}\right) : E_{\text{lin}}(\chi_j^u), \chi_i^\varphi),\\
&+ (1-\kappa)(\varphi p^+\mathbb{1} : E_{\text{lin}}(\chi_j^u), \chi_i^\varphi) + 2\rho(\varphi\nabla\cdot\chi_j^u, \chi_i^\varphi),\\
M_{i,j}^{up} =& \left((1-\kappa)\tilde{\varphi}^2+\kappa\right)\left(\chi_j^{p,+}\mathbb{1}, E_{\text{lin}}(\chi_i^u)\right) + \left((\chi_j^p - \chi_j^{p,+})\mathbb{1}, E_{\text{lin}}(\chi_i^u)\right),\\
M_{i,j}^{pp} =& -\frac{1}{\lambda}(\chi_j^p, \chi_i^p),\\
M_{i,j}^{\varphi p} =& (1-\kappa)(\varphi\chi_j^{p,+}\mathbb{1} : E_{\text{lin}}(u), \chi_i^\varphi),\\
M_{i,j}^{u\varphi} =& 0,\\
M_{i,j}^{p\varphi} =& 0,\\
M_{i,j}^{\varphi\varphi} =& (1-\kappa)\left(\chi_j^\varphi\left(\mu\max\left\{0, \operatorname{tr}\left(E_{\text{lin}}^+(u)\right)\right\}\mathbb{1} + 2\mu\left(E_{\text{lin}}^+(u) - \frac{1}{3}\operatorname{tr}\left(E_{\text{lin}}^+(u)\right)\mathbb{1}\right)\right) : E_{\text{lin}}(u), \chi_i^\varphi\right)\\
&+ (1-\kappa)\left(\chi_j^\varphi(p^+\mathbb{1} : E_{\text{lin}}(u)), \chi_i^\varphi\right) + 2\rho(\chi_j^\varphi\nabla\cdot u, \chi_i^\varphi)\\
&+ G_C\left(\frac{1}{\epsilon}(\chi_j^\varphi, \chi_i^\varphi) + \epsilon(\nabla\chi_j^\varphi, \nabla\chi_i^\varphi)\right).
\end{aligned}
$$

B.6 Mixed model formulation based on AT_1 with Amor's split, pressure driven

The block entries of the mixed Formulation 17 from Section 5.6, based on the AT_1 energy functional from Equation (7.4) and Amor's split from Equation (7.7), are given as follows:

$$
\begin{aligned}
F_i^u =& \left((1-\kappa)\tilde{\varphi}^2+\kappa\right)\left(\mu \max\left\{0, \operatorname{tr}\left(E_{\mathrm{lin}}^+(u)\right)\right\}\mathbb{1} + 2\mu\left(E_{\mathrm{lin}}^+(u) - \frac{1}{3}\operatorname{tr}\left(E_{\mathrm{lin}}^+(u)\right)\mathbb{1}\right) + p^+\mathbb{1}, E_{\mathrm{lin}}(\chi_i^u)\right)\\
&+ \left(\mu\left(\operatorname{tr}\left(E_{\mathrm{lin}}^+(u)\right) - \max\left\{0, \operatorname{tr}\left(E_{\mathrm{lin}}^+(u)\right)\right\}\right)\mathbb{1} + (p-p^+)\mathbb{1}, E_{\mathrm{lin}}(\chi_i^u)\right) + (\tilde{\varphi}^2\rho, \nabla\cdot\chi_i^u),\\
F_i^p =& \left((1-\kappa)\tilde{\varphi}^2+\kappa\right)(\nabla\cdot u, \chi_i^p) - \frac{1}{\lambda}(p, \chi_i^p),\\
F_i^\varphi =& (1-\kappa)\left(\varphi\left(\mu\max\left\{0, \operatorname{tr}\left(E_{\mathrm{lin}}^+(u)\right)\right\}\mathbb{1} + 2\mu\left(E_{\mathrm{lin}}^+(u) - \frac{1}{3}\operatorname{tr}\left(E_{\mathrm{lin}}^+(u)\right)\mathbb{1}\right) + p^+\mathbb{1}\right) : E_{\mathrm{lin}}(u), \chi_i^\varphi\right)\\
&+ 2\rho(\varphi\nabla\cdot u, \chi_i^\varphi) + G_C\left(-\frac{3}{8\epsilon}(1-\varphi), \chi_i^\varphi\right) + \frac{3}{4}G_C\epsilon(\nabla\varphi, \nabla\chi_i^\varphi).
\end{aligned}
$$

$$
\begin{aligned}
M_{i,j}^{uu} =& \left((1-\kappa)\tilde{\varphi}^2+\kappa\right)\left(\mu\max\left\{0, \operatorname{tr}\left(E_{\mathrm{lin}}^+(\chi_j^u)\right)\right\}\mathbb{1} + 2\mu\left(E_{\mathrm{lin}}^+(\chi_j^u) - \frac{1}{3}\operatorname{tr}\left(E_{\mathrm{lin}}^+(\chi_j^u)\right)\mathbb{1}\right), E_{\mathrm{lin}}(\chi_i^u)\right)\\
&+ \left(\mu\left(\operatorname{tr}\left(E_{\mathrm{lin}}^+(\chi_j^u)\right) - \max\left\{0, \operatorname{tr}\left(E_{\mathrm{lin}}^+(\chi_j^u)\right)\right\}\right)\mathbb{1}, E_{\mathrm{lin}}(\chi_i^u)\right),\\
M_{i,j}^{pu} =& \left((1-\kappa)\tilde{\varphi}^2+\kappa\right)(\nabla\cdot\chi_j^u, \chi_i^p),\\
M_{i,j}^{\varphi u} =& (1-\kappa)(\varphi\mu\max\left\{0, \operatorname{tr}\left(E_{\mathrm{lin}}^+(\chi_j^u)\right)\right\}\mathbb{1} + 2\mu\left(E_{\mathrm{lin}}^+(\chi_j^u) - \frac{1}{3}\operatorname{tr}\left(E_{\mathrm{lin}}^+(\chi_j^u)\right)\mathbb{1}\right) : E_{\mathrm{lin}}(u), \chi_i^\varphi)\\
&+ (1-\kappa)(\varphi\left(\mu\left(\operatorname{tr}\left(E_{\mathrm{lin}}^+(u)\right) - \max\left\{0, \operatorname{tr}\left(E_{\mathrm{lin}}^+(u)\right)\right\}\right)\mathbb{1}\right) : E_{\mathrm{lin}}(\chi_j^u), \chi_i^\varphi),\\
&+ (1-\kappa)(\varphi p^+\mathbb{1} : E_{\mathrm{lin}}(\chi_j^u), \chi_i^\varphi) + 2\rho(\varphi\nabla\cdot\chi_j^u, \chi_i^\varphi),\\
M_{i,j}^{up} =& \left((1-\kappa)\tilde{\varphi}^2+\kappa\right)\left(\chi_j^{p,+}\mathbb{1}, E_{\mathrm{lin}}(\chi_i^u)\right) + \left((\chi_j^p - \chi_j^{p,+})\mathbb{1}, E_{\mathrm{lin}}(\chi_i^u)\right),\\
M_{i,j}^{pp} =& -\frac{1}{\lambda}(\chi_j^p, \chi_i^p),\\
M_{i,j}^{\varphi p} =& (1-\kappa)(\varphi\chi_j^{p,+}\mathbb{1} : E_{\mathrm{lin}}(u), \chi_i^\varphi),\\
M_{i,j}^{u\varphi} =& 0,\\
M_{i,j}^{p\varphi} =& 0,\\
M_{i,j}^{\varphi\varphi} =& (1-\kappa)\left(\chi_j^\varphi\left(\mu\max\left\{0, \operatorname{tr}\left(E_{\mathrm{lin}}^+(u)\right)\right\}\mathbb{1} + 2\mu\left(E_{\mathrm{lin}}^+(u) - \frac{1}{3}\operatorname{tr}\left(E_{\mathrm{lin}}^+(u)\right)\mathbb{1}\right)\right) : E_{\mathrm{lin}}(u), \chi_i^\varphi\right)\\
&+ (1-\kappa)\left(\chi_j^\varphi(p^+\mathbb{1} : E_{\mathrm{lin}}(u)), \chi_i^\varphi\right) + 2\rho(\chi_j^\varphi\nabla\cdot u, \chi_i^\varphi) + \frac{6}{8}G_C\epsilon(\nabla\chi_j^\varphi, \nabla\chi_i^\varphi).
\end{aligned}
$$

B.7 Mixed model formulation based on Wu's approach with Amor's split, pressure driven

This is the model, mainly used in Chapter 7. The block entries of the mixed Formulation 17 from Section 5.6, based on Wu's energy functional from Equation (7.5) and Amor's split from Equation (7.7), are given as follows:

$$
\begin{aligned}
F_i^u =& \left((1-\kappa)\tilde{\varphi}^2+\kappa\right)\left(\mu \max\left\{0, \operatorname{tr}\left(E_{\text{lin}}^+(u)\right)\right\}\mathbb{1} + 2\mu\left(E_{\text{lin}}^+(u) - \frac{1}{3}\operatorname{tr}\left(E_{\text{lin}}^+(u)\right)\mathbb{1}\right) + p^+\mathbb{1}, E_{\text{lin}}(\chi_i^u)\right)\\
&+ \left(\mu\left(\operatorname{tr}\left(E_{\text{lin}}^+(u)\right) - \max\left\{0, \operatorname{tr}\left(E_{\text{lin}}^+(u)\right)\right\}\right)\mathbb{1} + (p-p^+)\mathbb{1}, E_{\text{lin}}(\chi_i^u)\right) + (\tilde{\varphi}^2\rho, \nabla\cdot\chi_i^u),\\
F_i^p =& \left((1-\kappa)\tilde{\varphi}^2+\kappa\right)(\nabla\cdot u, \chi_i^p) - \frac{1}{\lambda}(p, \chi_i^p),\\
F_i^\varphi =& (1-\kappa)\left(\varphi\left(\mu\max\left\{0, \operatorname{tr}\left(E_{\text{lin}}^+(u)\right)\right\}\mathbb{1} + 2\mu\left(E_{\text{lin}}^+(u) - \frac{1}{3}\operatorname{tr}\left(E_{\text{lin}}^+(u)\right)\mathbb{1}\right) + p^+\mathbb{1}\right) : E_{\text{lin}}(u), \chi_i^\varphi\right)\\
&+ 2\rho\left(\varphi\nabla\cdot u, \chi_i^\varphi\right)\\
&- G_C\frac{2}{\pi\epsilon}(1-\varphi, \chi_i^\varphi) + G_C\frac{2}{\pi}\epsilon(\nabla\varphi, \nabla\chi_i^\varphi).
\end{aligned}
$$

$$
\begin{aligned}
M_{i,j}^{uu} =& \left((1-\kappa)\tilde{\varphi}^2+\kappa\right)\left(\mu\max\left\{0, \operatorname{tr}\left(E_{\text{lin}}^+(\chi_j^u)\right)\right\}\mathbb{1} + 2\mu\left(E_{\text{lin}}^+(\chi_j^u) - \frac{1}{3}\operatorname{tr}\left(E_{\text{lin}}^+(\chi_j^u)\right)\mathbb{1}\right), E_{\text{lin}}(\chi_i^u)\right)\\
&+ \left(\mu\left(\operatorname{tr}\left(E_{\text{lin}}^+(\chi_j^u)\right) - \max\left\{0, \operatorname{tr}\left(E_{\text{lin}}^+(\chi_j^u)\right)\right\}\right)\mathbb{1}, E_{\text{lin}}(\chi_i^u)\right),\\
M_{i,j}^{pu} =& \left((1-\kappa)\tilde{\varphi}^2+\kappa\right)(\nabla\cdot\chi_j^u, \chi_i^p),\\
M_{i,j}^{\varphi u} =& (1-\kappa)(\varphi\mu\max\left\{0, \operatorname{tr}\left(E_{\text{lin}}^+(\chi_j^u)\right)\right\}\mathbb{1} + 2\mu\left(E_{\text{lin}}^+(\chi_j^u) - \frac{1}{3}\operatorname{tr}\left(E_{\text{lin}}^+(\chi_j^u)\right)\mathbb{1}\right) : E_{\text{lin}}(u), \chi_i^\varphi)\\
&+ (1-\kappa)(\varphi\left(\mu\left(\operatorname{tr}\left(E_{\text{lin}}^+(u)\right) - \max\left\{0, \operatorname{tr}\left(E_{\text{lin}}^+(u)\right)\right\}\right)\mathbb{1}\right) : E_{\text{lin}}(\chi_j^u), \chi_i^\varphi),\\
&+ (1-\kappa)(\varphi p^+\mathbb{1} : E_{\text{lin}}(\chi_j^u), \chi_i^\varphi) + 2\rho(\varphi\nabla\cdot\chi_j^u, \chi_i^\varphi),\\
M_{i,j}^{up} =& \left((1-\kappa)\tilde{\varphi}^2+\kappa\right)\left(\chi_j^{p,+}\mathbb{1}, E_{\text{lin}}(\chi_i^u)\right) + ((\chi_j^p - \chi_j^{p,+})\mathbb{1}, E_{\text{lin}}(\chi_i^u)),\\
M_{i,j}^{pp} =& -\frac{1}{\lambda}(\chi_j^p, \chi_i^p),\\
M_{i,j}^{\varphi p} =& (1-\kappa)(\varphi\chi_j^{p,+}\mathbb{1} : E_{\text{lin}}(u), \chi_i^\varphi),\\
M_{i,j}^{u\varphi} =& 0,\\
M_{i,j}^{p\varphi} =& 0,\\
M_{i,j}^{\varphi\varphi} =& (1-\kappa)\left(\chi_j^\varphi\left(\mu\max\left\{0, \operatorname{tr}\left(E_{\text{lin}}^+(u)\right)\right\}\mathbb{1} + 2\mu\left(E_{\text{lin}}^+(u) - \frac{1}{3}\operatorname{tr}\left(E_{\text{lin}}^+(u)\right)\mathbb{1}\right)\right) : E_{\text{lin}}(u), \chi_i^\varphi\right)\\
&+ (1-\kappa)\left(\chi_j^\varphi(p^+\mathbb{1}, E_{\text{lin}}(u)), \chi_i^\varphi\right) - G_C\frac{2}{\pi\epsilon}(\chi_j^\varphi, \chi_i^\varphi) + G_C\frac{2}{\pi}\epsilon(\nabla\chi_j^\varphi, \nabla\chi_i^\varphi).
\end{aligned}
$$

Bibliography

[1] R. A. Adams and J. J. Fournier. *Sobolev spaces*. Elsevier, 2003.

[2] H. W. Alt. Linear functional analysis. *An application oriented introduction*, 1992.

[3] M. Ambati, T. Gerasimov, and L. De Lorenzis. Phase-field modeling of ductile fracture. *Computational Mechanics*, 55(5):1017–1040, 2015.

[4] M. Ambati, T. Gerasimov, and L. De Lorenzis. A review on phase-field models of brittle fracture and a new fast hybrid formulation. *Computational Mechanics*, 55(2):383–405, 2015.

[5] L. Ambrosio and V. M. Tortorelli. Approximation of functional depending on jumps by elliptic functional via t-convergence. *Communications on Pure and Applied Mathematics*, 43(8):999–1036, 1990.

[6] L. Ambrosio and V. M. Tortorelli. On the approximation of free discontinuity problems. *Bollettino dell'unione matematica italiana B.*, 6(1):105–123, 1992.

[7] H. Amor, J.-J. Marigo, and C. Maurini. Regularized formulation of the variational brittle fracture with unilateral contact: Numerical experiments. *Journal of the Mechanics and Physics of Solids*, 57(8):1209–1229, 2009.

[8] B. Arash, W. Exner, and R. Rolfes. A finite deformation phase-field fracture model for the thermo-viscoelastic analysis of polymer nanocomposites. *Computer Methods in Applied Mechanics and Engineering*, 381:113821, 2021.

[9] D. Arndt, W. Bangerth, B. Blais, T. C. Clevenger, M. Fehling, A. V. Grayver, T. Heister, L. Heltai, M. Kronbichler, M. Maier, P. Munch, J.-P. Pelteret, R. Rastak, I. Thomas, B. Turcksin, Z. Wang, and D. Wells. The `deal.II` library, version 9.2. *Journal of Numerical Mathematics*, 28(3):131–146, 2020.

[10] D. Arndt, W. Bangerth, D. Davydov, T. Heister, L. Heltai, M. Kronbichler, M. Maier, J.-P. Pelteret, B. Turcksin, and D. Wells. The `deal.II` library, version 8.5. *Journal of Numerical Mathematics*, 2017.

[11] D. Arndt, W. Bangerth, D. Davydov, T. Heister, L. Heltai, M. Kronbichler, M. Maier, J.-P. Pelteret, B. Turcksin, and D. Wells. The `deal.II` finite element library: Design, features, and insights. *Computers & Mathematics with Applications*, 81:407–422, 2021.

[12] M. Artina, M. Fornasier, S. Micheletti, and S. Perotto. Anisotropic mesh adaptation for crack detection in brittle materials. *SIAM Journal on Scientific Computing*, 37(4):B633–B659, 2015.

[13] I. Babuška. Error-bounds for finite element method. *Numerische Mathematik*, 16(4):322–333, 1971.

[14] I. Babuška. The rate of convergence for the finite element method. *SIAM Journal on Numerical Analysis*, 8(2):304–315, 1971.

[15] I. Babuška and M. Suri. Locking effects in the finite element approximation of elasticity problems. *Numerische Mathematik*, 62(1):439–463, 1992.

[16] H. Badnava, M. A. Msekh, E. Etemadi, and T. Rabczuk. An h-adaptive thermo-mechanical phase field model for fracture. *Finite Elements in Analysis and Design*, 138:31 – 47, 2018.

[17] W. Bangerth, C. Burstedde, T. Heister, and M. Kronbichler. Algorithms and data structures for massively parallel generic adaptive finite element codes. *ACM Transactions on Mathematical Software (TOMS)*, 38(2):1–28, 2012.

[18] W. Bangerth, R. Hartmann, and G. Kanschat. `deal.II` – a general purpose object oriented finite element library. *ACM Trans. Math. Softw.*, 33(4):24/1–24/27, 2007.

[19] W. G. Barry F. Smith, Petter E. Bjørstad. *Domain decomposition: Parallel Multilevel Methods for Elliptic Partial Differential Equations*. Cambridge University Press, 1996.

[20] S. Bartels. *Numerical methods for nonlinear partial differential equations*, volume 47. Springer, 2015.

[21] S. Bartels. *Numerical approximation of partial differential equations*, volume 64. Springer, 2016.

[22] S. Basava, K. Mang, M. Walloth, T. Wick, and W. Wollner. Adaptive and pressure-robust discretization of incompressible pressure-driven phase-field fracture. *arXiv preprint arXiv:2006.16566*, 2020.

[23] H. R. Bayat, S. Wulfinghoff, S. Kastian, and S. Reese. On the use of reduced integration in combination with discontinuous galerkin discretization: application to volumetric and shear locking problems. *Advanced Modeling and Simulation in Engineering Sciences*, 5(1):1–16, 2018.

[24] G. Bellettini and A. Coscia. Discrete approximation of a free discontinuity problem. *Numerical Functional Analysis and Optimization*, 15(3-4):201–224, 1994.

[25] M. Benzi, G. H. Golub, and J. Liesen. Numerical solution of saddle point problems. *Acta numerica*, 14:1–137, 2005.

[26] S. Beuchler and S. V. Nepomnyaschikh. Overlapping additive Schwarz preconditioners for isotropic elliptic problems with degenerate coefficients. 2007.

[27] C. Bilgen, S. Homberger, and K. Weinberg. Phase-field fracture simulations of the brazilian splitting test. *International Journal of Fracture*, 220(1):85–98, 2019.

[28] D. Boffi, F. Brezzi, M. Fortin, et al. *Mixed finite element methods and applications*, volume 44. Springer, 2013.

[29] M. J. Borden. *Isogeometric analysis of phase-field models for dynamic brittle and ductile fracture*. PhD thesis, 2012.

[30] M. J. Borden, C. V. Verhoosel, M. A. Scott, T. J. Hughes, and C. M. Landis. A phase-field description of dynamic brittle fracture. *Computer Methods in Applied Mechanics and Engineering*, 217:77–95, 2012.

[31] B. Bourdin. Image segmentation with a finite element method. *ESAIM: Mathematical modelling and numerical analysis*, 33(2):229–244, 1999.

[32] B. Bourdin. Numerical implementation of the variational formulation for quasi-static brittle fracture. *Interfaces and free boundaries*, 9(3):411–430, 2007.

[33] B. Bourdin, C. P. Chukwudozie, K. Yoshioka, et al. A variational approach to the numerical simulation of hydraulic fracturing. In *SPE Annual Technical Conference and Exhibition*. Society of Petroleum Engineers, 2012.

[34] B. Bourdin and G. A. Francfort. Past and present of variational fracture. *SIAM News*, 52(9), 2019.

[35] B. Bourdin, G. A. Francfort, and J.-J. Marigo. Numerical experiments in revisited brittle fracture. *Journal of the Mechanics and Physics of Solids*, 48(4):797–826, 2000.

[36] B. Bourdin, C. Larsen, and C. Richardson. A time-discrete model for dynamic fracture based on crack regularization. *Int. J. Frac.*, 168(2):133–143, 2011.

[37] B. Bourdin, J.-J. Marigo, C. Maurini, and P. Sicsic. Morphogenesis and propagation of complex cracks induced by thermal shocks. *Physical review letters*, 112(1):014301, 2014.

[38] D. Braess. Stability of saddle point problems with penalty. *Mathematical Modelling and Numerical Analysis*, 30(6):731–742, 1996.

[39] D. Braess. *Finite elements: Theory, fast solvers, and applications in solid mechanics*. Cambridge University Press, 2007.

[40] A. Braides. *Approximation of free-discontinuity problems*. Number 1694 in Lecture notes in Mathematics. Springer Science & Business Media, 1998.

[41] A. Braides. *Gamma-convergence for Beginners*, volume 22. Clarendon Press, 2002.

[42] J. H. Bramble and J. E. Pasciak. A preconditioning technique for indefinite systems resulting from mixed approximations of elliptic problems. *Mathematics of Computation*, 50(181):1–17, 1988.

[43] S. Brenner and L. Scott. The mathematical theory of finite element methods. *New York*, 1994.

[44] F. Brezzi. On the existence, uniqueness and approximation of saddle-point problems arising from Lagrangian multipliers. *Revue Française D'Automatique, Informatique, Recherche Opérationnelle. Analyse Numérique*, 8(R2):129–151, 1974.

[45] R. Brighenti, T. Rabczuk, and X. Zhuang. Phase field approach for simulating failure of viscoelastic elastomers. *European Journal of Mechanics-A/Solids*, 85:104092, 2021.

[46] A. N. Brooks and T. J. Hughes. Streamline upwind/petrov-galerkin formulations for convection dominated flows with particular emphasis on the incompressible navier-stokes equations. *Computer methods in applied mechanics and engineering*, 32(1-3):199–259, 1982.

[47] M. K. Brun, T. Wick, I. Berre, J. M. Nordbotten, and F. A. Radu. An iterative staggered scheme for phase field brittle fracture propagation with stabilizing parameters. *Computer Methods in Applied Mechanics and Engineering*, 361:112752, 2020.

[48] E. C. Bryant and W. Sun. A mixed-mode phase field fracture model in anisotropic rocks with consistent kinematics. *Computer Methods in Applied Mechanics and Engineering*, 342:561–584, 2018.

[49] S. Burke, C. Ortner, and E. Süli. An adaptive finite element approximation of a variational model of brittle fracture. *SIAM Journal on Numerical Analysis*, 48(3):980–1012, 2010.

[50] F. Carleo, E. Barbieri, R. Whear, and J. Busfield. Limitations of viscoelastic constitutive models for carbon-black reinforced rubber in medium dynamic strains and medium strain rates. *Polymers*, 10(9):988, 2018.

[51] P. Charrier, E. Ostoja-Kuczynski, E. Verron, G. Marckmann, L. Gornet, and G. Chagnon. Theoretical and numerical limitations for the simulation of crack propagation in natural rubber components. *Constitutive Models for Rubber III*, pages 3–10, 2003.

[52] P. G. Ciarlet. *Mathematical Elasticity: Volume I: three-dimensional elasticity*. North-Holland, 1988.

[53] P. G. Ciarlet. The finite element method for elliptic problems. *Classics in Applied Mathematics*, 40:1–511, 2002.

[54] P. G. Ciarlet. *Linear and nonlinear functional analysis with applications*, volume 130. Siam, 2013.

[55] E. Cinatl. Finite element discretizations for linear elasticity. *Bachelor thesis, Clemson University, SC*, 2018.

[56] T. C. Clevenger and T. Heister. Comparison between algebraic and matrix-free geometric multigrid for a stokes problem on adaptive meshes with variable viscosity. *Numerical Linear Algebra with Applications*, page e2375, 2021.

[57] B. Cockburn, G. E. Karniadakis, and C.-W. Shu. The development of discontinuous Galerkin methods. In *Discontinuous Galerkin Methods*, pages 3–50. Springer, 2000.

[58] G. Dal Maso. *An introduction to Gamma convergence*. Birkhäuser, 1993.

[59] T. A. Davis. Algorithm 832: UMFPACK V4. 3–an unsymmetric-pattern multifrontal method. *ACM Transactions on Mathematical Software (TOMS)*, 30(2):196–199, 2004.

[60] T. A. Davis and I. S. Duff. An unsymmetric-pattern multifrontal method for sparse lu factorization. *SIAM Journal on Matrix Analysis and Applications*, 18(1):140–158, 1997.

[61] The step-20 tutorial program of deal.II. https://www.dealii.org/current/doxygen/deal.II/step_20.html.

[62] The Differential Equation and Optimization Environment: DOpElib. http://www.dopelib.net.

[63] H. C. Elman, D. J. Silvester, and A. J. Wathen. *Finite elements and fast iterative solvers: with applications in incompressible fluid dynamics*. Numerical Mathematics and Scie, 2014.

[64] C. Engwer and L. Schumacher. A phase field approach to pressurized fractures using discontinuous galerkin methods. *Mathematics and Computers in Simulation*, 137:266–285, 2017.

[65] A. Ern and J.-L. Guermond. *Theory and practice of finite elements*, volume 159. Springer, 2004.

[66] M. Fan, T. Wick, and Y. Jin. A phase-field model for mixed-mode fracture. In *Proceedings of the 8th GACM Colloquium on Computational Mechanics for Young Scientists from Academia and Industry*, 2019.

[67] P. E. Farrell and C. Maurini. Linear and nonlinear solvers for variational phase-field models of brittle fracture. *International Journal for Numerical Methods*, 109:648–667, 2017.

[68] A. Faye, Y. Lev, and K. Y. Volokh. Modeling dynamic fracture in rubberlike materials. *Constitutive Models for Rubber XI*, pages 505–511, 2019.

[69] A. Fehse, N. H. Kröger, K. Mang, and T. Wick. Crack path comparisons of a mixed phase-field fracture model and experiments in punctured epdm strips. *PAMM*, 20(1):e202000335, 2021.

[70] M. Focardi and F. Iurlano. Asymptotic analysis of ambrosio–tortorelli energies in linearized elasticity. *SIAM Journal on Mathematical Analysis*, 46(4):2936–2955, 2014.

[71] C. Fox. *An introduction to the calculus of variations*. Courier Corporation, 1987.

[72] G. A. Francfort and J.-J. Marigo. Revisiting brittle fracture as an energy minimization problem. *Journal of the Mechanics and Physics of Solids*, 46(8):1319–1342, 1998.

[73] F. Freddi and G. Royer-Carfagni. Regularized variational theories of fracture: a unified approach. *Journal of the Mechanics and Physics of Solids*, 58(8):1154–1174, 2010.

[74] M. W. Gee, C. M. Siefert, J. J. Hu, R. S. Tuminaro, and M. G. Sala. Ml 5.0 smoothed aggregation user's guide. Technical report, Technical Report SAND2006-2649, Sandia National Laboratories, 2006.

[75] O. Gehrmann, N. H. Kröger, P. Erren, and D. Juhre. Estimation of the compression modulus of a technical rubber via cyclic volumetric compression tests. *Technische Mechanik*, 37(1):28–36, 2017.

[76] T. Gerasimov and L. De Lorenzis. A line search assisted monolithic approach for phase-field computing of brittle fracture. *Computer Methods in Applied Mechanics and Engineering*, 312:276–303, 2016.

[77] T. Gerasimov, U. Römer, J. Vondřejc, H. G. Matthies, and L. De Lorenzis. Stochastic phase-field modeling of brittle fracture: computing multiple crack patterns and their probabilities. *Computer Methods in Applied Mechanics and Engineering*, 372:113353, 2020.

[78] V. Girault and P.-A. Raviart. Finite Element Methods for Navier–Stokes Equations: Theory and Algorithms, 1986.

[79] C. Goll, T. Wick, and W. Wollner. DOpElib: Differential equations and Optimization Environment; A goal oriented software library for solving PDEs and optimization problems with PDEs. *Archive of Numerical Software*, 5(2):1–14, 2017.

[80] S. Goswami, C. Anitescu, S. Chakraborty, and T. Rabczuk. Transfer learning enhanced physics informed neural network for phase-field modeling of fracture. *Theoretical and Applied Fracture Mechanics*, 106:102447, 2020.

[81] A. A. Griffith. The phenomena of flow and rupture in solids. *Transactions of the Royal Society A*, 221:163–198, 1920.

[82] W. Hackbusch. *Multi-grid methods and applications*, volume 4. Springer Science & Business Media, 2013.

[83] J. Hadamard. Le problème de cauchy et les équations aux dérivées partielles linéaires hyperboliques. *Paris*, 11:243–264, 1932.

[84] P. Hansbo and M. G. Larson. Discontinuous Galerkin methods for incompressible and nearly incompressible elasticity by Nitsche's method. *Computer Methods in Applied Mechanics and Engineering*, 191(17-18):1895–1908, 2002.

[85] F. Hausdorff. Dimension und äußeres Maß. *Mathematische Annalen*, 79(1):157–179, 1918.

[86] T. Heister, K. Mang, and T. Wick. Schur-type preconditioning of a phase-field fracture model in mixed form. In *accepted in PAMM*, volume 2021. Wiley Online Library, 2021.

[87] T. Heister, M. F. Wheeler, and T. Wick. A primal-dual active set method and predictor-corrector mesh adaptivity for computing fracture propagation using a phase-field approach. *Computer Methods in Applied Mechanics and Engineering*, 290:466–495, 2015.

[88] T. Heister and T. Wick. Parallel solution, adaptivity, computational convergence, and open-source code of 2d and 3d pressurized phase-field fracture problems. *PAMM*, 18(1):e201800353, 2018.

[89] T. Heister and T. Wick. pfm-cracks: A parallel-adaptive framework for phase-field fracture propagation. *Software Impacts*, 6:100045, 2020.

[90] M. A. Heroux, R. A. Bartlett, V. E. Howle, R. J. Hoekstra, J. J. Hu, T. G. Kolda, R. B. Lehoucq, K. R. Long, R. P. Pawlowski, E. T. Phipps, et al. An overview of the trilinos project. *ACM Transactions on Mathematical Software (TOMS)*, 31(3):397–423, 2005.

[91] M. A. Heroux, R. A. Bartlett, V. E. Howle, R. J. Hoekstra, J. J. Hu, T. G. Kolda, R. B. Lehoucq, K. R. Long, R. P. Pawlowski, E. T. Phipps, et al. Trilinos web page, 2021. [Online; accessed 25-November-2021].

[92] C. Hesch, A. J. Gil, R. Ortigosa, M. Dittmann, C. Bilgen, P. Betsch, M. Franke, A. Janz, and K. Weinberg. A framework for polyconvex large strain phase-field methods to fracture. *Computer Methods in Applied Mechanics and Engineering*, 317:649–683, 2017.

[93] M. Hintermüller, K. Ito, and K. Kunisch. The primal-dual active set strategy as a semismooth Newton method. *SIAM Journal on Optimization*, 13(3):865–888, 2002.

[94] N. A. Hocine, M. N. Abdelaziz, and A. Imad. Fracture problems of rubbers: J-integral estimation based upon η factors and an investigation on the strain energy density distribution as a local criterion. *International Journal of Fracture*, 117(1):1–23, 2002.

[95] G. A. Holzapfel. Nonlinear solid mechanics: a continuum approach for engineering science. *Meccanica*, 37(4):489–490, 2002.

[96] G. A. Holzapfel, R. Eberlein, P. Wriggers, and H. W. Weizsäcker. Large strain analysis of soft biological membranes: Formulation and finite element analysis. *Computer Methods in Applied Mechanics and Engineering*, 132(1-2):45–61, 1996.

[97] K. Ito and K. Kunisch. *Lagrange multiplier approach to variational problems and applications*. SIAM Series 15, 2008.

[98] D. Jodlbauer. *Parallel Multigrid Solvers for Nonlinear Coupled Field Problems*. PhD thesis, Johannes Kepler University Linz, Institute of Computational Mathematics, 2021.

[99] D. Jodlbauer, U. Langer, and T. Wick. Matrix-free multigrid solvers for phase-field fracture problems. *Computer Methods in Applied Mechanics and Engineering*, 372:113431, 2020.

[100] M. Kaliske, R. Behnke, R. Fleischhauer, K. Özenc, and I. M. Zreid. Theretical-numerical approaches to simulate fracture in polymeric materials. *Procedia Materials Science*, 3:2065–2070, 2014.

[101] G. Kanschat. Mixed finite element methods. 2017.

[102] N. Kikuchi and J. T. Oden. *Contact problems in elasticity: a study of variational inequalities and finite element methods*, volume 8. siam, 1988.

[103] D. Kinderlehrer and G. Stampacchia. *An introduction to variational inequalities and their applications*, volume 31. Siam, 1980.

[104] A. Klawonn and G. Starke. Block triangular preconditioners for nonsymmetric saddle point problems: field-of-values analysis. *Numerische Mathematik*, 81(4):577–594, 1999.

[105] M. Klüppel, G. Huang, and B. Bandow. Evaluation of tearing energy of elastomer materials. *Kautschuk, Gummi, Kunststoffe*, 61:656–659, 2008.

[106] L. Kolditz. Γ-convergence of a pressurized phase-field fracture model. Bachelor's thesis, Leibniz Universität Hannover, 2021.

[107] L. Kolditz and K. Mang. On the relation of Gamma-convergence parameters for pressure-driven quasi-static phase-field fracture. *Examples and Counterexamples*, 2:100047, 2022.

[108] R. Krause, A. Veeser, and M. Walloth. An efficient and reliable residual-type a posteriori error estimator for the Signorini problem. *Numerische Mathematik*, 130(1):151–197, 2015.

[109] E. Kreyszig. *Introductory functional analysis with applications*, volume 1. Wiley New York, 1978.

[110] M. Kronbichler, T. Heister, and W. Bangerth. High accuracy mantle convection simulation through modern numerical methods. *Geophysical Journal International*, 191(1):12–29, 2012.

[111] A. Kubo and Y. Umeno. Velocity mode transition of dynamic crack propagation in hyperviscoelastic materials: A continuum model study. *Scientific reports*, 7(1):1–8, 2017.

[112] C. Kuhn and R. Müller. A phase field model for fracture. In *PAMM: Proceedings in Applied Mathematics and Mechanics*, volume 8, pages 10223–10224. Wiley Online Library, 2008.

[113] A. Kumar, B. Bourdin, G. A. Francfort, and O. Lopez-Pamies. Revisiting nucleation in the phase-field approach to brittle fracture. *Journal of the Mechanics and Physics of Solids*, page 104027, 2020.

[114] A. Kumar, G. A. Francfort, and O. Lopez-Pamies. Fracture and healing of elastomers: A phase-transition theory and numerical implementation. *Journal of the Mechanics and Physics of Solids*, 112:523–551, 2018.

[115] O. Lampron, D. Therriault, and M. Lévesque. An efficient and robust monolithic approach to phase-field quasi-static brittle fracture using a modified newton method. *Computer Methods in Applied Mechanics and Engineering*, 386:114091, 2021.

[116] S. Lee, M. F. Wheeler, and T. Wick. Pressure and fluid-driven fracture propagation in porous media using an adaptive finite element phase field model. *Computer Methods in Applied Mechanics and Engineering*, 305:111 – 132, 2016.

[117] B. Li and N. Bouklas. A variational phase-field model for brittle fracture in polydisperse elastomer networks. *International Journal of Solids and Structures*, 182:193–204, 2020.

[118] X. Liu, J. Réthoré, and A. A. Lubrecht. An efficient matrix-free preconditioned conjugate gradient based multigrid method for phase field modeling of fracture in heterogeneous materials from 3d images. *Computer Methods in Applied Mechanics and Engineering*, 388:114266, 2022.

[119] P. J. Loew, B. Peters, and L. A. A. Beex. Fatigue phase-field damage modeling of rubber. *Constitutive Models for Rubber XI*, pages 408–412, 2019.

[120] P. J. Loew, B. Peters, and L. A. A. Beex. Rate-dependent phase-field damage modeling of rubber and its experimental parameter identification. *Journal of the Mechanics and Physics of Solids*, 127:266–294, 2019.

[121] D. S. Malkus and T. J. Hughes. Mixed finite element methods—reduced and selective integration techniques: a unification of concepts. *Computer Methods in Applied Mechanics and Engineering*, 15(1):63–81, 1978.

[122] T. K. Mandal, V. P. Nguyen, J.-Y. Wu, C. Nguyen-Thanh, and A. de Vaucorbeil. Fracture of thermo-elastic solids: Phase-field modeling and new results with an efficient monolithic solver. *Computer Methods in Applied Mechanics and Engineering*, 376:113648, 2021.

[123] K. Mang, A. Fehse, N. H. Kröger, and T. Wick. A mixed phase-field fracture model for crack propagation in punctured EPDM strips. *Theoretical and Applied Fracture Mechanics*, page 103076, 2021.

[124] K. Mang, M. Walloth, T. Wick, and W. Wollner. Mesh adaptivity for quasi-static phase-field fractures based on a residual-type a posteriori error estimator. *GAMM-Mitteilungen*, 43(1):e202000003, 2020.

[125] K. Mang, M. Walloth, T. Wick, and W. Wollner. Adaptive numerical simulation of a phase-field fracture model in mixed form tested on an L-shaped specimen with high poisson ratios. In *Numerical Mathematics and Advanced Applications ENUMATH 2019*, pages 1185–1193. Springer, 2021.

[126] K. Mang and T. Wick. Numerical methods for variational phase-field fracture problems. 2019.

[127] K. Mang and T. Wick. Numerical studies of different mixed phase-field fracture models for simulating crack propagation in punctured EPDM strips. In *14th WCCM-ECCOMAS Congress 2020*, volume 2100, 2021.

[128] K. Mang, T. Wick, and W. Wollner. A phase-field model for fractures in nearly incompressible solids. *Computational Mechanics*, 65(1):61–78, 2020.

[129] A. Mesgarnejad, B. Bourdin, and M. Khonsari. Validation simulations for the variational approach to fracture. *Computer Methods in Applied Mechanics and Engineering*, 290:420–437, 2015.

[130] C. Miehe, M. Hofacker, and F. Welschinger. A phase field model for rate-independent crack propagation: Robust algorithmic implementation based on operator splits. *Computer Methods in Applied Mechanics and Engineering*, 199:2765–2778, 2010.

[131] C. Miehe, L.-M. Schänzel, and H. Ulmer. Phase field modeling of fracture in multi-physics problems. part i. balance of crack surface and failure criteria for brittle crack propagation in thermo-elastic solids. *Computer Methods in Applied Mechanics and Engineering*, 294:449–485, 2015.

[132] C. Miehe, F. Welschinger, and M. Hofacker. Thermodynamically consistent phase-field models of fracture: variational principles and multi-field FE implementations. *International Journal for Numerical Methods in Fluids*, 83:1273–1311, 2010.

[133] A. Mikelić, M. F. Wheeler, and T. Wick. A quasi-static phase-field approach to pressurized fractures. *Nonlinearity*, 28(5):1371–1399, 2015.

[134] A. Mikelić, M. F. Wheeler, and T. Wick. Phase-field modeling through iterative splitting of hydraulic fractures in a poroelastic medium. *GEM - International Journal on Geomathematics*, 10(1), Jan 2019.

[135] D. B. Mumford and J. Shah. Optimal approximations by piecewise smooth functions and associated variational problems. *Communications on pure and applied mathematics*, 1989.

[136] J. Nocedal and S. J. Wright. *Numerical optimization*. Springer Series in Operations Research and Financial Engineering, 2006.

[137] R. R. M. Ozelo, P. Sollero, and A. L. A. Costa. An alternative technique to evaluate crack propagation path in hyperelastic materials. *Tire Science and Technology TSTCA*, 40(1):42–58, 2012.

[138] K. Pham, H. Amor, J.-J. Marigo, and C. Maurini. Gradient Damage Models and Their Use to Approximate Brittle Fracture. *International Journal of Damage Mechanics*, pages 1–36, May 2011.

[139] J. Plagge, A. Ricker, N. H. Kröger, P. Wriggers, and M. Klüppel. Efficient modeling of filled rubber assuming stress-induced microscopic restructurization. *International Journal of Engineering Science*, 151:103291, 2020.

[140] A. M. Quarteroni and A. Valli. *Domain decomposition methods for partial differential equations*. Oxford University Press, 1999.

[141] R. Rannacher. Numerische Mathematik 3 (Numerik von Problemen der Kontinuumsmechanik). *Institut für Angewandte Mathematik, Heidelberg*, 2008.

[142] A. Ricker and N. H. Kröger. Influence of various curing systems and carbon black content on the bulk modulus of EPDM rubber. *Constitutive Models for Rubber XI*, pages 200–205, 2019.

[143] R. S. Rivlin and A. G. Thomas. Rupture of rubber. I. characteristic energy for tearing. *Journal of polymer science*, 10(3):291–318, 1953.

[144] R. T. Rockafellar. Lagrange multipliers and optimality. *SIAM Review*, 35(2):183–238, 1993.

[145] D. Roucou, J. Diani, M. Brieu, and A. Mbiakop-Ngassa. Impact of strain-induced softening on the fracture of a carbon-black filled styrene butadiene rubber. *Constitutive Models for Rubber XI*, pages 528–532, 2019.

[146] D. Roucou, J. Diani, M. Brieu, and A. Mbiaskop-Ngassa. Critical strain energy release rate for rubbers: single edge notch tension versus pure shear tests. *International Journal of Fracture*, 216:31–39, 2019.

[147] D. Roucou, J. Diani, M. Brieu, J. F. Witz, and A. Mbiaskop-Ngassa. Experimental investigation of elastomer mode I fracture: An attempt to estimate the critical strain energy release rate using sent tests. *International Journal of Fracture*, 209:163–170, 2018.

[148] Y. Saad. *Iterative methods for sparse linear systems*. SIAM, 2003.

[149] R. J. Schaefer. Mechanical properties of rubber. *Harris' Shock and Vibration Handbook, Sixth edition, A. Piersol, T. Paez (Eds), McGraw-Hill Companies Inc*, pages 33–1, 2010.

[150] A. Schlüter, C. Kuhn, and R. Müller. Simulation of laser-induced controlled fracturing utilizing a phase field model. *Journal of Computing and Information Science in Engineering*, 17(2), 2017.

[151] M. Schmich. *Adaptive finite element methods for computing nonstationary incompressible flows*. PhD thesis, 2009.

[152] J. Schröder, P. Neff, and D. Balzani. A variational approach for materially stable anisotropic hyperelasticity. *International Journal of Solids and Structures*, 42(15):4352–4371, 2005.

[153] J. Schröder, T. Wick, S. Reese, P. Wriggers, R. Müller, S. Kollmannsberger, M. Kästner, A. Schwarz, M. Igelbüscher, N. Viebahn, et al. A selection of benchmark problems in solid mechanics and applied mathematics. *Archives of Computational Methods in Engineering*, 28(2):713–751, 2021.

[154] D. Silvester and A. Wathen. Fast iterative solution of stabilised stokes systems part ii: using general block preconditioners. *SIAM Journal on Numerical Analysis*, 31(5):1352–1367, 1994.

[155] I. N. Sneddon. The distribution of stress in the neighbourhood of a crack in an elastic solid. *Proc. R. Soc. Lond. A*, 187(1009):229–260, 1946.

[156] I. N. Sneddon and M. Lowengrub. *Crack problems in the classical theory of elasticity*. SIAM series in Applied Mathematics. John Wiley and Sons, Philadelphia, 1969.

[157] L. Sommer. *An Unfitted Discontinuous Galerkin Scheme for a Phase-field Approximation of Pressurized Fractures*. PhD thesis, Universitäts-und Landesbibliothek Münster, 2019.

[158] C. Steinke and M. Kaliske. A phase-field crack model based on directional stress decomposition. *Computational Mechanics*, 63(5):1019–1046, 2019.

[159] M. Strobl and T. Seelig. A novel treatment of crack boundary conditions in phase field models of fracture. *Pamm*, 15(1):155–156, 2015.

[160] K. Stüben. A review of algebraic multigrid. *Numerical Analysis: Historical Developments in the 20th Century*, pages 331–359, 2001.

[161] P. Šuštarič, M. R. R. Seabra, J. M. A. C. de Sa, and T. Rodič. Sensitivity analysis based crack propagation criterion for compressible and (near) incompressible hyperelastic materials. *Finite Elements in Analysis and Design*, 82:1–15, 2014.

[162] B. Talamini, Y. Mao, and L. Anand. Progressive damage and rupture in polymers. *Journal of the Mechanics and Physics of Solids*, 111:434–457, 2018.

[163] E. Tanné, T. Li, B. Bourdin, J.-J. Marigo, and C. Maurini. Crack nucleation in variational phase-field models of brittle fracture. *Journal of the Mechanics and Physics of Solids*, 110:80–99, 2018.

[164] R. Taylor. Isogeometric analysis of nearly incompressible solids. *International Journal for Numerical Methods in Engineering*, 87(1-5):273–288, 2011.

[165] T. E. Tezduyar, S. Mittal, S. Ray, and R. Shih. Incompressible flow computations with stabilized bilinear and linear equal-order-interpolation velocity-pressure elements. *Computer Methods in Applied Mechanics and Engineering*, 95(2):221–242, 1992.

[166] C. Timbrell, M. Wiehahn, G. Cook, and A. H. Muhr. Simulation of crack propagation in rubber. *Constitutive Models for Rubber III*, pages 11–20, 2003.

[167] A. Toselli and O. Widlund. *Domain decomposition methods-algorithms and theory*, volume 34. Springer Science & Business Media, 2006.

[168] R. S. Tuminaro and C. Tong. Parallel smoothed aggregation multigrid: Aggregation strategies on massively parallel machines. In *SC'00: Proceedings of the 2000 ACM/IEEE Conference on Supercomputing*, pages 5–5. IEEE, 2000.

[169] P. A. J. Van den Bogert, R. De Borst, G. T. Luiten, and J. Zeilmaker. Robust finite elements for 3d-analysis of rubber-like materials. *Engineering computations*, 1991.

[170] R. Verfürth. Error estimates for a mixed finite element approximation of the stokes equations. *RAIRO. Analyse numérique*, 18(2):175–182, 1984.

[171] B. Vexler and W. Wollner. Adaptive finite elements for elliptic optimization problems with control constraints. *SIAM Journal on Control and Optimization*, 47(1):509–534, 2008.

[172] K. Y. Volokh. Fracture as a material sink. *Materials Theory*, 1(3):1–9, 2017.

[173] M. Walloth. Residual-type a posteriori error estimator for a quasi-static signorini contact problem. *IMA Journal of Numerical Analysis*, 40(3):1937–1971, 2020.

[174] M. Walloth and W. Wollner. A posteriori estimator for the adaptive solution of a quasi-static fracture phase-field model with irreversibility constraints. *arXiv preprint arXiv:2106.09469*, 2021.

[175] D. Werner. *Funktionalanalysis*. Springer, 2004.

[176] M. F. Wheeler, T. Wick, and W. Wollner. An Augmented-Lagrangian method for the phase-field approach for pressurized fractures. *Computer Methods in Applied Mechanics and Engineering*, 271:69–85, 2014.

[177] T. Wick. *Adaptive finite element simulation of fluid-structure interaction with application to heart-valve dynamics*. PhD thesis, 2011.

[178] T. Wick. Solving monolithic fluid-structure interaction problems in arbitrary Lagrangian Eulerian coordinates with the `deal.II` library. *Archive of Numerical Software*, 1:1–19, 2013.

[179] T. Wick. Coupling fluid-structure interaction with phase-field fracture. *Journal of Computational Physics*, 327:67 – 96, 2016.

[180] T. Wick. Goal functional evaluations for phase-field fracture using PU-based DWR mesh adaptivity. *Computational Mechanics*, 57(6):1017–1035, 2016.

[181] T. Wick. An error-oriented Newton/Inexact Augmented Lagrangian Approach for Fully Monolithic Phase-Field Fracture Propagation. *SIAM Journal on Scientific Computing*, 39(4):B589–B617, 2017.

[182] T. Wick. Modified Newton methods for solving fully monolithic phase-field quasi-static brittle fracture propagation. *Computer Methods in Applied Mechanics and Engineering*, 325:577 – 611, 2017.

[183] T. Wick. Numerical methods for partial differential equations. Institute for Applied Mathematics, Leibniz Universitaet Hannover, Germany, 2018.

[184] T. Wick. *Multiphysics Phase-Field Fracture: Modeling, Adaptive Discretizations, and Solvers*, volume 28. Walter de Gruyter GmbH & Co KG, 2020.

[185] T. Wick. *Numerical methods for partial differential equations*. Hannover: Institutionelles Repositorium der Leibniz Universität Hannover, 2020.

[186] T. Wick. Dual-weighted residual a posteriori error estimates for a penalized phase-field slit discontinuity problem. *Computational Methods in Applied Mathematics*, 2021.

[187] T. Wihler. Locking-free adaptive discontinuous galerkin FEM for linear elasticity problems. *Mathematics of Computation*, 75(255):1087–1102, 2006.

[188] J. Wloka. *Partielle Differentialgleichungen: Sobolevräume und Randwertaufgaben*. Vieweg+ Teubner Verlag, 1982.

[189] J.-Y. Wu. A unified phase-field theory for the mechanics of damage and quasi-brittle failure. *Journal of the Mechanics and Physics of Solids*, 103:72–99, 2017.

[190] J.-Y. Wu. A geometrically regularized gradient-damage model with energetic equivalence. *Computer Methods in Applied Mechanics and Engineering*, 328:612–637, 2018.

[191] J.-Y. Wu and V. P. Nguyen. A length scale insensitive phase-field damage model for brittle fracture. *Journal of the Mechanics and Physics of Solids*, 119:20–42, 2018.

[192] J.-Y. Wu, V. P. Nguyen, C. T. Nguyen, D. Sutula, S. Sinaie, and S. P. Bordas. Phase-field modeling of fracture. *Advances in Applied Mechanics*, 53:1–183, 2020.

[193] B. Yin and M. Kaliske. Fracture simulation of viscoelastic polymers by the phase-field method. *Computational Mechanics*, 65(2):293–309, 2020.

[194] A. T. Zehnder. *Griffith Theory of Fracture*, pages 1570–1573. Springer US, Boston, MA, 2013.

[195] E. Zeidler. *Nonlinear Functional Analysis and Its Applications: II/B: Nonlinear Monotone Operators*. Springer Science & Business Media, 2013.

[196] X. Zhang, S. W. Sloan, C. Vignes, and D. Sheng. A modification of the phase-field model for mixed mode crack propagation in rock-like materials. *Computer Methods in Applied Mechanics and Engineering*, 322:123–136, 2017.

[197] H. Zheng, F. Liu, and X. Du. Complementarity problem arising from static growth of multiple cracks and mls-based numerical manifold method. *Computer Methods in Applied Mechanics and Engineering*, 295:150–171, 2015.

[198] S. Zhou, X. Zhuang, and T. Rabczuk. Phase-field modeling of fluid-driven dynamic cracking in porous media. *Computer Methods in Applied Mechanics and Engineering*, 350:169–198, 2019.

Acknowledgments

Most I thank my supervisor Prof. Dr. Thomas Wick, for his endless support and trust. Thanks for being open to discussions, being enthusiastic about changes, developments, and new ideas. I want to thank Prof. Dr. Winnifried Wollner and Dr. Mirjam Walloth for the fruitful discussions and working as a team in the Priority Program 1748 (SPP) over three years. In this regard, I thank the German Research Foundation for their support within the SPP 1748 and its speaker Prof. Dr.-Ing. habil. Jörg Schröder, for the additional financial support which gave me the chance to visit a summer school in Italy and attend a team mentoring course at the Leibniz Universität Hannover (LUH).
At the LUH, I thank all colleagues sincerely at the Institute for Applied Mathematics under the guidance of Prof. Dr. Sven Beuchler. Affiliated, I would like to thank Leon Kolditz for the enjoyable cooperation working on small but essential intermediate research questions within the SPP 1748 and further tasks. From the Deutsches Institut für Kautschuktechnologie e.V., Hannover, I thank Dr. Nils Hendrik Kröger, Andreas Fehse, and Pénélope Barbery for the pleasant collaboration and the exciting discussions on the conducted experiments and simulations. Thanks to Prof. Dr. Timo Heister from Clemson University, SC, USA, for inviting me in 2020 to spend one month in Clemson; special thanks for the helpful discussions on efficient preconditioning and its implementation.
As a GAMM Junior, I want to thank the GAMM for the nomination, their support for young researchers, and the other GAMM Juniors for the friendly events together, especially the successful organization of the first PreGAMM online in 2021.
Going with me not just in the time of my Ph.D., I owe my deepest gratitude to my parents, my sister, my grandparents, friends, and my boyfriend Marius. I appreciate their emotional support and thank you for listening, caring, and asking the right critical questions.

Katrin Mang,
Hanover, 2021

Curriculum vitae

Scientific vita

2018-today	Doctoral researcher and scientific assistant, supervised by Prof. Dr. Thomas Wick, Institute for Applied Mathematics, Leibniz Universität, Hannover
2015-2017	Study of Scientific Computing, Master of Science, Ruprecht-Karls-Universität Heidelberg, 2017, supervisor Prof. Dr. Vincent Heuveline
2011-2015	Study of Mathematics, Bachelor of Science, Ruprecht-Karls-Universität, Heidelberg, 2015, supervisor Prof. Dr. Thomas Richter

Publications

[1] K. Mang, A. Fehse, N. H. Kröger, T. Wick, *A mixed phase-field fracture model for crack propagation in punctured EPDM strips*, 2021, A mixed phase-field fracture model for crack propagation in punctured EPDM strips, Theoretical and Applied Fracture Mechanics 2021, https://doi.org/10.1016/j.tafmec.2021.103076

[2] K. Mang, T. Wick, W. Wollner, *A phase-field model for fractures in nearly incompressible solids*, Computational Mechanics, 65(1), pp. 61-78, 2020, https://link.springer.com/article/10.1007/s00466-019-01752-w

[3] K. Mang, M. Walloth, T. Wick, W. Wollner, *Mesh adaptivity for quasi-static phase-field fractures based on a residual-type a posteriori error estimator*, GAMM-Mitteilungen, 43(1), e202000003, 2019, https://onlinelibrary.wiley.com/doi/abs/10.1002/gamm.202000003

[4] A. Fehse, N. H. Kröger, K. Mang and T. Wick, *Crack path comparisons of a mixed phase-field fracture model and experiments in punctured EPDM strips*, PAMM 20 (1) pamm.202000335, 2020, https://onlinelibrary.wiley.com/doi/full/10.1002/pamm.202000335

[5] K. Mang, M. Walloth, T. Wick, W. Wollner, *Adaptive Numerical Simulation of a Phase-field Fracture Model in Mixed Form tested on an L-shaped Specimen with High Poisson Ratios*, in Numerical Mathematics and Advanced Applications ENUMATH 2019, Vol. 139, Springer, pp. 1185-1193, 2021, https://link.springer.com/chapter/10.1007/978-3-030-55874-1_118

[6] J. Schröder, T. Wick, S. Reese, P. Wriggers, R. Müller, S. Kollmannsberger, M. Kästner, A. Schwarz, M. Igelbüscher, N. Viebahn, H. R. Bayat, S. Wulfinghoff, K. Mang, E. Rank, T. Bog, D. D'Angella, M. Elhaddad, P. Hennig, A. Düster, W. Garhuom, S. Hubrich, M. Walloth, W. Wollner, C. Kuhn, and T. Heister, *A selection of benchmark problems in solid mechanics and applied mathematics*, Arch. Comput. Methods Eng., vol. 28, 2021, pp. 713-751, https://link.springer.com/article/10.1007/s11831-020-09477-3

[7] K. Mang, T. Wick, *Numerical studies of different mixed phase-field fracture models for simulating crack propagation in punctured EPDM strips*, in: 14th World Congress on Computational Mechanics (WCCM), ECCOMAS Congress 2020, https://www.scipedia.com/public/Mang_Wick_2021a

[8] S. Basava, K. Mang, M. Walloth, T. Wick, W. Wollner, *Adaptive and Pressure-Robust Discretization of Incompressible Pressure-Driven Phase-Field Fracture*, arXiv:2006.16566, 2020, https://arxiv.org/abs/2006.16566

[9] L. Kolditz, K. Mang, *On the relation of Gamma-convergence parameters for pressure-driven quasi-static phase-field fracture.* Examples and Counterexamples 2, 2022, 100047, https://www.sciencedirect.com/science/article/pii/S2666657X22000015

[10] K. Mang, T. Wick, *Numerical Methods for Variational Phase-Field Fracture Problems.* Hannover: Institutionelles Repositorium der Leibniz Universität Hannover, 207 pages, 2019, https://www.repo.uni-hannover.de/handle/123456789/5175

[11] S. Gawlok, P. Gerstner, S. Haupt, V. Heuveline, J. Kratzke, P. Lösel, K. Mang, M. Schmidtobreick, N. Schoch, N. Schween and others, *Hiflow3–technical report on release 2.0.* Preprint Series of the Engineering Mathematics and Computing Lab 06, 2017, https://journals.ub.uni-heidelberg.de/index.php/emcl-pp/article/view/42879